Chou (1945) proposed modeling the exact equation for ϵ. In terms of this formulation, the kinematic eddy viscosity and turbulence length scale are

$$\nu_T \sim k^2/\epsilon, \qquad \ell \sim k^{3/2}/\epsilon \tag{4.32}$$

Rotta (1951) first suggested a transport equation for the turbulence length scale and later (1968) proposed an equation for the product of k and ℓ. In either case,

$$\nu_T \sim k^{1/2}\ell, \qquad \epsilon \sim k^{3/2}/\ell \tag{4.33}$$

More recently, Zeierman and Wolfshtein (1986) introduced a transport equation for the product of k and a **turbulence dissipation time**, τ, which is essentially the reciprocal of Kolmogorov's ω. Also, Speziale, Abid and Anderson (1990) have postulated an equation for τ. For these models,

$$\nu_T \sim k\tau, \qquad \ell \sim k^{1/2}\tau, \qquad \epsilon \sim k/\tau \tag{4.34}$$

Regardless of the choice of the second variable in our two-equation model, we see a recurring theme. Specifically, the dissipation, eddy viscosity and length scale are all related on the basis of dimensional arguments. Historically, dimensional analysis has been one of the most powerful tools available for deducing and correlating properties of turbulent flows. However, we should always be aware that while dimensional analysis is extremely useful, it unveils nothing about the physics underlying its implied scaling relationships. The physics is in the choice of variables.

One of the key conclusions of the 1980-81 AFOSR-HTTM-Stanford Conference on Complex Turbulent Flows was that the greatest amount of uncertainty about two-equation models lies in the second transport equation complementing the equation for k. Further, it was even unclear about what the most appropriate choice of the second dependent variable is. In the quarter century following the Conference, interesting developments have occurred, most notably with the k-ω model, that help clear up most of the uncertainty.

Before proceeding to details of two-equation models, it is worthwhile to pause and note the following. As with one-equation models, there is no fundamental reason that ν_T should depend only upon turbulence parameters such as k, ℓ, ϵ or ω. In general, the ratio of individual Reynolds stresses to mean strain rate components depends upon both mean-flow and turbulence scales. Thus, two-equation turbulence models are no more likely than one-equation models to apply universally to turbulent flows, and can be expected to be inaccurate for many non-equilibrium turbulent flows.

Additionally, some researchers even argue that the addition of another differential equation invites unexpected numerical difficulties and miscellaneous unintended mathematical anomalies. We will indeed see some of this behavior

as we investigate two-equation turbulence models, and what has been done to deal with the additional complexities attending their implementation.

4.3.1 The k-ω Model

As noted above, Kolmogorov (1942) proposed the first two-equation model of turbulence. Kolmogorov chose the kinetic energy of the turbulence as one of his turbulence parameters and, like Prandtl (1945), modeled the differential equation governing its behavior. His second parameter was the dissipation per unit turbulence kinetic energy, ω. In his k-ω model, ω satisfies a differential equation similar to the equation for k. With no prior knowledge of Kolmogorov's work, Saffman (1970) formulated a k-ω model that would prove superior to the Kolmogorov model. As part of the Imperial College efforts on two-equation models, Spalding [see Launder and Spalding (1972)] offered an improved version of the Kolmogorov model that removed some of its flaws.

Shortly after formulation of Saffman's model and continuing to the present time, Wilcox et al. [Wilcox and Alber (1972), Saffman and Wilcox (1974), Wilcox and Traci (1976), Wilcox and Rubesin (1980), Wilcox (1988a) and Wilcox (1998)] have pursued further development and application of k-ω turbulence models. Coakley (1983) has developed a $k^{1/2}$-ω model. Speziale, Abid and Anderson (1990), Menter (1992c), Peng, Davidson and Holmberg (1997), Kok (2000) and Hellsten (2005) have also devised k-ω models. Robinson, Harris and Hassan (1995) have developed a k-ζ model, where $\zeta \sim \omega^2$ is **enstrophy**, i.e., the RMS fluctuating vorticity.

In formulating his model, Kolmogorov referred to ω as "the rate of dissipation of energy in unit volume and time." To underscore its physical relation to the " 'external scale' of turbulence, ℓ," he also called it "some mean 'frequency' determined by $\omega = ck^{1/2}/\ell$, where c is a constant." On the one hand, the reciprocal of ω is the time scale on which dissipation of turbulence energy occurs. While the actual process of dissipation takes place in the smallest eddies, the rate of dissipation is the transfer rate of turbulence kinetic energy to the smallest eddies. Hence, it is set by the properties of the large eddies, and thus scales with k and ℓ, wherefore ω is indirectly associated with dissipative processes. On the other hand, in analogy to molecular viscosity, we expect the eddy viscosity to be proportional to the product of length and velocity scales characteristic of turbulent fluctuations, which is consistent with Kolmogorov's argument that $\omega \sim k^{1/2}/\ell$. Of course, we should keep in mind that analogies between molecular and turbulent processes are not trustworthy, and Kolmogorov's argument is essentially an exercise in dimensional analysis, not fundamental physics.

The development of the Kolmogorov model (1942) is quite brief and doesn't even establish values for all of the closure coefficients. Since little formal development of the equations is given, we can only speculate about how this great

turbulence researcher may have arrived at his model equations. Since he makes no specific reference to any exact equations, it seems unlikely that he attempted to close the k equation or other moments of the Navier-Stokes equation term by term. Rather, as the great believer in the power of dimensional analysis that he was, it is easy to imagine that Kolmogorov's original reasoning may have gone something like this.

- Since k already appears in the postulated constitutive relation [Equation (4.8)], it is plausible that $\nu_T \propto k$.
- The dimensions of ν_T are (length)^2/(time) while the dimensions of k are (length)^2/(time)^2.
- Consequently ν_T/k has dimensions (time).
- Turbulence dissipation ϵ has dimensions (length)^2/(time)^3.
- Consequently ϵ/k has dimensions 1/(time).
- We can close Equations (4.8) and (4.11) by introducing a variable with dimensions (time) or 1/(time).

The next step is to postulate an equation for ω. In doing so, the avenue that Kolmogorov took was to recognize that there is a fairly small number of physical processes commonly observed in the motion of a fluid. The most common processes are unsteadiness, convection (often referred to as advection), diffusion, dissipation, dispersion and production. Combining physical reasoning with dimensional analysis, Kolmogorov postulated the following equation for ω.

$$\frac{\partial \omega}{\partial t} + U_j \frac{\partial \omega}{\partial x_j} = -\beta \omega^2 + \frac{\partial}{\partial x_j}\left[\sigma \nu_T \frac{\partial \omega}{\partial x_j}\right] \tag{4.35}$$

We have taken some notational liberties in writing Equation (4.35), and β and σ are two new closure coefficients. This equation has four particularly noteworthy features. **First**, there is no analog to the k-equation's turbulence production term. The absence of a production term is consistent with Kolmogorov's notion that ω is associated with the smallest scales of the turbulence, and thus has no direct interaction with the mean motion. His logic is flawed on this issue as the large-scale, energy-bearing eddies are primarily responsible for determining the appropriate time scale of the turbulence, and the rate of dissipation itself. **Second**, the equation is written in terms of ω rather than ω^2. As will be shown when we analyze the defect layer in Subsection 4.6.2, Kolmogorov's decision to write his equation in terms of ω was a somewhat prophetic choice. **Third**, there is no molecular diffusion term so that this equation applies strictly to high-Reynolds-number flows and cannot be integrated through the viscous sublayer as it stands. **Fourth**, it is entirely empirical, guided by physical reasoning.

The interpretation of ω has behaved a bit like the turbulent fluctuations it is intended to describe. Saffman (1970) described ω as "a frequency characteristic of the turbulence decay process under its self-interaction." He stated further, "The rough idea is that ω^2 is the mean square vorticity of the 'energy containing eddies' and $[k]$ is the kinetic energy of the motion induced by this vorticity." Spalding [Launder and Spalding (1972)], Wilcox and Alber (1972) and Robinson, Harris and Hassan (1995) identify ω as the RMS fluctuating vorticity, so that ω^2 is twice the enstrophy. Wilcox and Rubesin (1980), Wilcox (1988a, 1998) and Speziale et al. (1990) regard ω simply as the ratio of ϵ to k.

The ω equation has changed as the k-ω model has evolved over the past six decades. A production term has been added by all model developers subsequent to Kolmogorov. Like Kolmogorov, Wilcox (1988a, 1998), Speziale et al. (1990), Peng et al. (1997), Kok (2000) and Hellsten (2005) write the equation for ω in terms of ω, while most other models use an equation for ω^2. The following version of the k-ω model dramatically improves predictive accuracy of the Wilcox (1988a) model for free shear flows and strongly separated flows.[2]

Kinematic Eddy Viscosity:

$$\nu_T = \frac{k}{\tilde{\omega}}, \qquad \tilde{\omega} = \max\left\{\omega, \; C_{lim}\sqrt{\frac{2S_{ij}S_{ij}}{\beta^*}}\right\}, \qquad C_{lim} = \frac{7}{8} \tag{4.36}$$

Turbulence Kinetic Energy:

$$\frac{\partial k}{\partial t} + U_j\frac{\partial k}{\partial x_j} = \tau_{ij}\frac{\partial U_i}{\partial x_j} - \beta^* k\omega + \frac{\partial}{\partial x_j}\left[\left(\nu + \sigma^*\frac{k}{\omega}\right)\frac{\partial k}{\partial x_j}\right] \tag{4.37}$$

Specific Dissipation Rate:

$$\frac{\partial \omega}{\partial t} + U_j\frac{\partial \omega}{\partial x_j} = \alpha\frac{\omega}{k}\tau_{ij}\frac{\partial U_i}{\partial x_j} - \beta\omega^2 + \frac{\sigma_d}{\omega}\frac{\partial k}{\partial x_j}\frac{\partial \omega}{\partial x_j} + \frac{\partial}{\partial x_j}\left[\left(\nu + \sigma\frac{k}{\omega}\right)\frac{\partial \omega}{\partial x_j}\right] \tag{4.38}$$

Closure Coefficients and Auxiliary Relations:

$$\alpha = \frac{13}{25}, \quad \beta = \beta_o f_\beta, \quad \beta^* = \frac{9}{100}, \quad \sigma = \frac{1}{2}, \quad \sigma^* = \frac{3}{5}, \quad \sigma_{do} = \frac{1}{8} \tag{4.39}$$

$$\sigma_d = \begin{cases} 0, & \dfrac{\partial k}{\partial x_j}\dfrac{\partial \omega}{\partial x_j} \le 0 \\ \sigma_{do}, & \dfrac{\partial k}{\partial x_j}\dfrac{\partial \omega}{\partial x_j} > 0 \end{cases} \tag{4.40}$$

[2]These equations can be used for general compressible flows by replacing ν, ν_T, k/ω and $k/\tilde{\omega}$ by $\mu = \rho\nu$, $\mu_T = \rho\nu_T$, $\rho k/\omega$ and $\rho k/\tilde{\omega}$, respectively, and multiplying all but the diffusion terms by ρ. Also, a mean-energy and equation of state must be added — see Subsection 5.4.7 for complete details.

$$\beta_o = 0.0708, \quad f_\beta = \frac{1+85\chi_\omega}{1+100\chi_\omega}, \quad \chi_\omega \equiv \left| \frac{\Omega_{ij}\Omega_{jk}S_{ki}}{(\beta^*\omega)^3} \right| \tag{4.41}$$

$$\epsilon = \beta^*\omega k \quad \text{and} \quad \ell = k^{1/2}/\omega \tag{4.42}$$

To avoid confusion, from this point on, we will refer to Equations (4.36) – (4.42) as the **Wilcox (2006) k-ω model.**

The tensors Ω_{ij} and S_{ij} appearing in Equation (4.41) are the mean-rotation and mean-strain-rate tensors, respectively defined by

$$\Omega_{ij} = \frac{1}{2}\left(\frac{\partial U_i}{\partial x_j} - \frac{\partial U_j}{\partial x_i}\right), \qquad S_{ij} = \frac{1}{2}\left(\frac{\partial U_i}{\partial x_j} + \frac{\partial U_j}{\partial x_i}\right) \tag{4.43}$$

As can be easily verified, the quantity χ_ω is zero for two-dimensional flows. The dependence of β on χ_ω, patterned after the work of Pope (1978), has a significant effect for round and radial jets.

The most important differences between this version of the k-ω model and earlier versions created by Wilcox et al. are addition of a "cross-diffusion" term and a built-in "stress-limiter" modification that makes the eddy viscosity a function of k, ω and, effectively, the ratio of turbulence-energy production to turbulence-energy dissipation.

The term in Equation (4.38) proportional to σ_d is known as **cross diffusion**. The addition of cross diffusion to the ω equation was first suggested by Speziale (1990) as a remedy for the original k-ω model's sensitivity to the freestream value of ω. While Speziale and others, e.g., Menter (1992c), Wilcox (1993), Kok (2000) and Hellsten (2005) have succeeded in using cross diffusion to eliminate boundary-condition sensitivity, usually it has come at the expense of the ability to make reasonable predictions for free shear flows. Strictly speaking, models created in this spirit will be limited in applicability to wall-bounded flows.

The **stress-limiter** modification, i.e., the dependence of ν_T upon $\tilde{\omega}$ rather than strictly ω, was first introduced by Coakley (1983) and later implemented by Menter (1992c) and Durbin (1996). Huang (1999) shows that limiting the magnitude of the eddy viscosity when turbulence-energy production exceeds its dissipation yields larger separation bubbles and greatly improves incompressible- and transonic-flow predictions. Kandula and Wilcox (1995), for example, have verified for a transonic airfoil that it improves predictive accuracy of the k-ω model without cross diffusion and **blending functions**[3] and/or nonlinear constitutive relations such as those implemented by Menter (1992c) and Hellsten (2005). In point of fact, the success that has been achieved with the k-ω model stated in Equations (4.36) – (4.42) demonstrates that blending functions add little advantage and counter the elegance and simplicity of the k-ω model.

[3]Blending functions are designed to make closure coefficients α, β, β^*, σ, σ^* and σ_d assume one set of values near a solid boundary and another set near the edge of a shear layer.

The improvements to the k-ω model represent a significant expansion of its range of applicability. As we will see in the applications addressed in this Chapter and in Chapter 5, the new model retains the strengths of previous versions of the k-ω model. The model's improvement over earlier versions lies in its accuracy for free shear flows and for even more complicated separated flows. When we proceed to applications, we will see the following features of the k-ω model defined in Equations (4.36) – (4.42).

- The model is as accurate as the Wilcox (1988a) model for attached boundary layers, mildly separated flows and backward-facing steps. *This is important* because the Wilcox (1988a) model predicts properties for such flows that are in very close agreement with measurements. The new model is nearly identical for all attached boundary-layer computations, mildly separated flows and backward-facing steps attempted to date.

- The model's predicted free shear flow spreading rates are much closer to measurements, so that it is applicable to both wall-bounded and free shear flows. *Since most complex turbulent flows include both types of regions, this is a minimum requirement for any turbulence model that is proposed for use in complex flows.* With the exception of the enstrophy-equation model developed by Robinson, Harris and Hassan (1995) — using 11 closure coefficients and 2 closure functions — no other two-equation model known to this author satisfies this requirement.

- The model provides greatly improved predictions for shock-separated flows without introducing any compressibility modifications to the model. Chapter 5 includes comparisons of measurements with model predictions for Mach numbers from transonic to hypersonic speeds that reflect the model's extended range of applicability. Earlier versions of the k-ω model required compressibility modifications to achieve reasonable results.

4.3.2 The k-ϵ Model

By far, the most popular two-equation model until the last decade of the twentieth century was the k-ϵ model. The earliest development efforts based on this model were those of Chou (1945), Davidov (1961) and Harlow and Nakayama (1968). Widespread use of the model began with the version introduced by Jones and Launder (1972). Launder and Sharma (1974) subsequently "retuned" the model's closure coefficients and created what is generally referred to as the **Standard k-ϵ model**.

Again, we begin with Equations (4.8) and (4.11). In formulating the k-ϵ model, the idea is to derive the exact equation for ϵ and to find suitable closure

approximations for the exact equation governing its behavior. Recall that ϵ is defined by Equation (4.5). The exact equation for ϵ is derived by taking the following moment of the Navier-Stokes equation:

$$2\nu\overline{\frac{\partial u_i'}{\partial x_j}\frac{\partial}{\partial x_j}\left[\mathcal{N}(u_i)\right]} = 0 \tag{4.44}$$

where $\mathcal{N}(u_i)$ is the Navier-Stokes operator defined in Equation (2.26). After a considerable amount of algebra, the following exact equation for ϵ results.

$$\begin{aligned}\frac{\partial \epsilon}{\partial t} + U_j\frac{\partial \epsilon}{\partial x_j} = &-2\nu\left[\overline{u_{i,k}'u_{j,k}'} + \overline{u_{k,i}'u_{k,j}'}\right]\frac{\partial U_i}{\partial x_j} - 2\nu\,\overline{u_k'u_{i,j}'}\frac{\partial^2 U_i}{\partial x_k \partial x_j}\\ &-2\nu\,\overline{u_{i,k}'u_{i,m}'u_{k,m}'} - 2\nu^2\overline{u_{i,km}'u_{i,km}'}\\ &+\frac{\partial}{\partial x_j}\left[\nu\frac{\partial \epsilon}{\partial x_j} - \nu\,\overline{u_j'u_{i,m}'u_{i,m}'} - 2\frac{\nu}{\rho}\overline{p_{,m}'u_{j,m}'}\right]\end{aligned} \tag{4.45}$$

This equation is far more complicated than the turbulence kinetic energy equation and involves several new unknown double and triple correlations of fluctuating velocity, pressure and velocity gradients. These correlations are essentially impossible to measure with any degree of accuracy so that there is presently little hope of finding reliable guidance from experimentalists regarding suitable closure approximations. DNS studies [e.g. Mansour, Kim and Moin (1988)] provide some insight into the exact ϵ transport equation for low-Reynolds-number flows. However, the database for establishing closure approximations similar to those used for the k equation remains very sparse.

Many researchers have proceeded undaunted by the lack of a rational basis for establishing closure approximations with a feeling that using Equation (4.45) as their foundation adds rigor to their approach. The strongest claim that can actually be made is that conventional closure approximations used for Equation (4.45) are dimensionally correct. This is not very different from the Kolmogorov (1942) and Saffman (1970) approaches that are guided almost exclusively by physical reasoning and dimensional analysis. An important point we should keep in mind is to **avoid modeling the differential equations rather than the physics of turbulence**. That is not to say we should avoid any reference to the differential equations, for then we might formulate a model that violates a fundamental physical feature of the Navier-Stokes equation. Rather, we should avoid deluding ourselves by thinking that the **drastic surgery** approach to something as complex as Equation (4.45) is any more rigorous than dimensional analysis.

Even if we had demonstrably accurate closure approximations for the exact ϵ transport equation, there is a serious question of their relevance to our basic closure problem. That is, the length or time scale required is that of the energy-containing, Reynolds-stress-bearing eddies rather than the dissipating eddies represented by the exact ϵ equation. So, we must ask whether the modeled

equation for ϵ represents the dissipation as such [as Equation (4.45) does], or whether it is actually an empirical equation for the rate of energy transfer from the large eddies (equal, of course, to the rate of dissipation in the small eddies). The answer seems clear since the closure approximations normally used parameterize the various terms in the modeled ϵ equation as functions of large-eddy scales (our use of dimensional analysis does this implicitly). Consequently, the relation between the modeled equation for ϵ and the exact equation is so tenuous as not to need serious consideration. The **Standard k-ϵ model** is as follows.

Kinematic Eddy Viscosity:

$$\nu_T = C_\mu k^2/\epsilon \tag{4.46}$$

Turbulence Kinetic Energy:

$$\frac{\partial k}{\partial t} + U_j \frac{\partial k}{\partial x_j} = \tau_{ij}\frac{\partial U_i}{\partial x_j} - \epsilon + \frac{\partial}{\partial x_j}\left[(\nu + \nu_T/\sigma_k)\frac{\partial k}{\partial x_j}\right] \tag{4.47}$$

Dissipation Rate:

$$\frac{\partial \epsilon}{\partial t} + U_j \frac{\partial \epsilon}{\partial x_j} = C_{\epsilon 1}\frac{\epsilon}{k}\tau_{ij}\frac{\partial U_i}{\partial x_j} - C_{\epsilon 2}\frac{\epsilon^2}{k} + \frac{\partial}{\partial x_j}\left[(\nu + \nu_T/\sigma_\epsilon)\frac{\partial \epsilon}{\partial x_j}\right] \tag{4.48}$$

Closure Coefficients and Auxiliary Relations:

$$C_{\epsilon 1} = 1.44, \quad C_{\epsilon 2} = 1.92, \quad C_\mu = 0.09, \quad \sigma_k = 1.0, \quad \sigma_\epsilon = 1.3 \tag{4.49}$$

$$\omega = \epsilon/(C_\mu k) \quad \text{and} \quad \ell = C_\mu k^{3/2}/\epsilon \tag{4.50}$$

As noted above, the Launder-Sharma (1974) model is known as the Standard k-ϵ model. In addition to the equations quoted here, it involves viscous damping functions, which are discussed in Section 4.9.

A more recent version of the k-ϵ model has been developed by Yakhot and Orszag (1986) [see also Yakhot et al. (1992)]. Using techniques from renormalization group theory, they have developed what is known as the RNG k-ϵ model. The eddy viscosity, k and ϵ are still given by Equations (4.46), (4.47) and (4.48). However, the model uses a modified coefficient, $C_{\epsilon 2}$, defined by

$$C_{\epsilon 2} \equiv \tilde{C}_{\epsilon 2} + \frac{C_\mu \lambda^3 (1 - \lambda/\lambda_o)}{1 + \beta\lambda^3}, \qquad \lambda \equiv \frac{k}{\epsilon}\sqrt{2S_{ij}S_{ji}} \tag{4.51}$$

The closure coefficients for the RNG k-ϵ model are[4]

$$C_{\epsilon 1} = 1.42, \quad \tilde{C}_{\epsilon 2} = 1.68, \quad C_\mu = 0.085, \quad \sigma_k = 0.72, \quad \sigma_\epsilon = 0.72 \tag{4.52}$$

$$\beta = 0.012, \quad \lambda_o = 4.38 \tag{4.53}$$

[4]This version of the RNG k-ϵ model has been gleaned from the open literature. A proprietary improved version exists, but is available only in commercial computer programs for general turbulent-flow applications.

4.3.3 Other Two-Equation Models

Two-equation models based on the turbulence length scale, ℓ, and the turbulence time scale, τ, have received less attention than k-ω and k-ϵ models. Generally speaking, the level of agreement between measurements and predictions made with other models is comparable to k-ω and k-ϵ predictions for simple constant-pressure flows, but these models have not been pursued to any great extent. This subsection presents a brief overview of length-scale and time-scale models. More details can be found in the various papers referenced in the discussion.

The proposed foundation for Rotta's (1968) k-$k\ell$ model is the **two-point velocity correlation tensor** defined in Equation (2.49), viz.,

$$R_{ij}(\mathbf{x}, t; \mathbf{r}) = \overline{u_i'(\mathbf{x}, t)\; u_j'(\mathbf{x} + \mathbf{r}, t)} \tag{4.54}$$

As discussed in Subsection 2.5.2, the turbulence kinetic energy is simply one half the trace of R_{ij} with a displacement $\mathbf{r} = \mathbf{0}$. Rotta's second variable is the product of k and the **integral length scale**, ℓ, which is the integral of R_{ii} over all displacements, $r = |\mathbf{r}|$. Thus Rotta's variables are given by

$$k = \frac{1}{2} R_{ii}(\mathbf{x}, t; \mathbf{0}) \qquad \text{and} \qquad k\ell = \frac{3}{16} \int_{-\infty}^{\infty} R_{ii}(\mathbf{x}, t; r)\; dr \tag{4.55}$$

As with attempts to model the exact dissipation equation, no particular advantage has been gained by introducing the two-point velocity correlation tensor. While an exact equation for $k\ell$ can indeed be derived, Rotta (1968) still had to perform drastic surgery on the exact equation. Using standard closure approximations based largely on the strength of dimensional analysis, the following modeled version of the exact $k\ell$ equation results.

$$\begin{aligned} \frac{\partial}{\partial t}(k\ell) + U_j \frac{\partial}{\partial x_j}(k\ell) &= C_{L1} \ell \tau_{ij} \frac{\partial U_i}{\partial x_j} - C_{L2} k^{3/2} \\ &+ \frac{\partial}{\partial x_j} \left[\nu \frac{\partial}{\partial x_j}(k\ell) + (\nu_T / \sigma_{L1}) \ell \frac{\partial k}{\partial x_j} + (\nu_T / \sigma_{L2}) k \frac{\partial \ell}{\partial x_j} \right] \end{aligned} \tag{4.56}$$

For this model, k and ν_T are given by Equations (4.13) and (4.14). Rodi and Spalding (1970) and Ng and Spalding (1972) developed this model further. More recently, Smith (1990) has pursued development of a k-$k\ell$ model. Smith (1994) and Benay and Servel (2001) have developed k-ℓ models for which the dependent variable is ℓ rather than $k\ell$. Ng and Spalding found that for wall-bounded flows, the closure coefficient C_{L2} must vary with distance from the surface. They propose the following set of closure coefficients.

$$C_{L1} = 0.98, \quad C_{L2} = 0.059 + 702(\ell/y)^6, \quad C_D = 0.09, \quad \sigma_k = \sigma_{L1} = \sigma_{L2} = 1 \tag{4.57}$$

On a similar tack, Zeierman and Wolfshtein (1986) base their model upon the **autocorrelation tensor** defined in Equation (2.43), i.e.,

$$\mathcal{R}_{ij}(\mathbf{x}, t; t') = \overline{u_i'(\mathbf{x}, t) u_j'(\mathbf{x}, t + t')} \tag{4.58}$$

The turbulence kinetic energy is half the trace of $\mathcal{R}_{ij}$ with $t' = 0$, while the **integral time scale** is proportional to the integral of $\mathcal{R}_{ii}$ over all possible values of t'. Thus,

$$k = \frac{1}{2}\mathcal{R}_{ii}(\mathbf{x}, t; 0) \quad \text{and} \quad k\tau = \frac{1}{2}\int_0^\infty \mathcal{R}_{ii}(\mathbf{x}, t; t')\, dt' \tag{4.59}$$

The Zeierman-Wolfshtein k-$k\tau$ model is as follows.

Kinematic Eddy Viscosity:

$$\nu_T = C_\mu k\tau \tag{4.60}$$

Turbulence Kinetic Energy:

$$\frac{\partial k}{\partial t} + U_j \frac{\partial k}{\partial x_j} = \tau_{ij}\frac{\partial U_i}{\partial x_j} - \frac{k}{\tau} + \frac{\partial}{\partial x_j}\left[(\nu + \nu_T/\sigma_k)\frac{\partial k}{\partial x_j}\right] \tag{4.61}$$

Integral Time Scale:

$$\begin{aligned}\frac{\partial}{\partial t}(k\tau) + U_j \frac{\partial}{\partial x_j}(k\tau) &= C_{\tau 1}\tau\tau_{ij}\frac{\partial U_i}{\partial x_j} - C_{\tau 2}k \\ &\quad + \frac{\partial}{\partial x_j}\left[(\nu + \nu_T/\sigma_\tau)\frac{\partial}{\partial x_j}(k\tau)\right]\end{aligned} \tag{4.62}$$

Closure Coefficients and Auxiliary Relations:

$$C_{\tau 1} = 0.173, \quad C_{\tau 2} = 0.225, \quad C_\mu = 0.09, \quad \sigma_k = 1.46, \quad \sigma_\tau = 10.8 \tag{4.63}$$

$$\omega = 1/(C_\mu \tau), \qquad \epsilon = k/\tau \qquad \text{and} \qquad \ell = C_\mu k^{1/2}\tau \tag{4.64}$$

Note that because the eddy viscosity is proportional to $k\tau$, Equation (4.62) can also be regarded as an equation for ν_T.

Speziale, Abid and Anderson (1990) have taken a different approach in devising a k-τ model. Specifically, they introduce the formal change of dependent variables $\epsilon = k/\tau$ and transform the Standard k-ϵ model. The resulting equation for τ is as follows.

$$\begin{aligned}\frac{\partial \tau}{\partial t} + U_j \frac{\partial \tau}{\partial x_j} &= (1 - C_{\epsilon 1})\frac{\tau}{k}\tau_{ij}\frac{\partial U_i}{\partial x_j} + (C_{\epsilon 2} - 1) \\ &\quad + \frac{\partial}{\partial x_j}\left[(\nu + \nu_T/\sigma_{\tau 2})\frac{\partial \tau}{\partial x_j}\right] \\ &\quad + \frac{2}{k}(\nu + \nu_T/\sigma_{\tau 1})\frac{\partial k}{\partial x_k}\frac{\partial \tau}{\partial x_k} - \frac{2}{\tau}(\nu + \nu_T/\sigma_{\tau 2})\frac{\partial \tau}{\partial x_k}\frac{\partial \tau}{\partial x_k}\end{aligned} \tag{4.65}$$

Speziale, Abid and Anderson use the following revised set of closure coefficient values for their k-τ model that make it a bit different from the Standard k-ϵ model.

$$C_{\epsilon 1} = 1.44, \quad C_{\epsilon 2} = 1.83, \quad C_\mu = 0.09, \quad \sigma_k = \sigma_{\tau 1} = \sigma_{\tau 2} = 1.36 \tag{4.66}$$

In summary, the models listed above are representative of the various two-equation models that have been devised since Kolmogorov's (1942) k-ω model. While other models have been created, the intent of this text is to study models in a generic sense, as opposed to creating an encyclopedia of turbulence models. In the following sections we investigate several aspects of two-equation models including: (a) specifying closure-coefficient values; (b) surface boundary conditions for wall-bounded flows; and, (c) applications to a variety of flows.

4.4 Closure Coefficients

All of the two-equation models have closure coefficients that have been introduced in replacing unknown double and triple correlations with algebraic expressions involving known turbulence and mean-flow properties. The k-ω model, for example, has six, viz., α, β_o, β^*, σ, σ^* and σ_{do}. If our theory were exact, we could set the values of these coefficients from first principles much as we use the kinetic theory of gases to determine the viscosity coefficient in Stokes' approximation for laminar flows. However, the theory is not exact, but rather a model developed mainly on the strength of dimensional analysis. Consequently, the best we can do is to set the values of the closure coefficients to assure agreement with observed properties of turbulence.

This section describes the manner in which the closure coefficients have been determined for the k-ω model. There is no loss of generality in doing this since *these same general arguments have been used in establishing the values of the closure coefficients in most two-equation models.* The problems section at the end of the chapter examines some of the (relatively minor) differences among the various models.

We can establish the ratio of β^* to β_o by applying the model to decaying homogeneous, isotropic turbulence. In this kind of turbulence, there are no spatial gradients of any mean-flow properties wherefore Equations (4.37) and (4.38) simplify to

$$\frac{dk}{dt} = -\beta^* \omega k \quad \text{and} \quad \frac{d\omega}{dt} = -\beta_o \omega^2 \tag{4.67}$$

where we note that, because $\chi_\omega = 0$, we have $f_\beta = 1$ so that $\beta = \beta_o$ [see Equation (4.41)]. The asymptotic solution for k is readily found to be

$$k \sim t^{-\beta^*/\beta_o} \tag{4.68}$$

Experimental observations [see Townsend (1976)] indicate that $k \sim t^{-n}$ where $n = 1.25 \pm 0.06$ for decaying homogeneous, isotropic turbulence. Choosing $\beta^*/\beta_o = 1.27$ sets the ratio near the center of the range of accepted values.

Values for the coefficients α and β^* can be established by examining the **log layer**. Recall from Section 3.4 that the log layer is defined as the portion of the boundary layer sufficiently distant from the surface that molecular viscosity is negligible relative to eddy viscosity, yet close enough for convective effects to be negligible. In the limiting case of an incompressible constant-pressure boundary layer, the mean-momentum equation and the equations for k and ω simplify to the following.

$$\left.\begin{aligned} 0 &= \frac{\partial}{\partial y}\left[\nu_T \frac{\partial U}{\partial y}\right] \\ 0 &= \nu_T \left(\frac{\partial U}{\partial y}\right)^2 - \beta^* \omega k + \sigma^* \frac{\partial}{\partial y}\left[\frac{k}{\omega}\frac{\partial k}{\partial y}\right] \\ 0 &= \alpha \left(\frac{\partial U}{\partial y}\right)^2 - \beta_o \omega^2 + \frac{\sigma_d}{\omega}\frac{\partial k}{\partial y}\frac{\partial \omega}{\partial y} + \sigma \frac{\partial}{\partial y}\left[\frac{k}{\omega}\frac{\partial \omega}{\partial y}\right] \end{aligned}\right\} \tag{4.69}$$

We will justify the limiting form of these equations when we use perturbation methods to analyze the log layer in Subsection 4.6.1. We seek the conditions for which these simplified equations yield a solution consistent with the law of the wall. As can be easily verified, Equations (4.69) possess such a solution, viz.,

$$U = \frac{u_\tau}{\kappa} \ell n y + \text{constant}, \qquad k = \frac{u_\tau^2}{\sqrt{\beta^*}}, \qquad \omega = \frac{u_\tau}{\sqrt{\beta^*}\kappa y} \tag{4.70}$$

where u_τ is the conventional friction velocity and κ is Kármán's constant. There is one constraint imposed in the solution to Equations (4.69), namely, a unique relation exists between the implied value of Kármán's constant and the various closure coefficients. Specifically, the following equation must hold.

$$\alpha = \beta_o/\beta^* - \sigma\kappa^2/\sqrt{\beta^*} \tag{4.71}$$

Additionally, according to our solution the Reynolds shear stress, τ_{xy}, is constant and equal to u_τ^2. Inspection of Equations (4.70) shows that this implies $\tau_{xy} = \sqrt{\beta^*}\, k$ in the log layer. A variety of measurements [Townsend (1976)] indicate the ratio of τ_{xy} to k is about 3/10 (i.e., Bradshaw's constant) in the log layer. This is the same ratio Bradshaw, Ferriss and Atwell (1967) used in formulating their one-equation model [c.f. Equation (4.15)]. Thus, the predicted log-layer solution is consistent with experimental observations provided we select $\beta^* = 9/100$. Since we selected $\beta^*/\beta_o = 1.27$ above, necessarily $\beta_o = 0.0708$.

We must work a bit harder to determine the values of σ, σ^* and σ_{do}. As we will see in Subsections 4.6.2 and 4.6.3, detailed analysis of the defect layer and the sublayer indicates that the optimum choice is $\sigma = 1/2$. Analysis of free shear flows in Section 4.5 justifies setting $\sigma^* = 3/5$ and $\sigma_{do} = 1/8$. Finally, Equation (4.71) shows that selecting $\alpha = 13/25$ gives a value for the Kármán constant of 0.40. Thus, in summary, the values of the six primary closure coefficients in the k-ω model are

$$\alpha = \frac{13}{25}, \quad \beta_o = 0.0708, \quad \beta^* = \frac{9}{100}, \quad \sigma = \frac{1}{2}, \quad \sigma^* = \frac{3}{5}, \quad \sigma_{do} = \frac{1}{8} \tag{4.72}$$

These are the values quoted in Equations (4.39) and (4.41).

Other arguments have been used to determine closure coefficients prior to any applications or computer optimization. Saffman (1970), for example, uses estimates based on vortex-stretching processes in simple shear and pure extension to effectively establish bounds on a coefficient similar to α. He also requires that the length scale, ℓ, be discontinuous at a turbulent/nonturbulent interface and finds that his model requires $\sigma = \sigma^* = 1/2$ to guarantee such behavior.

Zeierman and Wolfshtein (1986) use the fact that very close to separation, measurements [Townsend (1976)] indicate the law of the wall is replaced by

$$U \to \frac{1}{0.24}\sqrt{\frac{y}{\rho}\frac{dP}{dx}} \qquad \text{as} \qquad y \to 0 \tag{4.73}$$

They also observe from measurements of Laufer (1950) and Clark (1968) that, for flow near the center of a channel, the turbulence kinetic energy and velocity are closely approximated by

$$\left.\begin{array}{lcl} k/k_o & \approx & 1 + 6.67(y/R)^2 \\ U/U_o & \approx & 1 - 0.242(y/R)^2 \\ u_\tau^2 & \approx & 0.048 U_o k_o^{1/2} \end{array}\right\} \qquad \text{as} \qquad y \to R \tag{4.74}$$

Briggs et al. (1996) provide another simple argument that can be used to establish closure-coefficient values. They have done a Large Eddy Simulation (LES – Chapter 8) of a shear-free mixing layer, an idealized flow that is relevant for geophysical studies. In this flow, the turbulent-transport (diffusion) terms balance dissipation terms in the k, ω, ϵ, etc. equations. For example, the k-ω model simplifies to

$$\left.\begin{array}{l} \dfrac{\partial}{\partial y}\left(\sigma^* \nu_T \dfrac{\partial k}{\partial y}\right) = \beta^* \omega k \\ \dfrac{\partial}{\partial y}\left(\sigma \nu_T \dfrac{\partial \omega}{\partial y}\right) = \beta_o \omega^2 - \dfrac{\sigma_{do}}{\omega}\dfrac{\partial k}{\partial y}\dfrac{\partial \omega}{\partial y} \end{array}\right\} \tag{4.75}$$

where we observe that, since the production terms are zero the stress limiter has no effect in this flow, necessarily $\nu_T = k/\omega$. Briggs et al. conclude that the asymptotic behavior of k and ν_T is

$$k \sim Ky^{-2.45} \quad \text{and} \quad \nu_T \sim Vy^{-0.42} \qquad \text{as} \quad y \to \infty \tag{4.76}$$

where K and V are constants. Matching this asymptotic behavior yields a constraint on the values of β_o, β^*, σ, σ^* and σ_{do}. In the absence of cross diffusion, for example, the Briggs et al. behavior is consistent with setting $\sigma\beta^* = \sigma^*\beta_o$. For the values given in Equation (4.72), the k-ω model predicts $k \sim Ky^{-2.68}$ and $\nu_T \sim Vy^{-0.34}$, which is fairly close to the LES behavior. Briggs et al. also show that the k-ϵ model predicts $k \sim Ky^{-4.9}$ and $\nu_T \sim Vy^{-1.5}$, which bears no resemblance to the LES results.

In conclusion, the specific flows selected for determination of the closure coefficients are a free choice of the developer. For example, using data for homogeneous turbulence *and* boundary layers assumes we have a degree of universality that may be grossly optimistic. That is, we are implicitly assuming our model is valid for grid turbulence, boundary layers, and many flows in between. Dropping homogeneous turbulence in favor of more boundary-layer data may yield a model optimized for boundary layers but restricted to such flows. Ideally, we would find flows that isolate each closure coefficient. Often, more than one is involved [e.g., Equation (4.71)]. In any event, for the sake of clarity, the arguments should be as simple as possible.

4.5 Application to Free Shear Flows

Our first applications will be for free shear flows. In this section, we seek similarity solutions to determine farfield behavior for the plane wake, mixing layer, plane jet, round jet and radial jet. In addition to developing the similarity solutions for the k-ω and k-ϵ models, we also discuss several aspects of the solutions and differences between the k-ω and k-ϵ models. These include: solution sensitivity to freestream boundary conditions; (b) cross diffusion; and, (c) the round-jet/plane-jet anomaly.

Solution sensitivity to freestream boundary conditions is an issue that previously has not been completely understood. We will find that solutions for two-equation turbulence models are sensitive to the freestream value of ω, ϵ, etc. even when boundary conditions are chosen so that k and ν_T are both very small in the freestream. Cross diffusion is a term appearing in the ω, ϵ or other second transport equation that results from making a formal change of variables in transforming from one set of turbulence parameters (e.g., k and ω) to another (e.g., k and ϵ or k and ℓ). We will see how cross diffusion affects free-shear-layer predictions. The round-jet/plane-jet anomaly is a classical problem that has

plagued turbulence models. Many models predict that the round jet grows faster than the plane jet, while measurements show the opposite to be true. We will see which models suffer from the anomaly and which do not.

4.5.1 Developing the Similarity Solution

There are two noteworthy changes in our approach to obtaining a solution for free shear flows.

1. For the mixing layer and the jets we can choose our similarity variable to be $\eta = y/x$. That is, with no loss of generality, we can set all scaling constants such as A in Equations (3.70) and (3.71) equal to one. We had to carry such scaling coefficients for the mixing-length model because, by hypothesis, the mixing length is proportional to the width of the layer, which is proportional to the coefficient A. With two-equation models, the turbulence length scale is determined as part of the solution so that the way in which we scale the similarity variable η is of no consequence.

2. While the rest of the methodology is the same, the addition of two extra differential equations complicates the problem somewhat. Because they are the most widely used two-equation models, we confine our attention to the k-ω and k-ϵ models.

With the standard boundary-layer/shear-layer approximations, the equations of motion become:

$$\frac{1}{x^m}\frac{\partial}{\partial x}\left[x^m U\right] + \frac{1}{y^j}\frac{\partial}{\partial y}\left[y^j V\right] = 0 \tag{4.77}$$

$$U\frac{\partial U}{\partial x} + V\frac{\partial U}{\partial y} = \frac{1}{y^j}\frac{\partial}{\partial y}\left[y^j \tau_{xy}\right] \tag{4.78}$$

$$\tau_{xy} = \nu_T \frac{\partial U}{\partial y} \tag{4.79}$$

k-ω Model:

$$\left.\begin{aligned} U\frac{\partial k}{\partial x} + V\frac{\partial k}{\partial y} &= \tau_{xy}\frac{\partial U}{\partial y} - \beta^* \omega k + \frac{1}{y^j}\frac{\partial}{\partial y}\left[y^j \sigma^* \frac{k}{\omega}\frac{\partial k}{\partial y}\right] \\ U\frac{\partial \omega}{\partial x} + V\frac{\partial \omega}{\partial y} &= \alpha\frac{\omega}{k}\tau_{xy}\frac{\partial U}{\partial y} - \beta\omega^2 + \frac{\sigma_d}{\omega}\frac{\partial k}{\partial y}\frac{\partial \omega}{\partial y} + \frac{1}{y^j}\frac{\partial}{\partial y}\left[y^j \sigma \frac{k}{\omega}\frac{\partial \omega}{\partial y}\right] \\ \nu_T &= \frac{k}{\tilde{\omega}}, \qquad \tilde{\omega} = \max\left\{\omega,\ C_{lim}\frac{|\partial U/\partial y|}{\sqrt{\beta^*}}\right\} \end{aligned}\right\} \tag{4.80}$$

k-ϵ Model:

$$\left.\begin{aligned} U\frac{\partial k}{\partial x}+V\frac{\partial k}{\partial y} &= \tau_{xy}\frac{\partial U}{\partial y}-\epsilon+\frac{1}{y^j}\frac{\partial}{\partial y}\left[y^j\frac{\nu_T}{\sigma_k}\frac{\partial k}{\partial y}\right] \\ U\frac{\partial \epsilon}{\partial x}+V\frac{\partial \epsilon}{\partial y} &= C_{\epsilon 1}\frac{\epsilon}{k}\tau_{xy}\frac{\partial U}{\partial y}-C_{\epsilon 2}\frac{\epsilon^2}{k}+\frac{1}{y^j}\frac{\partial}{\partial y}\left[y^j\frac{\nu_T}{\sigma_\epsilon}\frac{\partial \epsilon}{\partial y}\right] \\ \nu_T &= C_\mu k^2/\epsilon \end{aligned}\right\} \tag{4.81}$$

In Equations (4.77) – (4.81), $j = 1$ for the round jet and $m = 1$ for the radial jet. Otherwise, j and m are zero. The similarity solution for the various free shear flows can be written in the following compact form.

Far Wake:

$$\left.\begin{aligned} U(x,y) &= U_\infty-\sqrt{\frac{D}{\rho x}}\mathcal{U}(\eta), \quad k(x,y)=\frac{D}{\rho x}K(\eta) \\ \omega(x,y) &= \frac{U_\infty}{x}W(\eta) \quad \epsilon(x,y)=\frac{DU_\infty}{\rho x^2}E(\eta) \\ \eta &= y\sqrt{\frac{\rho U_\infty^2}{Dx}} \end{aligned}\right\} \tag{4.82}$$

Mixing Layer:

$$\left.\begin{aligned} U(x,y) &= U_1\mathcal{U}(\eta), \quad k(x,y)=U_1^2K(\eta) \\ \omega(x,y) &= \frac{U_1}{x}W(\eta), \quad \epsilon(x,y)=\frac{U_1^3}{x}E(\eta) \\ \eta &= \frac{y}{x} \end{aligned}\right\} \tag{4.83}$$

Jet:

$$\left.\begin{aligned} U(x,y) &= \frac{J^{1/2}}{x^{(m+j+1)/2}}\mathcal{U}(\eta), \quad k(x,y)=\frac{J}{x^{(m+j+1)}}K(\eta) \\ \omega(x,y) &= \frac{J^{1/2}}{x^{(m+j+3)/2}}W(\eta), \quad \epsilon(x,y)=\frac{J^{3/2}}{x^{(3m+3j+5)/2}}E(\eta) \\ \eta &= \frac{y}{x} \end{aligned}\right\} \tag{4.84}$$

Substituting these self-similar representations into the mean-momentum equation yields the general form

$$\mathcal{V}\frac{d\mathcal{U}}{d\eta} - \frac{1}{\eta^j}\frac{d}{d\eta}\left[\eta^j f_N N \frac{d\mathcal{U}}{d\eta}\right] = S_u \mathcal{U} \tag{4.85}$$

where the functions $N(\eta)$ and $\mathcal{V}(\eta)$ are transformed eddy viscosity and normal velocity-like functions, respectively. The two terms on the left-hand side of Equation (4.85) are essentially vertical convection and diffusion. The term on the right-hand side is a source term that originates from the streamwise convection of momentum, while the function $f_N(\eta)$ reflects the k-ω model's stress limiter. Table 4.3 lists the coefficient S_u and the normal-velocity function, $\mathcal{V}(\eta)$, for each of the free shear flows considered. The transformed k, ω and ϵ equations are:

k-ω Model:

$$\left.\begin{aligned}
&\mathcal{V}\frac{dK}{d\eta} - \frac{1}{\eta^j}\frac{d}{d\eta}\left[\eta^j \sigma^* N \frac{dK}{d\eta}\right] = S_k K + f_N N\left(\frac{d\mathcal{U}}{d\eta}\right)^2 - \beta^* W K \\
&\mathcal{V}\frac{dW}{d\eta} - \frac{1}{\eta^j}\frac{d}{d\eta}\left[\eta^j \sigma N \frac{dW}{d\eta}\right] = S_w W + \alpha f_N N \frac{W}{K}\left(\frac{d\mathcal{U}}{d\eta}\right)^2 \\
&\qquad\qquad - \beta W^2 + \frac{\sigma_d}{W}\frac{dK}{d\eta}\frac{dW}{d\eta} \\
&N = \frac{K}{W}, \qquad f_N = \min\left\{1,\ C_{lim}^{-1}\frac{\sqrt{\beta^*}\,W}{|d\mathcal{U}/d\eta|}\right\}
\end{aligned}\right\} \tag{4.86}$$

k-ϵ Model:

$$\left.\begin{aligned}
&\mathcal{V}\frac{dK}{d\eta} - \frac{1}{\eta^j}\frac{d}{d\eta}\left[\eta^j \frac{N}{\sigma_k}\frac{dK}{d\eta}\right] = S_k K + N\left(\frac{d\mathcal{U}}{d\eta}\right)^2 - E \\
&\mathcal{V}\frac{dE}{d\eta} - \frac{1}{\eta^j}\frac{d}{d\eta}\left[\eta^j \frac{N}{\sigma_\epsilon}\frac{dE}{d\eta}\right] = S_e E + C_{\epsilon 1}\frac{E}{K}N\left(\frac{d\mathcal{U}}{d\eta}\right)^2 - C_{\epsilon 2}\frac{E^2}{K} \\
&N = C_\mu \frac{K^2}{E}, \qquad f_N = 1
\end{aligned}\right\} \tag{4.87}$$

The k, ω and ϵ equations contain convective terms, diffusion terms, and additional source terms corresponding to streamwise convection, production, dissipation and cross diffusion. Table 4.3 lists the convective source-term coefficients, S_k, S_w and S_e. The table also lists the exponents j and m for each free shear flow.

Table 4.3: *Free Shear Flow Parameters.*

Flow	S_u	S_k	S_w	S_e	j	m	$\mathcal{V}(\eta)$
Far Wake	$\frac{1}{2}$	1	1	2	0	0	$-\frac{1}{2}\eta$
Mixing Layer	0	0	$\mathcal{U}$	$\mathcal{U}$	0	0	$-\int_0^\eta \mathcal{U}(\eta')d\eta'$
Plane Jet	$\frac{1}{2}\mathcal{U}$	$\mathcal{U}$	$\frac{3}{2}\mathcal{U}$	$\frac{5}{2}\mathcal{U}$	0	0	$-\frac{1}{2}\int_0^\eta \mathcal{U}(\eta')d\eta'$
Round Jet	$\mathcal{U}$	$2\mathcal{U}$	$2\mathcal{U}$	$4\mathcal{U}$	1	0	$-\frac{1}{\eta}\int_0^\eta \mathcal{U}(\eta')\eta'd\eta'$
Radial Jet	$\mathcal{U}$	$2\mathcal{U}$	$2\mathcal{U}$	$4\mathcal{U}$	0	1	$-\int_0^\eta \mathcal{U}(\eta')d\eta'$

To complete the solution, we must specify the vortex-stretching parameter χ_ω defined by

$$\chi_\omega \equiv \left| \frac{\Omega_{ij}\Omega_{jk}S_{ki}}{(\beta^*\omega)^3} \right| \tag{4.88}$$

to specify the function f_β [see Equation (4.41)] appearing in the k-ω model. Because evaluation of this parameter involves matrix multiplication, it is worthwhile to illustrate details of the mathematics. For two-dimensional shear flows, the strain-rate and rotation tensors are

$$[S_{ij}] \approx \begin{bmatrix} \frac{\partial U}{\partial x} & \frac{1}{2}\frac{\partial U}{\partial y} & 0 \\ \frac{1}{2}\frac{\partial U}{\partial y} & \frac{\partial V}{\partial y} & 0 \\ 0 & 0 & 0 \end{bmatrix} \quad \text{and} \quad [\Omega_{ij}] \approx \begin{bmatrix} 0 & \frac{1}{2}\frac{\partial U}{\partial y} & 0 \\ -\frac{1}{2}\frac{\partial U}{\partial y} & 0 & 0 \\ 0 & 0 & 0 \end{bmatrix} \tag{4.89}$$

where x and y denote streamwise and normal directions, respectively. Hence, for two-dimensional incompressible flow, we have

$$\begin{aligned} \Omega_{ij}\Omega_{jk}S_{ki} &= \Omega_{12}\Omega_{21}S_{11} + \Omega_{21}\Omega_{12}S_{22} \\ &\approx -\frac{1}{4}\left(\frac{\partial U}{\partial y}\right)^2\left(\frac{\partial U}{\partial x} + \frac{\partial V}{\partial y}\right) = 0 \end{aligned} \tag{4.90}$$

where we use the fact that the divergence of the velocity vanishes for incompressible flow. This corresponds to the fact that vortex stretching is exactly zero in two-dimensional flows. Thus, we conclude that

$$\chi_\omega = 0, \qquad \text{Plane jet} \tag{4.91}$$

By contrast, for general axisymmetric flows, these two tensors are

$$[S_{ij}] \approx \begin{bmatrix} \frac{\partial U_r}{\partial r} & 0 & \frac{1}{2}\left(\frac{\partial U_r}{\partial x} + \frac{\partial U_x}{\partial r}\right) \\ 0 & \frac{U_r}{r} & 0 \\ \frac{1}{2}\left(\frac{\partial U_r}{\partial x} + \frac{\partial U_x}{\partial r}\right) & 0 & \frac{\partial U_x}{\partial x} \end{bmatrix} \tag{4.92}$$

$$[\Omega_{ij}] \approx \begin{bmatrix} 0 & 0 & \frac{1}{2}\left(\frac{\partial U_r}{\partial x} - \frac{\partial U_x}{\partial r}\right) \\ 0 & 0 & 0 \\ -\frac{1}{2}\left(\frac{\partial U_r}{\partial x} - \frac{\partial U_x}{\partial r}\right) & 0 & 0 \end{bmatrix} \tag{4.93}$$

where x and r denote axial and radial directions, respectively. So, for incompressible flow, there follows

$$\begin{aligned} \Omega_{ij}\Omega_{jk}S_{ki} &= \Omega_{13}\Omega_{31}S_{11} + \Omega_{31}\Omega_{13}S_{33} \\ &= -\frac{1}{4}\left(\frac{\partial U_r}{\partial x} - \frac{\partial U_x}{\partial r}\right)^2 \left(\frac{\partial U_r}{\partial r} + \frac{\partial U_x}{\partial x}\right) \\ &= \frac{1}{4}\left(\frac{\partial U_r}{\partial x} - \frac{\partial U_x}{\partial r}\right)^2 \frac{U_r}{r} \end{aligned} \tag{4.94}$$

where we use the fact that the continuity equation in axisymmetric flows is

$$\frac{\partial U_x}{\partial x} + \frac{\partial U_r}{\partial r} + \frac{U_r}{r} = 0 \quad \Longrightarrow \quad \frac{U_r}{r} = -\left(\frac{\partial U_x}{\partial x} + \frac{\partial U_r}{\partial r}\right) \tag{4.95}$$

Hence, χ_ω is nonzero for axisymmetric flows. This reflects the fact that rings of vorticity with an axis parallel to the direction of flow can be stretched as the flow spreads radially.

Finally, we must make this equation consistent with the notation used in Equations (4.77) – (4.79). For the round jet we have $U_x = U$, $U_r = V$, $x = x$ and $r = y$, while the radial jet has $U_x = V$, $U_r = U$, $x = y$ and $r = x$. Noting that $\partial U/\partial y \gg \partial V/\partial x$ for shear layers, the parameter χ_ω is

$$\chi_\omega = \begin{cases} 0, & \text{Plane jet} \\ \dfrac{1}{4}\dfrac{(\partial U/\partial y)^2}{(\beta^*\omega)^3}\left|\dfrac{V}{y}\right|, & \text{Round jet} \\ \dfrac{1}{4}\dfrac{(\partial U/\partial y)^2}{(\beta^*\omega)^3}\dfrac{U}{x}, & \text{Radial jet} \end{cases} \tag{4.96}$$

In terms of the similarity solution, we have[5]

$$\chi_\omega = \begin{cases} 0, & \text{Plane jet} \\ \dfrac{1}{4}\left(\dfrac{d\mathcal{U}}{d\eta}\right)^2 \dfrac{|\mathcal{U} - \mathcal{V}/\eta|}{(\beta^* W)^3}, & \text{Round jet} \\ \dfrac{1}{4}\left(\dfrac{d\mathcal{U}}{d\eta}\right)^2 \dfrac{\mathcal{U}}{(\beta^* W)^3}, & \text{Radial jet} \end{cases} \tag{4.97}$$

Finally, we must specify the parameter λ appearing in the RNG k-ϵ model [Equation (4.51)]. In terms of similarity variables, λ is

$$\lambda = \frac{K}{E}\left|\frac{d\mathcal{U}}{d\eta}\right| \tag{4.98}$$

Boundary conditions on the velocity are the same as in Chapter 3. We must also specify boundary conditions for K, W and E. Solutions for two-equation models often feature (nonphysical) sharp turbulent/nonturbulent interfaces for free shear flows, i.e., interfaces at which derivatives of flow properties are discontinuous (see Subsection 7.2.2). Consequently, the most sensible boundary conditions in the freestream are those corresponding to nonturbulent flow, i.e., $K(\eta)$, $W(\eta)$ and $E(\eta)$ all vanish approaching the edge of the shear layer. As it turns out, two-equation-model solutions are affected by finite values of K, W and E in the freestream, and are sensitive to the freestream value of E or W. Subsection 4.5.3 focuses in more detail on this sensitivity. The most appropriate boundary conditions for K, W and E are as follows.

Wake and Jet:

$$K'(0) = W'(0) = E'(0) = 0 \tag{4.99}$$

Wake, Jet and Mixing Layer:

$$K(\eta) \to 0, \quad W(\eta) \to 0, \quad \text{and} \quad E(\eta) \to 0 \quad \text{as} \quad |\eta| \to \infty \tag{4.100}$$

This completes formulation of the similarity solution for the k-ω and k-ϵ models. We have demonstrated that all pertinent equations and boundary conditions transform to a set of equations and boundary conditions that can be written in terms of the similarity variable, η. In so doing, we have formulated a nonlinear, two-point boundary-value problem that obviously cannot be solved in closed form. In the next section, we discuss the numerical solution.

[5] In terms of similarity variables, the radial velocity, $V(x, y)$, for the round jet transforms to $\bar{V}(\eta) = dF/d\eta - F(\eta)/\eta$, where $F(\eta)$ is the transformed streamfunction. We have defined $\mathcal{U}(\eta) \equiv \eta^{-1} dF/d\eta$ and $\mathcal{V}(\eta) \equiv F(\eta)/\eta$. Thus, the similarity form of $|V(x, y)/y|$ is $|\mathcal{U} - \mathcal{V}/\eta|$.

4.5.2 Numerical Solution

As in Section 4.2, we use the conventional definition of **spreading rate for the wake**, which is the value of η given in Equation (4.82), where the velocity defect is half its maximum value. Similarly **for plane, round and radial jets, the spreading rate** is the value of y/x where the velocity is half its centerline value. **For the mixing layer, the spreading rate** is the difference between the values of y/x where $(U-U_2)^2/(U_1-U_2)^2$ is 9/10 and 1/10. Table 4.4 compares computed (using Programs **WAKE, MIXER** and **JET** — see Appendix C) and measured spreading rates for the k-ω, k-ϵ and RNG k-ϵ models. Figures 4.8 through 4.11 compare computed and measured velocity profiles for these three models.

Table 4.4: *Free Shear Flow Spreading Rates for Two-Equation Models.*

Flow	k-ω Model	k-ϵ Model	RNG k-ϵ Model	Measured
Far Wake	0.326	0.256	0.290	0.320-0.400
Mixing Layer	0.096	0.098	0.099	0.103-0.120
Plane Jet	0.108	0.109	0.147	0.100-0.110
Round Jet	0.094	0.120	0.185	0.086-0.096
Radial Jet	0.099	0.094	0.111	0.096-0.110

Of the three models, the k-ω model is closest to measured spreading rates. With the exception of the mixing layer, computed spreading rates fall within the range of measured values. The predicted mixing-layer spreading rate is 6% below the lower bound of measured values. Using the average values from the measured ranges, the average difference between theory and experiment is 6%.

The k-ϵ model predicts a spreading rate that is 20% lower than the lower bound of measured values for the far wake, 5% lower than measured for the mixing layer, 2% lower for the radial jet and 25% higher than the upper bound measured for the round jet. Only for the plane jet does its predicted spreading rate fall within the range of measured values. The average difference between computed and average measured spreading rates for the k-ϵ model is 17%. The RNG k-ϵ model yields even larger differences (an average of 36%), including a predicted round-jet spreading rate that is double the measured value.

Figures 4.8 – 4.12 reveal an especially noteworthy feature of the k-ω solutions. The figures show the smooth variation of the velocity profiles approaching the freestream for all five free shear flows, which is consistent with measurements. By contrast, the k-ϵ model predicts a nonphysical discontinuous slope in the velocity profile at the edge of the shear layer for the wake, the mixing layer and the radial jet. The RNG k-ϵ model predicts discontinuous slope for all five cases.

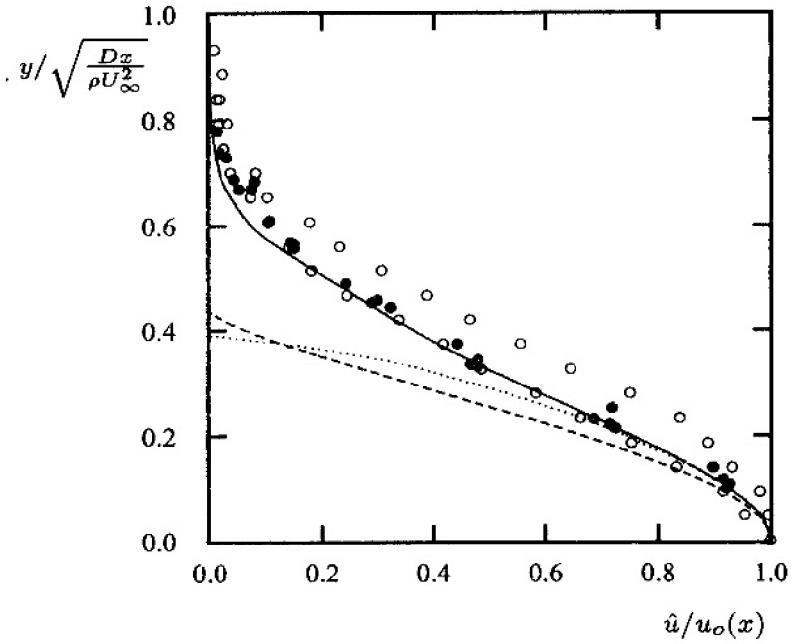

Figure 4.8: *Comparison of computed and measured velocity profiles for the far wake;* —— *k-ω model;* - - - *k-ϵ model;* · · · · *RNG k-ϵ model;* • *Fage and Falkner (1932);* ○ *Weygandt and Mehta (1995).*

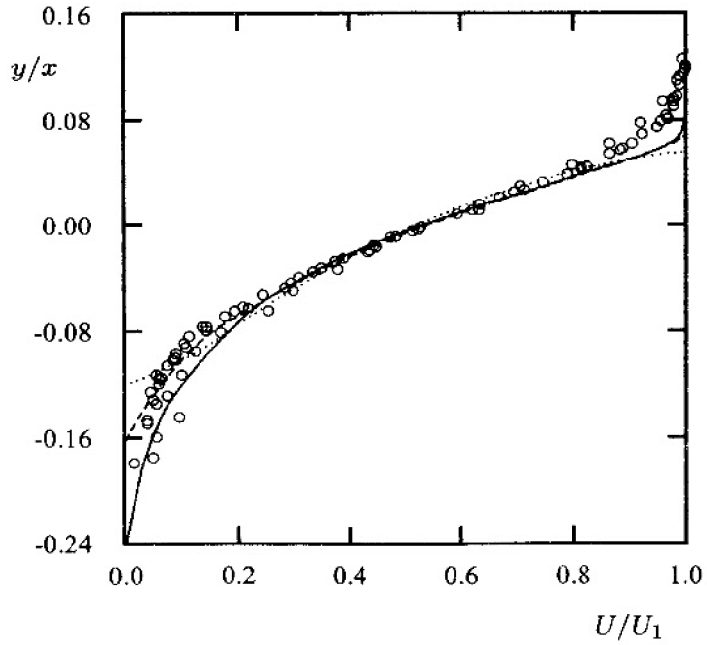

Figure 4.9: *Comparison of computed and measured velocity profiles for the mixing layer;* —— *k-ω model;* - - - *k-ϵ model;* · · · · *RNG k-ϵ model;* ○ *Liepmann and Laufer (1947).*

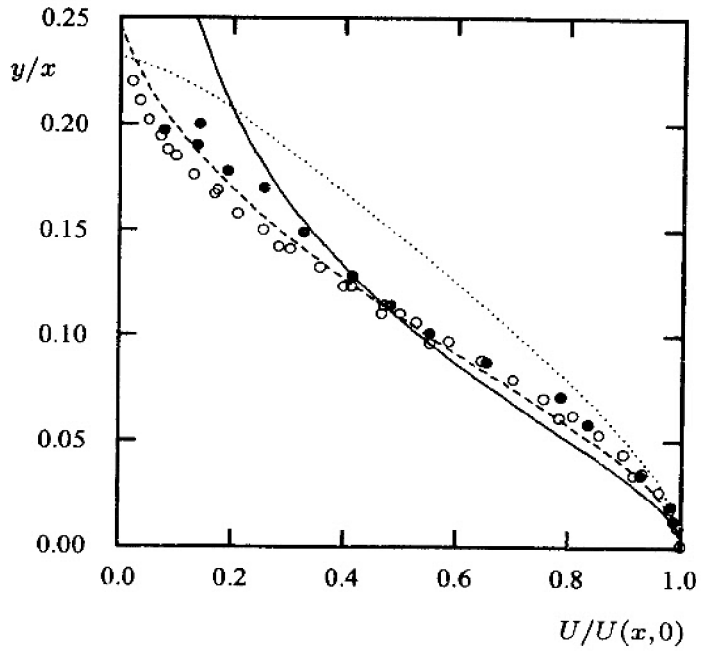

Figure 4.10: *Comparison of computed and measured velocity profiles for the plane jet; —— k-ω model; - - - k-ϵ model; · · · · RNG k-ϵ model; ○ Bradbury (1965); • Heskestad (1965).*

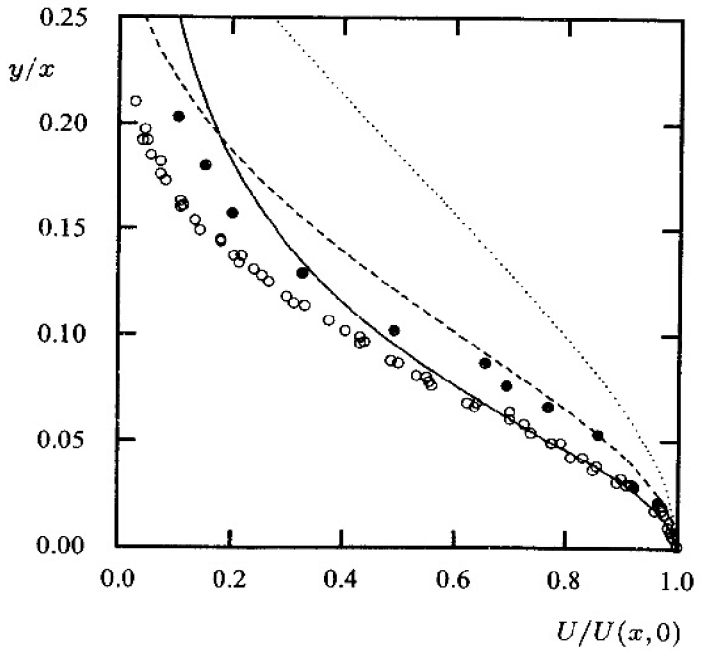

Figure 4.11: *Comparison of computed and measured velocity profiles for the round jet; —— k-ω model; - - - k-ϵ model; · · · · RNG k-ϵ model; ○ Wygnanski and Fiedler (1969); • Rodi (1975).*

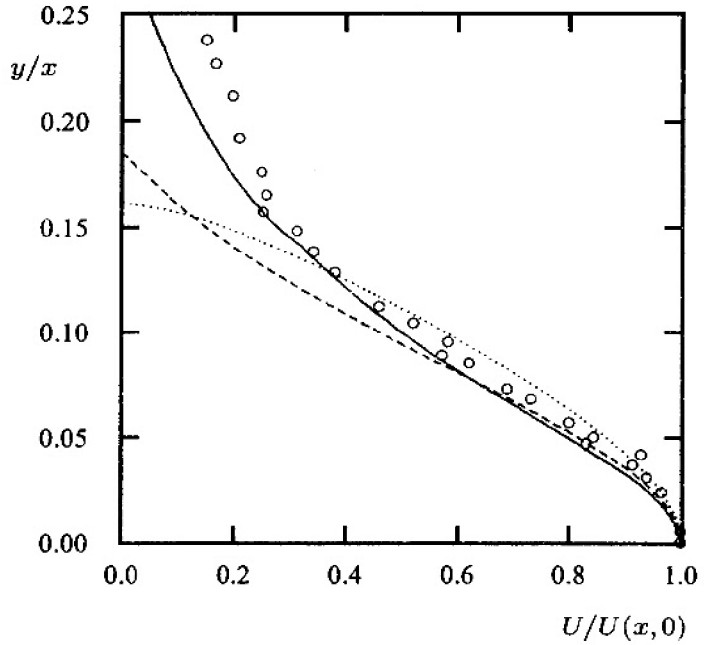

Figure 4.12: *Comparison of computed and measured velocity profiles for the radial jet:* —— *k-ω model;* - - - *k-ϵ model;* · · · · *RNG k-ϵ model;* o *Witze and Dwyer (1976).*

Table 4.5 lists computed spreading rates for five other models that illustrates how difficult it has proven to be to develop a model that adequately describes free shear flows. Values listed for the k-ζ model are from Robinson et al. (1995). All other values have been obtained using modified versions of Programs **WAKE**, **MIXER** and **JET** – see problems section. The Robinson et al. (1995) enstrophy-equation (k-ζ) model predicts spreading rates that are quite close to measured values for all five free shear flows. By contrast, the Speziale et al. (1990) k-τ model and the Peng et al. (1997) and Kok k-ω models predict spreading rates that are significantly smaller than measured. Finally, the Wilcox (1988a) k-ω model predicts spreading rates that are larger than measured for all five cases.

Table 4.5: *More Two-Equation Model Free Shear Flow Spreading Rates.*

Flow	Robinson et al., k-ζ	Speziale et al., k-τ	Peng et al. k-ω	Kok k-ω	Wilcox (1988a) k-ω	Measured
Far Wake	0.313	0.221	0.206	0.191	0.496	0.320-0.400
Mixing Layer	0.112	0.082	0.071	0.056	0.141	0.103-0.120
Plane Jet	0.115	0.089	–	0.083	0.135	0.100-0.110
Round Jet	0.091	0.102	0.096	0.107	0.369	0.086-0.096
Radial Jet	0.097	0.073	0.040	0.068	0.317	0.096-0.110

The latter results provide a definitive measure of how the addition of cross diffusion and the modification to β defined in Equations (4.39) – (4.42) improves the k-ω model. The addition of cross diffusion produces more production relative to dissipation in the ω equation. This, in turn, increases ω and thus the dissipation in the k equation, which reduces computed spreading rates for free shear flows in general. The variation of β with χ_ω reduces dissipation relative to production in the ω equation for round and radial jets, which further increases dissipation in the k equation. Hence, both modifications counter the Wilcox (1988a) model's excess production, relative to dissipation, for free shear flows.

4.5.3 Sensitivity to Finite Freestream Boundary Conditions

Two-equation models have a unique, and unexpected feature when nonzero freestream boundary conditions are specified for k, ω, ϵ, etc. Specifically, even if we select k and the second turbulence property (ω, ϵ, etc.) to be sufficiently small that both k and ν_T are negligible, the solution is sensitive to our choice of the second turbulence property's freestream value. This is an important consideration since most computations are done with these assumptions.

Figure 4.13 shows how the spreading rate, δ', varies with the freestream value of ω for the k-ω model defined in Equations (4.36) – (4.42) and the Wilcox (1988a) k-ω model for the far wake, the mixing layer and the plane jet. It also shows the variation of δ' with the freestream value of ϵ for the Standard k-ϵ model defined in Equations (4.46) – (4.50). In all three graphs, δ'_o is the predicted spreading rate for the limiting case $\omega_\infty \to 0$ for the k-ω models and $\epsilon_\infty \to 0$ for the k-ϵ model. All computations have been done with the dimensionless eddy viscosity, $N(\infty)$, equal to 10^{-6}.

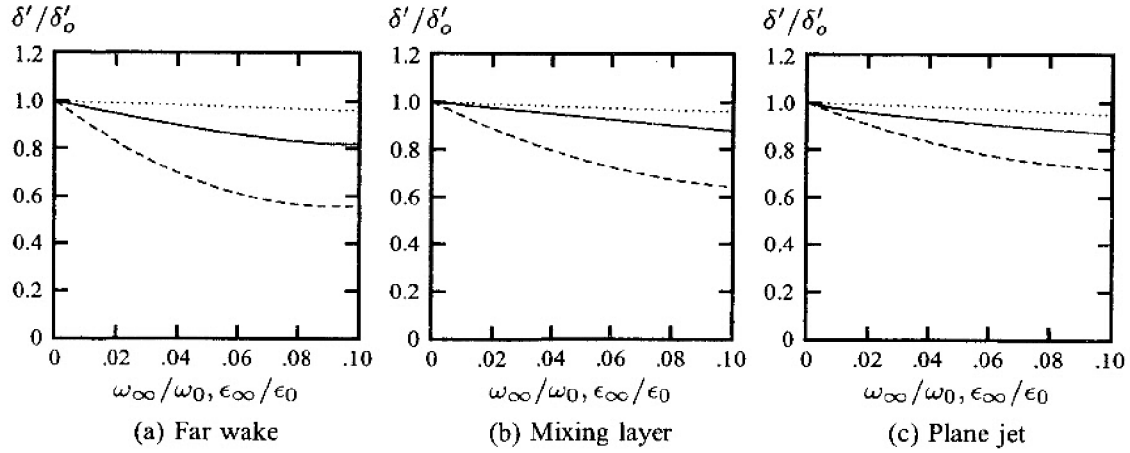

Figure 4.13: *Sensitivity of free shear flow spreading rates to freestream conditions:* $\cdots$ *k-ϵ model;* —— *Wilcox (2006) k-ω model;* - - - *Wilcox (1988a) k-ω model. ω_0 and ϵ_0 are for $\eta = 0$.*

All three models predict a decrease in spreading rate as the freestream value of ω or ϵ increases. In all three graphs, the freestream value is scaled with respect to the value at $\eta = 0$, which is very close to the maximum value for each flow. As shown, without cross diffusion, the k-ω model displays a strong sensitivity to the freestream value of ω. The addition of cross diffusion greatly reduces the sensitivity. The k-ϵ model predicts very little sensitivity to the freestream value of ϵ. The graphs also show that if the freestream value is less than 1% of the maximum value [$\omega_\infty/\omega_0 < 0.01$, $\epsilon_\infty/\epsilon_0 < 0.01$] there is virtually no effect on the predicted spreading rate. Certainly this is not an unreasonable constraint because using a freestream value of ω or ϵ in excess of 1% of the peak value would very likely correspond to using a physically unrealistic value.

There is no mystery about why the solution should have some sensitivity to freestream boundary conditions. We are, after all, solving a two-point boundary-value problem, which requires freestream boundary conditions on all variables, including ω and ϵ. In light of this, it is clear that there must be some range of boundary values that affect the solution. Figure 4.13 shows that there is a well defined limiting form of the solution for vanishing freestream boundary values, further validating the claim that Equations (4.99) and (4.100) are the proper freestream boundary conditions.

It is the odd nature of the differential equation for ϵ that makes the k-ϵ model much less sensitive to freestream conditions than the k-ω model. Specifically, because its dissipation term is proportional to ϵ^2/k, the equation is singular as $k \longrightarrow 0$ for finite freestream values of ϵ. This unusual behavior of the ϵ equation obviates the need to invest enough thought to avoid prescribing physically unrealistic freestream values for a quantity such as ϵ. While this may be comforting to engineers who don't care to invest such thought, the next example should serve as a wake-up call that being sloppy with freestream boundary conditions can foil the "protection" provided by the ϵ equation. As we will see, using nomenclature coined by Menter (1992c), the k-ϵ model has "degenerate"[6] solutions for excessively large freestream values of ϵ.

To further demonstrate how farfield boundary conditions affect two-equation model predictions we now focus on one-dimensional propagation of a turbulent front into a quiescent fluid. This problem has been analyzed by several authors, including Lele (1985) and Wilcox (1995b). Briefly, we imagine a planar source of turbulence at $x = 0$ where we maintain constant values of $k = k_o$ and $\omega = \omega_o$ or $\epsilon = \epsilon_o$ for all time. The turbulence source is instantaneously "turned on" at time $t = 0$, and a front propagates into the fluid at a finite rate.

Figure 4.14 shows computed dimensionless ν_T and ω profiles for farfield values of ω equal to $0.001\omega_o$ and $0.5\omega_o$ based on the Wilcox (1988a) k-ω model. Both computations have been done with the farfield value of k chosen

[6] Although his nomenclature is incorrect in a strict mathematical sense, Menter refers to a solution that differs greatly from the zero freestream boundary conditions solution as being degenerate.

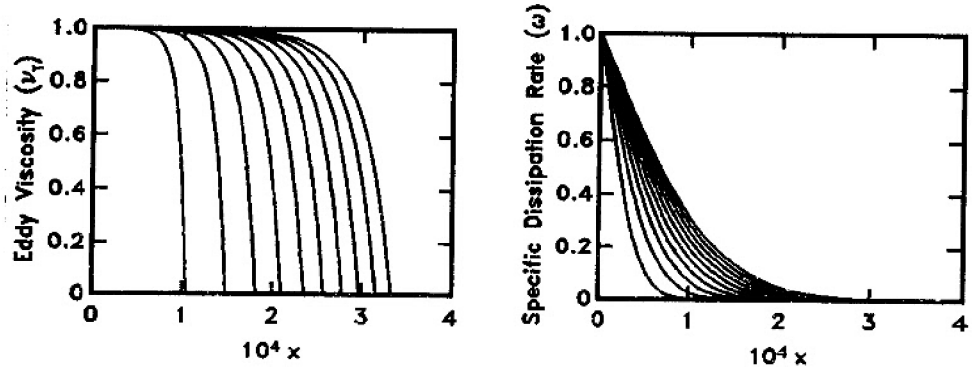

(a) Profiles for $\omega_\infty = 0.001\omega_o$

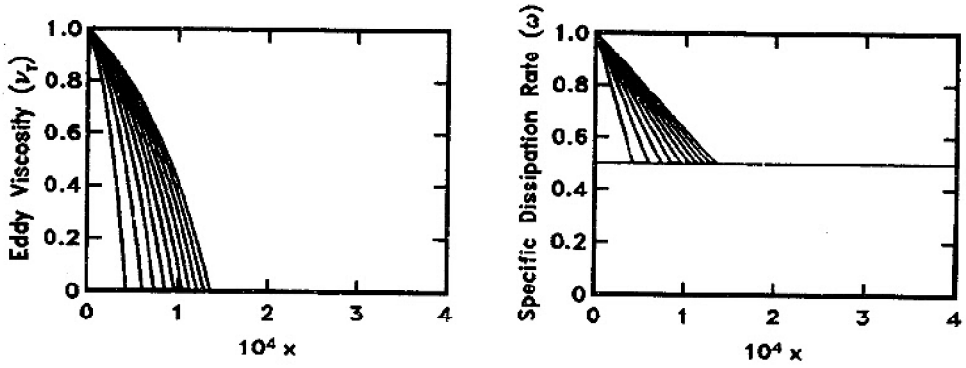

(b) Profiles for $\omega_\infty = 0.5\omega_o$

Figure 4.14: *Turbulent front propagation — Wilcox (1988a) k-ω model. The 10 curves displayed in each graph are computed profiles at 10 different times as the front advances to the right.*

so that the farfield eddy viscosity is 10^{-6} times the value at $x = 0$. The graphs all include a family of curves corresponding to 10 different times, with the front advancing to the right. The motion of the front is clearly indicated by the ν_T curves, which exhibit the sharp interface between the spreading turbulence and the nonturbulent fluid.

Inspection of the curves shows that when the freestream value of ω is $0.001\omega_o$, the ω curves all tend smoothly to the farfield value as the front advances. By contrast, when $\omega = 0.5\omega_o$, the farfield value has a strong effect on the solution. It places a large lower bound on ω, and causes the solution to have discontinuous slope at the front. It also retards the rate at which the front advances. Specifically, when $\omega = 0.5\omega_o$, the rate of advance of the front is only about 40% of the rate for $\omega = 0.001\omega_o$. Results that follow for the k-ϵ model strongly suggest that this effect would be reduced — but not eliminated — if the computations were repeated with cross diffusion included in the k-ω model.

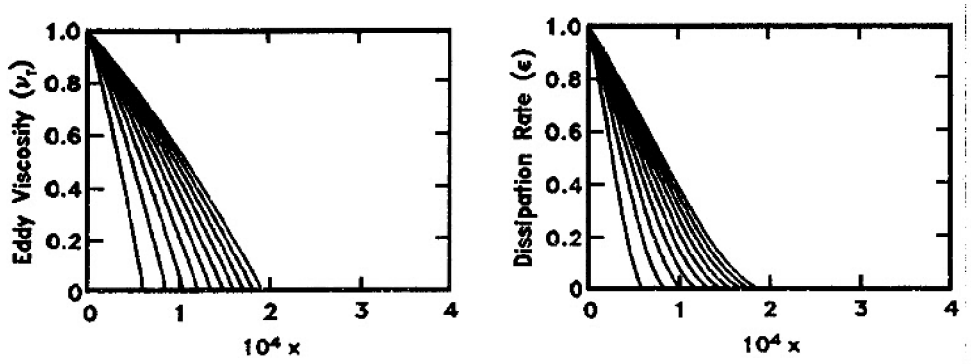

(a) Profiles for $\epsilon_\infty = 0.001\epsilon_o$

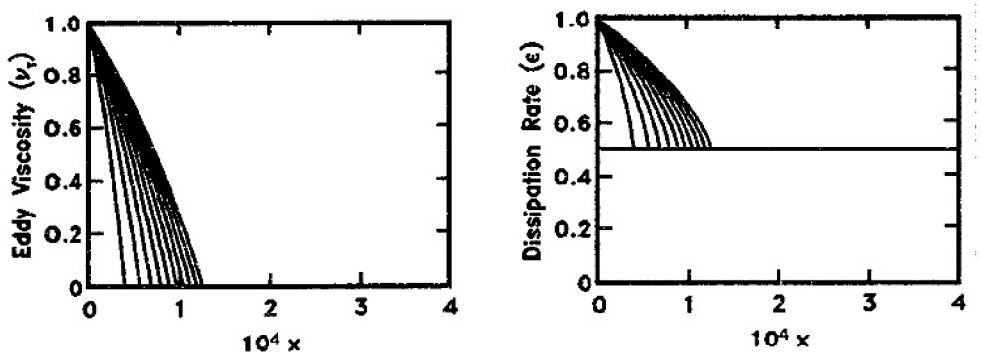

(b) Profiles for $\epsilon_\infty = 0.5\epsilon_o$

Figure 4.15: *Turbulent front propagation — k-ϵ model. The 10 curves displayed in each graph are computed profiles at 10 different times as the front advances to the right.*

Figure 4.15 includes similar graphs for the Standard k-ϵ model, corresponding to farfield values of ϵ equal to $0.001\epsilon_o$ and $0.5\epsilon_o$. Again, both computations have been done with k_∞ chosen so that the farfield eddy viscosity is 10^{-6} times the value at the origin. The rate of advance of the turbulent front for $\epsilon = 0.5\epsilon_o$ is 65% of the rate for $\epsilon = 0.001\epsilon_o$. Thus, while the effect of the farfield condition is smaller for the k-ϵ model than for the k-ω model, it is nevertheless very substantial.

Clearly, some degree of care must be exercised when selecting freestream or farfield boundary conditions for two-equation models. It is not sufficient to simply select small values for k and ν_T, as the choice can imply a nonphysically large value of the second turbulence parameter, viz., ω, ϵ or ℓ. In complex flows, estimates should be made regarding the peak value of the second variable in regions of intense shear, to be sure the freestream value is small enough. To be certain appropriately small values are used in the freestream, the values can always be adjusted as the computation proceeds.

4.5.4 Cross Diffusion

There is an interesting relationship between k-ϵ and k-ω models (or any pair of models whose second variable is $k^m\epsilon^n$ for some m and n) that helps delineate some of the key differences. Specifically, if we let $\epsilon = C_\mu k\omega$ define a change of dependent variables from ϵ to ω, it is a straightforward matter to demonstrate that the resulting equation for ω is

$$\frac{\partial \omega}{\partial t} + U_j \frac{\partial \omega}{\partial x_j} = \alpha \frac{\omega}{k} \tau_{ij} \frac{\partial U_i}{\partial x_j} - \beta \omega^2 + \frac{\partial}{\partial x_j}\left[(\nu + \sigma \nu_T) \frac{\partial \omega}{\partial x_j} \right] + 2 \frac{(\nu + \sigma \nu_T)}{k} \frac{\partial k}{\partial x_j} \frac{\partial \omega}{\partial x_j} + \frac{\omega}{k} \frac{\partial}{\partial x_j}\left[(\sigma - \sigma^*) \nu_T \frac{\partial k}{\partial x_j} \right] \quad (4.101)$$

where $\beta^* = C_\mu$. Also, α, β, σ and σ^* are simple functions of the k-ϵ model's closure coefficients (see problems section). Focusing on free shear flows, we can ignore molecular viscosity, ν. Also, if we assume $\sigma = \sigma^*$ for simplicity, Equation (4.101) simplifies to

$$\frac{\partial \omega}{\partial t} + U_j \frac{\partial \omega}{\partial x_j} = \alpha \frac{\omega}{k} \tau_{ij} \frac{\partial U_i}{\partial x_j} - \beta \omega^2 + \sigma_d \frac{1}{\omega} \frac{\partial k}{\partial x_j} \frac{\partial \omega}{\partial x_j} + \frac{\partial}{\partial x_j}\left[\sigma \nu_T \frac{\partial \omega}{\partial x_j} \right] \quad (4.102)$$

where $\sigma_d = 2\sigma$. The term proportional to σ_d in Equation (4.102) is referred to as **cross diffusion**, depending upon gradients of both k and ω.

The cross-diffusion term as listed in Equation (4.102) appears only because we started with the k-ϵ model. To argue that the cross-diffusion term is "missing" from the k-ω model, as several authors have done, assumes the modeled ϵ equation is in some sense more fundamental than the modeled ω equation. Given how poorly the k-ϵ model fares in predicting turbulent flows, especially wall-bounded flows (see Sections 4.6 through 4.10), the argument is obviously a non sequitur.

In free shear flows the cross-diffusion term enhances production of ω, which in turn increases dissipation of k (assuming $\sigma_d > 0$). This occurs for small freestream values of k and ω, for which both quantities decrease approaching the shear-layer edge. The overall effect is to reduce the net production of k, which reduces the predicted spreading rates from the values listed in Table 4.5.

Several authors, including Speziale et al. (1990), Menter (1992c), Wilcox (1993a), Peng et al. (1997), Kok (2000) and Hellsten (2005) have attempted to improve the k-ω model by adding cross diffusion. While all have achieved some degree of success in wall-bounded flows, the models are far less realistic for free shear flows. Inspection of Table 4.5 shows that spreading rates predicted by such models differ significantly from measured values.[7]

[7]The spreading rates predicted by the Speziale et al. k-ω model are identical to those of the Speziale et al. k-τ model, which are much smaller than measured.

Menter (1992c) and Hellsten (2005) have enjoyed more success with cross diffusion than Speziale et al. and Peng et al. Both introduce "blending functions" that cause all of the model's closure coefficients to assume values appropriate for the k-ω model near solid boundaries, and to asymptotically approach values similar to those used with the k-ϵ model otherwise. The net result is a model that behaves very much like the Wilcox (1988a) k-ω model for wall-bounded flows, and more like the k-ϵ model for free shear flows.

Wilcox (1993a) and, more recently, Kok (2000) have tried a similar concept with the cross diffusion coefficient, σ_d, given by

$$\sigma_d = \begin{cases} 0, & \dfrac{\partial k}{\partial x_j}\dfrac{\partial \omega}{\partial x_j} \le 0 \\ \sigma_{do}, & \dfrac{\partial k}{\partial x_j}\dfrac{\partial \omega}{\partial x_j} > 0 \end{cases} \tag{4.103}$$

Additionally, the value of σ^* assumes a value larger than $1/2$. As we will see in Subsection 4.6.2, it is important to suppress this cross-diffusion term close to solid boundaries for wall-bounded flows. Just as Menter's blending function causes σ_d to approach 0 near a solid boundary, so does Equation (4.103) since k increases and ω decreases in the viscous sublayer. While simpler than Menter's blending-function approach, Wilcox and Kok chose values for σ_{do} that yield free shear layer spreading rates that are farther from measurements than those predicted by the k-ϵ model. Specifically, Wilcox set $\sigma_{do} = 3/10$, $\sigma = 3/5$ and $\sigma^* = 1$, while Kok opted for $\sigma_{do} = \sigma = 1/2$ and $\sigma^* = 2/3$.

However, other values of the k-ω model's closure coefficients exist that yield closer agreement with measured spreading rates. Note first that based on the analysis of a turbulent front by Lele (1985), there are two necessary conditions for the front to propagate. Specifically, we must have

$$\sigma_{do} > \sigma^* - \sigma \qquad \text{and} \qquad \sigma^* > \sigma_{do} \tag{4.104}$$

These constraints also follow from analysis of a turbulent/nonturbulent interface (see Section 7.2.2). Figure 4.16 shows how predicted spreading rates vary with σ_{do} for the far wake, the mixing layer and the plane jet. The curves shown have been computed with all other closure coefficients as specified in Equations (4.39) and (4.41). To isolate effects of cross diffusion, results shown correspond to having no stress limiter, i.e., $\tilde{\omega} = \omega$ in Equation (4.36). The limiter has virtually no effect on the far wake and the plane jet. It reduces the mixing-layer spreading rate by less than 6%. Of greatest relevance to the present discussion, the value of σ^* is $3/5$. As shown, spreading rates for all three cases are greatest when σ_{do} is equal to its minimum permissible value according to Equation (4.104), viz., $\sigma_{do} = \sigma^* - \sigma$. The predicted values decrease monotonically as σ_{do} increases and fall below the lower bound of measured spreading rates for all three cases when $\sigma_{do} = 1/5$, which is much less than the maximum allowable value of $3/5$.

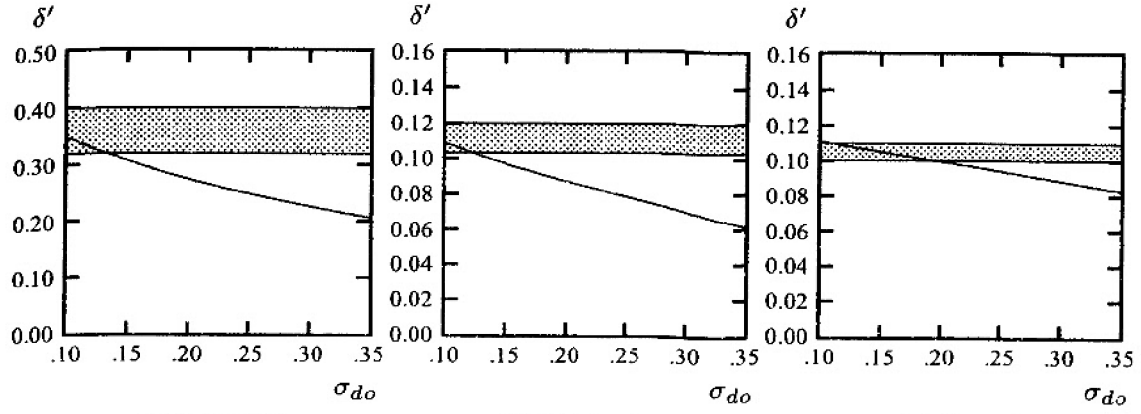

(a) Far wake (b) Mixing layer (c) Plane jet

Figure 4.16: *Effect of cross diffusion on free shear flow spreading rates for* $\sigma^* = 3/5$ *and* $\sigma = 1/2$. *The shaded areas depict measured-value ranges.*

Figure 4.17 shows how predicted spreading rates vary with σ^* when we set σ_{do} equal to its minimum permissible value. As above, computations have been done with all closure coefficients other than σ^* as specified in Equations (4.39) and (4.41) in the absence of the stress limiter. Computed spreading rates, δ', for all three cases decrease monotonically as σ^* increases. Computed δ' values lie above the range of measured δ' for all three cases when $\sigma^* < 0.55$, and below when $\sigma^* < 0.70$. Thus, we conclude that

$$0.55 < \sigma^* < 0.70 \qquad (\text{for } \sigma = 1/2) \tag{4.105}$$

These results provide the rationale for selecting $\sigma^* = 3/5$ and $\sigma_{do} = 1/8$ in the Wilcox (2006) version of the k-ω model [see Equations (4.39) and (4.40)].

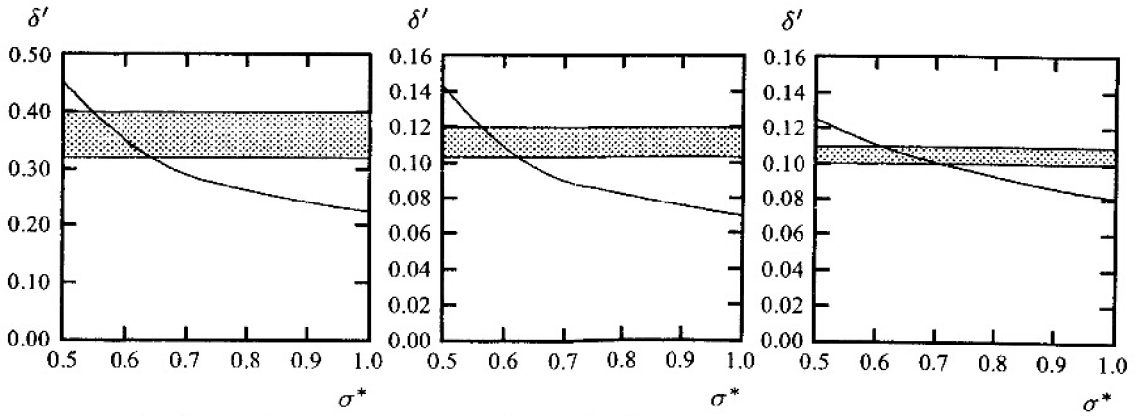

(a) Far wake (b) Mixing layer (c) Plane jet

Figure 4.17: *Effect of cross diffusion on free shear flow spreading rates for* $\sigma_{do} = \sigma^* - \sigma$ *and* $\sigma = 1/2$. *The shaded areas depict measured-value ranges.*

4.5.5 The Round-Jet/Plane-Jet Anomaly

Inspection of Tables 4.1, 4.4 and 4.5 shows that all but two of the turbulence models listed predict that the round jet spreads more rapidly than the plane jet. The two exceptions are the k-ω model and the Robinson et al. (1995) enstrophy-equation model. However, measurements indicate the opposite trend, with the round-jet spreading rate being about 10% lower than that of the plane jet. This shortcoming, common to most turbulence models, is known as the **round-jet/plane-jet anomaly**.

Pope (1978) has proposed a modification to the ϵ equation that resolves the round-jet/plane-jet anomaly for the k-ϵ model. In Pope's modification, the *dissipation of dissipation* term in the ϵ equation is replaced by

$$C_{\epsilon 2}\frac{\epsilon^2}{k} \rightarrow \left[C_{\epsilon 2} - C_{\epsilon 3}\chi_p\right]\frac{\epsilon^2}{k} \tag{4.106}$$

where χ_p is a "nondimensional measure of vortex stretching" defined as

$$\chi_p \equiv \frac{\Omega_{ij}\Omega_{jk}S_{ki}}{(\epsilon/k)^3} \tag{4.107}$$

The tensors Ω_{ij} and S_{ij} are the mean-rotation and mean-strain-rate tensors defined in Equation (4.43).

Pope's reasoning is that the primary mechanism for transfer of energy from large to small eddies is vortex stretching. Any mechanism that enhances vortex stretching will increase this rate of transfer. Since the energy is being transferred to the smallest eddies where dissipation occurs, necessarily the dissipation, ϵ, must increase. Because mean-flow vortex lines cannot be stretched in a two-dimensional flow, χ_p is zero for the plane jet. By contrast, as shown earlier [see Equations (4.89) – (4.96)], the vortex-stretching parameter is nonzero for an axisymmetric mean flow. As argued by Pope, this corresponds to the fact that vortex rings are being stretched radially. Thus, we expect to have $\chi_p \neq 0$ for a round jet.

Using $C_{\epsilon 3} = 0.79$ reduces the k-ϵ model's predicted spreading rate to 0.86, consistent with measurements. However, as pointed out by Rubel (1985), the Pope correction has an adverse effect on model predictions for the radial jet, which also has nonzero χ_p. Without the Pope correction, the k-ϵ model predicts a radial-jet spreading rate of 0.094 which is close to the measured range of 0.096 to 0.110 [see Tanaka and Tanaka (1976) and Witze and Dwyer (1976)]. Using the Pope correction for the radial jet reduces the k-ϵ model-predicted spreading rate to 0.040. Hence, as noted by Rubel, "the round jet/plane jet anomaly has been exchanged for a round jet/radial jet anomaly."

In contrast to the k-ϵ model, as indicated in Table 4.5, the Wilcox (1988a) k-ω model predicts comparable spreading rates for both the round and radial

jets, both larger than the predicted plane-jet spreading rate. The same is true of the k-ω model defined in Equations (4.36) – (4.42). When a constant value of $\beta = 0.0708$ is used for the latter, the predicted round- and radial-jet spreading rates are 0.177 and 0.168, respectively. Numerical experimentation shows that if β is reduced to 0.06, the model's spreading rates for both the round and radial jets are close to the measured values. Since Pope's argument implies nothing regarding the functional dependence of the modification upon the dimensionless vortex-stretching parameter, χ_p, it is completely consistent to propose that β depend upon this parameter in a manner that reduces the value of β as needed for both flows. Thus, as a generalization of the Pope modification, the k-ω model uses the following prescription for β.

$$\beta = \beta_o f_\beta \tag{4.108}$$

where

$$\beta_o = 0.0708, \qquad f_\beta = \frac{1 + 85\chi_\omega}{1 + 100\chi_\omega} \tag{4.109}$$

and

$$\chi_\omega \equiv \left| \frac{\Omega_{ij}\Omega_{jk}S_{ki}}{(\beta^*\omega)^3} \right| \tag{4.110}$$

Comparison of Equations (4.107) and (4.110) shows that $\chi_\omega = |\chi_p|$. Also, the functional form of f_β is such that its asymptotic value is 0.85, so that $\beta = 0.06$ for large values of χ_ω. Finally, note that the vortex-stretching parameter normally is very small in axisymmetric boundary layers because ω is very large.

Interestingly, the Robinson et al. (1995) enstrophy-equation model contains a term similar to the Pope modification. The vortex-stretching mechanism that it represents plays an important role in the model's ability to predict the measured spreading rates for all three jets within a few percent of measurements. Although the usefulness of Pope's correction as represented by Equations (4.106) and (4.107) is limited by a flaw in the k-ϵ model, the concepts underlying the formulation are not. We can reasonably conclude that Pope's analysis provides a sensible reflection of the physics of turbulent jets, at least in the context of ω-based two-equation models.

Our analysis of free shear flows is now complete. In the following sections we turn our attention to wall-bounded flows. To demonstrate how two-equation models fare for such flows, we are going to use a powerful mathematical tool to analyze fine details of model-predicted structure of the turbulent boundary layer. In particular, we will use **perturbation methods** to analyze the various regions in the turbulent boundary layer.

4.6 Perturbation Analysis of the Boundary Layer

The differential equations for all but the simplest turbulence models are sufficiently complicated for most flows that closed-form solutions do not exist. This is especially true for boundary layers because of nonlinearity of the convection terms and the turbulent diffusion terms attending introduction of the eddy viscosity. Our inability to obtain closed-form solutions is unfortunate because such solutions are invaluable in design studies and for determining trends with a parameter such as Reynolds number, or more generally, for establishing laws of similitude. Furthermore, without analytical solutions, our ability to check the accuracy of numerical solutions is limited.

There is a powerful mathematical tool available to us to generate approximate solutions that are valid in special limiting cases, viz., **perturbation analysis**. The idea of perturbation analysis is to develop a solution in the form of an **asymptotic expansion** in terms of a parameter, the error being small for sufficiently small values of the parameter. Our desire in developing such an expansion is for the first few terms of the expansion to illustrate all of the essential physics of the problem and to provide a close approximation to the exact solution. Fortunately, this is usually the case in fluid mechanics. This section shows how perturbation analysis can be used to dissect model-predicted structure of the turbulent boundary layer. Appendix B introduces basic concepts of perturbation theory for the reader with no prior background in the field.

4.6.1 The Log Layer

We direct our focus to the turbulent boundary layer. Experimental observations provide a strong argument for using perturbation analysis. Specifically, Coles' description of the turbulent boundary layer as a "wake-like structure constrained by a wall" (see Figure 3.9) suggests that different scales and physical processes are dominant in the inner (near-wall) and outer (main body) parts of the layer. These are concepts upon which perturbation analysis is based. Coles [see Coles and Hirst (1969)] makes an explicit connection with perturbation theory in saying:

> *"The idea that there are two distinct scales in a turbulent boundary layer is an old one, although quantitative expressions of this idea have evolved very slowly... To the extent that the outer velocity boundary condition for the inner (wall) profile is the same as the inner velocity boundary condition for the outer (wake) profile, the turbulent boundary layer is a singular perturbation problem of classical type. In fact, we can claim to have discovered the first two terms in a composite expansion, complete with logarithmic behavior."*

Often perturbation solutions are guided by dimensional considerations and a knowledge of physical aspects of the problem. For the turbulent boundary layer, we can draw from empirically established laws to aid us in developing our perturbation solution. We observe that close to a solid boundary, the **law of the wall** holds. As discussed in Subsection 1.3.5, we can write this symbolically as

$$U(x,y) = u_\tau(x) f(u_\tau y/\nu), \qquad u_\tau = \sqrt{\tau_w/\rho} \tag{4.111}$$

Similarly, the main body of the turbulent boundary layer behaves according to Clauser's (1956) well-known **defect law**, viz.,

$$U(x,y) = U_e(x) - u_\tau(x) F[y/\Delta(x)], \qquad \Delta(x) = U_e \delta^*/u_\tau \tag{4.112}$$

The reader should keep in mind that Equation (4.112) only applies to a special class of boundary layers, i.e., boundary layers that are self preserving. Thus, we seek solutions where $F(y/\Delta)$ is independent of x. As we will see, the model equations predict existence of such solutions under precisely the same conditions Clauser discovered experimentally.

We develop the leading terms in a perturbation solution for the turbulent boundary layer in the following subsections. There are two small parameters in our problem, the first being the reciprocal of the Reynolds number. This is consistent with the standard boundary-layer approximations. The second small parameter is u_τ/U_e. Clauser's defect law suggests this parameter since the velocity is expressed as a (presumably) small deviation from the freestream velocity that is proportional to u_τ. The analysis will lead to a relation between these two parameters.

The analysis in this section, which is patterned after the work of Bush and Fendell (1972) and Fendell (1972), shows in Subsection 4.6.3 that the inner expansion is of the form quoted in Equation (4.111) and is valid in the **viscous sublayer** (see Figure 3.8). We also show in Subsection 4.6.2 that the outer expansion is identical in form to Equation (4.112) and holds in the **defect layer**. Formal matching of the sublayer and defect-layer solutions occurs in an overlap region that is often described as the **log layer**. In fact, the common part of the inner and outer expansions is precisely the law of the wall. Thus, although it is not formally a separate layer, establishing flow properties in the log layer permits independent analysis of the sublayer and defect layer. It also forms the basis of surface boundary conditions for many two-equation turbulence models. We discuss the log layer in this subsection.

Before performing any analysis, we anticipate that we will be solving a **singular-perturbation problem**. We expect this, but not because of a reduction in order of the differential equations. Rather, we have no hope of satisfying the no-slip condition with our outer solution because of the assumed form in the defect layer, i.e., velocity being a small perturbation from the freestream value.

Likewise, the sublayer solution, if it is consistent with measurements, predicts velocity increasing logarithmically with distance from the surface as $y \to \infty$ so that we cannot satisfy the freestream boundary condition with our inner solution. This is the irregular behavior near boundaries alluded to in Appendix B where we define a singular-perturbation problem.

We begin our analysis with the incompressible boundary-layer equations. Conservation of mass and momentum are sufficient for establishing the form of the expansions, so that we have no need to introduce the model equations now. For two-dimensional flow, we have

$$\frac{\partial U}{\partial x} + \frac{\partial V}{\partial y} = 0 \tag{4.113}$$

$$U\frac{\partial U}{\partial x} + V\frac{\partial U}{\partial y} = -\frac{1}{\rho}\frac{dP}{dx} + \frac{\partial}{\partial y}\left[(\nu + \nu_T)\frac{\partial U}{\partial y}\right] \tag{4.114}$$

The easiest way to arrive at the **log-layer** equations is to derive the **sublayer** equations and then to determine the limiting form of the sublayer equations for $y^+ \to \infty$. Consistent with the normal boundary-layer concept that variations in the streamwise (x) direction are much less rapid than those in the normal (y) direction, we scale x and y differently. Letting L denote a dimension characteristic of distances over which flow properties change in the x direction, we scale x and y according to

$$\xi = x/L \qquad \text{and} \qquad y^+ = u_\tau y/\nu \tag{4.115}$$

The appropriate expansions for the streamfunction and kinematic eddy viscosity are

$$\psi_{inner}(x,y) \sim \nu[f_0(\xi,y^+) + \phi_1 f_1(\xi,y^+) + O(\phi_2)] \tag{4.116}$$

$$\nu_{T_{inner}}(x,y) \sim \nu[N_0(\xi,y^+) + \phi_1 N_1(\xi,y^+) + O(\phi_2)] \tag{4.117}$$

where the asymptotic sequence $\{1, \phi_1, \phi_2, \ldots\}$ is to be determined. Consequently, the streamwise velocity becomes

$$U(x,y) \sim u_\tau\left[\hat{u}_0(\xi,y^+) + \phi_1\hat{u}_1(\xi,y^+) + O(\phi_2)\right], \qquad \hat{u}_n \equiv \frac{\partial f_n}{\partial y^+} \tag{4.118}$$

Substituting into the momentum equation, we obtain

$$\frac{\partial}{\partial y^+}\left[(1+N_0)\frac{\partial \hat{u}_0}{\partial y^+}\right] + O(\phi_1) = \frac{\nu}{u_\tau \delta^*}\left[\beta_T + O\left(\frac{\delta^*}{L}\right)\right] \tag{4.119}$$

where the quantity β_T is the so-called **equilibrium parameter** [see Coles and Hirst (1969)] defined by

$$\beta_T \equiv \frac{\delta^*}{\tau_w}\frac{dP}{dx} \tag{4.120}$$

In general, we regard β_T as being of order one. In fact, when we analyze the defect layer, this will be the key parameter quantifying the effect of pressure gradient on our solution. Additionally, $u_\tau \delta^*/\nu \gg 1$ and $\delta^* \ll L$. Hence, we conclude that

$$\phi_1 = \frac{\nu}{u_\tau \delta^*} \tag{4.121}$$

and

$$\frac{\partial}{\partial y^+}\left[(1+N_0)\frac{\partial \hat{u}_0}{\partial y^+}\right] = 0 \tag{4.122}$$

To enhance physical understanding of what we have just proven, it is worthwhile to return to dimensional variables. We have shown that, to leading order, the convective terms and the pressure gradient are small compared to the other terms in the sublayer so that the momentum equation simplifies to

$$\frac{\partial}{\partial y}\left[(\nu+\nu_T)\frac{\partial U}{\partial y}\right] = 0 \tag{4.123}$$

Integrating once tells us that the sum of the specific molecular and Reynolds shear stress is constant in the sublayer, i.e.,

$$(\nu+\nu_T)\frac{\partial U}{\partial y} = \frac{\tau_w}{\rho} \tag{4.124}$$

Equation (4.123) or (4.124) is the equation for the leading-order term in the inner expansion for a turbulent boundary layer. As we will demonstrate in greater detail in Subsection 4.6.3, we can satisfy the no-slip condition ($U = 0$) at $y = 0$ while the solution as $y^+ \to \infty$ asymptotes to the law of the wall, i.e., velocity increasing logarithmically with distance from the surface. Another feature of the solution is that the eddy viscosity increases linearly with y^+ as $y^+ \to \infty$ so that the eddy viscosity becomes very large compared to the molecular viscosity. Consistent with this behavior, the molecular viscosity can be neglected in Equation (4.123) or (4.124) for the limiting case $y^+ \to \infty$. As noted above, we refer to the form of the differential equations in this limit as the **log-layer equations**. Thus, we conclude that in the log layer we can neglect convection, pressure gradient and molecular diffusion. The momentum equation thus simplifies to the following:

$$0 = \frac{\partial}{\partial y}\left[\nu_T \frac{\partial U}{\partial y}\right] \tag{4.125}$$

To the same degree of approximation, in the log layer, the k-ω model equations for two-dimensional flow (so that $\chi_\omega = 0 \Rightarrow \beta = \beta_o$) simplify to:

k-ω Model:

$$\left.\begin{aligned} 0 &= \nu_T \left(\frac{\partial U}{\partial y}\right)^2 - \beta^* \omega k + \sigma^* \frac{\partial}{\partial y}\left[\frac{k}{\omega}\frac{\partial k}{\partial y}\right] \\ 0 &= \alpha \left(\frac{\partial U}{\partial y}\right)^2 - \beta_o \omega^2 + \frac{\sigma_d}{\omega}\frac{\partial k}{\partial y}\frac{\partial \omega}{\partial y} + \sigma \frac{\partial}{\partial y}\left[\frac{k}{\omega}\frac{\partial \omega}{\partial y}\right] \\ \nu_T &= \frac{k}{\tilde{\omega}}, \qquad \tilde{\omega} = \max\left\{\omega,\ C_{lim}\frac{\partial U/\partial y}{\sqrt{\beta^*}}\right\} \end{aligned}\right\} \tag{4.126}$$

As can be shown by direct substitution, the solution to Equations (4.125) and (4.126) is

$$U = \frac{u_\tau}{\kappa}\ell n y + C, \qquad k = \frac{u_\tau^2}{\sqrt{\beta^*}}, \qquad \omega = \frac{u_\tau}{\sqrt{\beta^*}\kappa y} \tag{4.127}$$

where C is a constant and the implied value of the Kármán constant, κ, is

$$\kappa^2 = \sqrt{\beta^*}(\beta_o/\beta^* - \alpha)/\sigma \tag{4.128}$$

Note that the terms proportional to σ^* and σ_d disappear because $\partial k/\partial y = 0$. Also, because Equation (4.127) tells us that $\partial U/\partial y = \sqrt{\beta^*}\omega$, there follows $\tilde{\omega} = \max\{\omega,\ C_{lim}\omega\} = \omega$, i.e., the stress limiter has no effect in the sublayer. The closure coefficient values specified in Equation (4.39) have been chosen to give $\kappa = 0.40$. We discussed the log-layer solution in Section 4.4 to illustrate how values for some of the closure coefficients have been selected. There are additional features of the solution worthy of mention. For example, the eddy viscosity varies linearly with distance from the surface and is given by

$$\nu_T = \kappa u_\tau y \tag{4.129}$$

This variation is equivalent to the mixing-length variation, $\ell_{mix} = \kappa y$. Also, the ratio of the Reynolds shear stress to turbulence kinetic energy is constant, i.e.,

$$\tau_{xy} = \sqrt{\beta^*}\, k \tag{4.130}$$

In a similar way, the k-ϵ model equations simplify to the following:

k-ϵ Model:

$$\left.\begin{aligned} 0 &= \nu_T \left(\frac{\partial U}{\partial y}\right)^2 - \epsilon + \frac{\partial}{\partial y}\left[\frac{\nu_T}{\sigma_k}\frac{\partial k}{\partial y}\right] \\ 0 &= C_{\epsilon 1} C_\mu k \left(\frac{\partial U}{\partial y}\right)^2 - C_{\epsilon 2}\frac{\epsilon^2}{k} + \frac{\partial}{\partial y}\left[\frac{\nu_T}{\sigma_\epsilon}\frac{\partial \epsilon}{\partial y}\right] \\ \nu_T &= C_\mu k^2/\epsilon \end{aligned}\right\} \tag{4.131}$$

The solution to Equations (4.125) and (4.131) is

$$U = \frac{u_\tau}{\kappa}\ell ny + \text{constant}, \qquad k = \frac{u_\tau^2}{\sqrt{C_\mu}}, \qquad \epsilon = \frac{u_\tau^3}{\kappa y} \tag{4.132}$$

where we again find an implied value for the Kármán constant, κ, viz.,

$$\kappa^2 = \sqrt{C_\mu}(C_{\epsilon 2} - C_{\epsilon 1})\sigma_\epsilon \tag{4.133}$$

Using the closure coefficient values for the Standard k-ϵ model [Equation (4.49)], κ assumes a somewhat large value of 0.433. For the RNG k-ϵ model [Equations (4.51) – (4.53)], we find $\kappa = 0.399$.

Keep in mind that the turbulent boundary layer consists of the sublayer and the defect layer. The sublayer is a thin near-wall region, while the defect layer constitutes most of the boundary layer. In the spirit of matched asymptotic expansions, the log layer is the overlap region which, in practice, is usually much thicker than the sublayer (see Figure 3.8). Part of our reason for focusing on this region of the boundary layer is of historical origin. Aside from the k-ω model, most two-equation models fail to agree satisfactorily with experiment in the viscous sublayer unless the coefficients are made empirical functions of an appropriate turbulence Reynolds number (which we discuss in Subsection 4.9.1). Consequently, the log-layer solution has often been used as a replacement for the no-slip boundary condition. Early k-ϵ model solutions, for example, were generated by enforcing the asymptotic behavior given in Equation (4.132). We must postpone further discussion of surface boundary conditions pending detailed analysis of the sublayer. Analysis of the log layer can also prove useful in determining leading-order effects of complicating factors such as surface curvature, coordinate-system rotation, and compressibility. As our most immediate goal, we have, in effect, done our matching in advance. Thus, we are now in a position to analyze the defect layer and the sublayer independent of one another. We turn first to the defect layer.

4.6.2 The Defect Layer

In this subsection, we make use of singular-perturbation methods to analyze model-predicted structure of the classical defect layer, including effects of pressure gradient. Our analysis includes three turbulence models, viz.: the Wilcox (2006) k-ω model; the Standard k-ϵ model; and the RNG k-ϵ model. First, we generate the perturbation solution. Next, we compare solutions for the three models in the absence of pressure gradient. Then, we examine effects of pressure gradient for the models. Finally, as promised in Section 4.4, we further justify the values chosen for σ, σ^* and σ_d in the k-ω model.

To study the defect layer, we continue to confine our analysis to incompressible flow so that we begin with Equations (4.113) and (4.114). The perturbation expansion for the defect layer proceeds in terms of the ratio of friction velocity to the boundary-layer-edge velocity, u_τ/U_e, and the dimensionless coordinates, ξ and η, defined by

$$\xi = x/L \quad \text{and} \quad \eta = y/\Delta(x), \quad \Delta = U_e\delta^*/u_\tau \tag{4.134}$$

where δ^* is displacement thickness and L is a characteristic streamwise length scale that is presumed to be very large compared to δ^*. As in our approach to the log layer, we first establish the general form of the solution for the mean momentum equation. We expand the streamfunction and kinematic eddy viscosity as follows.

$$\psi_{outer}(x,y) \sim U_e\Delta\left[\eta - \frac{u_\tau}{U_e}F_1(\xi,\eta) + o\left(\frac{u_\tau}{U_e}\right)\right] \tag{4.135}$$

$$\nu_{T_{outer}}(x,y) \sim U_e\delta^*\left[N_0(\xi,\eta) + o(1)\right] \tag{4.136}$$

Observe that, as is so often the case in perturbation analysis, we needn't continue the expansions beyond the first one or two terms to capture most of the important features of the solution. For the specified streamfunction, the velocity becomes:

$$U(x,y) \sim U_e\left[1 - \frac{u_\tau}{U_e}U_1(\xi,\eta) + o\left(\frac{u_\tau}{U_e}\right)\right], \qquad U_1 = \frac{\partial F_1}{\partial\eta} \tag{4.137}$$

Substituting Equations (4.134) – (4.137) into the mean conservation equations [Equations (4.113) and (4.114)] yields the transformed momentum equation, viz.,

$$2\sigma_T\xi\frac{\partial U_1}{\partial\xi} = (\alpha_T - 2\beta_T - 2\omega_T)\eta\frac{\partial U_1}{\partial\eta} + (\beta_T - 2\omega_T)U_1 + \frac{\partial}{\partial\eta}\left[N_0\frac{\partial U_1}{\partial\eta}\right] \tag{4.138}$$

where the parameters α_T, β_T, σ_T and ω_T are defined in terms of δ^*, u_τ and skin friction, $c_f = 2(u_\tau/U_e)^2$, i.e.,

$$\alpha_T \equiv \frac{2}{c_f}\frac{d\delta^*}{dx}, \quad \beta_T \equiv \frac{\delta^*}{\tau_w}\frac{dP}{dx}, \quad \sigma_T \equiv \frac{\delta^*}{c_f x}, \quad \omega_T \equiv \frac{\delta^*}{c_f u_\tau}\frac{du_\tau}{dx} \tag{4.139}$$

Equation (4.138) must be solved subject to two boundary conditions. First, to satisfy the requirement that $U \to U_e$ as $y \to \infty$, necessarily

$$U_1 \to 0 \quad \text{as} \quad \eta \to \infty \tag{4.140}$$

Also, we must asymptote to the log-layer solution as $\eta \to 0$. One way to insure this is to insist that

$$\frac{\partial U_1}{\partial\eta} \to -\frac{1}{\kappa\eta} \quad \text{as} \quad \eta \to 0 \tag{4.141}$$

At this point, we have not greatly simplified our problem. Equation (4.138), like the original momentum equation, is a partial differential equation. The only simplification thus far is that molecular viscosity is negligible relative to the eddy viscosity. However, even this is not necessarily advantageous since the no-slip velocity boundary condition has been replaced by singular behavior approaching the surface. And, of course, we are now working in a transformed coordinate system (ξ, η) rather than the familiar Cartesian coordinate system (x, y). So why go to all this trouble? The answer is, we have only just begun.

Reexamination of the steps we have taken thus far should reveal a familiar tack; specifically, we appear to be developing a similarity solution. Indeed this is intentional, and inspection of Clauser's defect law [Equation (4.112)] shows that there has been method in our madness. Comparison of Equation (4.112) with the assumed form of our perturbation expansion for U given in Equation (4.137) shows that U_1 must be a function only of η. Thus, we now pose the question as to what conditions must be satisfied in order for a similarity solution to exist.

Clearly, the coefficients α_τ, β_τ and ω_τ must be independent of x, for then the coefficients of all terms on the right-hand side of Equation (4.138) will be independent of x. The coefficient σ_τ is of no consequence since, if U_1 is independent of x, the left-hand side of Equation (4.138) vanishes regardless of the value of σ_τ.

The coefficients α_τ and ω_τ are simple algebraic functions of β_τ. To show this, we begin by performing the formal matching of the defect-layer and sublayer solutions. As shown in the preceding section,

$$U_{inner}(\xi, y^+) \sim u_\tau \left[\frac{1}{\kappa}\ell n y^+ + C\right] \quad \text{as} \quad y^+ \to \infty \tag{4.142}$$

Assuming that a similarity solution exists so that U_1 depends only upon η, straightforward substitution into Equation (4.138) with a vanishing left-hand side shows that

$$U_1 \sim \frac{1}{\kappa}[-\ell n\eta + u_0 - u_1\eta\ell n\eta + \cdots] \quad \text{as} \quad \eta \to 0 \tag{4.143}$$

where the constants $u_0, u_1, \ldots$ depend upon the complete solution which, in turn, depends upon what turbulence model is used. We now do a formal matching of the inner and outer expansions noting that $y^+ = \eta Re_{\delta^*}$ and the outer solution is $U_{outer}(\xi, \eta) \sim [U_e - u_\tau U_1(\eta) + \cdots]$. To match through first order, we require the following:

$$\left[\frac{1}{\kappa}\ell n y^+ + C\right] - \left[\frac{U_e}{u_\tau} + \frac{1}{\kappa}\ell n\eta - \frac{u_0}{\kappa}\right] \to 0 \quad \text{as} \quad y^+ \to \infty, \quad \eta \to 0 \tag{4.144}$$

Hence, we conclude from matching that:

$$\frac{U_e}{u_\tau} = \left(C + \frac{u_0}{\kappa}\right) + \frac{1}{\kappa}\ell n Re_{\delta^*} \tag{4.145}$$

This is a useful result that enables us to compute the skin friction from our defect-layer solution, a point we will return to later. For our present purpose, Equation (4.145) enables us to determine ω_T. That is, since

$$u_\tau = \frac{U_e}{\left(C + \frac{u_0}{\kappa}\right) + \frac{1}{\kappa}\ell n Re_{\delta^*}} \tag{4.146}$$

Differentiating with respect to x yields

$$\begin{aligned}
\frac{du_\tau}{dx} &= \frac{dU_e/dx}{\left(C + \frac{u_0}{\kappa}\right) + \frac{1}{\kappa}\ell n Re_{\delta^*}} - \frac{U_e dRe_{\delta^*}/dx}{\kappa Re_{\delta^*}\left[\left(C + \frac{u_0}{\kappa}\right) + \frac{1}{\kappa}\ell n Re_{\delta^*}\right]^2} \\
&= \frac{u_\tau}{U_e}\frac{dU_e}{dx} - \frac{u_\tau^2}{\kappa U_e Re_{\delta^*}}\frac{dRe_{\delta^*}}{dx}
\end{aligned} \tag{4.147}$$

Substituting Equation (4.147) into the definition of ω_T [see Equation (4.139)] and using the fact that $u_\tau^2 = \frac{1}{2}U_e^2 c_f$, we find

$$\begin{aligned}
\omega_T &= \frac{\delta^*}{c_f U_e}\frac{dU_e}{dx} - \frac{\delta^*}{c_f u_\tau}\frac{\frac{1}{2}U_e^2 c_f}{\kappa U_e^2 \delta^*/\nu}\frac{d}{dx}\left(\frac{U_e\delta^*}{\nu}\right) \\
&= \frac{\delta^*}{c_f U_e}\frac{dU_e}{dx} - \frac{1}{2\kappa u_\tau}\frac{d}{dx}\left(U_e\delta^*\right) \\
&= \frac{\delta^*}{c_f U_e}\left[1 - \frac{1}{\kappa}\frac{c_f}{2}\frac{U_e}{u_\tau}\right]\frac{dU_e}{dx} - \frac{1}{2\kappa}\frac{U_e}{u_\tau}\frac{d\delta^*}{dx} \\
&= \frac{\delta^*}{c_f U_e}\left[1 - \frac{1}{\kappa}\frac{u_\tau}{U_e}\right]\frac{dU_e}{dx} - \frac{1}{2\kappa}\frac{U_e}{u_\tau}\frac{d\delta^*}{dx}
\end{aligned} \tag{4.148}$$

We can compute $d\delta^*/dx$ and dU_e/dx from the definitions of α_T and β_T given in Equation (4.139), i.e.,

$$\frac{d\delta^*}{dx} = \frac{c_f\,\alpha_T}{2} \quad \text{and} \quad \frac{dU_e}{dx} = -\frac{1}{\rho U_e}\frac{dP}{dx} = -\frac{\tau_w}{\rho U_e \delta^*}\beta_T \tag{4.149}$$

Combining Equations (4.148) and (4.149), we have

$$\begin{aligned}
\omega_T &= \frac{\delta^*}{c_f U_e}\left[1 - \frac{1}{\kappa}\frac{u_\tau}{U_e}\right]\left(-\frac{\tau_w}{\rho U_e\delta^*}\right)\beta_T - \frac{1}{2\kappa}\frac{U_e}{u_\tau}\left(\frac{c_f\,\alpha_T}{2}\right) \\
&= -\underbrace{\frac{\tau_w}{\rho U_e^2 c_f}}_{=2\tau_w}\left[1 - \frac{1}{\kappa}\frac{u_\tau}{U_e}\right]\beta_T - \frac{1}{4\kappa}\underbrace{c_f\frac{U_e}{u_\tau}}_{=2u_\tau/U_e}\alpha_T \\
&= -\frac{1}{2}\beta_T\left[1 - \frac{1}{\kappa}\frac{u_\tau}{U_e}\right] - \frac{1}{2\kappa}\frac{u_\tau}{U_e}\alpha_T
\end{aligned} \tag{4.150}$$

Therefore, regrouping terms, we conclude that

$$\omega_T = -\frac{1}{2}\beta_T + \frac{1}{2\kappa}\left(\beta_T - \alpha_T\right)\frac{u_\tau}{U_e} \tag{4.151}$$

Finally, since we seek a solution valid in the limit $u_\tau/U_e \to 0$, we have

$$\omega_T = -\frac{1}{2}\beta_T + O\left(\frac{u_\tau}{U_e}\right) \tag{4.152}$$

Note that Bush and Fendell (1972) incorrectly argue that $\omega_T = o(1)$ in the limit $u_\tau/U_e \to 0$. Using arguments similar to those above, Tennekes and Lumley (1983) and Henkes (1998a) also show that ω_T is given by Equation (4.152).

This reduces the requirement for existence of a similarity solution to only α_T and β_T being independent of x. However, we can also show that α_T and β_T are uniquely related to leading order. To see this, we examine the classical momentum-integral equation that follows from integrating the mean-momentum equation across the boundary layer [c.f., Gersten-Schlichting (1999)], viz.,

$$\frac{c_f}{2} = \frac{d\theta}{dx} - (2+H)\frac{\theta}{\rho U_e^2}\frac{dP}{dx} \tag{4.153}$$

where θ is momentum thickness and $H = \delta^*/\theta$ is the shape factor. In terms of α_T and β_T, the momentum-integral equation can be rewritten as

$$\alpha_T \frac{d\theta}{dx} = \left[1 + \frac{(2+H)}{H}\beta_T\right]\frac{d\delta^*}{dx} \tag{4.154}$$

If we evaluate the displacement and momentum thickness using our perturbation solution we find two important facts. First, evaluating the displacement thickness integral yields an integral constraint on our solution for U_1, U_2, etc. Second, we find to leading order that δ^* and θ are equal, i.e., the shape factor approaches 1 as $Re_{\delta^*} \to \infty$ and/or $u_\tau/U_e \to 0$. The proof of these facts is straightforward and thus left for the problems section; the results are:

$$\int_0^\infty U_1(\eta)\,d\eta = 1, \qquad \int_0^\infty U_n(\eta)\,d\eta = 0, \quad n \geq 2 \tag{4.155}$$

$$H \sim 1 + O\left(\frac{u_\tau}{U_e}\right) \qquad \text{as} \qquad Re_{\delta^*} \to \infty, \quad \frac{u_\tau}{U_e} \to 0 \tag{4.156}$$

The perturbation solution for $U_1(\eta)$ provides sufficient information to determine the $O(u_\tau/U_e)$ term[8] for H (see problems section). Hence, Equation (4.154) yields the following relationship between α_T and β_T.

$$\alpha_T = 1 + 3\beta_T \tag{4.157}$$

[8]The coefficient of this term is generally large, and realistic shape factors (e.g., $H \approx 1.3$ for a flat-plate) follow from the perturbation solution.

Thus, we see that the requirement for existence of a similarity solution to Equation (4.138) for large Reynolds number is simply that the **equilibrium parameter**, β_T, be constant. This is a very satisfactory state of affairs because it is consistent with experimental observations at finite (laboratory-scale) Reynolds numbers. That is, Clauser found that, outside the viscous sublayer, turbulent boundary layers assume a self-similar form when the equilibrium parameter is constant.

Appealing to Equations (4.152) and (4.157), the coefficients appearing in Equation (4.138) are

$$\alpha_T - 2\beta_T - 2\omega_T = 1 + 2\beta_T \quad \text{and} \quad \beta_T - 2\omega_T = 2\beta_T \tag{4.158}$$

Then, the problem we must solve to determine $U_1(\eta)$ is:

$$\frac{d}{d\eta}\left[N_0 \frac{dU_1}{d\eta}\right] + (1 + 2\beta_T)\eta \frac{dU_1}{d\eta} + 2\beta_T U_1 = 0 \tag{4.159}$$

$$\frac{dU_1}{d\eta} \to -\frac{1}{\kappa\eta} \quad \text{as} \quad \eta \to 0 \qquad \text{and} \qquad U_1(\eta) \to 0 \quad \text{as} \quad \eta \to \infty \tag{4.160}$$

The integral constraint, Equation (4.155), must also be enforced. The dimensionless eddy viscosity, $N_0(\eta)$, depends upon the turbulence model selected. For our purposes, we will consider three different turbulence models, viz.: the Wilcox (2006) k-ω model [Equations (4.36) – (4.42)]; the Standard k-ϵ model [Equations (4.46) – (4.49)]; and the RNG k-ϵ model [Equations (4.46) – (4.48) and (4.51) – (4.53)].

Making standard boundary-layer approximations for the model equations, we seek a perturbation solution for k, ω and ϵ of the following form.

$$\left.\begin{aligned} k &\sim \frac{u_\tau^2}{\sqrt{\beta^*}}\left[K_0(\eta) + o(1)\right] \\ \omega &\sim \frac{u_\tau}{\sqrt{\beta^*}\Delta}\left[W_0(\eta) + o(1)\right] \\ \epsilon &\sim \frac{u_\tau^3}{\Delta}\left[E_0(\eta) + o(1)\right] \end{aligned}\right\} \tag{4.161}$$

Note that for the k-ϵ models, we make the identification $\beta^* = C_\mu$. The precise form of the equations and auxiliary relations are specific to each model. The transformed equations are as follows.

k-ω Model:

$$\left.\begin{aligned}
&\sigma^* \frac{d}{d\eta}\left[\frac{K_0}{W_0}\frac{dK_0}{d\eta}\right] + (1+2\beta_T)\eta\frac{dK_0}{d\eta} + 2\beta_T K_0 \\
&\quad + \sqrt{\beta^*}\left[N_0\left(\frac{dU_1}{d\eta}\right)^2 - W_0 K_0\right] = 0 \\
&\sigma \frac{d}{d\eta}\left[\frac{K_0}{W_0}\frac{dW_0}{d\eta}\right] + (1+2\beta_T)\eta\frac{dW_0}{d\eta} + (1+4\beta_T)W_0 \\
&\quad + \sqrt{\beta^*}\left[\alpha N_0 \frac{W_0}{K_0}\left(\frac{dU_1}{d\eta}\right)^2 - \frac{\beta_o}{\beta^*}W_0^2\right] \\
&\quad + \frac{\sigma_d}{W_0}\frac{dK_0}{d\eta}\frac{dW_0}{d\eta} = 0 \\
&N_0 = \frac{K_0}{\tilde{W}_0}, \qquad \tilde{W}_0 = \max\left\{W_0,\ C_{lim}\left|\frac{dU_1}{d\eta}\right|\right\}
\end{aligned}\right\} \tag{4.162}$$

k-ϵ Model:

$$\left.\begin{aligned}
&\sigma_k^{-1}\frac{d}{d\eta}\left[N_0\frac{dK_0}{d\eta}\right] + (1+2\beta_T)\eta\frac{dK_0}{d\eta} + 2\beta_T K_0 \\
&\quad + \sqrt{C_\mu}\left[N_0\left(\frac{dU_1}{d\eta}\right)^2 - E_0\right] = 0 \\
&\sigma_\epsilon^{-1}\frac{d}{d\eta}\left[N_0\frac{dE_0}{d\eta}\right] + (1+2\beta_T)\eta\frac{dE_0}{d\eta} + (1+6\beta_T)E_0 \\
&\quad + \sqrt{C_\mu}\left[C_{\epsilon 1}K_0\left(\frac{dU_1}{d\eta}\right)^2 - C_{\epsilon 2}\frac{E_0^2}{K_0}\right] = 0 \\
&N_0 = \frac{K_0^2}{E_0}
\end{aligned}\right\} \tag{4.163}$$

We must specify boundary conditions on the dimensionless functions K_0, W_0 and E_0 both in the freestream and approaching the surface. For nonturbulent flow in the freestream, we require that the turbulence parameters all vanish as the similarity variable $\eta \to \infty$. However, we also stipulate that these quantities

approach zero in such a way that the transformed eddy viscosity, N_0, vanishes.[9] Thus, the freestream boundary conditions are

$$K_0(\eta) \to 0, \quad W_0(\eta) \to 0, \quad E_0(\eta) \to 0, \quad U_1(\eta) \to 0 \quad \text{as} \quad \eta \to \infty \tag{4.164}$$

Approaching the surface, we must formally match to the law of the wall. Matching is a bit different for each model but is nevertheless straightforward; we omit details of the algebra in the interest of brevity. The limiting forms used for $\eta \to 0$ are

$$\left.\begin{aligned} K_0(\eta) &\sim [1 + k_1 \eta \ell n \eta + \cdots] \\ E_0(\eta) &\sim \frac{1}{\kappa\eta}[1 + e_1 \eta \ell n \eta + \cdots] \\ W_0(\eta) &\sim \frac{1}{\kappa\eta}[1 + w_1 \eta \ell n \eta + \cdots] \\ U_1(\eta) &\sim \frac{1}{\kappa}[-\ell n \eta + u_0 - u_1 \eta \ell n \eta + \cdots] \end{aligned}\right\} \tag{4.165}$$

The coefficients k_1, u_1, w_1 and e_1 are given below, where for notational consistency, we define

$$\alpha^* \equiv \sqrt{\beta^*} = \sqrt{C_\mu} \tag{4.166}$$

Also, we write some of the results in terms of σ^* with the understanding that $\sigma^* = 1/\sigma_k$ for the k-ϵ models.

All Models:

$$k_1 = \frac{2\beta_T/\kappa}{\sigma^*\kappa^2/(2\alpha^*) - 1} \tag{4.167}$$

***k*-ω Model:**

$$\left.\begin{aligned} u_1 &= \frac{[\beta_o/(\alpha\beta^*) + \sigma_{do}/(\alpha\sigma^*)]\left[\sigma^*\kappa^2/(2\alpha^*)\right]}{1 - \beta_o/(\alpha\beta^*)} k_1 \\ w_1 &= \frac{[1 + \sigma_{do}/(\alpha\sigma^*)]\left[\sigma^*\kappa^2/(2\alpha^*)\right]}{1 - \beta_o/(\alpha\beta^*)} k_1 \end{aligned}\right\} \tag{4.168}$$

Standard *k*-ε Model:

$$\left.\begin{aligned} u_1 &= \frac{\left(1 + \sigma^*\kappa^2/\alpha^*\right) C_{\epsilon 2} - C_{\epsilon 1}}{2\left(C_{\epsilon 1} - C_{\epsilon 2}\right)} k_1 \\ e_1 &= \frac{\left(1 + \sigma^*\kappa^2/\alpha^*\right) C_{\epsilon 1} - C_{\epsilon 2}}{2\left(C_{\epsilon 1} - C_{\epsilon 2}\right)} k_1 \end{aligned}\right\} \tag{4.169}$$

[9]The k-ω model also has a similarity solution with W_0 approaching a nonzero value in the freestream. It is the solution that normally prevails and is used in Program DEFECT.

RNG k-ϵ Model:

$$\left.\begin{aligned} u_1 &= \left\{(\sigma_\epsilon/2)\left[1/\sigma_\epsilon - \sigma^*\left(C_{\epsilon 1} - C'_{\epsilon 2}\right)\right] - \left[1 + \sigma^*\kappa^2/\left(2\alpha^*\right)\right]\right\} k_1 \\ e_1 &= (\sigma_\epsilon/2)\left[1/\sigma_\epsilon - \sigma^*\left(C_{\epsilon 1} - C'_{\epsilon 2}\right)\right] k_1 \\ C'_{\epsilon 2} &= \frac{1 - 1/\left(\lambda_o \alpha^*\right)}{2\alpha^*\left[1 + \beta/(\alpha^*)^3\right]}\left[3 - \frac{1}{\lambda_o\alpha^* - 1} - \frac{3\beta/(\alpha^*)^3}{1 + 3\beta/(\alpha^*)^3}\right] \end{aligned}\right\} \quad (4.170)$$

Additionally, the coefficient u_0 is determined from the integral constraint for mass conservation, which is the first of Equations (4.155). Table 4.6 summarizes the equations for the leading-order terms in the defect-layer solution.

Table 4.6: *Summary of the Defect-Layer Equations.*

Mass Conservation (Integral Constraint)	Equation (4.155)
Momentum Conservation	Equation (4.159)
Velocity Boundary Conditions	Equation (4.160)
Turbulence Energy, Specific Dissipation (k-ω Model)	Equation (4.162)
Turbulence Energy, Dissipation (k-ϵ Model)	Equation (4.163)
k, ω, ϵ Boundary Conditions for $\eta \to \infty$	Equation (4.164)
k, ω, ϵ Boundary Conditions for $\eta \to 0$	Equation (4.165)

Before proceeding to discussion of the defect-layer similarity solution, there are two quantities of interest that follow from the leading-order solution, viz., the skin friction, c_f, and Coles' **wake-strength parameter**, Π. Recall that from matching defect-layer and sublayer velocity profiles, we deduced Equation (4.145). Noting that $c_f = 2(u_\tau/U_e)^2$, we conclude that

$$\sqrt{\frac{2}{c_f}} = \left(C + \frac{u_0}{\kappa}\right) + \frac{1}{\kappa}\ell n Re_{\delta^*} \quad (4.171)$$

The **composite law of the wall, law of the wake** profile according to Coles' meticulous correlation of experimental data [see Coles and Hirst (1969)] is given by

$$\frac{U}{u_\tau} = \frac{1}{\kappa}\ell n\left(\frac{u_\tau y}{\nu}\right) + C + \frac{2\Pi}{\kappa}\sin^2\left(\frac{\pi}{2}\frac{y}{\delta}\right) \quad (4.172)$$

The $\sin^2$ function is purely a curve fit: several other functions have been suggested, including forms that yield $\partial U/\partial y = 0$ at $y = \delta$ [which is not the case for Equation (4.172)]. At the boundary-layer edge, $y = \delta$, we have

$$\frac{U_e}{u_\tau} = \frac{1}{\kappa}\ell n\left(\frac{u_\tau \delta}{\nu}\right) + C + \frac{2\Pi}{\kappa} \quad (4.173)$$

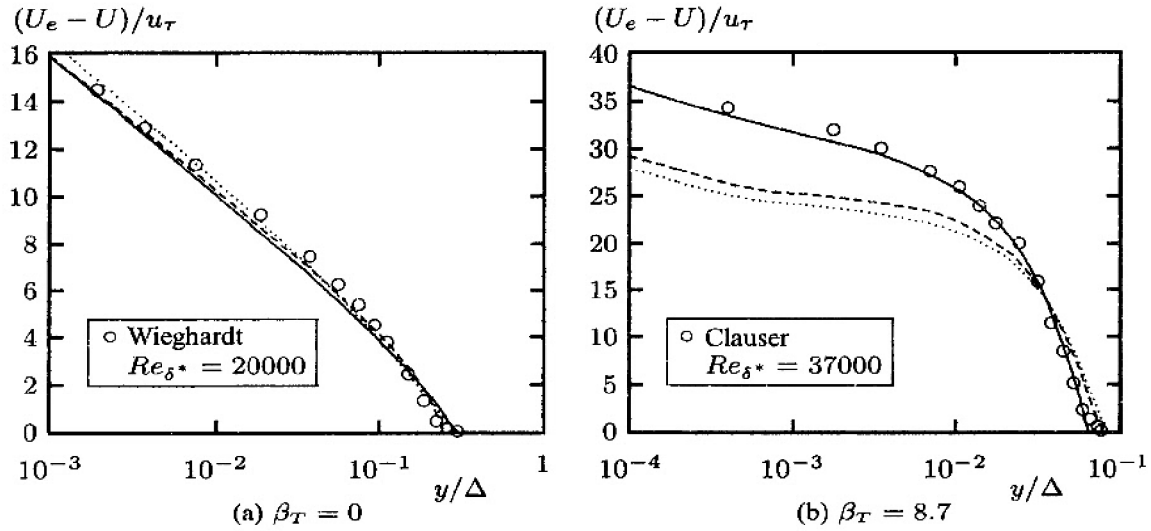

Figure 4.18: *Comparison of computed and measured defect-layer velocity profiles;* —— *k-ω model;* - - - *Standard k-ϵ model;* ···· *RNG k-ϵ model.*

Combining Equations (4.145) and (4.173) and canceling the constant C yields

$$\frac{1}{\kappa}\ell n\left(\frac{u_\tau \delta}{\nu}\right) + \frac{2\Pi}{\kappa} = \frac{u_0}{\kappa} + \frac{1}{\kappa}\ell n Re_{\delta^*} \tag{4.174}$$

Hence, solving for Π, we find

$$\Pi = \frac{1}{2}u_0 + \frac{1}{2}\ell n\left(\frac{U_e\delta^*}{\nu}\right)\left(\frac{\nu}{u_\tau\delta}\right) = \frac{1}{2}u_0 - \frac{1}{2}\ell n\left(\frac{u_\tau\delta}{U_e\delta^*}\right) \tag{4.175}$$

Finally, defect-layer solutions include sharp (nonphysical) turbulent/nonturbulent interfaces so that the edge of the defect-layer lies at a finite value $\eta = \eta_e$, i.e.,

$$\eta_e = \frac{\delta}{\Delta} = \frac{u_\tau\delta}{U_e\delta^*} \tag{4.176}$$

Therefore, combining Equations (4.175) and (4.176) leads to the following expression for the wake-strength parameter.

$$\Pi = \frac{1}{2}(u_0 - \ell n\eta_e) \tag{4.177}$$

Figure 4.18(a) compares the defect-layer solution for the three models with corresponding experimental data of Wieghardt as tabulated by Coles and Hirst (1969). The experimental data presented are those at the highest Reynolds number for which data are reported. This is consistent with the defect-layer solution that is formally valid for very large Reynolds number. As shown, all three models

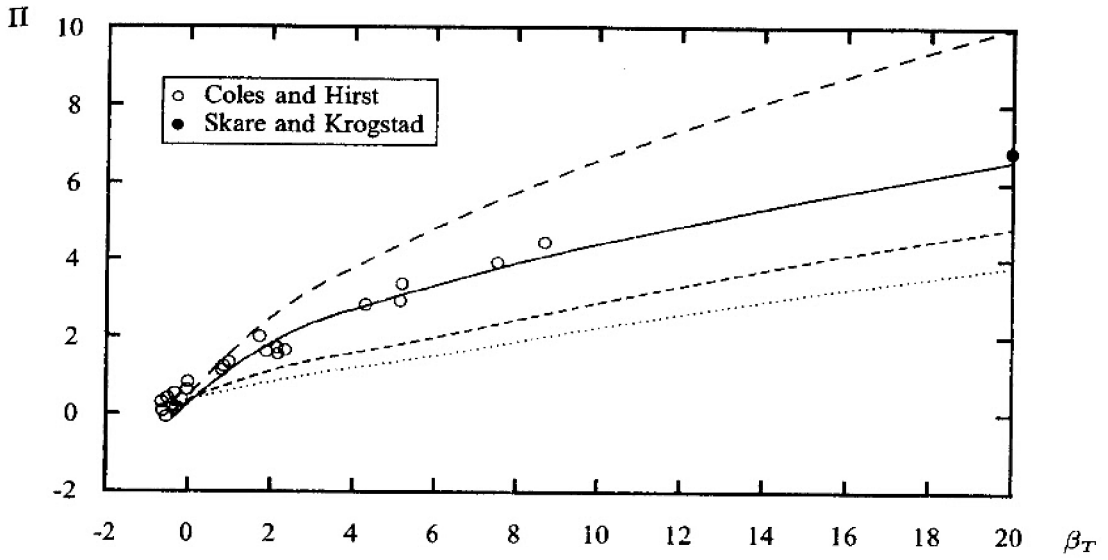

Figure 4.19: *Computed and measured wake-strength parameter;* —— *k-ω model;* - - - *Standard k-ϵ model;* · · · · *RNG k-ϵ model;* – – *Baldwin-Barth model.*

predict velocity profiles that differ from measured values by no more than about three percent of scale. Thus, based on analysis of the constant-pressure defect layer, there is little difference amongst the three models.

Turning now to the effect of pressure gradient, we consider defect-layer solutions for the equilibrium parameter, β_T, ranging from -1/2 to +20, where positive β_T corresponds to an adverse pressure gradient. The choice of this range of β_T has been dictated by the requirement of the perturbation solution that β_T be constant. This appears to be the maximum range over which experimental data have been taken with β_T more-or-less constant. Figure 4.18(b) compares computed velocity profiles with experimental data of Clauser [see Coles and Hirst (1969)] for $\beta_T = 8.7$. As shown, the k-ω model yields a velocity profile that is within 3% of measurements while the k-ϵ models show much larger differences.

Figure 4.19 compares computed wake strength, Π, with values inferred by Coles and Hirst (1969) and Skare and Krogstad (1994) from experimental data. In addition to results for the two-equation models, the figure includes predicted Π according to the Baldwin-Barth (1990) one-equation model. Inspection of Figure 4.19 reveals provocative differences amongst the four models. Most notably, the k-ω model yields wake strengths closest to values inferred from data over the complete range considered. Consistent with the velocity-profile discrepancies shown in Figure 4.18(b), the k-ϵ models exhibit much larger differences, with predicted wake strength 30%-40% lower than inferred values when β_T is as small as two! Also, the Baldwin-Barth model predicts values of Π that are typically 30% higher than measured.

To appreciate the significance of these results, observe that since we know $U_e/u_\tau = \sqrt{2/c_f}$, we can rewrite Equation (4.173) as follows.

$$\sqrt{\frac{2}{c_f}} = \frac{1}{\kappa}\ell n\left(\frac{u_\tau \delta}{\nu}\right) + C + \frac{2\Pi}{\kappa} \tag{4.178}$$

Although this is not an explicit equation for c_f as a function of Π, if we assume the logarithmic term varies more slowly than the term proportional to Π, reducing the value of Π increases the value of c_f, and vice versa. This indeed turns out to be the case as summarized in the following observations.

1. If a model's predicted values of Π are smaller than measured, its predicted skin friction is larger than observed. We will see in Sections 4.8 through 4.10 that the k-ϵ model consistently predicts values of skin friction that are significantly larger than measured.

2. If the values of Π are larger than measured, predicted skin friction is smaller than observed. Inspection of Figure 4.4 confirms that the Baldwin-Barth model predicts skin friction values that are substantially below corresponding measured values.

3. If a turbulence model predicts values of Π similar to measured values over the entire range of β_τ, its skin-friction (and other boundary-layer property) predictions will be consistent with measurements. We will see in subsequent sections and chapters that the k-ω model accurately predicts boundary-layer properties, including effects of pressure gradient. Although we have not shown the results here, the Baldwin-Lomax, Cebeci-Smith, Johnson-King and Spalart-Allmaras models all predict Π versus β_τ curves that are much closer to the k-ω curve than the Baldwin-Barth and k-ϵ models. Correspondingly, they all predict boundary-layer features that are reasonably close to measurements (cf. Figures 3.17, 3.19 and 4.4).

Thus, we see that using perturbation methods to analyze the defect layer provides an excellent test of how well any turbulence model will ultimately perform for attached boundary layers. Although the analysis is confined to equilibrium boundary layers, in the sense that β_τ is constant (and is strictly valid only in the limit of very large Reynolds number), it is nevertheless an objective and important test. This is true because, if the boundary layer is not changing too rapidly, its properties will be consistent with those of the equilibrium case corresponding to the local value of β_τ.

Table 4.7: *Coefficients A, B, L and* Π *for* $\beta_T = 20$.

Model	A	B	L	Π
k-ω (1988a)	25.89	5.81	-4.42	6.88
k-ω (2006)	24.87	8.88	-5.58	6.54
Standard k-ϵ	15.67	30.51	-13.02	4.85
RNG k-ϵ	11.96	36.07	-15.39	3.82
Measured	—	—	—	6.80

The explanation of the k-ϵ models' poor performance for adverse pressure gradient can be developed from inspection of asymptotic solution behavior as $\eta \to 0$. For the models analyzed, the velocity behaves as

$$\frac{U_e - U}{u_\tau} \sim -\frac{1}{\kappa}\ell n\eta + A - \beta_T B\eta\ell n\eta + \cdots \qquad \text{as} \qquad \eta \to 0 \tag{4.179}$$

where Table 4.7 summarizes the constants A and B, defined by

$$A \equiv \frac{u_0}{\kappa} \qquad \text{and} \qquad B \equiv \frac{u_1}{\beta_T \kappa} \tag{4.180}$$

Note that, while the coefficient A is determined as part of the solution (from the integral constraint that mass be conserved), the coefficient B follows directly from the limiting form of the solution as $\eta \to 0$. As seen from Table 4.7, B is largest for the RNG k-ϵ model and is smallest for the Wilcox (1988a) k-ω model, which has no cross diffusion. Because the coefficient of its cross diffusion term is not very large, B is relatively small for the Wilcox (2006) k-ω model. The presence of the $\eta\ell n\eta$ term gives rise to an inflection in the velocity profile as $\eta \to 0$ that is most pronounced for the k-ϵ models.

In terms of turbulence properties, the turbulence length scale, ℓ, behaves according to

$$\ell \sim \beta^{*1/4}\kappa\eta[1 + \beta_T L\eta\ell n\eta + \cdots] \qquad \text{as} \qquad \eta \to 0 \tag{4.181}$$

Table 4.7 also includes the coefficient L for each model. Again, we see that the contribution of the $\eta\ell n\eta$ term is much larger for the k-ϵ models than it is for the k-ω models. Thus, for adverse pressure gradient, the k-ϵ models' turbulence length scales tend to be too large in the near-wall region. Note, of course, that this shortcoming is not evident in the constant-pressure case, which has $\beta_T = 0$.

The manner in which the k-ω model achieves smaller values of ℓ than the k-ϵ models can be seen by changing dependent variables. That is, starting with

the k-ω formulation and defining $\epsilon = \beta^* \omega k$, we can deduce the following incompressible equation for ϵ implied by the k-ω model.[10]

$$U\frac{\partial \epsilon}{\partial x} + V\frac{\partial \epsilon}{\partial y} = (1+\alpha)k\left(\frac{\partial U}{\partial y}\right)^2 - (1+\beta_o/\beta^*)\frac{\epsilon^2}{k} + \frac{\partial}{\partial y}\left[\sigma\nu_T\frac{\partial \epsilon}{\partial y}\right] - 2\sigma\nu_T\frac{\partial k}{\partial y}\frac{\partial(\epsilon/k)}{\partial y} \tag{4.182}$$

All terms except the last on the right-hand side of Equation (4.182) are identical in form to those of the Standard k-ϵ model [see Equation (4.48)]. The **cross-diffusion term**, which is discussed in detail in Subsection 4.5.4, is negligibly small as $\eta \to 0$ for constant-pressure boundary layers because $k \to$ constant as $\eta \to 0$. However, $\partial k/\partial y$ is nonvanishing when $\beta_T \neq 0$ and $\partial(\epsilon/k)/\partial y$ generally is quite large as $\eta \to 0$. The net effect of this additional term is to suppress the rate of increase of ℓ close to the surface.

We can draw an important conclusion from these observations about cross diffusion. Specifically, with a change of dependent variables to ω from the second parameter being used (e.g., ϵ, ℓ, τ), any two-equation model can be rewritten as a k-ω model. In general, the implied equation for ω includes a cross-diffusion term. Since excessive amounts of cross diffusion have such an undesirable effect on boundary-layer predictions, additional corrections to the model will be needed to counter the undesirable effects of the term. Rodi and Scheuerer (1986), Yap (1987) and Henkes (1998b), for example, have proposed corrections to the k-ϵ model which implicitly counter the effects of cross diffusion (relative to the k-ω model) with varying degrees of success.

As with free shear flows, the freestream value of ω has an effect on k-ω model defect-layer solutions when the freestream eddy viscosity is negligibly small. However, the sensitivity is far less significant than it is for free shear cases (see Subsection 4.5.3), even when the k-ω model has no cross diffusion term. The freestream value of ϵ has virtually no effect for the k-ϵ model.

Computations done using Program **DEFECT** (see Appendix C) demonstrate the sensitivity. All computations have been done with $\beta_T = 0$ and have a freestream eddy viscosity of $N(\eta_e) = 10^{-4}$. Self-similar solutions exist for $W_0(\eta_e) = 0$ and for $W_0(\eta_e) = \sqrt{\beta^*}/\beta_o = 4.24$, which is a relatively large value. Regarding this as the upper bound on $W_0(\eta_e)$, computations have been performed to determine the sensitivity of skin friction, c_f, to the freestream value of W_0.

Figure 4.20 shows the variation of c_f with $W_0(\eta_e)$. The quantity c_{fo} denotes the value of c_f for zero freestream conditions. As shown, the effect is small. For the largest value of $W_0(\eta_e)$, the change in c_f is less than 3%. Note that, in

[10] This equation was derived assuming $\sigma = \sigma^*$ and $\sigma_d = 0$ to simplify the algebra. With $\sigma \neq \sigma^*$ there is an additional benign diffusion term that is of no consequence to the present discussion.

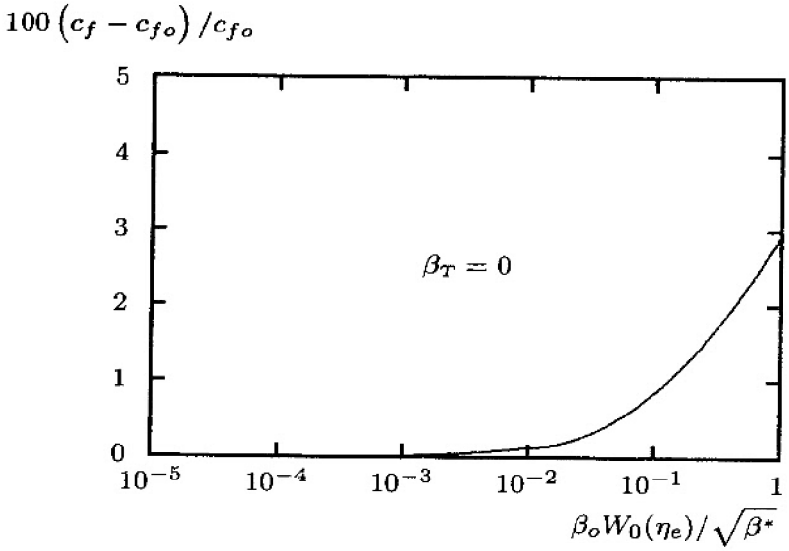

Figure 4.20: *Effect of the freestream value of ω on k-ω model skin friction.*

typical numerical computations, large values of ω diffuse from the wall toward the boundary-layer edge, so that $W_0(\eta_e)$ normally tends toward $\sqrt{\beta^*}/\beta_o$, which corresponds to $U d\omega/dx = -\beta_o \omega^2$ in the freestream.

Equation (4.168) shows that the coefficient $B = u_1/(\beta_T \kappa)$ is proportional to σ^*, so that smaller values of σ^* enhance the model's predictions for boundary layers with variable pressure. The computed variation of Π with β_T (Figure 4.19) closely matches experimental results when $\sigma^* = 3/5$ and $\sigma_{do} = 1/8$. Thus, our analysis of free shear flows and of the defect layer provides further credence to the values of these coefficients that have been chosen for the k-ω model.

However, we have implicitly assumed that the appropriate value for σ is $1/2$ and promised to justify this choice later. In Subsection 4.6.3, we will find that using $\sigma = 1/2$ yields an excellent solution in the viscous sublayer, almost independent of the values of σ^* and σ_{do}.

4.6.3 The Viscous Sublayer

In order to facilitate integration of the model equations through the viscous sublayer, we must, at a minimum, have molecular diffusion terms in the equations of motion. Potentially, we might also have to allow the various closure coefficients to be functions of viscosity (i.e., turbulence Reynolds number) as well. This should come as no surprise since even the mixing-length model requires the Van Driest damping factor and one-equation models need similar viscous damping [Wolfshtein (1967), Baldwin and Barth (1990), Spalart and Allmaras (1992)]. In this section, we use perturbation methods to analyze viscous-sublayer structure predicted by several two-equation models. As we will see, with the exception

of some k-ω models, virtually all two-equation models require Reynolds-number dependent corrections in order to yield a realistic sublayer solution.

We have already derived the sublayer solution in Subsection 4.6.1 when we discussed the **log layer**. Recapping the highlights of the expansion procedure, the velocity is given by an expansion of the form

$$U(x,y) \sim u_\tau[\hat{u}_0(y^+) + Re_{\delta^*}^{-1}\hat{u}_1(\xi,y^+) + o(Re_{\delta^*}^{-1})] \tag{4.183}$$

To leading order, the convective terms and pressure gradient are negligible. Thus, for example, the leading-order equations for the k-ω model expressed in terms of dimensional quantities are given by

$$\left.\begin{aligned}
&(\nu+\nu_T)\frac{dU}{dy} = u_\tau^2 \\
&\frac{d}{dy}\left[\left(\nu+\sigma^*\frac{k}{\omega}\right)\frac{dk}{dy}\right] + \nu_T\left(\frac{dU}{dy}\right)^2 - \beta^*\omega k = 0 \\
&\frac{d}{dy}\left[\left(\nu+\sigma\frac{k}{\omega}\right)\frac{d\omega}{dy}\right] + \alpha\left(\frac{dU}{dy}\right)^2 + \frac{\sigma_d}{\omega}\frac{dk}{dy}\frac{d\omega}{dy} - \beta_o\omega^2 = 0 \\
&\nu_T = \frac{k}{\tilde{\omega}}, \qquad \tilde{\omega} = \max\left\{\omega,\ C_{lim}\frac{dU/dy}{\sqrt{\beta^*}}\right\}
\end{aligned}\right\} \tag{4.184}$$

Because the Reynolds shear stress is constant, the viscous sublayer is often referred to as the **constant-stress layer**. Five boundary conditions are needed for this fifth-order system, two of which follow from matching to the law of the wall as $y^+ \to \infty$, viz.,

$$k \to \frac{u_\tau^2}{\sqrt{\beta^*}} \quad \text{and} \quad \omega \to \frac{u_\tau}{\sqrt{\beta^*}\,\kappa y} \quad \text{as} \quad y^+ \to \infty \tag{4.185}$$

where $y^+ \equiv u_\tau y/\nu$. Two more boundary conditions follow from **no slip** at the surface, which implies that U and k vanish at $y = 0$. Thus,

$$U = k = 0 \quad \text{at} \quad y^+ = 0 \tag{4.186}$$

The final condition follows from examination of the differential equations for k and ω approaching the surface. The k-ω model possesses two kinds of solutions. The first type of solution has a finite value of ω at the surface. This fact was first observed by Saffman (1970) who speculated that the constant in the law of the wall, C, would vary with the surface value of ω. This feature is unique to k-ω and k-ω^2 models and we will explore it in detail in Section 4.7.

The second type of solution is common to all two-equation models and this is the one we will focus on now. Examination of the differential equations approaching $y = 0$ shows that for all two-equation models,

$$k \sim y^n \quad \text{and} \quad \beta^* y^2 \omega/\nu \sim \text{constant} \quad \text{as} \quad y \to 0 \tag{4.187}$$

Table 4.8 lists the values of n and the constant for several models. As shown, none of the models predicts the exact theoretical value of 2 for both n and $\beta^* y^2 \omega/\nu$. This can only be accomplished with additional modification of the model equations.

Table 4.8: *Sublayer Behavior Without Viscous Damping.*

Model	Type	C	n	$\beta^* y^2 \omega/\nu$
Wilcox-Rubesin (1980)	k-ω^2	7.1	4.00	12.00
Saffman (1970)	k-ω^2	6.0	3.7-4.0	12.00
Launder-Spalding (1972)	k-ω^2	5.7	3.79	12.00
Wilcox (2006)	k-ω	5.5	3.31	7.63
Wilcox (1988a)	k-ω	5.1	3.23	7.20
Kolmogorov (1942)	k-ω	3.1	3.62	7.20
Launder-Sharma (1974)	k-ϵ	-2.2	1.39	0.53
Speziale (1990)	k-τ	-2.2	1.39	0.53
Exact/Measured		5.0-5.5	2.00	2.00

The exact values follow from expanding the fluctuating velocity in Taylor series near a solid boundary. That is, we know that the fluctuating velocity satisfies the no-slip boundary condition and also satisfies conservation of mass (see Section 2.3). Consequently, the three velocity components must behave as follows.

$$\left.\begin{array}{rcl} u' & \sim & A(x,z,t)y + O(y^2) \\ v' & \sim & B(x,z,t)y^2 + O(y^3) \\ w' & \sim & C(x,z,t)y + O(y^2) \end{array}\right\} \quad \text{as} \quad y \to 0 \tag{4.188}$$

Hence, the turbulence kinetic energy and dissipation are given by

$$k \sim \frac{1}{2}\left(\overline{A^2 + C^2}\right) y^2 + O(y^3) \quad \text{and} \quad \epsilon \sim \nu \left(\overline{A^2 + C^2}\right) + O(y) \tag{4.189}$$

Assuming that $\epsilon = \beta^* \omega k$, Equation (4.189) tells us that

$$k \sim y^2 \quad \text{and} \quad \beta^* y^2 \omega/\nu \sim 2 \quad \text{as} \quad y \to 0 \tag{4.190}$$

Thus, using the asymptotic behavior of ω for $y \to 0$ appropriate to each model as the fifth boundary condition, we can solve the sublayer equations (see

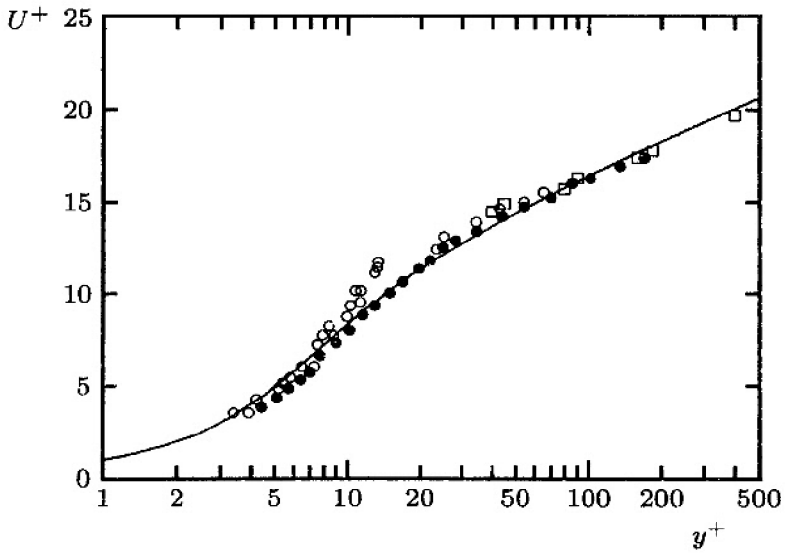

Figure 4.21: *Computed and measured sublayer velocity:* ○ *Laufer;* • *Andersen et al.;* □ *Wieghardt;* —— *k-ω model.*

Subsection 7.2.1 for an explanation of how to handle the singular behavior of ω numerically). One of the most interesting features of the solution is the constant in the law of the wall, C, that is evaluated from the following limit.

$$C = \lim_{y^+ \to \infty} \left[U^+ - \frac{1}{\kappa} \ell n y^+ \right] \tag{4.191}$$

In practice, integrating from $y^+ = 0$ to $y^+ = 500$ is sufficient for numerical solution of the sublayer equations. Program **SUBLAY** (see Appendix C) can be used to solve the sublayer equations for the k-ω model.

Table 4.8 also lists the computed value of C for the various two-equation models. As shown, the Spalding (1972) k-ω^2 model, the Wilcox (1988a) k-ω model and the k-ω model defined in Equations (4.36) – (4.42) are sufficiently close to the standard value of 5.0 to be used with no additional viscous modifications. The Standard k-ϵ model and the Speziale et al. k-τ model are farthest from the generally accepted value for C.

Figure 4.21 compares k-ω model velocity profiles with corresponding measurements of Laufer (1952), Andersen, Kays and Moffat (1972), and Wieghardt [as tabulated by Coles and Hirst (1969)]. As shown, computed velocities generally fall within experimental data scatter for all values of y^+ considered.

Figure 4.22 compares computed production and dissipation with Laufer's (1952) near-wall pipe-flow measurements. Again, predictions are close to measurements. However, note that Laufer's dissipation data are incorrect for values of y^+ less than 10, a point we will discuss further in Subsection 4.8.1.

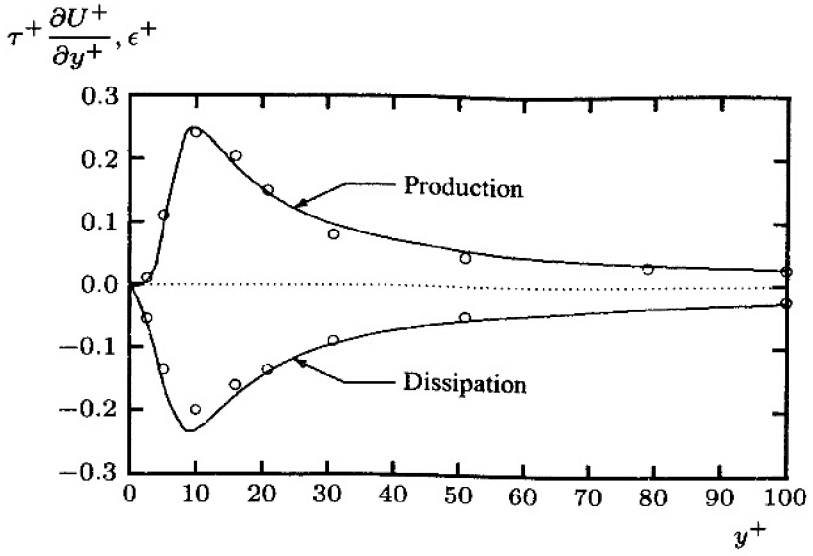

Figure 4.22: *Computed and measured production and dissipation:* ○ *Laufer;* —— *k-ω model.*

The value of the constant C in the law of the wall is remarkably insensitive to the value of σ^*. With all other closure coefficients as specified in Equations (4.39) – (4.42), computations show that as σ^* increases from 0.5 to 1.0, the value of C decreases by 0.5%. There is no sensitivity to the cross-diffusion coefficient because $dk/dy\, d\omega/dy < 0$, which means $\sigma_d = 0$ in the sublayer.

The value chosen for σ does affect the value of C. Figure 4.23 shows the functional dependence. Computations have been done with the value of the Kármán constant, κ, held invariant by setting $\alpha = \beta_o/\beta^* - \sigma\kappa^2/\sqrt{\beta^*}$. This justifies selecting $\sigma = 1/2$ for the k-ω model.

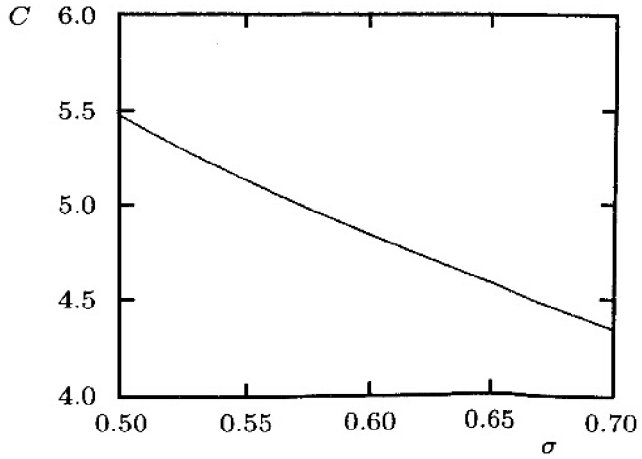

Figure 4.23: *Variation of C with closure coefficient σ.*

This concludes our perturbation analysis of the turbulent boundary layer. As we have seen, using perturbation analysis, we have been able to dissect model-predicted structure of the defect layer, log layer and sublayer, never having to solve more than an ordinary differential equation. This is a great advantage in testing a turbulence model in light of the ease and accuracy with which ordinary differential equations can be solved. The equations are not trivial to solve however since we are dealing with two-point boundary-value problems, and the resulting systems of equations are of sixth order for the defect layer and fifth order for the sublayer. However, this is far easier to handle than the partial differential equations we started with, and parametric studies (e.g., varying the equilibrium parameter, β_T) are much simpler. As a final comment, results obtained in this section should make the following statement obvious.

> *Given the demonstrated power and utility of perturbation analysis in analyzing the turbulent boundary layer, this type of analysis can, and should, be used in developing all turbulence models. Failure to use these methods is the primary reason so many turbulence models have been devised that fail to accurately predict properties of incompressible, equilibrium boundary layers.*

4.7 Surface Boundary Conditions

In order to apply a two-equation turbulence model to wall-bounded flows, we must specify boundary conditions appropriate to a solid boundary for the velocity and the two turbulence parameters. As shown in the preceding section, many two-equation models fail to predict a satisfactory value of the constant C in the law of the wall (see Table 4.8). Consequently, for these models, applying the no-slip boundary condition and integrating through the viscous sublayer yields unsatisfactory results.

One approach we can take to remove this deficiency is to introduce viscous damping factors analogous to the Van Driest correction for the mixing-length model. Since introduction of damping factors accomplishes much more than improving predictions of the velocity profile in the sublayer, we defer detailed discussion of such modifications to Section 4.9. The k-ω model is, in fact, unique because viscous modifications to its closure coefficients are not needed to achieve a satisfactory value of C.

An alternative approach is to circumvent the inability to predict a satisfactory log-layer solution by simply matching to the law of the wall using a suitable value for C. This is what we did in analyzing the defect layer, and the procedure is equally valid for general wall-bounded flows.

4.7.1 Wall Functions

Historically, researchers implementing this matching procedure have referred to the functional forms used in the limit $y \rightarrow 0$ as **wall functions**. This procedure uses the law of the wall as the constitutive relation between velocity and surface shear stress. That is, in terms of the velocity at the mesh point closest to the surface (the "matching point"), we can regard the law of the wall, viz.,

$$U = u_\tau \left[\frac{1}{\kappa} \ell n \left(\frac{u_\tau y}{\nu} \right) + C \right] \tag{4.192}$$

as a transcendental equation for the friction velocity and, hence, the shear stress. Once the friction velocity is known, we use Equations (4.127) for the k-ω model or Equations (4.132) for the k-ϵ model to define the values of k and ω or ϵ at the grid points closest to the surface. Because ω and ϵ are odd functions of u_τ and both quantities are positive definite, care must be taken for separated flows. We can either use the absolute value of u_τ or combine the equations for k and ω or k and ϵ so that the **wall functions** for k, ω and ϵ become:

$$k = \frac{u_\tau^2}{\sqrt{\beta^*}}, \qquad \omega = \frac{k^{1/2}}{\beta^{*1/4} \kappa y}, \qquad \epsilon = \beta^{*3/4} \frac{k^{3/2}}{\kappa y} \tag{4.193}$$

The wall-function approach is not entirely satisfactory for several reasons. Most importantly, numerical solutions generally are sensitive to the point above the surface where the wall functions are used, i.e., the point where the matching occurs (see Subsection 7.2.1 for an in-depth discussion of this problem). Furthermore, the law of the wall doesn't always hold for flow near solid boundaries, most notably for separated flows.

There is a more subtle danger attending the use of wall functions. Specifically, when poor results are obtained with a two-equation model, researchers sometimes mistakenly blame their difficulties on the use of non-optimum wall functions. This assessment is too often made when the wall functions are not the real cause of the problem. For example, the k-ϵ model just doesn't perform well for boundary layers with adverse pressure gradient, even when accurately matched to the log law. Many articles have appeared claiming that discrepancies between the k-ϵ model's predicted skin friction and corresponding measurements for such flows are caused by the wall functions. This incorrectly assumes that the surface shear is a localized force that depends only upon sublayer structure. As shown in the defect-layer solution of the preceding section, no viscous modification is likely to remove the curious inflection [Figure 4.18(b)] in the k-ϵ model's velocity profile unless viscous effects (unrealistically) penetrate far above the viscous sublayer. We must not lose sight of the fact that the momentum flux through a boundary layer affects the surface shear stress and vice versa [see

Equation (4.153)]. Hence, inaccurate skin friction predictions can be caused by inaccuracies in the velocity profile anywhere in the layer.

Wilcox (1989) demonstrates that pressure gradient must be included in order to achieve solutions independent of the matching point. Retaining pressure gradient in the log-layer equations [i.e., retaining the term β_T/Re_{δ^*} in Equation (4.119)], then the asymptotic behavior for the k-ω model [as defined in Equations (4.36) – (4.42)] approaching the surface is given by the following equations:

$$\left.\begin{aligned} U &= u_\tau\left[\frac{1}{\kappa}\ell n\left(\frac{u_\tau y}{\nu}\right)+C-1.13\frac{u_\tau y}{\nu}P^+ + O(P^+)^2\right] \\ k &= \frac{u_\tau^2}{\sqrt{\beta^*}}\left[1+1.16\frac{u_\tau y}{\nu}P^+ + O(P^+)^2\right] \\ \omega &= \frac{u_\tau}{\sqrt{\beta^*}\,\kappa y}\left[1-0.30\frac{u_\tau y}{\nu}P^+ + O(P^+)^2\right] \end{aligned}\right\} \tag{4.194}$$

where P^+ is the dimensionless pressure-gradient parameter defined by

$$P^+ = \frac{\nu}{\rho u_\tau^3}\frac{dP}{dx} \tag{4.195}$$

The expansions in Equation (4.194) have been derived assuming that P^+ is a small parameter.

Two recent efforts aimed at developing wall functions have built upon the early work of Spalding (1961). Shih et al. (1999) have developed wall functions that explicitly account for effects of pressure gradient. Nichols and Nelson (2004) have developed wall functions that include effects of both pressure gradient and surface heat transfer. The Nichols-Nelson wall functions are particularly effective and provide more-or-less grid independent solutions using the Spalart-Allmaras one-equation model and the k-ω model for both attached and separated flows.

4.7.2 Surface Roughness

As noted in the preceding section, a key advantage of the k-ω^2 and k-ω formulations over the k-ϵ formulation is the fact that ω-oriented equations possess solutions in which the value of ω may be arbitrarily specified at the surface. This is an advantage because it provides a natural way to incorporate effects of surface roughness through surface boundary conditions. This feature of the equations was originally recognized by Saffman (1970). If we write the surface boundary condition on ω as

$$\omega = \frac{u_\tau^2}{\nu}S_R \qquad \text{at} \qquad y=0 \tag{4.196}$$

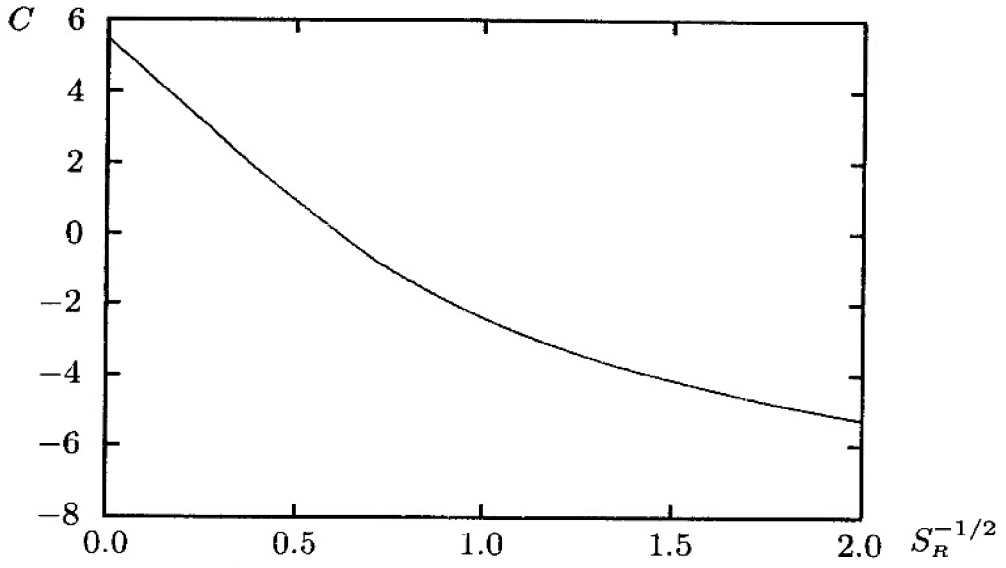

Figure 4.24: *Variation of the constant in the law of the wall, C, with the surface value of the specific dissipation rate.*

we can generate sublayer solutions for arbitrary S_R, including the limiting cases $S_R \to 0$ and $S_R \to \infty$. Figure 4.24 shows the computed value of C for a wide range of values of S_R. As shown, in the limit $S_R \to \infty$, C tends to 5.47. In the limit $S_R \to 0$, an excellent correlation of the numerical predictions is given by

$$C \to 8.0 + \frac{1}{\kappa} \ell n(S_R/100) \qquad \text{as} \qquad S_R \to 0 \tag{4.197}$$

Correlation of measurements [see Gersten-Schlichting (1999)] indicate that for flow over very rough surfaces (see Figure 1.8),

$$C \to 8.0 + \frac{1}{\kappa} \ell n \left(1/k_s^+\right), \qquad k_s^+ = u_\tau k_s/\nu \tag{4.198}$$

where k_s is the average height of sand-grain roughness elements. (Thus, if we make the correlation

$$S_R = 100/k_s^+, \qquad k_s^+ \gg 1 \tag{4.199}$$

then Equations (4.197) and (4.198) are identical. Figure 4.25 compares computed velocity profiles with the correlation of rough-wall data, which is obtained by using Equation (4.198) in the law of the wall, viz.,

$$U^+ = \frac{1}{\kappa} \ell n \left(y/k_s\right) + 8.0, \qquad \kappa = 0.41 \tag{4.200}$$

for three values of k_s^+. Computed velocities are very close to the correlation. The most remarkable fact about this correlation is that Equation (4.200) is the form

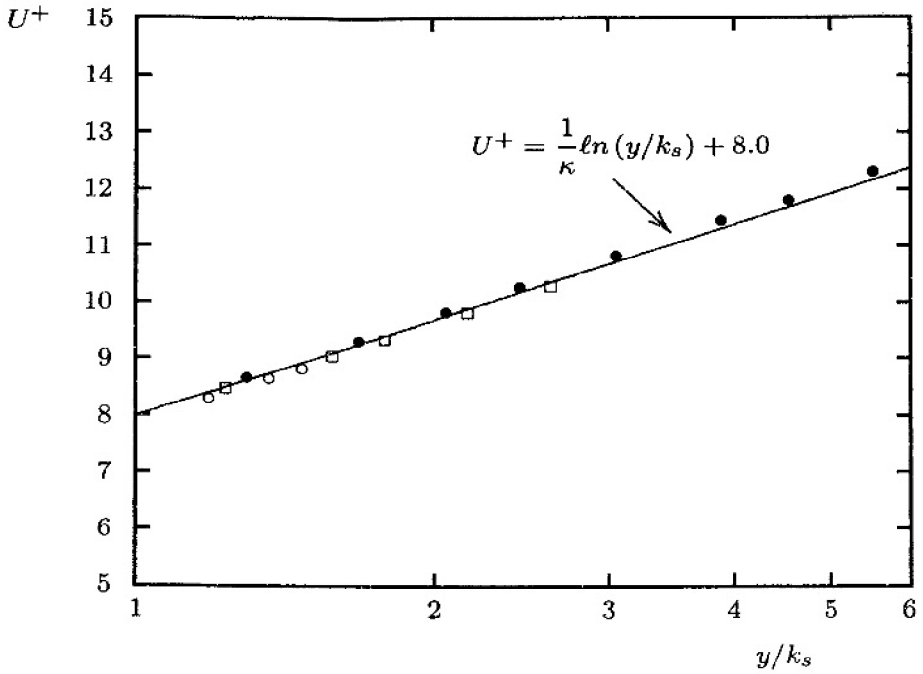

Figure 4.25: *Comparison of computed sublayer velocity profiles for "completely rough" surfaces with correlation of measurements:* ○ *computed,* $k_s^+ = 340$*;* □ *computed,* $k_s^+ = 190$*;* • *computed,* $k_s^+ = 42.5$*.*

the law of the wall assumes for flow over "completely-rough" surfaces [recall Equation (1.31)], including the value of the additive constant.

By making a qualitative argument based on flow over a wavy wall, Wilcox and Chambers (1975) [see problems section] show that for small roughness heights, we should expect to have

$$S_R \sim (1/k_s^+)^2 \qquad \text{as} \qquad k_s^+ \to 0 \tag{4.201}$$

Comparison with Nikuradse's data (see Figure 1.8) permits us to infer the value of S_R corresponding to a given value of k_s^+. Figure 4.26 shows the results for the k-ω model. The following correlation between S_R and k_s^+ reproduces measured effects of sand-grain roughness for values of k_s^+ up to about 400.

$$S_R = \begin{cases} \left(\dfrac{200}{k_s^+}\right)^2, & k_s^+ \le 5 \\ \dfrac{100}{k_s^+} + \left[\left(\dfrac{200}{k_s^+}\right)^2 - \dfrac{100}{k_s^+}\right] e^{5-k_s^+}, & k_s^+ > 5 \end{cases} \tag{4.202}$$

As a final comment, the solution for $k_s^+ \to 0$ is identical to the sublayer solution discussed in Subsection 4.6.3 [see Equation (4.187)]. The analysis

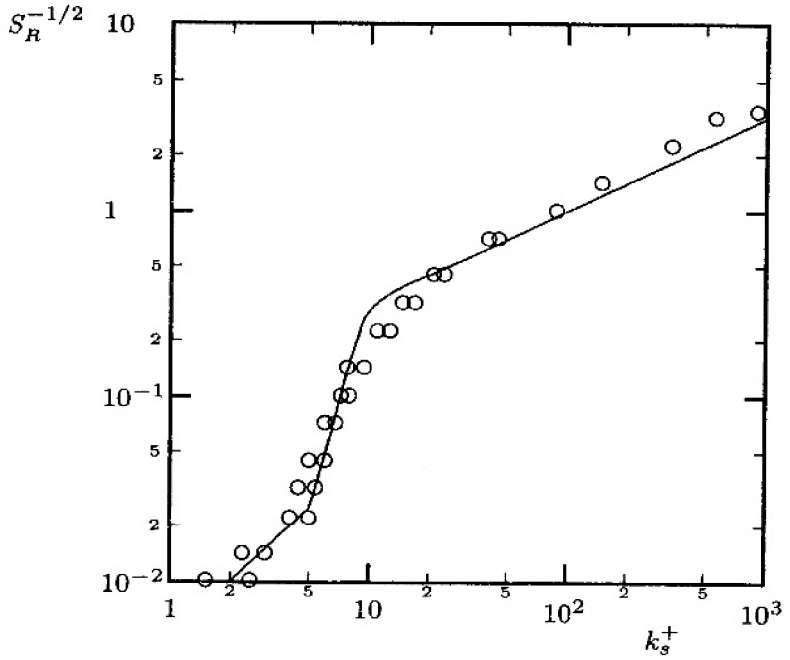

Figure 4.26: *Correlation of S_R with dimensionless sand-grain roughness height, k_s^+; ○ Inferred from Nikuradse data; —— Equation (4.202).*

of this section shows that the singular case corresponds to the perfectly-smooth surface. In practice, Equation (4.202) should be used rather than Equation (4.187) even if a perfectly-smooth surface is desired. Specifically, we can combine Equations (4.196) and the first of Equations (4.202) to arrive at the **slightly-rough-surface boundary condition** on ω, viz.,

$$\omega = \frac{40000\nu_w}{k_s^2} \qquad \text{at} \qquad y = 0 \tag{4.203}$$

It is important to select a small enough value of k_s to insure that $k_s^+ < 5$, corresponding to a "hydraulically-smooth surface" as defined by Gersten-Schlichting (1999). If too large a value is selected, the skin friction values will be larger than smooth-wall values. The advantage in using either Equation (4.202) or Equation (4.203) is obvious for several reasons.

- Local geometry (e.g., distance normal to the surface) does not appear so it can be applied even in three-dimensional geometries.
- k_s need only be small enough to have a hydraulically smooth surface, i.e., $u_\tau k_s/\nu < 5$. Resulting surface values of ω are rarely ever large enough to cause numerical error provided a sensible finite-difference grid is used (see Subsection 7.2.1).
- Experience shows that Equation (4.202) works well for separated flows.

4.7.3 Surface Mass Injection

For boundary layers with surface mass injection, the introduction of an additional velocity scale (v_w = area-averaged normal flow velocity through the porous surface) suggests that the scaling for ω at the surface may differ from Equation (4.196). Andersen, Kays and Moffat (1972) provide further evidence that the specific-dissipation-rate boundary condition must be revised when mass injection is present by showing, from correlation of their experimental data, that both κ and C are functions of $v_w^+ = v_w/u_\tau$. Because rough-surface computations show that the value of C is strongly affected by the surface value of the specific dissipation rate, this suggests that the surface value of ω will depend in some manner upon v_w. Following Wilcox and Traci (1976), examination of the limiting form of the model equations for $y^+ \to \infty$ (i.e., in the log layer) shows immediately that the effective Kármán "constant", κ_v, varies with v_w^+ according to

$$\kappa_v = \frac{\kappa}{1 + \Xi v_w^+} \tag{4.204}$$

where Ξ is given by

$$\Xi = \frac{1}{2}\left(C_o - \frac{3\sigma - 2}{2\sigma\kappa}\right) + \frac{1}{4\kappa}\ell n y^+ = 3.36 + 0.63\ell n y^+ \tag{4.205}$$

Note that $C_o = 5.47$ is the k-ω model-predicted constant in the law of the wall for a perfectly-smooth wall with no surface mass transfer.[11]

The variation of κ_v predicted in Equations (4.204) and (4.205) is consistent with the Andersen et al. data. Including appropriate convective terms in Equations (4.184), we can use Program **SUBLAY** (see Appendix C) to perform sublayer computations for the cases experimentally documented by Andersen et al. In each case, the surface value of ω is given by

$$\omega = \frac{u_\tau^2}{\nu} S_B \qquad \text{at} \qquad y = 0 \tag{4.206}$$

Following Wilcox (1988a), we vary the value of S_B to achieve optimum agreement between measured and computed velocities. The correlation between S_B and v_w^+ is given in analytical form as

$$S_B = \frac{25}{v_w^+(1 + 5v_w^+)} \tag{4.207}$$

Figure 4.27 compares measured velocities with values computed using Equations (4.206) and (4.207).

[11] For boundary layers with suction, i.e., for $v_w < 0$, the k-ω model provides close agreement with measured velocity profiles treating the wall as being smooth. That is, ω should be given either by Equation (4.187) or by Equation (4.203) with $k_s^+ < 5$.

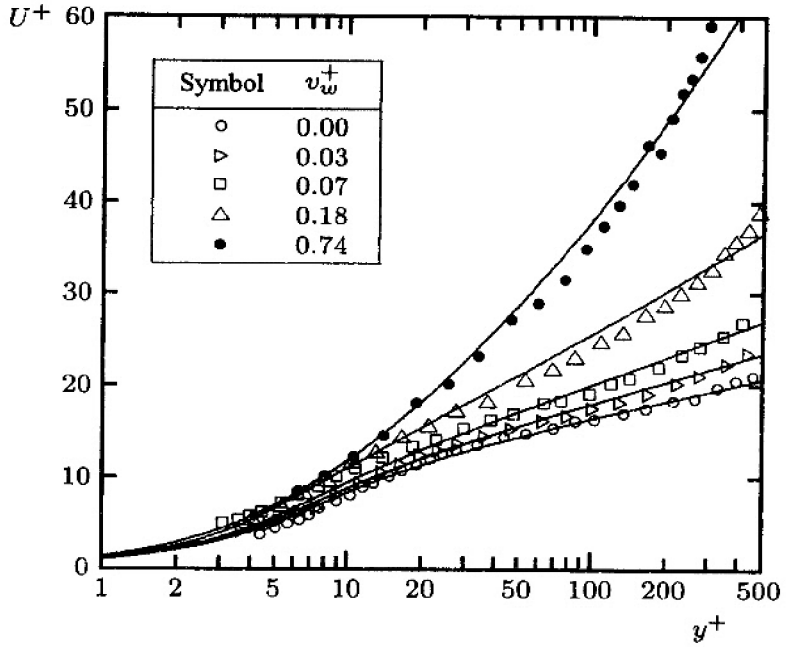

Figure 4.27: *Sublayer velocity profiles for boundary layers with surface mass injection;* —— *Wilcox (2006) k-ω model;* ○ ▷ □ △ • *Andersen et al.*

4.8 Application to Wall-Bounded Flows

Using the surface boundary conditions devised in Section 4.7, we can now apply two-equation turbulence models to wall-bounded flows. Because of their relative simplicity, we consider pipe and channel flow first using the k-ω model. Then, we will consider several incompressible boundary-layer applications. We exercise the k-ω model and the Standard k-ϵ model in the boundary-layer applications.

4.8.1 Channel and Pipe Flow

Figures 4.28 and 4.29 compare computed (using Program **PIPE** – see Appendix C) and measured channel and pipe flow properties, respectively. Six different comparisons are shown in each figure, including mean velocity, skin friction, Reynolds shear stress, turbulence kinetic energy, turbulence-energy production and dissipation rate.

Figure 4.28 compares k-ω model channel-flow predictions with the Direct Numerical Simulation (DNS) data of Mansour, Kim and Moin (1988). Reynolds number based on channel height and average velocity is 13750. Velocity profiles and Reynolds shear stress profiles differ by less than 3%. Computed skin friction differs from Halleen and Johnston's (1967) correlation [Equation (3.139)] by less than about 2% except at the lowest Reynolds number shown. Although the model fails to predict the peak value of k near the channel wall, computed

values of k differ from DNS values by less than 5% over 80% of the channel. Despite the fact that the model is not asymptotically consistent approaching the surface (Subsection 4.9.1), even dimensionless turbulence-energy production, $\mathcal{P}^+ = \nu\tau_{xy}(\partial U/\partial y)/u_\tau^4$, and dissipation, $\epsilon^+ = \nu\epsilon/u_\tau^4$, nearly duplicate DNS results except very close to the surface (see discussion of pipe flow below). On balance, k-ω results are a bit closer to DNS results than either the Cebeci-Smith or Baldwin-Lomax models (Subsection 3.5.1).

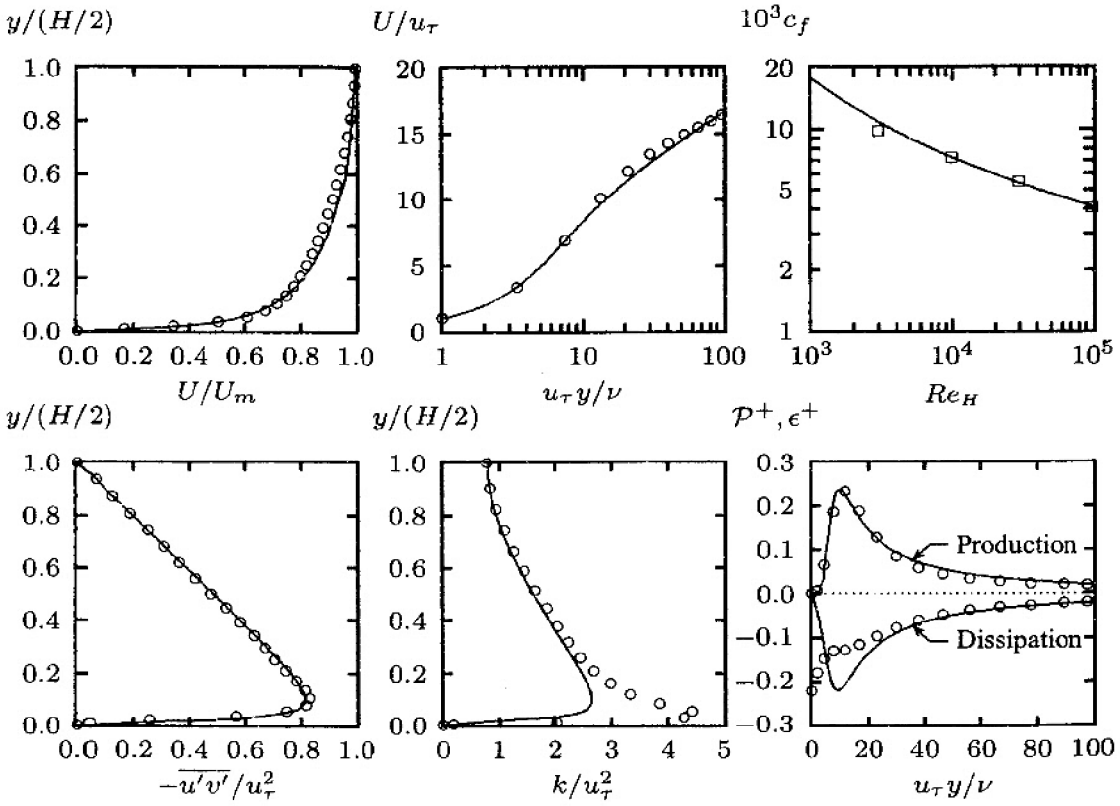

Figure 4.28: *Comparison of computed and measured channel-flow properties,* $Re_H = 13750$. —— *Wilcox (2006) k-ω model;* ○ *Mansour et al. (DNS);* □ *Halleen-Johnston correlation.*

Figure 4.29 compares k-ω model pipe-flow results with Laufer's (1952) measurements at a Reynolds number based on pipe diameter and average velocity of 40000. As shown, computed and measured velocity and Reynolds shear stress profiles differ by less than 6%. As with channel flow, computed and measured turbulence kinetic energy differ by about 4% except close to the surface where the sharp peak occurs. Computed production and dissipation differ from measured values by less than 5%. However, dissipation is really nonzero at the surface (see the DNS results in Figure 4.28), wherefore Laufer's dissipation measurements are certainly incorrect as $y^+ \to 0$. Hence, the model is matching erroneous data!

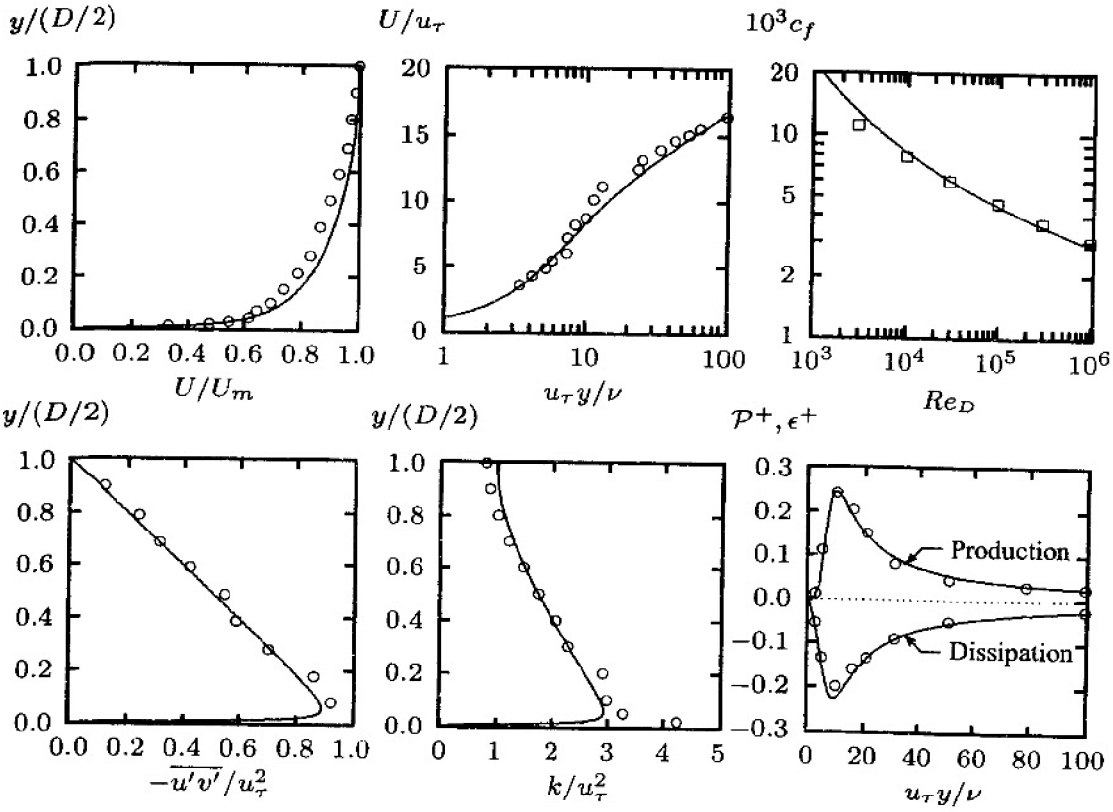

Figure 4.29: *Comparison of computed and measured pipe-flow properties,* $Re_D = 40000$. —— *Wilcox (2006) k-ω model;* ○ *Laufer;* □ *Prandtl correlation.*

Computed skin friction is within 4% of Prandtl's universal law of friction [Equation (3.140)]. Overall, velocity and Reynolds-stress predictions are as close to measurements as those of the Cebeci-Smith and Baldwin-Lomax models.

It is interesting, and perhaps illuminating, that the most important flow properties are accurately predicted even though the sharp peak in turbulence energy is underestimated by 40% and 25%, respectively, for channel and pipe flow. That is, for engineering applications, the most important quantity is the skin friction. The next most important quantity typically is the velocity profile. Only for specialized applications is a subtle feature such as the peak value of k important. Thus, we see that even though the k-ω model fails to predict this subtle feature, this is apparently of little consequence for most engineering applications.

4.8.2 Boundary Layers

We turn now to application of the k-ω and k-ϵ model equations to the same 16 incompressible boundary layers considered for algebraic (Figure 3.17), 1/2-equation (Figure 3.19) and one-equation models (Figure 4.4). All of the k-ω model results

use the surface boundary conditions described in Subsection 4.7.2. The k-ϵ model computations were done using the Launder-Sharma (1974) low-Reynolds-number version subject to appropriate surface boundary conditions [see Subsection 4.9.1, Equations (4.211) – (4.215), (4.217) and (4.221)]. All computations have been done with Program **EDDYBL** (see Appendix C).

Favorable Pressure Gradient. The top row of graphs in Figure 4.30 compares computed and measured c_f for the constant-pressure boundary layer (Flow 1400) and three boundary layers with favorable pressure gradient (Flows 1300, 2700 and 6300). For the k-ω model, computed c_f virtually duplicates measurements for all four cases — differences between computed and measured c_f are no more than 4%. The k-ϵ predictions are also quite close to measurements for Flows 1400 and 6300. However, k-ϵ skin friction is 10% below measured values for Flows 1300 and 2700. Thus, as no great surprise, the k-ω and k-ϵ models are quite accurate for the flat-plate boundary layer and boundary layers with favorable pressure gradient. The average difference between computed and measured c_f at the final station is 3% and 7% for the k-ω and k-ϵ models, respectively.

Mild Adverse Pressure Gradient. The second row of graphs in Figure 4.30 compares computed and measured c_f for boundary layers with "mild" adverse pressure gradient. These flows (1100, 2100, 2500 and 4800) correspond to values of the equilibrium parameter, β_T, less than about 2. The k-ω predictions are again very close to measurements, even for Flow 4800, which is approaching separation. By contrast, the k-ϵ model's skin friction is close to corresponding measured values only for Flow 2100. The model's predicted skin friction is almost three times the measured value for Flow 4800, and the average difference between computed and measured c_f for the four cases is 28%.

Moderate Adverse Pressure Gradient. Turning to "moderate" adverse ∇p (β_T between about 2 and 4), we focus on the next to bottom row of graphs in Figure 4.30, i.e., Flows 2400, 2600, 3300 and 4500. As shown, there is no significant increase in differences between computed and measured c_f for the k-ω model even for the nearly-separated Flow 4500, with the average difference being 9%. However, the k-ϵ model's predictions show even greater deviations from measured c_f, with the computed value being nearly 4 times the measured value for Flow 4500. The average difference at the end of each computation is 40%. Flow 3300, Bradshaw (1969) Flow C, was one of the most difficult cases considered in Stanford Olympics I. Throughout the flow, the k-ω model's c_f is within 5% of measurements, while the k-ϵ model predicts a final value of c_f that exceeds the measured value by 29%. The difference can be reduced to about 20% using wall functions [Chambers and Wilcox (1977)]. Because the equilibrium parameter $\beta_T \approx 2$ for this flow, the poor results for the k-ϵ model are unsurprising.

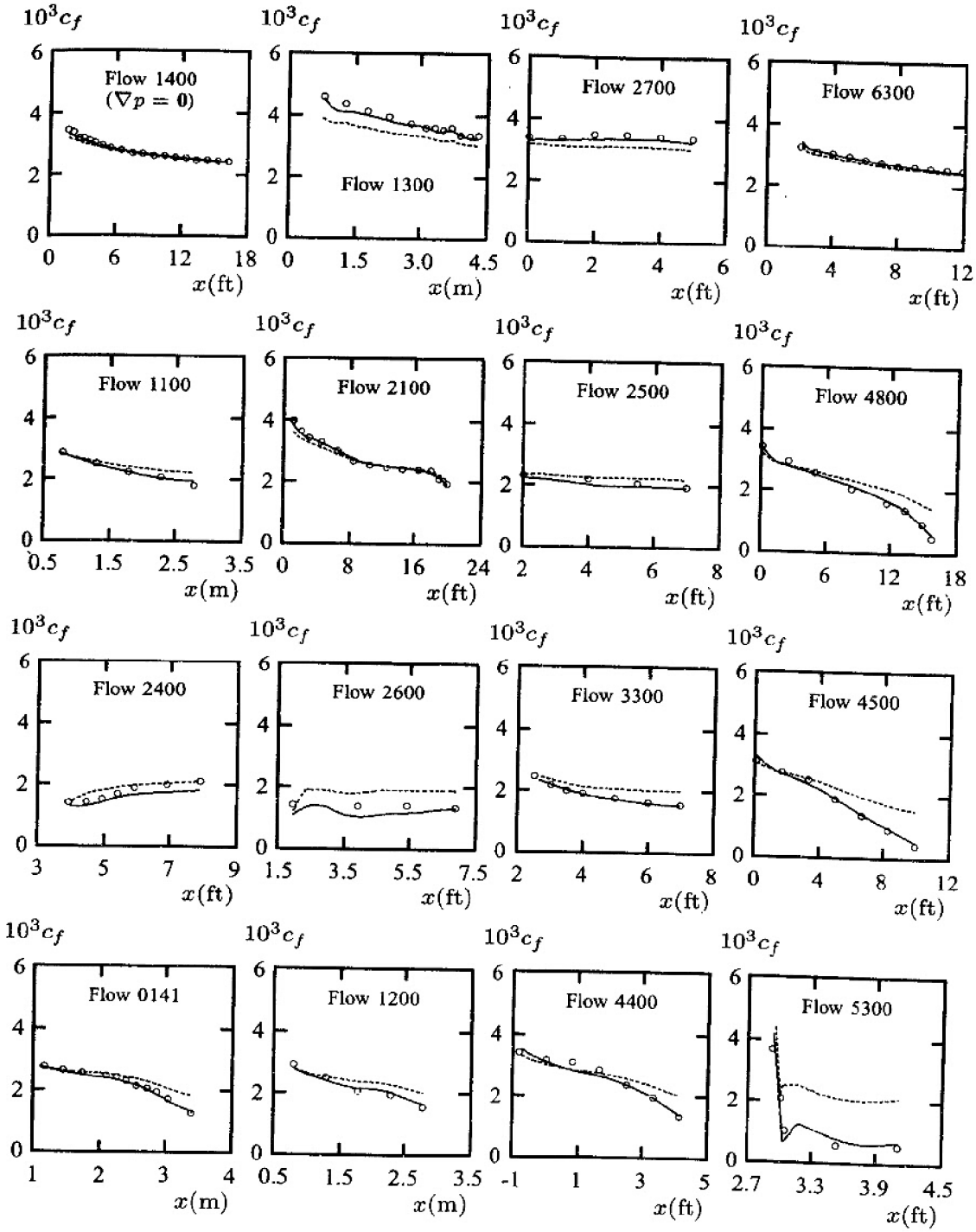

Figure 4.30: *Computed and measured skin friction for boundary layers subjected to a pressure gradient. Top row - favorable ∇p; next to top row - mild adverse ∇p; next to bottom row - moderate adverse ∇p; bottom row - strong adverse ∇p. — Wilcox (2006) k-ω model; - - - Launder-Sharma (1974) k-ϵ model; ○ measured.*

Strong Adverse Pressure Gradient. The bottom-row graphs in Figure 4.30 correspond to "strong" adverse pressure gradient, which corresponds to $\beta_T > 4$. Inspection of Figure 4.19 suggests that the k-ω model should be expected to continue predicting boundary-layer properties close to measurements, while differences between k-ϵ predictions and measurements should continue to increase. This is indeed the case. For example, Flow 0141 has increasingly adverse pressure gradient, the experimental data being those of Samuel and Joubert [see Kline et al. (1981)]. For the k-ω model, computed and measured skin friction differ by less than 5% of scale. Since β_T exceeds 9 toward the end of the computation, the poor performance of the k-ϵ model (computed c_f exceeds measured values by as much as 47%) is consistent with the defect-layer analysis of Subsection 4.6.2. While the k-ω model's skin friction is 28% higher than measured for the Stratford (1959) "incipient-separation" flow, this prediction is closer to the measured c_f than any of the algebraic, 1/2-equation and one-equation models considered in Chapters 3 and 4. The k-ϵ model's c_f is 4 times the measured value.

Table 4.9 summarizes differences between computed and measured c_f at the final station for the various pressure gradients. The overall average difference for all 16 cases is 6% for the k-ω model and 37% for the Standard k-ϵ model.

Table 4.9: *Differences Between Computed and Measured Skin Friction.*

Pressure Gradient	Flows	k-ω	k-ϵ
Favorable	1400, 1300, 2700, 6300	3%	7%
Mild Adverse	1100, 2100, 2500, 4800	5%	28%
Moderate Adverse	2400, 2600, 3300, 4500	9%	40%
Strong Adverse	0141, 1200, 4400, 5300	8%	72%
All	–	6%	37%

4.9 Low-Reynolds-Number Effects

Thus far, the turbulence models we have considered are restricted to high-Reynolds number applications. Even in the case of the k-ω model, while we have been able to obtain acceptably accurate results by integrating through the viscous sublayer, we have paid no attention to low-Reynolds-number effects. For example, the model fails to predict the sharp peak in turbulence kinetic energy close to the surface for pipe and channel flow (see Figures 4.28 and 4.29). Most two-equation models fail to predict a realistic value of the additive constant, C, in the law of the wall, and require viscous damping in order to do so. Finally, there are applications for which viscous effects must be accurately represented. This section will discuss commonly used low-Reynolds-number corrections.

4.9.1 Asymptotic Consistency

In formulating viscous corrections for two-equation models, we can obtain some guidance from looking at the limiting behavior of the fluctuating velocities approaching a solid boundary. That is, we assume standard Taylor-series expansions for each of the fluctuating velocities and substitute into the exact equations of motion, viz., the instantaneous continuity and Navier-Stokes equations. We did this in Subsection 4.6.3 when we were formulating surface boundary conditions for the viscous-sublayer perturbation solution. Thus, we again begin by assuming

$$\left.\begin{array}{rcl} u' & \sim & f_x(x,z,t)y + O(y^2) \\ v' & \sim & f_y(x,z,t)y^2 + O(y^3) \\ w' & \sim & f_z(x,z,t)y + O(y^2) \end{array}\right\} \quad \text{as} \quad y \to 0 \tag{4.208}$$

where $f_x(x,z,t)$, $f_y(x,z,t)$ and $f_z(x,z,t)$ must have zero time average and satisfy the equations of motion. Note that the no-slip surface boundary condition dictates the fact that $\mathbf{u}'$ must go to zero as $y \to 0$. Since we expect Navier-Stokes solutions to be analytic everywhere, we conclude that the fluctuating velocity components u' and w' vary linearly with y. Also, substituting Equations (4.208) into the continuity equation shows that v' varies quadratically with y. While we don't know the precise values of f_x, f_y and f_z without solving the complete Navier-Stokes equation, we can still use the exact asymptotic variations of u', v' and w' with y to deduce the limiting behavior of time-averaged properties approaching the surface. For example, the turbulence kinetic energy and dissipation are

$$k \sim \frac{1}{2}(\overline{f_x^2 + f_z^2})y^2 + O(y^3) \quad \text{and} \quad \epsilon \sim \nu\,(\overline{f_x^2 + f_z^2}) + O(y) \tag{4.209}$$

Also, the Reynolds shear stress is given by

$$\tau_{xy} \sim -\overline{f_x f_y}\; y^3 + O(y^4) \tag{4.210}$$

A model that duplicates the power-law forms of k, ϵ and τ_{xy} given in Equations (4.209) and (4.210) is said to be **asymptotically consistent** with the near-wall behavior of the exact equations of motion.

Many researchers have attempted to devise viscous corrections for k-ϵ and other two-equation models to permit their integration through the viscous sublayer. All have achieved some degree of **asymptotic consistency**. Jones and Launder (1972) were the first to propose viscous modifications for the k-ϵ model. Other proposals have been made by Launder and Sharma (1974), Hoffmann (1975), Reynolds (1976), Hassid and Poreh (1978), Lam and Bremhorst (1981), Dutoya and Michard (1981), Chien (1982), Myong and Kasagi (1990), Speziale, Abid and Anderson (1990), Shih and Hsu (1991), Durbin (1991), Zhang, So,

Speziale and Lai (1993), Yang and Shih (1993), Fan, Lakshminarayana and Barnett (1993), Hwang and Lin (1998) and Rahman and Siikonen (2002). For steady, incompressible boundary layers, most of these models can be written compactly as follows.

$$U\frac{\partial k}{\partial x}+V\frac{\partial k}{\partial y}=\nu_T\left(\frac{\partial U}{\partial y}\right)^2-\epsilon+\frac{\partial}{\partial y}\left[(\nu+\nu_T/\sigma_k)\frac{\partial k}{\partial y}\right] \tag{4.211}$$

$$U\frac{\partial \tilde{\epsilon}}{\partial x}+V\frac{\partial \tilde{\epsilon}}{\partial y}=C_{\epsilon 1}f_1\frac{\tilde{\epsilon}}{k}\nu_T\left(\frac{\partial U}{\partial y}\right)^2-C_{\epsilon 2}f_2\frac{\tilde{\epsilon}^2}{k}+E+\frac{\partial}{\partial y}\left[(\nu+\nu_T/\sigma_\epsilon)\frac{\partial \tilde{\epsilon}}{\partial y}\right] \tag{4.212}$$

where the dissipation, ϵ, is related to the quantity $\tilde{\epsilon}$ by

$$\epsilon=\epsilon_o+\tilde{\epsilon} \tag{4.213}$$

The quantity ϵ_o is the value of ϵ at $y=0$, and is defined differently for each model. The eddy viscosity is defined as

$$\nu_T=C_\mu f_\mu k^2/\tilde{\epsilon} \tag{4.214}$$

Equations (4.211) – (4.214) contain five empirical **damping functions**, f_1, f_2, f_μ, ϵ_o and E. These functions depend upon one or more of the following three dimensionless parameters.

$$Re_T=\frac{k^2}{\tilde{\epsilon}\nu},\qquad R_y=\frac{k^{1/2}y}{\nu},\qquad y^+=\frac{u_\tau y}{\nu} \tag{4.215}$$

The models devised by Jones and Launder (1972), Launder and Sharma (1974), Lam and Bremhorst (1981), and Chien (1982) exemplify most of the features incorporated in k-ϵ model viscous damping functions. The damping functions and closure coefficients for these four low-Reynolds-number k-ϵ models are as follows.

Jones-Launder Model

$$\left.\begin{aligned}
&f_\mu=e^{-2.5/(1+Re_T/50)}\\
&f_1=1\\
&f_2=1-0.3e^{-Re_T^2}\\
&\epsilon_o=2\nu\left(\frac{\partial\sqrt{k}}{\partial y}\right)^2\\
&E=2\nu\nu_T\left(\frac{\partial^2 U}{\partial y^2}\right)^2\\
&C_{\epsilon 1}=1.55,\quad C_{\epsilon 2}=2.00,\quad C_\mu=0.09,\quad \sigma_k=1.0,\quad \sigma_\epsilon=1.3
\end{aligned}\right\} \tag{4.216}$$

Launder-Sharma Model

$$\left.\begin{aligned} f_\mu &= e^{-3.4/(1+Re_T/50)^2} \\ f_1 &= 1 \\ f_2 &= 1 - 0.3e^{-Re_T^2} \\ \epsilon_o &= 2\nu\left(\frac{\partial\sqrt{k}}{\partial y}\right)^2 \\ E &= 2\nu\nu_T\left(\frac{\partial^2 U}{\partial y^2}\right)^2 \\ C_{\epsilon 1} &= 1.44, \quad C_{\epsilon 2} = 1.92, \quad C_\mu = 0.09, \quad \sigma_k = 1.0, \quad \sigma_\epsilon = 1.3 \end{aligned}\right\} \quad (4.217)$$

Lam-Bremhorst Model

$$\left.\begin{aligned} f_\mu &= \left(1 - e^{-0.0165R_y}\right)^2 \ (1 + 20.5/Re_T) \\ f_1 &= 1 + (0.05/f_\mu)^3 \\ f_2 &= 1 - e^{-Re_T^2} \\ \epsilon_o &= 0 \\ E &= 0 \\ C_{\epsilon 1} &= 1.44, \quad C_{\epsilon 2} = 1.92, \quad C_\mu = 0.09, \quad \sigma_k = 1.0, \quad \sigma_\epsilon = 1.3 \end{aligned}\right\} \quad (4.218)$$

Chien Model

$$\left.\begin{aligned} f_\mu &= 1 - e^{-0.0115y^+} \\ f_1 &= 1 \\ f_2 &= 1 - 0.22e^{-(Re_T/6)^2} \\ \epsilon_o &= 2\nu\frac{k}{y^2} \\ E &= -2\nu\frac{\tilde{\epsilon}}{y^2}e^{-y^+/2} \\ C_{\epsilon 1} &= 1.35, \quad C_{\epsilon 2} = 1.80, \quad C_\mu = 0.09, \quad \sigma_k = 1.0, \quad \sigma_\epsilon = 1.3 \end{aligned}\right\} \quad (4.219)$$

By examining the limiting behavior of each of these models close to a solid boundary where $y = 0$, it is easy to demonstrate that, consistent with Equation (4.209), all four models guarantee

$$k \sim y^2 \quad \text{and} \quad \epsilon/k \to 2\nu/y^2 \quad \text{as} \quad y \to 0 \qquad (4.220)$$

Additionally, the Lam-Bremhorst model predicts $\tau_{xy} \sim y^4$ while the other three models predict $\tau_{xy} \sim y^3$. Thus, all except the Lam-Bremhorst model are consistent with Equation (4.210) as well.

Surface boundary conditions for low-Reynolds-number k-ϵ models are not entirely straightforward. On the one hand, the no-slip boundary condition tells us that k must vanish at a solid boundary. On the other hand, the strongest

thing we can say about the surface value of ϵ is the second of Equations (4.220). That is, we invariably must tie the surface value of ϵ to the second derivative of k at the surface. The Jones-Launder, Launder-Sharma and Chien models build in the proper asymptotic behavior through introduction of the function ϵ_o. Consequently, the boundary conditions appropriate at the surface are

$$k = \tilde{\epsilon} = 0 \qquad \text{at} \qquad y = 0 \tag{4.221}$$

By contrast, Lam and Bremhorst deal directly with ϵ and specify the surface boundary condition on ϵ by requiring

$$\epsilon = \nu \frac{\partial^2 k}{\partial y^2} \qquad \text{at} \qquad y = 0 \tag{4.222}$$

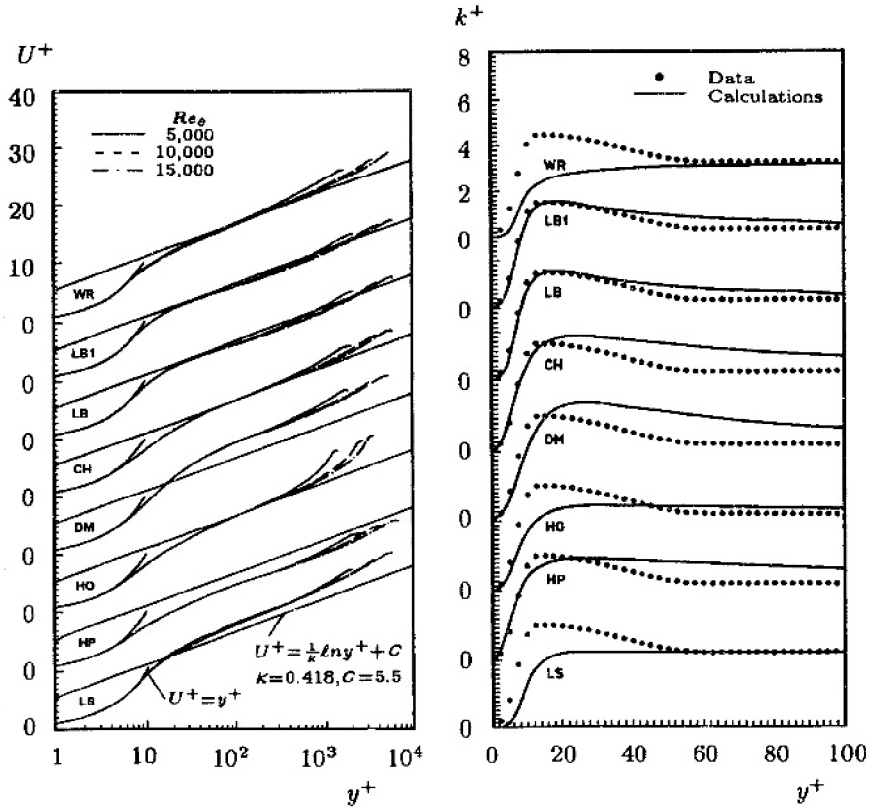

Figure 4.31: *Flat-plate boundary layer properties. CH = Chien; DM = Dutoya-Michard; HO = Hoffman; HP = Hassid-Poreh; LB = Lam-Bremhorst with $\epsilon = \nu \partial^2 k / \partial y^2$ at $y = 0$; LB1 = Lam-Bremhorst with $\partial \epsilon / \partial y = 0$ at $y = 0$; LS = Launder-Sharma; WR = Wilcox-Rubesin. [From Patel, Rodi and Scheuerer (1985) — Copyright © AIAA 1985 — Used with permission.]*

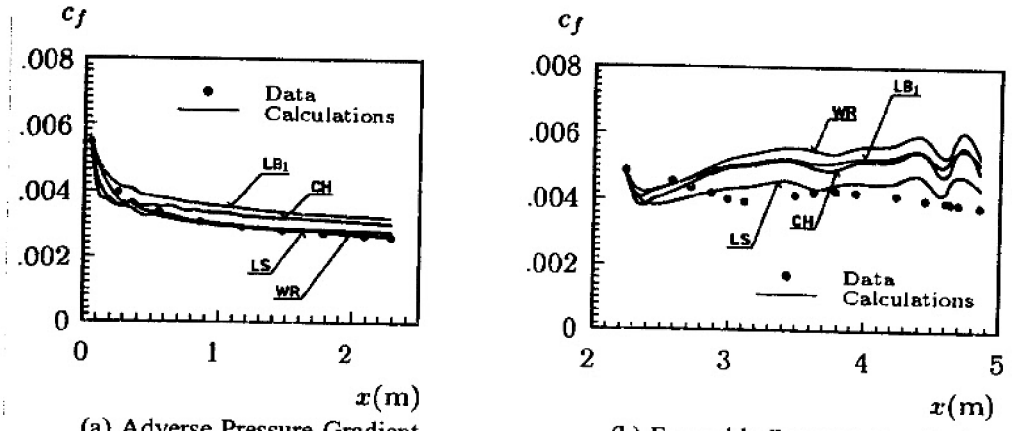

(a) Adverse Pressure Gradient (b) Favorable Pressure Gradient

Figure 4.32: *Comparison of computed and measured skin friction for low-Reynolds-number flows with pressure gradient. CH = Chien; LB1 = Lam-Bremhorst with $\partial\epsilon/\partial y = 0$ at $y = 0$; LS = Launder-Sharma; WR = Wilcox-Rubesin. [From Patel, Rodi and Scheuerer (1985) — Copyright © AIAA 1985 — Used with permission.]*

As an alternative, Lam and Bremhorst propose using

$$\frac{\partial \epsilon}{\partial y} = 0 \qquad \text{at} \qquad y = 0 \tag{4.223}$$

While Equation (4.223) is easier to implement than Equation (4.222), there is no a priori reason to expect that the next term in the Taylor-series expansion for ϵ should vanish.

In a review article, Patel, Rodi and Scheuerer (1985) compare seven low-Reynolds-number variants of the k-ϵ model and the Wilcox-Rubesin (1980) k-ω^2 model. Figure 4.31 compares computed and measured velocity and dimensionless turbulence kinetic energy ($k^+ = k/u_\tau^2$) profiles for the flat-plate boundary layer. As shown, several models fail to provide accurate velocity profiles for the incompressible flat-plate boundary layer.

Figure 4.32(a) shows that for adverse pressure gradient, the Wilcox-Rubesin model (which was not designed with low-Reynolds-number applications in mind) most faithfully matches measured [Andersen et al. (1972)] skin friction. Figure 4.32(b) shows that none of the models reproduces the measured skin friction for the low-Reynolds-number, favorable pressure gradient flow of Simpson and Wallace (1975). This further demonstrates that the only thing low-Reynolds-number modifications do is fix the k-ϵ model's problems in predicting the constant C in the law of the wall.

There is a popular misconception that low-Reynolds-number modifications to the k-ϵ model can remove its deficiencies for adverse pressure gradient flows.

This mistaken notion overlooks the volumes of data on and physical understanding of turbulent boundary layers established during the twentieth century, most notably by Clauser and Coles. Recall from Subsection 4.6.1 that Coles describes the turbulent boundary layer as a "wake-like structure constrained by a wall" and notes that different scales and physical processes are dominant in the sublayer and defect layer. As noted above, since perturbation analysis shows that the k-ϵ model predicts defect-layer data rather poorly, we cannot reasonably expect viscous corrections (which are negligible in the physical defect layer) to correct the problem.

Figure 4.33 clearly illustrates this point. The figure compares computed and measured skin friction for the 12 incompressible boundary layers with adverse pressure gradient considered earlier (see Figure 4.30). Results are presented for the Jones-Launder, Launder-Sharma, Lam-Bremhorst and Chien k-ϵ models and for the Wilcox (1998) k-ω model. Discrepancies between computed and measured c_f increase for all four k-ϵ models as the strength of the pressure gradient increases. As discussed in the last section, k-ω results are close to measured values for all twelve cases, including the nearly separated Flow 5300 (the Chien model predicts separation for this case). In terms of the final values of c_f, the average difference between computation and measurement for the 12 cases is 6% for the k-ω model,[12] 43% for the Jones-Launder model, 46% for the Chien model, 47% for the Launder-Sharma model and 58% for the Lam-Bremhorst model.

These results confirm the defect-layer perturbation solution presented in Subsection 4.6.2, which shows that [see Equation (4.179)]:

$$\frac{U_e - U}{u_\tau} \sim -\frac{1}{\kappa}\ell n\eta + A - \beta_T B\eta\ell n\eta + O\left(\eta^2\ell n\eta\right) \qquad \text{as} \qquad \eta \to 0 \quad (4.224)$$

where the coefficient B is given in Table 4.7. Combining Equation (4.224) with Equation (4.171), the effective law of the wall predicted by the k-ϵ model is

$$U^+ \sim \frac{1}{\kappa}\ell n y^+ + C + \beta_T B\eta\ell n\eta \qquad \text{as} \qquad y^+ \to \infty \quad (4.225)$$

Since $\eta < 1$, the term $\beta_T B\eta\ell n\eta$ is negative, so that we should expect the computed velocity profile to lie below the classical law-of-the-wall line on a semi-log plot. Figure 4.34 compares the computed Launder-Sharma model velocity profile with experimental data, the standard law of the wall and a defect-layer solution for $\beta_T = 2$. Examination of the numerical solution tells us that the implied constant in the law of the wall, C, is 5.5. As shown, the numerical solution indeed lies below the law-of-the-wall line, while the defect-layer profile shape is similar to the computed profile. We should not expect exact agreement

[12] The average difference increases to 7% for the Wilcox (2006) k-ω model.

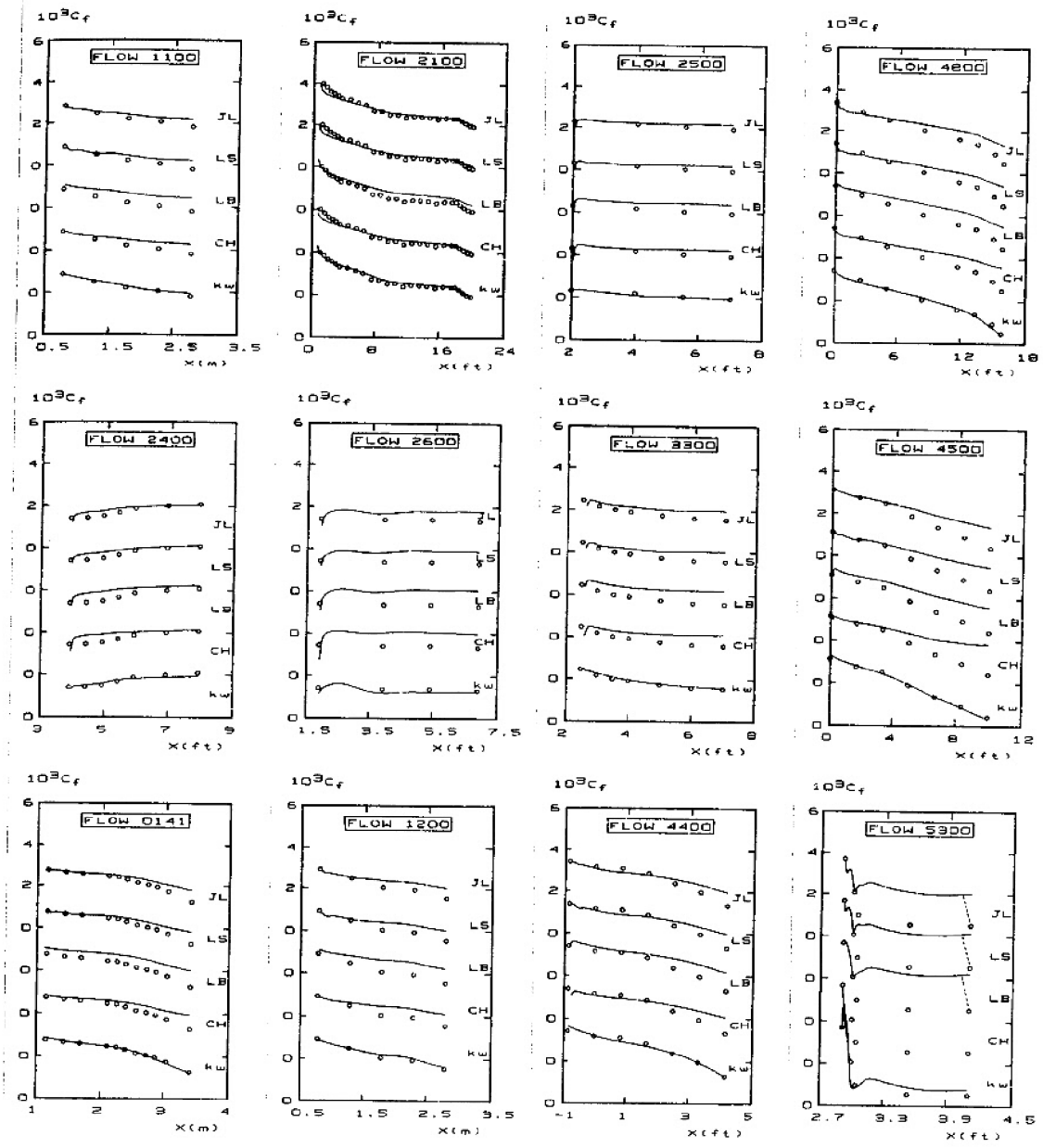

Figure 4.33: *Computed and measured skin friction for boundary layers with adverse pressure gradient; CH = Chien; JL = Jones-Launder; LB = Lam-Bremhorst; LS = Launder-Sharma; kw = Wilcox (1998) k-ω.*

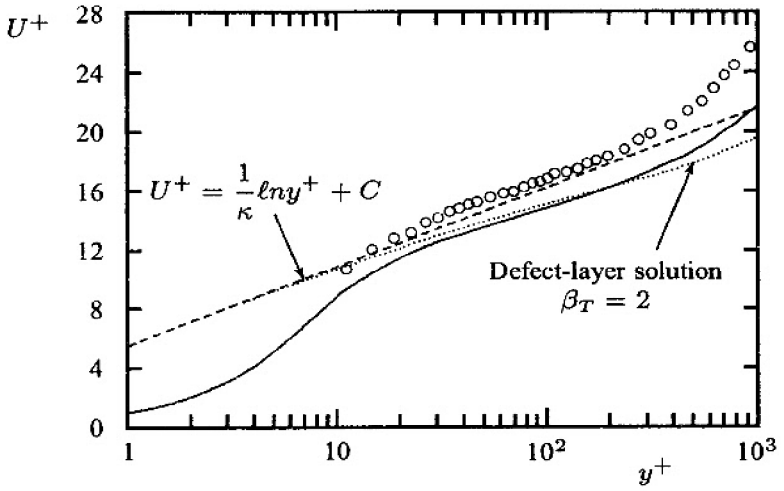

Figure 4.34: *Computed and measured near-wall velocity profiles for Samuel and Joubert's adverse pressure gradient flow, $x = 3.40$ m: —— Launder-Sharma (1974) k-ϵ model with $\kappa = 0.43$ and $C = 5.5$; o Samuel-Joubert.*

between the computed profile and the defect-layer profile since β_T varies quite rapidly with x for the Samuel-Joubert flow. However, the similarity of their shapes is striking. The important point to note is the impact of the term in Equation (4.225) proportional to the equilibrium parameter, β_T. Its effect is to distort the velocity profile throughout the defect layer, including its asymptotic form approaching the viscous sublayer from above.

As a final comment on low-Reynolds-number corrections for the k-ϵ model, using the dimensionless parameters R_y and y^+ [Equation (4.215)] is ill advised. Both depend on distance normal to the surface, which can cause difficulty in complex geometries such as a wing-fuselage junction. Also, it is ironic that several additional closure coefficients and functions are needed for the k-ϵ model to behave properly in the near-wall region of a turbulent boundary layer. Dissipation is, after all, a phenomenon that occurs in the smallest eddies, which is all we find in the near-wall region. This further underscores the fact that there is virtually no connection between the exact equation for ϵ and its modeled counterpart.

4.9.2 Transition

Turbulence model equations can be integrated through transition from laminar to turbulent flow, although most models predict transition at Reynolds numbers that are at least an order of magnitude too low. The following discussion focuses mostly on the k-ω model, whose behavior through transition is easiest to understand. The discussion also demonstrates why the k-ϵ model is so much harder to implement for transitional flows. To understand why and how the k-ω model

predicts transition, consider the flat-plate boundary layer. For the k-ω model, the incompressible, two-dimensional boundary-layer form of the equations for k and ω is as follows.

$$U\frac{\partial U}{\partial x}+V\frac{\partial U}{\partial y}=\frac{\partial}{\partial y}\left[(\nu+\nu_T)\frac{\partial U}{\partial y}\right] \tag{4.226}$$

$$U\frac{\partial k}{\partial x}+V\frac{\partial k}{\partial y}=\nu_T\left(\frac{\partial U}{\partial y}\right)^2-\beta^*\omega k+\frac{\partial}{\partial y}\left[\left(\nu+\sigma^*\alpha^*\frac{k}{\omega}\right)\frac{\partial k}{\partial y}\right] \tag{4.227}$$

$$U\frac{\partial \omega}{\partial x}+V\frac{\partial \omega}{\partial y}=\alpha\frac{\omega}{k}\nu_T\left(\frac{\partial U}{\partial y}\right)^2-\beta\omega^2+\frac{\sigma_d}{\omega}\frac{\partial k}{\partial y}\frac{\partial \omega}{\partial y}+\frac{\partial}{\partial y}\left[\left(\nu+\sigma\alpha^*\frac{k}{\omega}\right)\frac{\partial \omega}{\partial y}\right] \tag{4.228}$$

$$\nu_T=\alpha^*\frac{k}{\tilde{\omega}},\qquad \tilde{\omega}=\max\left\{\omega,\ C_{lim}\frac{\partial U/\partial y}{\sqrt{\beta_o^*/\alpha^*}}\right\} \tag{4.229}$$

where $\beta_o^*=9/100$ [Equation (4.229)] is the value of β^* appropriate for fully-turbulent flow. With one other exception, all notation and closure coefficients are as defined in Equations (4.36) – (4.42). The only difference is the appearance of an additional closure coefficient α^* in Equations (4.227) – (4.229). This coefficient is equal to unity for the standard high-Reynolds-number version of the k-ω model. We can most clearly illustrate how the model equations predict transition by rearranging terms in Equations (4.227) and (4.228) as follows.

$$U\frac{\partial k}{\partial x}+V\frac{\partial k}{\partial y}=P_k\beta^*\omega k+\frac{\partial}{\partial y}\left[\left(\nu+\sigma^*\alpha^*\frac{k}{\omega}\right)\frac{\partial k}{\partial y}\right] \tag{4.230}$$

$$U\frac{\partial \omega}{\partial x}+V\frac{\partial \omega}{\partial y}=P_\omega\beta\omega^2+\frac{\sigma_d}{\omega}\frac{\partial k}{\partial y}\frac{\partial \omega}{\partial y}+\frac{\partial}{\partial y}\left[\left(\nu+\sigma\alpha^*\frac{k}{\omega}\right)\frac{\partial \omega}{\partial y}\right] \tag{4.231}$$

The **net production per unit dissipation** terms in the two equations, P_k and P_ω, are defined by:[13]

$$P_k=\frac{\alpha^*}{\beta^*}\left(\frac{\partial U/\partial y}{\omega}\right)^2-1,\quad P_\omega=\frac{\alpha\alpha^*}{\beta}\left(\frac{\partial U/\partial y}{\omega}\right)^2-1 \tag{4.232}$$

There are two important observations worthy of mention at this point. **First**, if the turbulence kinetic energy is zero, Equation (4.231) has a well-behaved solution. That is, when $k=0$, the eddy viscosity vanishes and the ω equation uncouples from the k equation. Consequently, the k-ω model has a nontrivial laminar-flow solution, with $\nu_T=0$, for ω. **Second**, the signs of P_k and P_ω determine whether k and ω are amplified or reduced in magnitude. However,

[13] For this discussion, we assume that $\tilde{\omega}=\omega$, which reflects the fact that production is less than dissipation until transition has occurred.

it is not obvious from Equation (4.232) how the signs of these terms vary with Reynolds number as we move from the plate leading edge to points downstream. We can make the variation obvious by rewriting Equation (4.232) in terms of the Blasius transformation for a laminar boundary layer.

Before we introduce the Blasius transformation, we must determine the appropriate scaling for ω. To do this, we note that close to the surface of a flat-plate boundary layer (laminar or turbulent), the specific dissipation rate behaves according to[14] [see Equation (4.187) and Table 4.8]:

$$\omega \to \frac{6\nu}{\beta_o y^2} \qquad \text{as} \qquad y \to 0 \tag{4.233}$$

In terms of the Blasius similarity variable, η, defined by

$$\eta = \frac{y}{\sqrt{\nu x / U_\infty}} \tag{4.234}$$

where U_∞ is freestream velocity, the asymptotic behavior of ω approaching the surface is

$$\omega \to \frac{U_\infty}{x}\frac{6}{\beta_o \eta^2} \qquad \text{as} \qquad \eta \to 0 \tag{4.235}$$

Since U_∞/x has dimensions of 1/time, we conclude that the appropriate scaling for ω in the Blasius boundary layer is given by

$$\omega = \frac{U_\infty}{x} W(x, \eta) \tag{4.236}$$

where $W(x, \eta)$ is a dimensionless function to be determined as part of the solution. Also, we write the velocity in terms of dimensionless velocity, $\mathcal{U}(x, \eta)$, according to

$$U = U_\infty \mathcal{U}(x, \eta) \tag{4.237}$$

Noting that $\beta = \beta_o = 0.0708$ for two-dimensional flows, the **net production-per-unit-dissipation** terms become

$$P_k = \frac{\alpha^*}{\beta^*} Re_x \left(\frac{\partial \mathcal{U}/\partial \eta}{W} \right)^2 - 1, \quad P_\omega = \frac{\alpha \alpha^*}{\beta_o} Re_x \left(\frac{\partial \mathcal{U}/\partial \eta}{W} \right)^2 - 1 \tag{4.238}$$

Thus, both P_k and P_ω increase linearly with Reynolds number, Re_x. From the exact laminar solution for $\mathcal{U}(\eta)$ and $W(\eta)$ [the x dependence vanishes for the Blasius boundary layer], the maximum value (with respect to η) of the ratio of $\partial \mathcal{U}/\partial \eta$ to W is

$$\left(\frac{\partial \mathcal{U}/\partial \eta}{W} \right)_{max} \approx \frac{1}{300} \tag{4.239}$$

[14] Keep in mind that dissipation is $\epsilon = \beta^* \omega k$ so that ω can be finite even when k and ϵ vanish.

The precise value of this ratio is a weak function of the freestream value of ω, ranging between 0.0025 and 0.0040. The maximum occurs about midway through the boundary layer ($y/\delta = 0.56$), a point above which the exact near-wall behavior of ω [Equation (4.235)] does not hold. Hence, a complete boundary-layer solution is needed to determine the maximum ratio of $\partial \mathcal{U}/\partial \eta$ to W.

As long as the eddy viscosity remains small compared to the molecular viscosity, we can specify the precise points where P_k and P_ω change sign, which impact the beginning and end of transition, respectively. Using Equation (4.239), we conclude that the sign changes occur at the following Reynolds numbers.

$$(Re_x)_k = 9 \cdot 10^4 \frac{\beta^*}{\alpha^*}, \qquad (Re_x)_\omega = 9 \cdot 10^4 \frac{\beta_o}{\alpha \alpha^*} \tag{4.240}$$

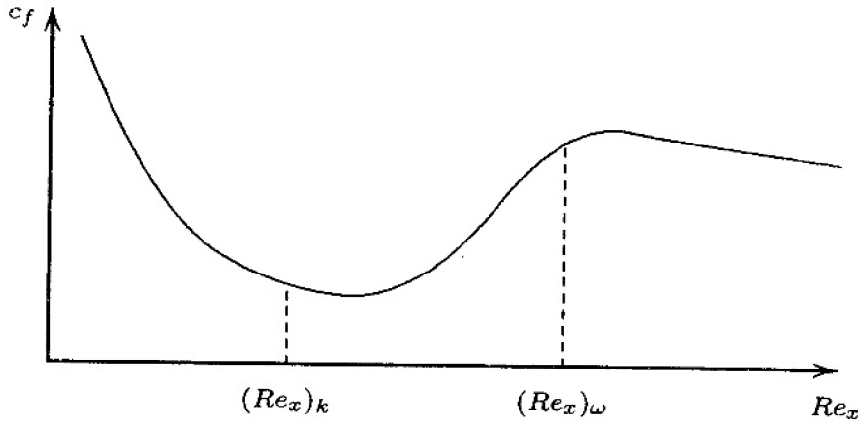

Figure 4.35: *Skin friction variation for a boundary layer undergoing transition from laminar to turbulent flow.*

With no viscous modifications, the closure coefficients α, α^*, β_o and β^* are 13/25, 1, 0.0708 and 9/100, respectively. Using these **fully-turbulent** values, we find $(Re_x)_k = 8100$ and $(Re_x)_\omega = 12254$. Thus, starting from laminar flow at the leading edge of a flat plate (see Figure 4.35), the following sequence of events occurs.

1. The computation starts in a laminar region with $k = 0$ in the boundary layer and a small freestream value of k.

2. Initially, because $P_k < 0$ and $P_\omega < 0$, dissipation of both k and ω exceeds production. Turbulence kinetic energy is entrained from the freestream and spreads through the boundary layer by molecular diffusion. Neither k nor ω is amplified and the boundary layer remains laminar.

3. At the **critical Reynolds number**, $Re_{x_c} = 8100$, production overtakes dissipation in the k equation. Downstream of x_c, production exceeds

dissipation in the k equation and turbulence kinetic energy is amplified. At some point in this process, the eddy viscosity grows rapidly and this corresponds to the onset of transition.

4. k continues to be amplified and, beyond $Re_x = 12254$ production overtakes dissipation in the ω equation. ω is now amplified and continues growing until a near balance between production and dissipation is achieved in the k equation. When this near balance is achieved, transition from laminar to turbulent flow is complete.

Consistent with experimental measurements, the entire process is very sensitive to the freestream value of k. There is also a sensitivity to the freestream value of ω, although the sensitivity is more difficult to quantify. These observations make the following three points obvious.

- **First**, turbulence kinetic energy begins growing at a Reynolds number of 8100. By contrast, linear-stability theory tells us that Tollmien-Schlichting waves begin forming in the Blasius boundary layer at a Reynolds number of 90000. This is known as the **minimum critical Reynolds number** for infinitesimal disturbances. Correspondingly, we find that the model predicts transition at much too low a Reynolds number.

- **Second**, inspection of Equation (4.240) shows that the ratio of β_o to $\alpha\alpha^*$ controls the value of $(Re_x)_w$, and hence the width of the transition region.

- **Third**, transition will never occur if P_ω reaches zero earlier than P_k. Thus, occurrence of transition requires

$$\alpha\alpha^* < \alpha^*\beta_o/\beta^* \qquad \text{as} \qquad Re_T \to 0 \tag{4.241}$$

where the quantity Re_T is turbulence Reynolds number defined by

$$Re_T = \frac{k}{\omega\nu} \tag{4.242}$$

This fact must be preserved in any viscous modification to the model.

Our goal is to devise viscous modifications that depend only upon Re_T. As noted in the preceding subsection, this quantity is independent of flow geometry and thus preserves the universal nature of the model. We also proceed with two key objectives in mind. The most important objective is to match the **minimum critical Reynolds number**. Reference to Equation (4.240) shows that, in order to have $(Re_x)_k = 90000$, we must require

$$\beta^*/\alpha^* \to 1 \qquad \text{as} \qquad Re_T \to 0 \tag{4.243}$$

On the one hand, our primary objective is to devise viscous modifications that make a realistic description of the gross aspects of the transition from laminar to turbulent flow possible with the k-ω model. On the other hand, there is a secondary objective that can be accomplished as well. That is, we would also like to achieve **asymptotic consistency** with the exact behavior of k and dissipation, $\epsilon = \beta^* k\omega$, approaching a solid boundary. Specifically, we would like to have $k/y^2 \rightarrow$ constant and $\epsilon/k \rightarrow 2\nu/y^2$ as $y \rightarrow 0$. Close to a solid boundary, the dissipation and molecular-diffusion terms balance in both the k and ω equations. The very-near-wall solution for ω is given by Equation (4.233). The solution for k is of the form

$$k/y^n \rightarrow \text{constant} \qquad \text{as} \qquad y \rightarrow 0 \tag{4.244}$$

where n is given by

$$n = \frac{1}{2}\left[1 + \sqrt{1 + 24\frac{\beta^*}{\beta_o}}\right] \tag{4.245}$$

Noting that dissipation is related to k and ω by

$$\epsilon = \beta^* k\omega \tag{4.246}$$

we can achieve the desired asymptotic behavior of k provided

$$\beta^*/\beta_o \rightarrow 1/3 \qquad \text{as} \qquad Re_T \rightarrow 0 \tag{4.247}$$

Requiring this limiting behavior as $Re_T \rightarrow 0$ is sufficient to achieve the desired asymptotic behavior as $y \rightarrow 0$ since the eddy viscosity, and hence, Re_T vanishes at a solid boundary.

If we choose to have β_o constant for all values of Re_T, Equations (4.241), (4.243) and (4.247) are sufficient to determine the limiting values of α^* and β^* and an upper bound for $\alpha\alpha^*$ as turbulence Reynolds number becomes vanishingly small. Specifically, we find

$$\left.\begin{array}{lcl} \alpha\alpha^* & < & \beta_o \\ \alpha^* & \rightarrow & \beta_o/3 \\ \beta^* & \rightarrow & \beta_o/3 \end{array}\right\} \qquad \text{as} \qquad Re_T \rightarrow 0 \tag{4.248}$$

Wilcox and Rubesin (1980) make the equivalent of $\alpha\alpha^*$ and α^* in their k-ω^2 model approach the same limiting value and obtain excellent agreement with measured transition width for incompressible boundary layers. Numerical experimentation with the k-ω model indicates the optimum choice for incompressible boundary layers is $\alpha\alpha^* \rightarrow 0.80\beta_o$, or

$$\alpha\alpha^* \rightarrow 0.057 \qquad \text{as} \qquad Re_T \rightarrow 0 \tag{4.249}$$

Following Wilcox (1992a), we postulate functional dependencies upon Re_T that guarantee the limiting values in Equations (4.248) and (4.249), as well as the original fully-turbulent values for $Re_T \to \infty$.

$$\alpha^* = \frac{\alpha_o^* + Re_T/R_k}{1 + Re_T/R_k} \tag{4.250}$$

$$\alpha = \frac{13}{25} \cdot \frac{\alpha_o + Re_T/R_\omega}{1 + Re_T/R_\omega} \cdot (\alpha^*)^{-1} \tag{4.251}$$

$$\beta^* = \frac{9}{100} \cdot \frac{100\beta_o/27 + (Re_T/R_\beta)^4}{1 + (Re_T/R_\beta)^4} \tag{4.252}$$

$$\beta_o = 0.0708, \quad \sigma = \frac{1}{2}, \quad \sigma^* = \frac{3}{5}, \quad \sigma_{do} = \frac{1}{8}, \quad \alpha_o^* = \frac{1}{3}\beta_o, \quad \alpha_o = \frac{1}{9} \tag{4.253}$$

$$\sigma_d = \begin{cases} 0, & \dfrac{\partial k}{\partial x_j}\dfrac{\partial \omega}{\partial x_j} \le 0 \\ \sigma_{do}, & \dfrac{\partial k}{\partial x_j}\dfrac{\partial \omega}{\partial x_j} > 0 \end{cases} \tag{4.254}$$

$$R_\beta = 8, \qquad R_k = 6, \qquad R_\omega = 2.61 \tag{4.255}$$

The three coefficients R_β, R_k and R_ω control the rate at which the closure coefficients approach their fully-turbulent values. We can determine their values by using perturbation methods to analyze the viscous sublayer.[15] Implementing the procedure discussed in Subsection 4.6.3, we can solve for the constant in the law of the wall, C. For given values of R_β and R_k, there is a unique value of R_ω that yields a constant in the law of the wall of 5.47, which is the value given by the model with no viscous modifications. For example, Figure 4.36 shows how R_ω varies with R_k when $R_\beta = 8$.

For small values of R_β the peak value of k near the surface is close to the value achieved without viscous corrections, viz., $u_\tau^2/\sqrt{\beta^*}$. As R_β increases, the maximum value of k near the surface increases. Figure 4.37 shows how R_ω and $k_{max}^+ = k_{max}/u_\tau^2$ vary with R_β when $R_k = 6$. Again, the value of R_ω corresponds to $C = 5.47$. Comparison of computed sublayer structure with Direct Numerical Simulation (DNS) results of Mansour, Kim and Moin (1988) shows that the optimum choice for these three coefficients is as indicated in Equation (4.255).

The only flaw in the model's asymptotic consistency occurs in the Reynolds shear stress, τ_{xy}. While the exact asymptotic behavior is $\tau_{xy} \sim y^3$, the model

[15] Note that this approach reflects a degree of optimism that the same viscous corrections can be expected to capture the physics of the viscous sublayer *and* transitional flows.

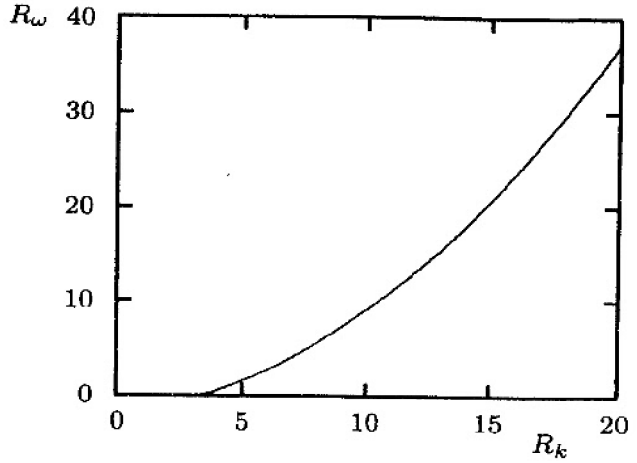

Figure 4.36: *Variation of R_ω with R_k when $R_\beta = 8$.*

predicts $\tau_{xy} \sim y^4$. This discrepancy could easily be removed with another viscous modification. However, as will be shown later in this subsection, this is of no significant consequence. It has no obvious bearing on either the model's ability to predict transition or properties of interest in turbulent boundary layers. The additional complexity and uncertainty involved in achieving this subtle feature of the very-near-wall behavior of τ_{xy} does not appear to be justified.

Finally, to complete formulation of the low-Reynolds-number k-ω model, we must specify surface boundary conditions. Again exercising Program **SUBLAY** (see Appendix C), we find that Equation (4.207) for surface mass injection is replaced by

$$S_B = \frac{14}{v_w^+(1 + 5v_w^+)} \tag{4.256}$$

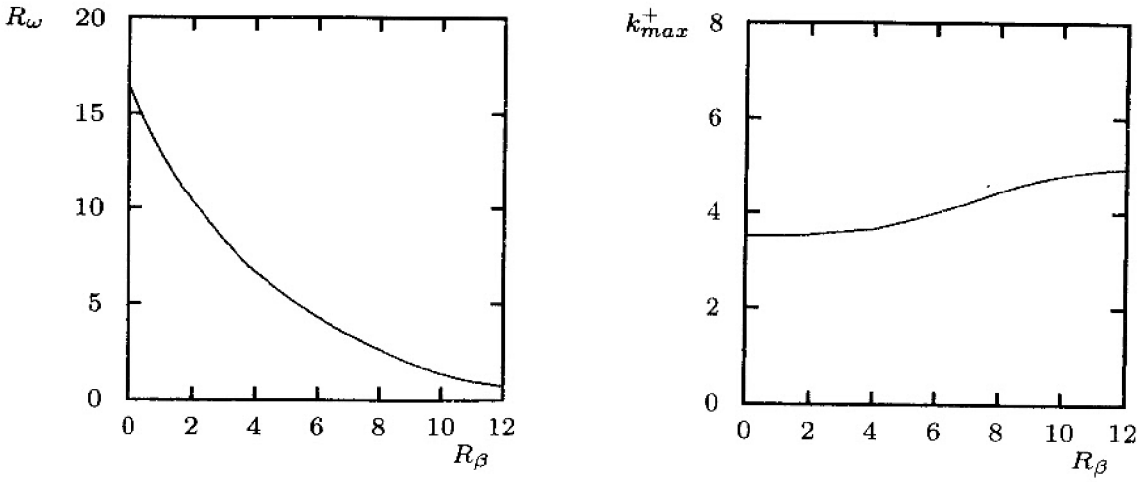

Figure 4.37: *Variation of R_ω and the peak value of k^+ with R_β when $R_k = 6$.*

Similarly, Equation (4.202) for rough surfaces is replaced by

$$S_R = \begin{cases} \left(\dfrac{200}{k_s^+}\right)^2, & k_s^+ \leq 5 \\ \dfrac{60}{k_s^+} + \left[\left(\dfrac{200}{k_s^+}\right)^2 - \dfrac{60}{k_s^+}\right] e^{5-k_s^+}, & k_s^+ > 5 \end{cases} \tag{4.257}$$

It is a simple matter to explain why little progress has been made in predicting transition with the k-ϵ model. The primary difficulties can be easily demonstrated by focusing upon incompressible boundary layers. If we use the standard form of the k-ϵ model, Equations (4.227) – (4.229) are replaced by

$$U\frac{\partial k}{\partial x} + V\frac{\partial k}{\partial y} = \nu_T \left(\frac{\partial U}{\partial y}\right)^2 - \epsilon + \frac{\partial}{\partial y}\left[(\nu + \nu_T/\sigma_k)\frac{\partial k}{\partial y}\right] \tag{4.258}$$

$$U\frac{\partial \epsilon}{\partial x} + V\frac{\partial \epsilon}{\partial y} = C_{\epsilon 1}\frac{\epsilon}{k}\nu_T \left(\frac{\partial U}{\partial y}\right)^2 - C_{\epsilon 2}\frac{\epsilon^2}{k} + \frac{\partial}{\partial y}\left[(\nu + \nu_T/\sigma_\epsilon)\frac{\partial \epsilon}{\partial y}\right] \tag{4.259}$$

$$\nu_T = C_\mu k^2/\epsilon \tag{4.260}$$

Equations (4.258) – (4.260) underscore a critical difference from the k-ω model, viz., if k is zero, ϵ must also be zero. We cannot simply drop the eddy viscosity in the ϵ equation, because of the presence of k in the denominator of the ϵ equation's dissipation term. The model does possess a laminar-flow solution for the ratio of ϵ to k. If we make the formal change of variables

$$\epsilon = C_\mu k\omega = \beta^* k\omega \tag{4.261}$$

and assume $\nu_T \ll \nu$, the following laminar-flow equation for ω results.

$$U\frac{\partial \omega}{\partial x} + V\frac{\partial \omega}{\partial y} = (C_{\epsilon 1} - 1)f_\mu \left(\frac{\partial U}{\partial y}\right)^2 - (C_{\epsilon 2} - 1)C_\mu \omega^2 + \nu\frac{\partial^2 \omega}{\partial y^2} + \frac{2\nu}{k}\frac{\partial k}{\partial y}\frac{\partial \omega}{\partial y} \tag{4.262}$$

Equation (4.262) is nearly identical to the limiting form of Equation (4.228) for $\nu_T/\nu \to 0$. The only significant difference is the last term on the right-hand side of Equation (4.262). Except close to the surface where k must be exactly zero, this term is unlikely to have a significant effect on the solution for small nonzero

values of k. However, establishing starting conditions is clearly more difficult with the k-ϵ model than with the k-ω model because of this ill-behaved term.

Given the diverse nature of viscous modifications that have been proposed for the k-ϵ model, it is impossible to make any universal statements about why a specific model fails to predict realistic transition Reynolds numbers. Perhaps the strongest statement that can be made is, **few researchers have approached the problem from the transition point of view**. Most have sought only to achieve asymptotic consistency as $y \rightarrow 0$ (Subsection 4.9.1) and attempted transition predictions only as an afterthought. We can gain some insight by examining the net production per unit dissipation terms for the k and ϵ equations that are analogous to Equation (4.238), viz.,

$$P_k = \frac{f_\mu}{C_\mu} Re_x \left(\frac{\partial \mathcal{U}/\partial \eta}{W} \right)^2 - 1, \quad P_\epsilon = \frac{C_{\epsilon 1} f_\mu}{C_{\epsilon 2} C_\mu} Re_x \left(\frac{\partial \mathcal{U}/\partial \eta}{W} \right)^2 - 1 \quad (4.263)$$

On the one hand, without viscous damping, if we assume Equation (4.239) is valid, we find $(Re_x)_k = 8100$ and $(Re_x)_\epsilon = 10800$. Consequently, as with the high-Reynolds-number version of the k-ω model, transition will occur at too low a Reynolds number. **On the other hand**, because C_μ, $C_{\epsilon 2}$ and sometimes $C_{\epsilon 1}$ are multiplied by functions of distance from the surface and/or functions of Re_T (c.f. f_μ, f_1 and f_2 in Subsection 4.9.1) in low-Reynolds-number k-ϵ models, we cannot simply use Equation (4.239). Furthermore, as discussed in the preceding subsection, some modelers add terms to the k and ϵ equations in addition to damping the closure coefficients. Each set of values for the closure coefficients and additional terms must be used in solving Equation (4.262) to determine the laminar-flow solution for ϵ/k. While it is clearly impossible to make a quantitative evaluation of all variants of the k-ϵ model, we can nevertheless make two general observations.

First, Rumsey et al. (2006) have shown that if $C_{\epsilon_1} = f_2 C_{\epsilon_2}$ at any point, the k-ϵ model has "arbitrary steady-state converged solutions that are highly dependent on numerical considerations such as initial conditions and solution procedure." This can occur, for example, with the Jones-Launder (1972), Launder-Sharma (1974) and Lam-Bremhorst (1981) models. Nonphysical dependence on initial conditions is a serious cause for alarm in transition computations.

Second, although this discussion is not intended as an exhaustive survey of the numerous low-Reynolds-number versions of the k-ϵ model, it does illustrate how difficult it can be to apply the model to the transition problem. Given enough additional closure coefficients and damping functions, the k-ϵ model can probably be modified to permit satisfactory transition predictions. However, even if this is done, establishing starting conditions will ultimately require a solution to Equation (4.262). That is, to initialize the computation, we must effectively

transform to the k-ω model. Since this is the natural starting point, it seems illogical to perform subsequent computations in terms of k and ϵ.

4.9.3 Channel and Pipe Flow

Figure 4.38 compares low-Reynolds-number k-ω model channel-flow skin friction, c_f, with the Halleen and Johnston (1967) correlation [Equation (3.139))]. Reynolds number based on channel height, H, and average velocity ranges from 10^3 to 10^5. Computed c_f differs from the correlation by less than 3% except at the lowest Reynolds number shown where the correlation probably is inaccurate. Velocity, Reynolds shear stress, and turbulence kinetic energy profiles differ by less than 7%. Most notably, the model predicts the peak value of k near the channel wall to within 4% of the DNS value. Approaching the surface, the dimensionless turbulence-energy production, $\mathcal{P}^+ = \nu\tau_{xy}(\partial U/\partial y)/u_\tau^4$, and dissipation, $\epsilon^+ = \nu\epsilon/u_\tau^4$, are within 10% of the DNS results except very close to the surface.

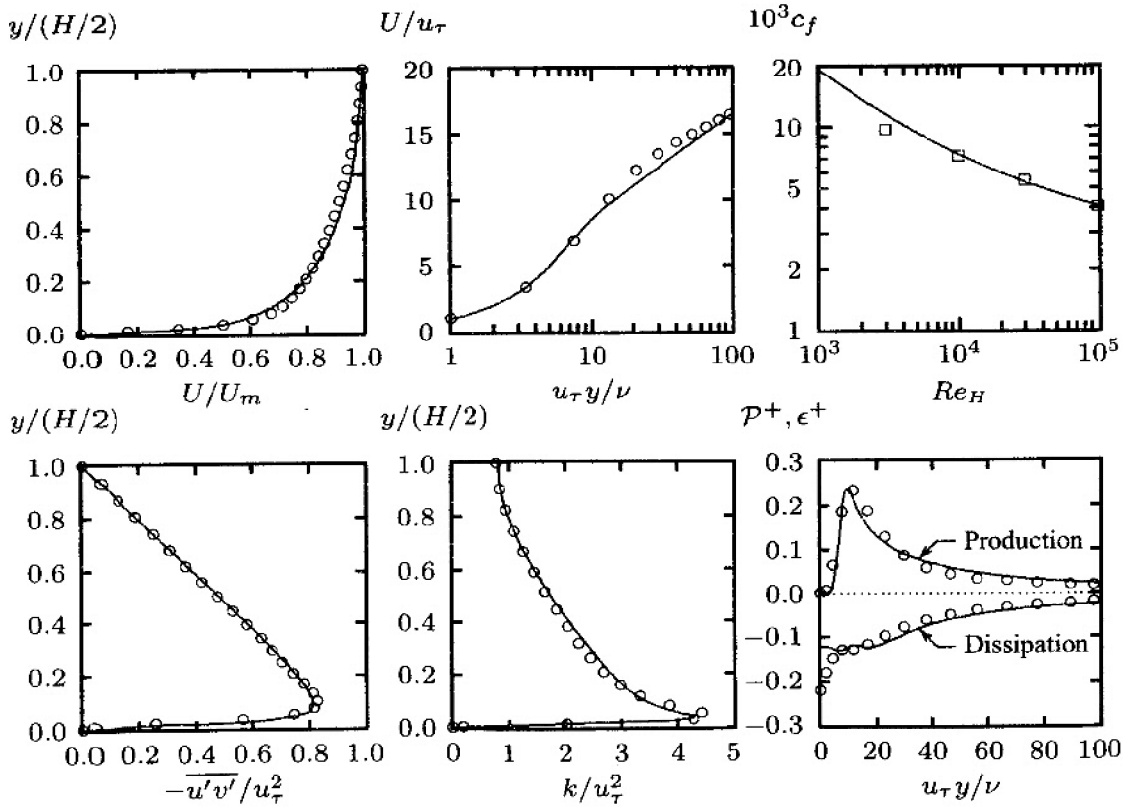

Figure 4.38: *Comparison of computed and measured channel-flow properties, $Re_H = 13750$.* —— *Low-Reynolds-number k-ω model;* ○ *Mansour et al. (DNS);* □ *Halleen-Johnston correlation.*

Figure 4.39 compares computed pipe flow c_f with Prandtl's universal law of friction [Equation (3.140)]. Reynolds number based on pipe diameter, D, and average velocity varies from 10^3 to 10^6. As with channel flow, computed c_f falls within 5% of the correlation except at the lowest Reynolds number shown where the correlation is likely to be in error. Computed and measured velocity and Reynolds shear stress profiles differ by less than 8%. Computed and measured turbulence kinetic energy differ by about 5% including the region close to the surface where the sharp peak occurs. Computed turbulence-energy production, $\mathcal{P}^+$, and dissipation, ϵ^+, differ from measured values by less than 10% except where Laufer's measurements are inaccurate close to the surface.

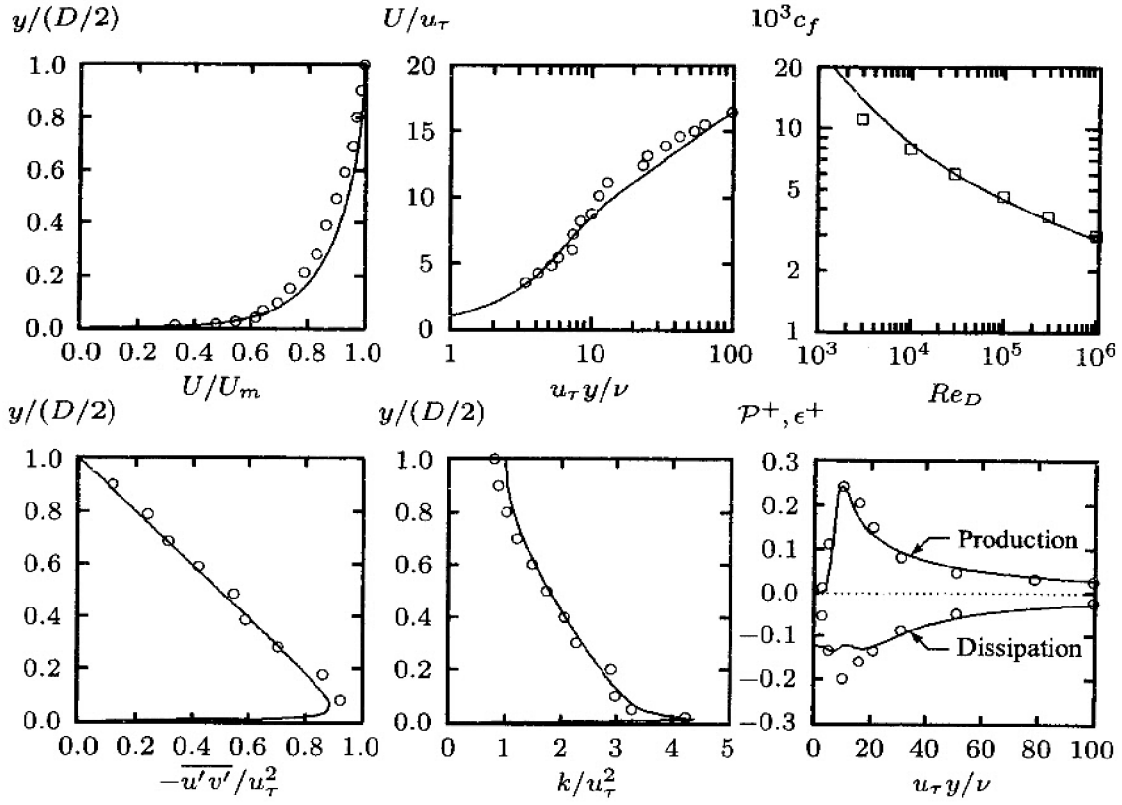

Figure 4.39: *Comparison of computed and measured pipe-flow properties,* $Re_D = 40000$. —— *Low-Reynolds-number k-ω model;* ○ *Laufer;* □ *Prandtl correlation.*

Aside from the sharp peak in k near the surface and dissipation approaching a finite, non-zero value at the surface, these results for channel and pipe flow are nearly identical to those obtained with no viscous modifications. Thus, in the context of the k-ω model, these are benign features of the turbulence that have little significance for prediction of skin friction, Reynolds shear stress and velocity profiles.

4.9.4 Boundary-Layer Applications

Figure 4.40 compares computed and measured skin friction for the 16 baseline test cases considered for algebraic and one-equation models. Computations have been done using Program **EDDYBL** (see Appendix C). Additionally, Table 4.10 summarizes average differences between computed and measured c_f at the end of each computation. As indicated in the table, both the low-Reynolds-number (Low-Re) and high-Reynolds-number (High-Re) versions of the k-ω model reproduce measured skin friction to well within measurement error.

Table 4.10: *Differences Between Computed and Measured Skin Friction.*

Pressure Gradient	Flows	Low-Re k-ω	High-Re k-ω
Favorable	1400, 1300, 2700, 6300	4%	3%
Mild Adverse	1100, 2100, 2500, 4800	4%	5%
Moderate Adverse	2400, 2600, 3300, 4500	8%	9%
Strong Adverse	0141, 1200, 4400, 5300	7%	8%
All	–	6%	6%

With just one exception, differences between the Low-Re and High-Re versions of the k-ω model are almost imperceptible. This is expected since the low-Reynolds-number modifications are confined almost exclusively to the viscous sublayer. The skin friction, by contrast, is controlled by the overall balance of forces (pressure gradient and surface shear stress) and the momentum flux through the entire boundary layer.

The only noteworthy differences between Low-Re and High-Re model predictions occur for the incipient separation case, Flow 5300. The Low-Re model provides a solution with $c_f = 3.1 \cdot 10^{-4}$ at the final station, compared to $c_f = 6.8 \cdot 10^{-4}$ for the high-Reynolds-number version of the model. The measured value of $c_f = 5.3 \cdot 10^{-4}$ lies midway between model predictions with and without viscous modifications.

The disparate results obtained for Flow 5300 are likely due to the fact that, approaching separation, the specific dissipation rate is reduced to smaller levels than those prevailing in attached boundary layers. Recall that in the sublayer, ω scales with u_τ^2/ν. Consequently, since the viscous modification to the closure coefficient α directly impacts the production of ω, the percentage change will be much greater when ω is small. This will, in turn, have a nontrivial effect throughout the boundary layer, and thus have a noticeable impact on the skin friction.

As a final comment, k-ω model-predicted skin friction and velocity for Flow 5300 — with or without viscous modifications — are much closer to measurements than those of any other turbulence model known to this author.

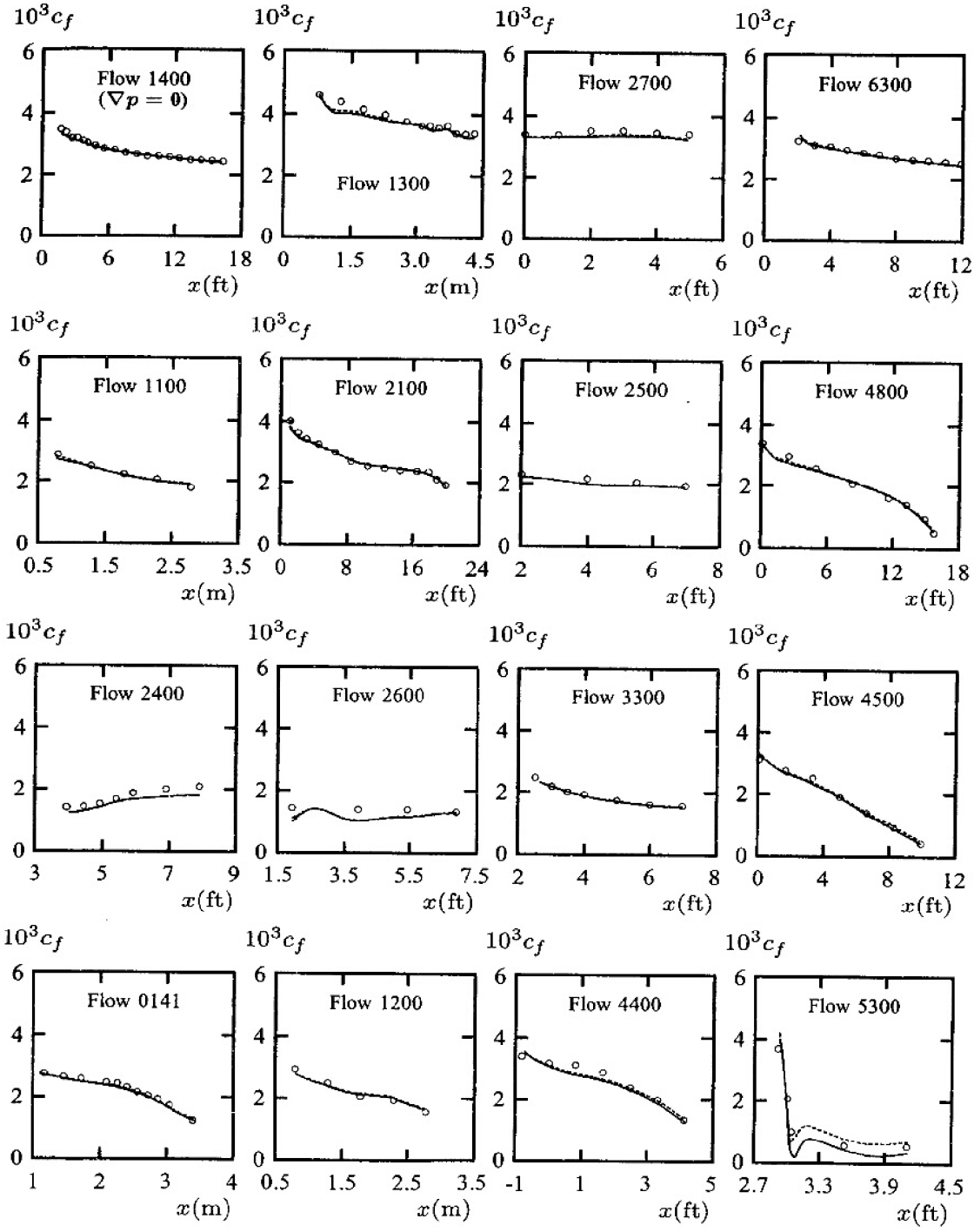

Figure 4.40: *Computed and measured skin friction for boundary layers subjected to a pressure gradient. Top row - favorable ∇p; next to top row - mild adverse ∇p; next to bottom row - moderate adverse ∇p; bottom row - strong adverse ∇p. —— Low-Reynolds-number k-ω model; - - - High-Reynolds-number k-ω model; ○ measured.*

Turning now to transition, Figure 4.41 compares computed and measured transition Reynolds number, Re_{θ_t}, for an incompressible flat-plate boundary layer. We define the transition Reynolds number as the point where the skin friction achieves its minimum value. Results are displayed as a function of freestream turbulence intensity, T', defined by

$$T' = 100\sqrt{\frac{2}{3}\frac{k_e}{U_e^2}} \tag{4.264}$$

where subscript e denotes the value at the boundary-layer edge. As shown, consistent with the data compiled by Dryden (1959), Re_{θ_t} increases as the freestream intensity decreases. Because ω can be thought of as an averaged frequency of the freestream turbulence, it is reasonable to expect the predictions to be sensitive to the freestream value of ω. To assess the effect, the freestream value of the turbulence length scale $\ell = k^{1/2}/\omega$ has been varied from 0.001δ to 0.100δ where δ is boundary-layer thickness. As shown, computed Re_{θ_t} values bracket most of the data. Unlike the situation for free shear flows, the k-ω model's sensitivity to the freestream value of ω is a *desirable feature* for transition applications. Physical transition location is not simply a function of T', but rather is frequency dependent. While it is unclear how the freestream value of ω should be specified, consistent with measurements, the model is not confined to a single transition location for a given T' regardless of the frequency of the disturbance.

Figure 4.42 compares computed width of the transition region with measurements of Dhawan and Narasimha (1958), Schubauer and Skramstad (1948), and Fisher and Dougherty (1982). We define transition width, Δx_t, as the distance between minimum and maximum skin-friction points. The computed width, $Re_{\Delta x_t}$, falls within experimental data scatter for $10^4 < Re_{x_t} < 10^7$. Δx_t is unaffected by the freestream value of ω.

While these results are interesting, keep in mind that transition is a complicated phenomenon. It is triggered by a disturbance in a boundary layer only if the frequency of the disturbance falls in a specific band. Reynolds averaging has masked all spectral effects, and all the model can represent with k and ω is the intensity of the disturbance and an average frequency. Hence, it is possible for the turbulence model to predict transition when it shouldn't occur. The model equations thus are sensible in the transition context only if the triggering disturbance is broad band, i.e., contains all frequencies.

Additionally, we have only guaranteed that the point where k is first amplified matches the minimum critical Reynolds number for the incompressible, flat-plate boundary layer. To simulate transition with complicating effects such as pressure gradient, surface heat transfer, surface roughness, compressibility, etc., the values of α_o^* and α_o must change [see Wilcox (1977)]. Their values can be deduced from linear-stability theory results, or perhaps from a correlation based

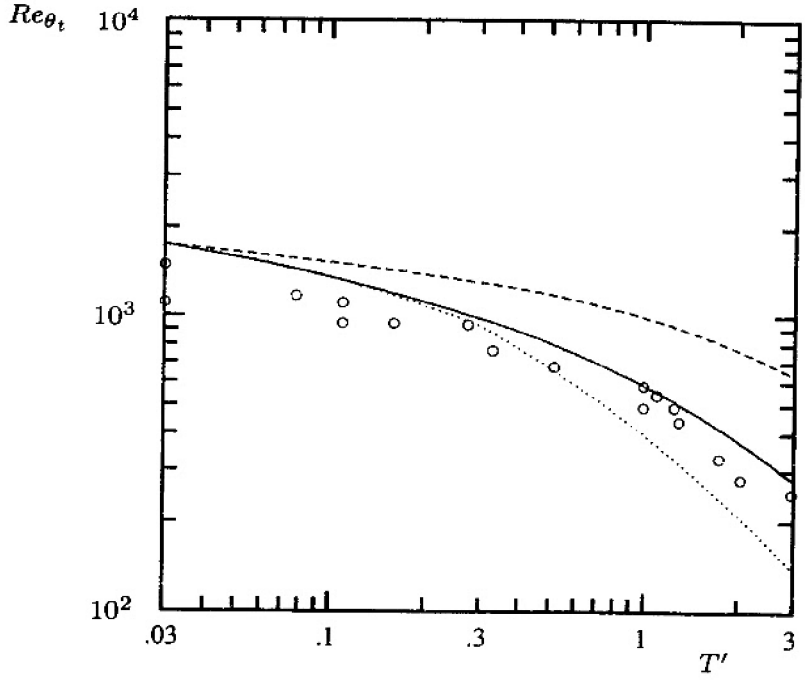

Figure 4.41: *Transition location for an incompressible flat-plate boundary layer:* - - - $\ell/\delta = 0.001$; —— $\ell/\delta = 0.010$; $\cdots$ $\ell/\delta = 0.100$; ○ *Dryden.*

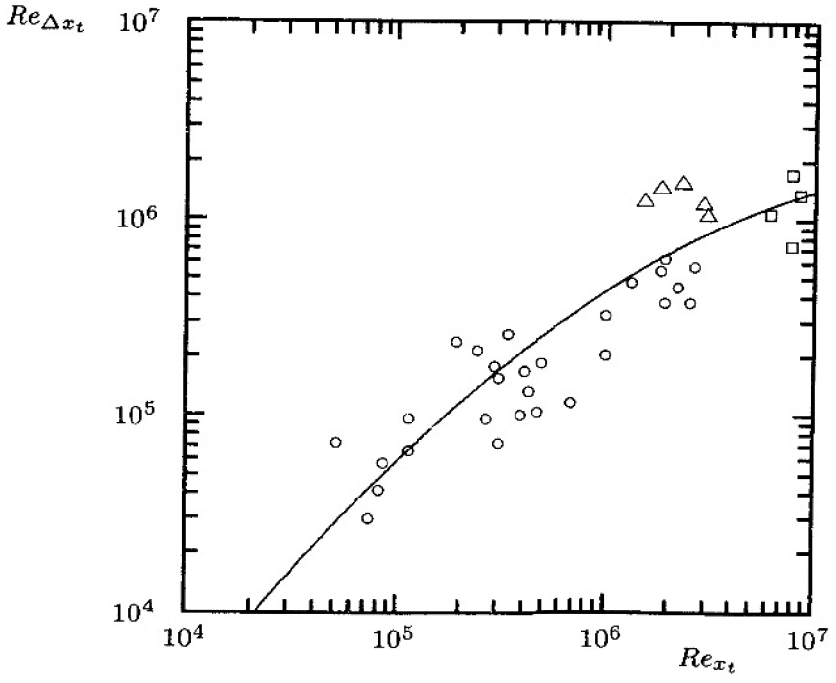

Figure 4.42: *Transition width for an incompressible flat-plate boundary layer:* —— *Wilcox (2006) k-ω model;* ○ *Dhawan and Narasimha;* △ *Schubauer and Skramstad;* □ *Fisher and Dougherty.*

on stability theory. Nevertheless, some information must be provided regarding the minimum critical Reynolds number for each new application.

In general, we can always match the measured transition point by adjusting the freestream value of k. This is satisfactory when the transition point occurs at a large Reynolds number, which requires k_∞ to be small relative to U_∞^2. Figure 4.43, for example, compares computed and measured skin friction for an incompressible flat-plate boundary layer [Schubauer and Klebanoff (1955)]. The computation was done with $T' = 0.05\%$, which was selected by trial and error to best match the measured transition point.

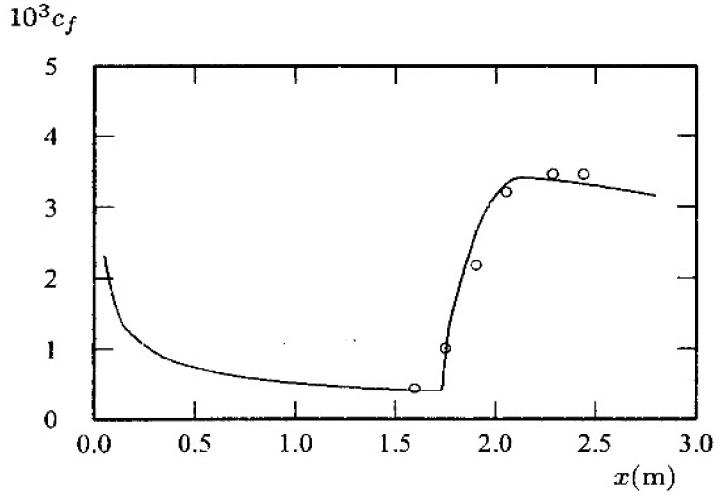

Figure 4.43: *Computed and measured skin friction for a transitional flat-plate boundary layer;* —— *Wilcox (2006) k-ω model;* ○ *Schubauer and Klebanoff.*

However, for a high-speed flow in which transition has been triggered at a relatively small Reynolds number, often unreasonably large values of k_∞ are needed to cause transition, so large as to affect the total energy in the freestream in a physically unrealistic manner. Thus, a new method for triggering transition is needed.

Wilcox (1994) offers an alternative to depending upon the model to predict the onset of transition, known as the **numerical roughness strip**. The foundation of the concept rests upon the fact that by using a finite value for ω at the surface, the model simulates surface roughness (Subsection 4.7.2). Since increasing the surface roughness height corresponds to decreasing the surface value of ω (and thus the dissipation in the k equation), the model predicts that roughness will have a destabilizing effect. This is consistent with measurements, and patches of surface roughness are often used to trigger transition in experiments.

Using Equations (4.196) and (4.202) to simulate a roughness strip, Wilcox (1994) has run more than 20 transitional boundary layer cases to test this idea. In all cases, computation begins at the plate leading edge, and the turbulence kinetic

energy is initially set to an extremely small value, viz., $10^{-15}U_\infty^2$, throughout the boundary layer. This value is too small to trigger transition naturally. The initial ω profile is given by the exact laminar-flow solution to the model equations. Using this approach, the numerical roughness strip triggers transition at the desired location for all of the cases considered using a roughness strip with k_s and the streamwise extent of the strip, Δs, given by the following correlations.

$$\frac{k_s}{\delta_t} = \max\left\{\frac{5000}{\sqrt{Re_{x_t}}}, 3\right\} \tag{4.265}$$

$$\frac{\Delta s}{\delta_t} = 0.015\sqrt{Re_{x_t}} \tag{4.266}$$

The quantities δ_t and Re_{x_t} are the boundary-layer thickness and transition Reynolds number based on arclength.

Figure 4.44 compares computed and measured [Blair and Werle (1981), Blair (1983)] Stanton number, St, for transitional boundary layers with surface heat transfer. According to Equations (4.265) and (4.266), the dimensions of the roughness strip required to match the measured transition point for the case with favorable pressure gradient are $(k_s/\delta_t,\ \Delta s/\delta_t) = (8.5,\ 8.7)$. As shown, differences between computed and measured Stanton numbers are no more than 15% for the two cases shown.

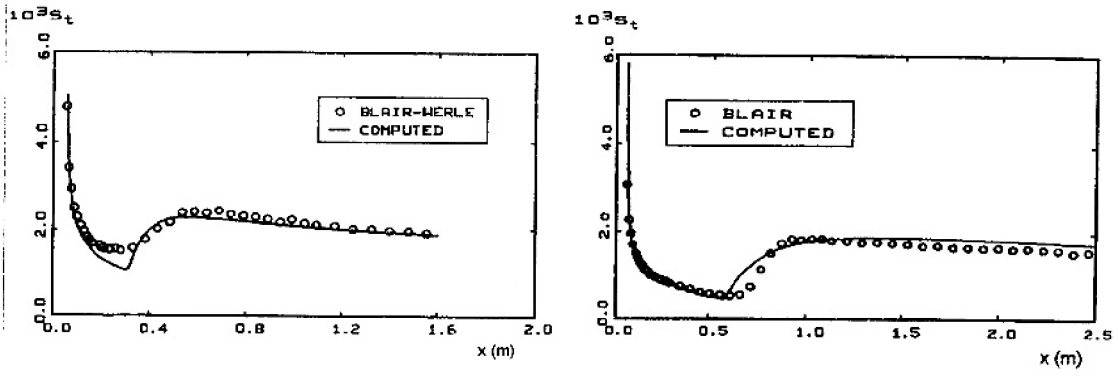

(a) Mildly favorable pressure gradient

(b) Constant pressure

Figure 4.44: *Computed and measured Stanton number for transitional boundary layers with surface heat transfer. [From Wilcox (1994) — Copyright © AIAA 1994 — Used with permission.]*

Perhaps the most practical way to use the model for transitional flows is in describing the transitional region, as opposed to predicting transition onset. Of course, the question of sensitivity to spectral effects in the transition region must be raised. Using linear-stability computations, Wilcox (1981a) shows that after

the initial disturbance has grown to a factor of e^4 times its initial value, the turbulence model closure coefficients lose all memory of spectral effects. Thus, we can conclude that not far downstream of the minimum critical Reynolds number, Reynolds averaging is sensible. This tells us that, if the point at which the transition begins is known, using a numerical roughness strip is a practical and accurate way of simulating transitional boundary layers.

Low-Reynolds-number corrections increase the complexity of two-equation models significantly. The high-Re k-ω model has just 6 closure coefficients and 2 closure functions. The low-Re version described in this subsection has 11 closure coefficients and 5 closure functions. The various low-Reynolds-number models discussed in Subsection 4.9.1 involve a similar increase in the number of closure coefficients and damping functions. The Launder-Sharma (1974) model, for example, has 9 closure coefficients and 4 closure functions.

If viscous effects are insignificant for a given application, it is advisable to use the simpler high-Reynolds-number version of the model. In the case of the k-ϵ model, if you need to integrate through the viscous sublayer, you have no choice but to use one of the low-Reynolds-number models, preferably one that yields a satisfactory solution for simple flows such as the incompressible flat-plate boundary layer. In the case of the k-ω model, integration through the sublayer can be done without introducing viscous corrections, and there is virtually no difference in model-predicted skin friction and velocity profiles with and without viscous corrections for turbulent boundary layers.

4.10 Application to Separated Flows

Turning to separated flows, we first consider the axisymmetric flow with strong adverse pressure gradient experimentally investigated by Driver (1991). Figure 4.45 compares measurements with computed skin friction and surface pressure for the k-ω model defined in Equations (4.36) – (4.42). The computations were done using Program **EDDY2C** (see Appendix C). As shown, the k-ω model yields a separation bubble of length quite close to the measured value, with the separation point slightly upstream of the measured location. Although pressure downstream of reattachment is 10% higher than measured, results are clearly much closer to measurements than those obtained with the Baldwin-Lomax, Baldwin-Barth and Spalart-Allmaras models (see Figures 3.18 and 4.5).

Because the stress-limiter modification to the model [Equation (4.36)] suppresses the magnitude of the Reynolds shear stress, the viscous stress opposing the adverse pressure gradient is reduced. This is attended by an increase in separation-bubble size. To asses the impact of the stress limiter, Figure 4.45 also includes computed results using the Wilcox (1988a) k-ω model. This model includes neither cross diffusion nor a stress limiter. Separation-bubble length is

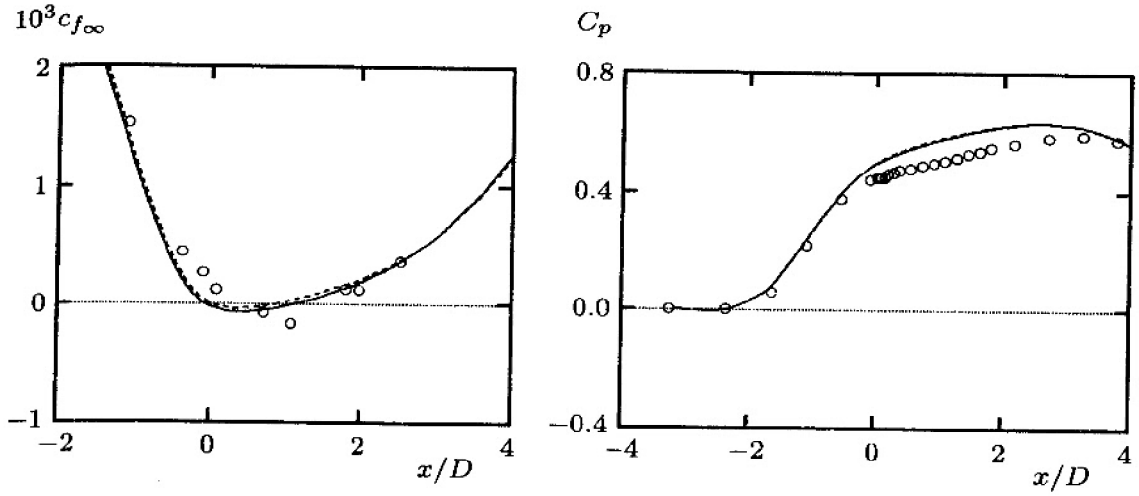

Figure 4.45: *Computed and measured flow properties for Driver's separated flow;* — *Wilcox (2006) k-ω model;* - - - *Wilcox (1988a) k-ω model;* o *Driver.*

about three-quarters of that predicted by the new k-ω model, while the separation points are nearly coincident. Aside from the separation-bubble size difference, computed results are very similar. Hence, we conclude that: (a) the stress-limiter effect is small for this flow and (b) its use with the k-ω model yields flow properties that are closer to measurements than the Wilcox (1988a) version.

Menter (1992c) applied a hybrid k-ω/k-ϵ model to this flow using a stress limiter. While computed pressure is very close to measured downstream of reattachment, the predicted separation bubble is 57% longer than measured (see Table 4.11). The table also includes results for several other turbulence models to provide a comprehensive comparison of several models considered in Chapters 3 and 4. Note that, consistent with its muted response to adverse pressure gradient, the Standard k-ϵ model fails to predict any flow separation [Menter (1992c)].

Table 4.11: *Separation-Bubble Length for Driver's Separated Flow.*

Model	Reference	$\Delta x/D$	Deviation from Measured
One-Equation	Baldwin-Barth (1990)	3.22	+130%
Algebraic	Baldwin-Lomax (1978)	2.89	+106%
One-Equation	Spalart-Allmaras (1992)	2.24	+60%
k-ω/k-ϵ	Menter (1992c)	2.20	+57%
Half-Equation	Johnson-King (1985)	1.69	+21%
k-ω	Wilcox (2006)	1.18	-16%
k-ω	Wilcox (1988a)	0.84	-40%
k-ϵ	Launder-Sharma (1974)	0.00	-100%
Measured	Driver (1991)	1.40	—

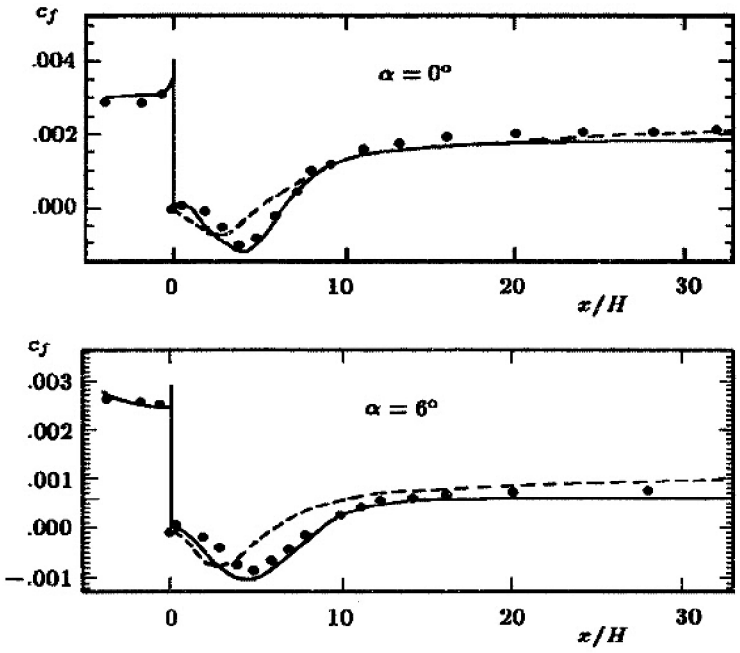

Figure 4.46: *Computed and measured skin friction for flow past a backward-facing step; $Re_H = 37500$; —— Wilcox (1988a) k-ω model; - - - k-ϵ model; • Driver-Seegmiller data. [From Menter (1992c).]*

Next, we consider the backward-facing step (see Figure 4.6 for the geometry). Figure 4.46 compares computed and measured [Driver and Seegmiller (1985)] skin friction for backstep flow with the upper channel wall inclined to the lower wall at angles of 0° and 6°. Computed results are shown for the Wilcox (1988a) k-ω model and for the Standard k-ϵ model with wall functions; neither model includes viscous corrections. As summarized in Table 4.12, the k-ϵ model predicts reattachment well upstream of the measured point for both cases, while the k-ω model is within 4% of the measured location for both cases.

Table 4.12: *Backstep Reattachment Length.*

Model	Reference	$\alpha = 0°$	$\alpha = 6°$
k-ϵ	Launder-Sharma (1974)	5.20	5.50
One-Equation	Spalart-Allmaras (1992)	6.10	8.60
k-ω	Wilcox (1988a)	6.18	8.45
k-ω/k-ϵ	Menter (1992c)	6.80	—
k-ω	Wilcox (2006)	7.07	—
Measured	Driver-Seegmiller (1985)	6.26	8.10

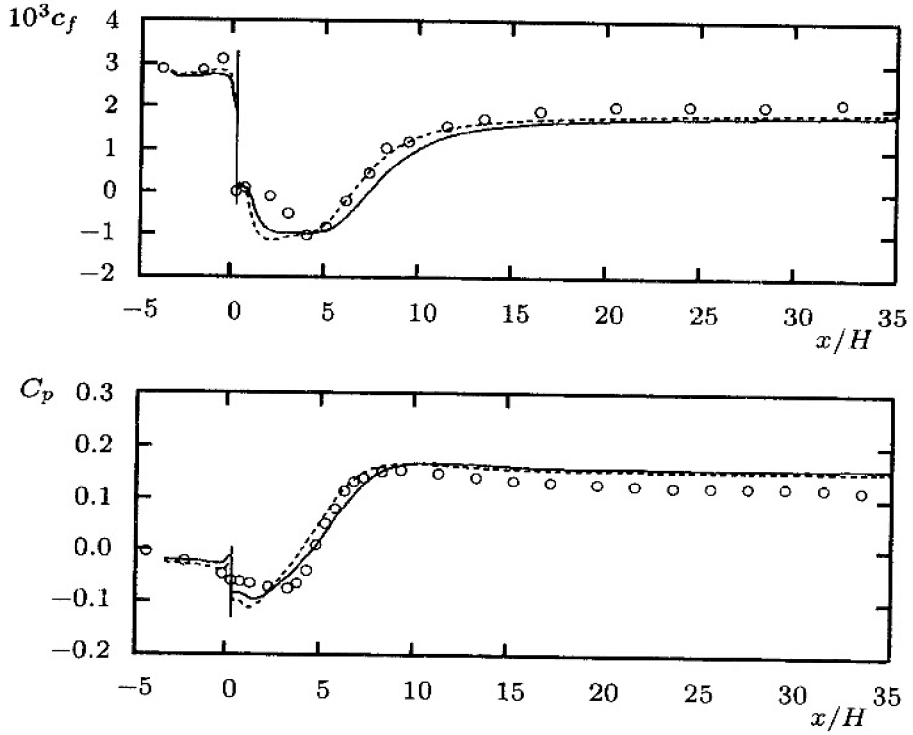

Figure 4.47: *Computed and measured skin friction and surface pressure for flow past a backward-facing step; Re_H = 37500; — Wilcox (2006) k-ω model; - - - Wilcox (1988a) k-ω model; ○ Driver-Seegmiller.*

Note that, despite the apparent simplicity of the geometry, backstep computations require a relatively large number of grid points. Menter (1992c), for example, reports a reattachment length of 6.40 step heights for the Wilcox (1988a) k-ω model that he computed with a 120x120 finite-difference grid. Using a 301x163 grid with Program **EDDY2C** yields a shorter reattachment length of 6.18 step heights, which is the value quoted in Table 4.12.

Focusing on a channel with a horizontal upper wall ($\alpha = 0°$), Figure 4.47 compares computed and measured skin friction and surface pressure coefficient, C_p, for the Wilcox (2006) k-ω model. The figure also includes values predicted by the Wilcox (1988a) version to help discern the effect of the stress limiter. With the exception of the reattachment point, all computed flow properties are nearly identical. As listed in Table 4.12, the reattachment length is 13% longer with the stress limiter. Menter (1992c) found a similar effect in his computations.

Flow past a backward-facing step is mildly dependent on Reynolds number. As summarized by Jovic and Driver (1995), reattachment length is somewhat shorter at low Reynolds numbers. To assess the effect of Reynolds number on k-ω model backward-facing step predictions, we now consider the case documented by Jovic and Driver (1994). Reynolds number based on step height for the

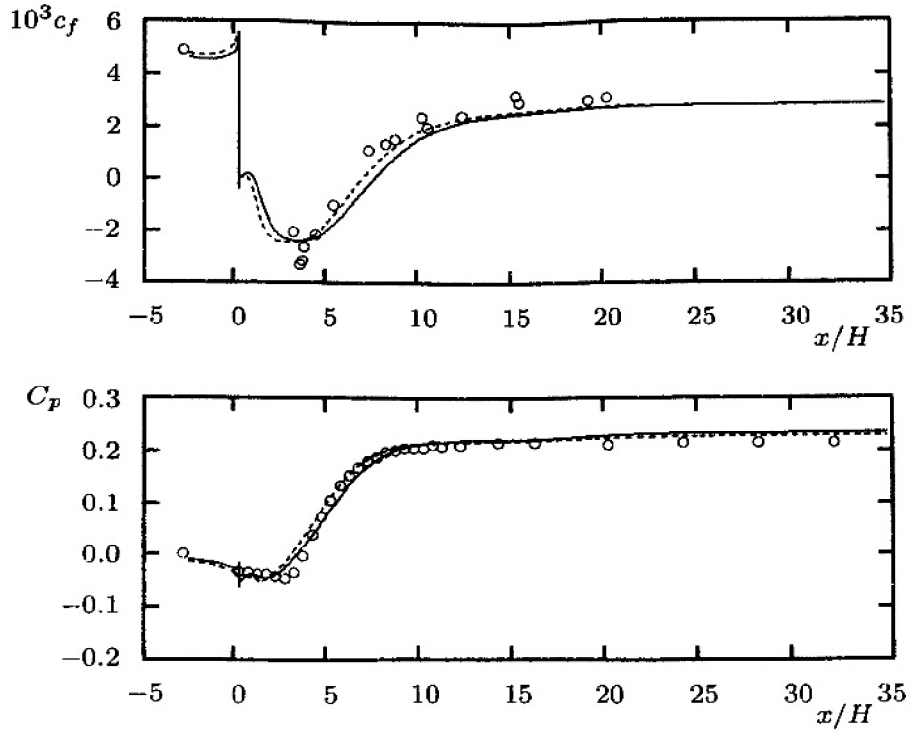

Figure 4.48: *Computed and measured skin friction and surface pressure for flow past a backward-facing step;* $Re_H = 5000$*;* —— *Wilcox (2006) k-ω model;* - - - *Wilcox (1988a) k-ω model;* ○ *Jovic-Driver.*

Jovic-Driver backward-facing step experiment is $Re_H = 5000$. By contrast, the Driver-Seegmiller case considered above has $Re_H = 37500$.

Figure 4.48 compares computed and measured skin friction and surface pressure coefficient. Both versions of the k-ω model predict c_f and C_p variations that fall within a few percent of measured values over most of the flowfield. Predicted reattachment length is $6.64H$ (a 7% *increase* over the $Re_H = 37500$ prediction) for the Wilcox (1988a) k-ω model and $7.28H$ (a 3% *increase*) for the Wilcox (2006) version. Since the measured length is $6.00H$ (a 4% *decrease*), neither model reflects the measured reduction of recirculation-region length.

All three of these examples show that the using the stress limiter with the k-ω model increases the size of the separated region. On the one hand, for Driver's separated axisymmetric flow (Figure 4.45), the stress limiter reduces differences between computed and measured flow properties. This is unsurprising since the separation bubble length is 40% smaller than measured without the limiter. On the other hand, the stress limiter increases differences between predicted and measured reattachment length for flow past backward-facing steps (Figures 4.47 and 4.48). This is also understandable because the model yields reattachment lengths that are very close to measured in the absence of the stress limiter.

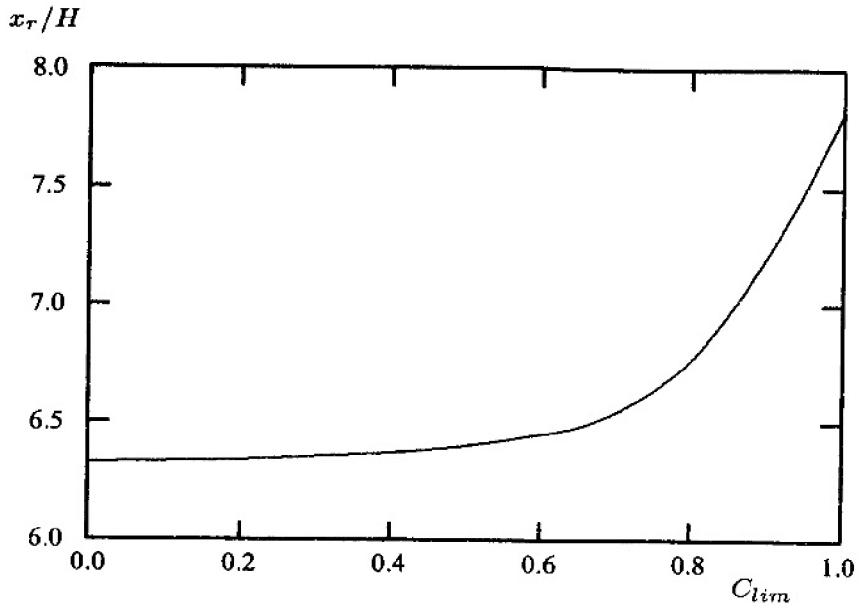

Figure 4.49: *Effect of the stress-limiter coefficient, C_{lim}, on computed reattachment length for a backward-facing step with $Re_H = 37500$.*

To gain some insight into the stress-limiter's nature, recall that we compute the eddy viscosity according to

$$\nu_T = \frac{k}{\tilde{\omega}}, \qquad \tilde{\omega} = \max\left\{\omega, \; C_{lim}\sqrt{\frac{2S_{ij}S_{ij}}{\beta^*}}\right\}, \qquad C_{lim} = \frac{7}{8} \tag{4.267}$$

In implementing the stress-limiter concept for his k-ω/k-ϵ model, Menter (1992c) selects $C_{lim} = 1$ and excludes it from the hybrid ω/ϵ equation. Durbin (1996) recommends $C_{lim} = 1.03$ for use with a pure k-ω model.

Figure 4.49 indicates how reattachment length, x_r, for the $Re_H = 37500$ backward-facing step varies with C_{lim}. As shown, reattachment length increases in a monotone fashion as C_{lim} increases. The asymptotic value for no stress limiter, i.e., for $C_{lim} = 0$, is $x_r = 6.33H$, which is 1% larger than the measured value.[16] Selecting $C_{lim} = 7/8$ yields a value of $x_r = 7.07H$, which is within 13% of the measured length.

We have only briefly touched on the impact of the stress limiter in this chapter, mainly to demonstrate that its effect on incompressible flows is relatively small for the k-ω model. However, as we will see in Chapter 5, it has a much more significant effect for compressible flows. Selecting $C_{lim} = 7/8$ proves to be optimum for shock-separated flows. We defer further discussion of the stress limiter to the next chapter (see Subsection 5.8.4).

[16]The value differs from the Wilcox (1988a) k-ω model's value of $x_r = 6.18H$ because of closure-coefficient differences and the inclusion of cross diffusion in the Wilcox (2006) model.

Han (1989) has applied the k-ϵ model with wall functions to flow past a simplified three-dimensional bluff body with a ground plane. The object considered is known as Ahmed's body [Ahmed et al. (1984)] and serves as a simplified automobile-like geometry. In his computations, Han considers a series of afterbody slant angles. Figure 4.50(a) illustrates the shape of Ahmed's body with a 30° slant angle afterbody. Figure 4.50(b) compares computed and measured surface pressure contours on the rear-end surface for a 12.5° slant angle.

As shown, computed pressure contours are similar on the slanted surface, but quite different on the vertical base. For slant angles up to 20°, the computed base pressures are significantly lower than measured. Consequently, the computed drag coefficient is about 30% higher than measured. Considering how poorly the k-ϵ model performs for boundary layers in adverse pressure gradient and for the two-dimensional backward-facing step, it is not surprising that the model would predict such a large difference from the measured drag in this extremely complicated three-dimensional, massively-separated flow.

This is a quintessential example of how important turbulence modeling is to Computational Fluid Dynamics. Recall that there are three key elements to CFD, viz., the numerical algorithm, the grid and the turbulence model. Han uses an efficient numerical procedure and demonstrates grid convergence of his solutions. Han's computational tools also include state-of-the-art grid-generation procedures. Han's research efforts on this problem are exemplary on both counts. However, using the k-ϵ model undermines the entire computation for the following reasons.

- Because the model fails to respond in a physically realistic manner to the adverse pressure gradient on the rear-end surface, the predicted skin friction is too high.
- This means the vorticity at the surface is too large, so that too much vorticity diffuses from the surface.
- This vorticity is swept into the main flow and too strong a vortex forms when the flow separates.
- This, of course, reduces the base pressure.

Thus, the k-ϵ model's inability to accurately respond to adverse pressure gradient distorts the entire flowfield.

These results debunk the notion that a turbulence model needn't do particularly well in predicting attached flows as long as it provides satisfactory results for a particular advanced application that might involve complicated flow phenomena like massive separation. Most likely, such a model has been fine tuned for precisely that advanced application and, just as likely, does not apply very far beyond the specifics of the application.

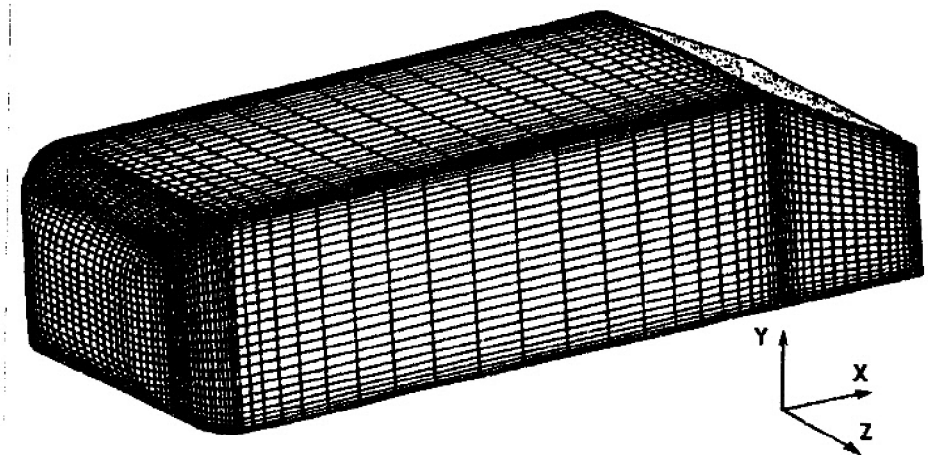

(a) Body geometry and surface grid

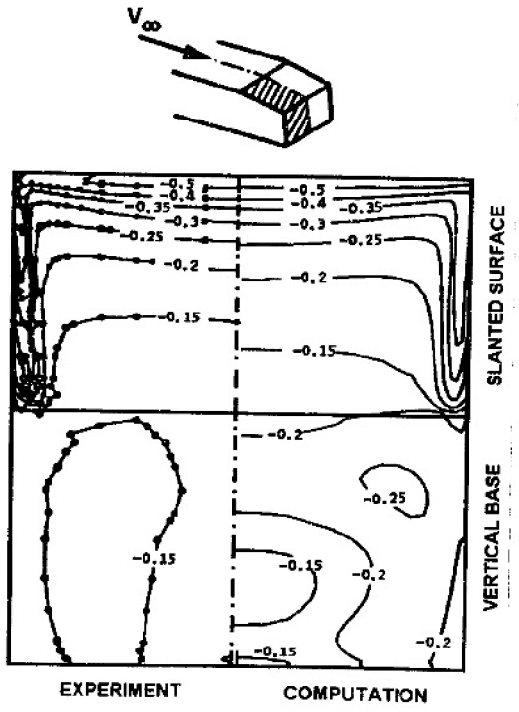

(b) Static-pressure contours

Figure 4.50: *Flow past Ahmed's body – high-Re k-ϵ computations. [From Han (1989) — Copyright © AIAA 1989 -- Used with permission.]*

Our final separated-flow application is particularly difficult to simulate, i.e., blood flow in an **arterial stenosis**. The word stenosis, common in bioengineering literature, means "narrowing of a passage." Thus, we consider the flow of blood through an artery that has a narrowing due to the deposit of plaque caused by excess cholesterol in the blood stream. One feature characteristic of blood flow is the low Reynolds number, Re, associated with the human body. For example, Re ranges from about 400 in the common carotid artery to 1500 in the ascending aorta. In the absence of stenosis, the flow is laminar since fully-developed pipe flow does not experience transition to turbulence until the Reynolds number based on diameter and average flow speed exceeds about 2300. However, the obstruction presented by stenosis leads to flow separation, which in turn causes transition to turbulence. Thus, the problem we address is a low-Reynolds-number flow that includes transition, separation and, ultimately, reattachment.

Figure 4.51 shows the geometry and streamlines of arterial stenosis computations performed by Ghalichi et al. (1998). The Ghalichi et al. computations have been done using the Wilcox (1994) low-Reynolds-number version of the k-ω model, which is very similar to the low-Re k-ω model described in Subsection 4.9.2. The flows indicated in Figures 4.51(a) and (b) correspond to a reduction in cross-sectional area of 50% and 75%, respectively. In both cases, a separation bubble is present downstream of the stenosis.

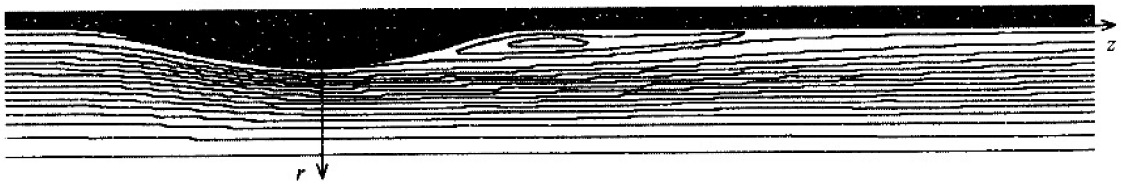

(a) 50% Stenosis

(b) 75% Stenosis

Figure 4.51: *Computed streamlines for blood flow through arteries with 50% and 75% stenosis; $Re = 1000$.*

Figure 4.52(a) compares computed and measured [Saad and Giddens (1983)] reattachment length, L_a, for the two different stenoses — the quantity D denotes the diameter of the unobstructed artery. The largest difference between theory

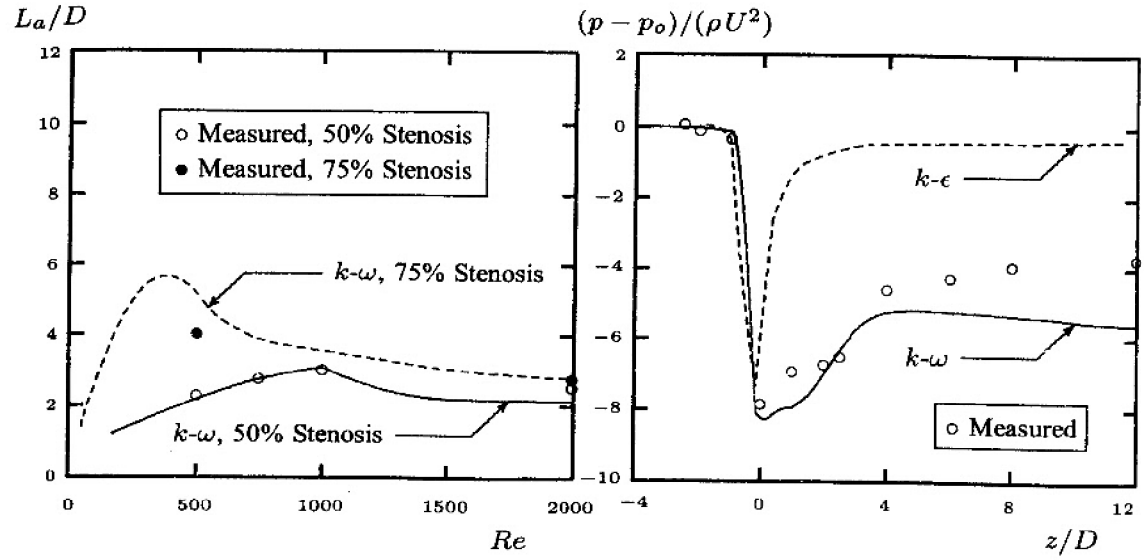

(a) Reattachment Length (b) Surface Pressure, 50% Stenosis

Figure 4.52: *Computed and measured flow properties for blood flow in arterial stenoses.*

and experiment is 10% of scale (for 75% stenosis and $Re = 500$). One of the most remarkable features of the computed flowfields is the critical Reynolds number at which transition to turbulence occurs. Consistent with measurements, the k-ω model predicts transition at about $Re = 1100$ for a 50% stenosis and at $Re = 400$ for a 75% stenosis.

Figure 4.52(b) compares computed and measured static pressure at the surface in a 50% stenosis for one of the Ghalichi et al. k-ω based computations, and for results obtained in an earlier study by Zijlema et al. (1995) using the Standard k-ϵ model. While differences between computed and measured pressures for the k-ω model are no more than 20% downstream of the stenosis, the Standard k-ϵ model predicts pressures that bear no resemblance to measured values.

4.11 Range of Applicability

Early one-equation models were based on the turbulence kinetic energy equation, and were **incomplete**. As discussed in Section 4.2, only a modest advantage is gained in using such models rather than an algebraic model. The primary difficulty is the need to specify the length scale for each new application. There is no natural way to accommodate an abrupt change from a wall-bounded flow to a free shear flow such as near an airfoil trailing edge or beyond the trunk lid of an automobile. The only real advantage of using this type of one-equation

model rather than a two-equation model is that numerical solution is simpler. One-equation models tend to be nearly as well behaved as algebraic models, while two-equation models, especially low-Re k-ϵ models, can be quirky.

By contrast, more recent one-equation models based on a postulated equation for eddy viscosity are **complete**. Two of the most commonly used models are those of Baldwin and Barth (1990) and of Spalart and Allmaras (1992).

The Baldwin-Barth model is very inaccurate for attached boundary layers, consistently predicting values of skin friction that are typically 25% below corresponding measurements. The model's predictions are even farther from measurements for separated flows, and its equation often presents serious numerical difficulties. Thus, it is clear that the Baldwin-Barth model is of little value for general turbulent-flow applications.

The Spalart-Allmaras model predicts skin friction for attached boundary layers that is as close to measurements as algebraic models. The model's predictions are far superior to those of algebraic models for separated flows, and the differential equation presents no serious numerical difficulties. Its only shortcoming for incompressible flows appears to be in predicting the asymptotic spreading rates for plane, round and radial jets. Also, as we will see in Chapter 5, the model is quite inaccurate for flows with shock-induced separation at Mach numbers in excess of 3. Nevertheless, results of experience to date indicate that the Spalart-Allmaras model is an excellent engineering tool for predicting properties of turbulent flows from incompressible through transonic speeds, especially for the aircraft applications it has been optimized for.

Two-equation models are **complete**. Until the 1990s, the k-ϵ model was the most widely used two-equation model. It has been applied to many flows with varying degrees of success. Unfortunately, it is even more inaccurate than the Baldwin-Barth one-equation model for flows with adverse pressure gradient, and that poses a serious limitation to its general utility. Because of its inability to respond to adverse pressure gradient (see Table 4.9), the model is inaccurate for separated flows. Its predictions for free shear flows are also a bit erratic. The k-ϵ model is extremely difficult to integrate through the viscous sublayer and requires viscous corrections simply to reproduce the law of the wall for an incompressible flat-plate boundary layer. No consensus has been achieved on the optimum form of the viscous corrections as evidenced by the number of researchers who have created low-Reynolds-number versions of the model (see Subsection 4.9.1). While the model can be fine tuned for a given application, it is not clear that this represents an improvement over algebraic models. The primary shortcoming of algebraic models is their need of fine tuning for each new application. Although saying the k-ϵ model always needs such fine tuning would be a bit exaggerated, it still remains that such tuning is too often needed. Given all of these well-documented flaws, it remains a mystery to this author why the model had such widespread use for nearly three decades.

The k-ω model, which has replaced the k-ϵ model as the most widely-used two-equation model, enjoys several advantages. Most importantly, the model is significantly more accurate for two-dimensional boundary layers with both adverse and favorable pressure gradient. Also, without any special viscous corrections, the model can be easily integrated through the viscous sublayer. The model accurately reproduces measured spreading rates for all five free shear flows (Table 4.4). Finally, the model matches measured properties of separated flows with no changes to the basic model and its closure coefficients. With viscous corrections included, the k-ω model accurately reproduces subtle features of turbulence kinetic energy behavior close to a solid boundary and even describes boundary-layer transition reasonably well.

Other two-equation models have been created, but they have had far less use than k-ω and k-ϵ models. Before such models can be taken seriously, they should be tested for simple incompressible boundary layers with adverse pressure gradient. How many interesting flows are there, after all, with constant pressure?

The use of perturbation methods to dissect model-predicted boundary-layer structure is perhaps the most important diagnostic tool presented in this chapter. Experience has shown that a turbulence model's ability to accurately predict effects of pressure gradient on boundary layers can be assessed by analyzing its defect-layer behavior. Specifically, models that faithfully replicate measured variation of Coles' wake-strength parameter, Π, with the equilibrium (pressure-gradient) parameter, β_T, (see Figure 4.19) also closely reproduce boundary-layer properties for non-equilibrium cases. Conversely, models that deviate significantly from the Π vs. β_T data predict large deviations from measurements for non-equilibrium boundary layers.

While two-equation models, especially the k-ω model, are more general than less complex models, they nevertheless fail in some applications. On the one hand, we will see in Chapter 5 that the k-ω model with a stress limiter is very reliable for describing boundary-layer separation induced by interaction with a shock wave. On the other hand, in Chapter 6, we will see that two-equation models are inaccurate for flows over curved surfaces. Also, two-equation models as presented in this chapter cannot predict secondary motions in noncircular duct flow. In both of these examples, the difficulty can be traced to the Boussinesq eddy-viscosity approximation.

Problems

4.1 We wish to create a new two-equation turbulence model. Our first variable is turbulence kinetic energy, k, while our second variable is the "eddy acceleration," a. Assuming a has dimensions (length)/(time)^2, use dimensional arguments to deduce plausible algebraic dependencies of eddy viscosity, ν_T, turbulence kinetic energy dissipation rate, ϵ, and turbulence length scale, ℓ, upon k and a.

4.2 Starting with Equations (4.4) and (4.45), define $\epsilon = \beta^* \omega k$ and derive an "exact" ω equation.

4.3 Verify that the exact equation for the dissipation, ϵ, is given by Equation (4.45). That is, derive the equation that follows from taking the following moment of the Navier-Stokes equation:

$$2\nu \overline{\frac{\partial u_i'}{\partial x_j} \frac{\partial}{\partial x_j} [\mathcal{N}(u_i)]} = 0$$

where $\mathcal{N}(u_i)$ is the Navier-Stokes operator defined in Equation (2.26).

4.4 Derive the exact equation for the **enstrophy**, ω^2, defined by

$$\omega^2 \equiv \frac{1}{2}\overline{\omega_i' \omega_i'} \qquad \text{where} \qquad \omega_i' = \epsilon_{ijk} \partial u_k' / \partial x_j$$

That is, ω_i' is the fluctuating vorticity. **HINT:** Beginning with the Navier-Stokes equation, derive the equation for the vorticity, multiply by ω_i', and time average. The vector identity $\mathbf{u} \cdot \nabla \mathbf{u} = \nabla \left(\frac{1}{2} \mathbf{u} \cdot \mathbf{u} \right) - \mathbf{u} \times (\nabla \times \mathbf{u})$ should prove useful in deriving the vorticity equation.

4.5 Beginning with the k-ϵ model, make the formal change of variables $\epsilon = C_\mu \omega k$ and derive the implied k-ω model. Express your final results in standard k-ω model notation and determine the implied values for α, β, β^*, σ, σ^* and σ_d in terms of C_μ, $C_{\epsilon 1}$, $C_{\epsilon 2}$, σ_k and σ_ϵ.

4.6 Beginning with the k-ω model and with $\sigma = \sigma^* = 1/2$ and $\sigma_d = 0$, make the formal change of variables $\epsilon = \beta^* \omega k$ and derive the implied k-ϵ model. Express your final results in standard k-ϵ model notation and determine the implied values for C_μ, $C_{\epsilon 1}$, $C_{\epsilon 2}$, σ_k and σ_ϵ in terms of α, β, β^*, σ and σ^*. Assume $f_\beta = 1$ and omit the stress limiter.

4.7 Simplify the k-ϵ, k-$k\ell$, k-$k\tau$ and k-τ models for the log layer. Determine the value of Kármán's constant, κ, implied by the closure coefficient values quoted in Equations (4.49), (4.57), (4.63) and (4.66). Make a table of your results and include the value 0.40 for the k-ω model. **NOTE:** For all models, assume a solution of the form $dU/dy = u_\tau/(\kappa y)$, $k = u_\tau^2/\sqrt{C_\mu}$ and $\nu_T = \kappa u_\tau y$. Also, $C_\mu = C_D$ for the k-$k\ell$ model.

4.8 Simplify the k-ϵ, k-$k\ell$, k-$k\tau$ and k-τ models for homogeneous, isotropic turbulence. Determine the asymptotic decay rate for k as a function of the closure coefficient values quoted in Equations (4.49), (4.57), (4.63) and (4.66). Make a table of your results and include the decay rate of $t^{-1.27}$ for the k-ω model. (**NOTE:** You can ignore the $(\ell/y)^6$ contribution to C_{L2} for the k-$k\ell$ model.)

4.9 Beginning with Equations (4.83), derive the self-similar form of the k-ω model equations for the mixing layer between a fast stream moving with velocity U_1 and a slow stream with velocity U_2. Omit the stress limiter so that $\nu_T = k/\omega$.

(a) Assuming a streamfunction of the form $\psi(x, y) = U_1 x F(\eta)$, transform the momentum equation, and verify that $\mathcal{V}$ is as given in Table 4.3.

(b) Transform the equations for k and ω.

(c) State the boundary conditions on $\mathcal{U}$ and K for $|\eta| \to \infty$ and for $\mathcal{V}(0)$. Assume $k \to 0$ as $|y| \to \infty$.

(d) Verify that if $\omega \neq 0$ in the freestream, the only boundary conditions consistent with the similarity solution are:

$$W(\eta) \to \begin{cases} \dfrac{1}{\beta_o}, & \eta \to +\infty \\ \dfrac{U_1/U_2}{\beta_o}, & \eta \to -\infty \end{cases}$$

4.10 Using Programs **WAKE**, **MIXER** and **JET** (see Appendix C), determine the spreading rates for the five basic free shear flows according to the k-ω model with and without the stress limiter. Compare your results in tabular form. **HINT:** The limiter is defined in the array *climit(j)*, whose value is set in Subroutine *CALCS*.

4.11 Derive Equation (4.145).

4.12 Demonstrate the integral constraint on $U_1(\eta)$ in the defect-layer solution.

4.13 Determine the shape factor to $O(u_\tau/U_e)$ according to the defect-layer solution. Express your answer in terms of an integral involving $U_1(\eta)$.

4.14 Using Program **DEFECT** (see Appendix C), determine the variation of Coles' wake strength, Π, as a function of the equilibrium parameter, β_T, for Kok's k-ω model. Modify the program, noting that Kok's model does not use the stress limiter and its closure coefficients are $\alpha = 5/9$, $\beta = 3/40$, $\beta^* = 9/100$, $\sigma = 1/2$, $\sigma^* = 2/3$ and $\sigma_{do} = 1/2$. Compare your results to the correlation $\Pi = 0.60 + 0.51\,\beta_T - 0.01\,\beta_T^2$. Do your computations for $-0.35 \leq \beta_T \leq 20$. **HINT:** You can accomplish all of the required modifications in Subroutine *START* by changing the values of the closure coefficients and noting that setting *clim* equal to zero turns the stress limiter off.

4.15 Using Program **DEFECT** (see Appendix C), determine the variation of Coles' wake strength, Π, as a function of the equilibrium parameter, β_T, for the Launder-Sharma k-ϵ model with a stress limiter included. Make a graph that includes values obtained with and without a stress limiter and the correlation $\Pi = 0.60 + 0.51\,\beta_T - 0.01\,\beta_T^2$. Do your computations for $-0.35 \leq \beta_T \leq 20$. **HINT:** The limiter is defined in the array *climit(j)*, whose value is set in Subroutine *CALCS*. Its algebraic form is identical for the k-ω and k-ϵ models, so all you have to do is activate it for the k-ϵ model. Set the constant *clim* equal to 1 to maximize the effect of the limiter.

4.16 Consider a flow with freestream velocity U_∞ past a wavy wall whose shape is

$$y = \frac{1}{2} k_s \sin\left(\frac{2\pi x}{N k_s}\right)$$

where k_s is the peak to valley amplitude and Nk_s is wavelength. The linearized incompressible solution is $U = U_\infty + u'$, $V = v'$ where

$$u' = \frac{\pi U}{N} \exp\left(-\frac{2\pi y}{N k_s}\right) \sin\left(\frac{2\pi y}{N k_s}\right), \qquad v' = \frac{\pi U}{N} \exp\left(-\frac{2\pi y}{N k_s}\right) \cos\left(\frac{2\pi y}{N k_s}\right)$$

Making an analogy between this linearized solution and the fluctuating velocity field in a turbulent flow, compute the specific dissipation rate, $\omega = \epsilon/(\beta^* k)$. Ignore contributions from the other fluctuating velocity component, w'.

4.17 For the k-ω model, very close to the surface and deep within the viscous sublayer, dissipation balances molecular diffusion in the ω equation. Assuming a solution of the form $\omega = \omega_w/(1 + Ay)^2$, solve this equation for $\omega = \omega_w$ at $y = 0$. Determine the limiting form of the solution as $\omega_w \to \infty$.

4.18 Using Program **SUBLAY** (see Appendix C), determine the variation of the constant C in the law of the wall for the k-ω model with the surface value of ω. Do your computations with (*nvisc* = 0) and without (*nvisc* = 1) viscous modifications. Let ω_w^+ assume the values 1, 3, 10, 30, 100, 300, 1000 and ∞. Be sure to use the appropriate value for input parameter *iruff*. Present your results in tabular form.

4.19 This problem studies the effect of viscous-modification closure coefficients for the k-ω model using Program **SUBLAY** (see Appendix C).

(a) Modify Subroutine *START* to permit inputting the values of R_k and R_ω (program variables *rk* and *rw*). Determine the value of R_ω that yields a smooth-wall constant in the law of the wall, C, of 5.0 for R_k = 4, 6, 8, 10 and 20.

(b) Now make provision for inputting the value of R_β (program variable *rb*). For $R_k = 6$, determine the value of R_ω that yields $C = 5.0$ when R_β = 2, 4, 8, and 12. Also, determine the maximum value of k^+ for each case.

4.20 Consider incompressible Couette flow with constant pressure, i.e., flow between two parallel plates separated by a distance H, the lower at rest and the upper moving with constant velocity U_w.

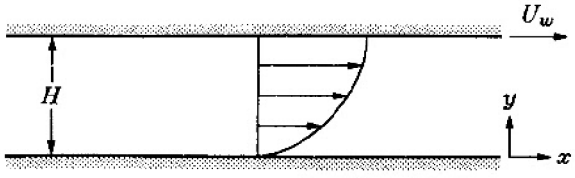

Problems 4.20 and 4.21

(a) Assuming the plates are infinite in extent, simplify the conservation of mass and momentum equations and verify that

$$(\nu + \nu_T)\frac{dU}{dy} = u_\tau^2$$

(b) Now ignore molecular viscosity. What boundary condition on U is appropriate at the lower plate?

(c) Introducing the mixing length given by

$$\ell_{mix} = \kappa y(1 - y/H)$$

solve for the velocity across the channel. **HINT:** Using partial fractions:

$$\frac{1}{y(1-y/H)} = \frac{1}{y} + \frac{1}{(H-y)}$$

Don't forget to use the boundary condition stated in Part (b).

(d) Develop a relation between friction velocity, u_τ, and the average velocity,

$$U_{avg} = \frac{1}{H}\int_0^H U(y)\, dy$$

(e) Using the k-ω model, simplify the equations for k and ω with the same assumptions made in Parts (a) and (b).

(f) Deduce the equations for k and ω that follow from changing independent variables from y to U so that

$$\nu_T \frac{d}{dy} = u_\tau^2 \frac{d}{dU}$$

(g) Assuming $k = u_\tau^2/\sqrt{\beta^*}$, simplify the equation for ω. **NOTE:** You might want to use the fact that $\sigma\sqrt{\beta^*}\kappa^2 = \beta_o - \alpha\beta^*$.

4.21 For incompressible, laminar Couette flow, we know that the velocity is given by

$$U = U_w \frac{y}{H}$$

where U_w is the velocity of the moving wall, y is distance form the stationary wall, and H is the distance between the walls.

(a) Noting that the stress limiter is inactive for laminar flow, determine the maximum Reynolds number,

$$Re_{H_c} = U_w H_c/\nu$$

at which the flow remains laminar according to the high-Reynolds-number version of the k-ω model. To arrive at your answer, you may assume that

$$\omega = \begin{cases} \dfrac{6\nu}{\beta_o y^2}, & 0 \le y \le H/2 \\ \dfrac{6\nu}{\beta_o (H-y)^2}, & H/2 \le y \le H \end{cases}$$

(b) Above what Reynolds number is ω amplified?

4.22 Using Program **PIPE** (see Appendix C), compute the skin friction for channel flow according to the Baldwin-Barth and Spalart-Allmaras models. Compare your results with the Halleen-Johnston correlation [Equation (3.139)] for $10^3 \leq Re_H \leq 10^5$. Also, compare the computed velocity profiles for $Re_H = 13750$ with the Mansour et al. DNS data, which are as follows.

$y/(H/2)$	U/U_m	$y/(H/2)$	U/U_m	$y/(H/2)$	U/U_m
0.000	0.000	0.404	0.887	0.805	0.984
0.103	0.717	0.500	0.917	0.902	0.995
0.207	0.800	0.602	0.945	1.000	1.000
0.305	0.849	0.710	0.968		

4.23 Using Program **PIPE** (see Appendix C), compute the skin friction for pipe flow according to the Baldwin-Barth and Spalart-Allmaras models. Compare your results with the Prandtl correlation [Equation (3.140)] for $10^3 \leq Re_D \leq 10^6$. Also, compare the computed velocity profiles for $Re_D = 40000$ with Laufer's data, which are as follows.

$y/(D/2)$	U/U_m	$y/(D/2)$	U/U_m	$y/(D/2)$	U/U_m
0.010	0.333	0.390	0.868	0.800	0.975
0.095	0.696	0.490	0.902	0.900	0.990
0.210	0.789	0.590	0.931	1.000	1.000
0.280	0.833	0.690	0.961		

4.24 The object of this problem is to compare predictions of one- and two-equation models with measured properties of a turbulent boundary layer with adverse ∇p. The experiment to be simulated was conducted by Schubauer and Spangenberg [see Coles and Hirst (1969) – Flow 4800]. Use Program **EDDYBL**, its menu-driven setup utility, Program **EDDYBL_DATA**, and the input data provided on the companion CD (see Appendix C). Do 3 computations using the Baldwin-Barth model, the k-ω model with viscous modifications and one of the k-ϵ models and compare computed skin friction with the following measured values.

s (ft)	c_f	s (ft)	c_f	s (ft)	c_f
2.000	$3.39 \cdot 10^{-3}$	10.333	$2.06 \cdot 10^{-3}$	17.000	$0.94 \cdot 10^{-3}$
4.500	$2.94 \cdot 10^{-3}$	13.667	$1.61 \cdot 10^{-3}$	17.833	$0.49 \cdot 10^{-3}$
7.000	$2.55 \cdot 10^{-3}$	15.333	$1.39 \cdot 10^{-3}$		

4.25 The object of this problem is to compare predictions of one- and two-equation models with measured properties of a turbulent boundary layer with adverse ∇p. The experiment to be simulated was conducted by Ludwieg and Tillman [see Coles and Hirst (1969) – Flow 1200]. Use Program **EDDYBL**, its menu-driven setup utility, Program **EDDYBL_DATA**, and the input data provided on the companion CD (see Appendix C). Do 3 computations using the k-ω, Baldwin-Barth and Jones-Launder models and compare computed skin friction with the following measured values.

s (m)	c_f	s (m)	c_f
0.782	$2.92 \cdot 10^{-3}$	2.282	$1.94 \cdot 10^{-3}$
1.282	$2.49 \cdot 10^{-3}$	2.782	$1.55 \cdot 10^{-3}$
1.782	$2.05 \cdot 10^{-3}$		

4.26 The object of this problem is to compare predictions of one- and two-equation models with measured properties of a turbulent boundary layer with adverse ∇p. The experiment to be simulated was conducted by Schubauer and Spangenberg [see Coles and Hirst (1969) – Flow 4400]. Use Program **EDDYBL**, its menu-driven setup utility, Program **EDDYBL_DATA**, and the input data provided on the companion CD (see Appendix C). Do 3 computations using the k-ω model, one of the k-ϵ models and the Spalart-Allmaras model and compare computed skin friction with the following measured values.

s (ft)	c_f	s (ft)	c_f	s (ft)	c_f
1.167	$3.40{\cdot}10^{-3}$	3.667	$2.86{\cdot}10^{-3}$	6.167	$1.33{\cdot}10^{-3}$
2.000	$3.17{\cdot}10^{-3}$	4.500	$2.38{\cdot}10^{-3}$		
2.833	$3.10{\cdot}10^{-3}$	5.333	$1.97{\cdot}10^{-3}$		

4.27 The object of this problem is to compare predictions of one- and two-equation models with measured properties of a turbulent boundary layer with adverse ∇p. The experiment to be simulated was conducted by Stratford [see Coles and Hirst (1969) – Flow 5300]. Use Program **EDDYBL**, its menu-driven setup utility, Program **EDDYBL_DATA**, and the input data provided on the companion CD (see Appendix C). Do 3 computations using the k-ω model, one of the k-ϵ models and the Spalart-Allmaras model and compare computed skin friction with the following measured values.

s (ft)	c_f	s (ft)	c_f
2.907	$3.68{\cdot}10^{-3}$	3.531	$0.55{\cdot}10^{-3}$
2.999	$2.07{\cdot}10^{-3}$	4.103	$0.53{\cdot}10^{-3}$
3.038	$0.99{\cdot}10^{-3}$		

4.28 The object of this problem is to predict the separation point for flow past a circular cylinder with the boundary-layer equations, using the measured pressure distribution. The experiment to be simulated was conducted by Patel (1968). Use Program **EDDYBL** and its menu-driven setup utility, Program **EDDYBL_DATA**, to do the computations (see Appendix C).

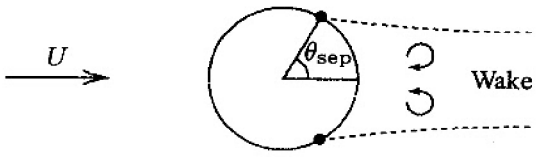

Problem 4.28

(a) Set freestream conditions to $p_{t_\infty} = 2147.7$ lb/ft^2, $T_{t_\infty} = 529.6°$ R, $M_\infty = 0.144$ (PT1, TT1, XMA); use an initial stepsize, initial arclength and final arclength given by $\Delta s = 0.001$ ft, $s_i = 0.262$ ft and $s_f = 0.785$ ft (DS, SI, SSTOP); set the initial boundary-layer properties so that $c_f = 0.00600$, $\delta = 0.006$ ft, $H = 1.40$, $Re_\theta = 929$, (CF, DELTA, H, RETHET); set the maximum number of steps to 1000 (IEND1); and set up for $N = 47$ points to define the pressure (NUMBER). Use the following data to define the pressure distribution. The initial and final pressure gradients are zero. Use zero heat flux at the cylinder surface. Finally, set the curvature, $\mathcal{R}^{-1}$, equal to 4 ft^{-1}.

s (ft)	p_e (lb/ft^2)	s (ft)	p_e (lb/ft^2)	s (ft)	p_e (lb/ft^2)
0.0000	$2.147540 \cdot 10^3$	0.1500	$2.116199 \cdot 10^3$	0.3500	$2.055516 \cdot 10^3$
0.0025	$2.147528 \cdot 10^3$	0.1625	$2.112205 \cdot 10^3$	0.3625	$2.056591 \cdot 10^3$
0.0050	$2.147491 \cdot 10^3$	0.1750	$2.107903 \cdot 10^3$	0.3750	$2.058435 \cdot 10^3$
0.0075	$2.147429 \cdot 10^3$	0.1875	$2.103448 \cdot 10^3$	0.3875	$2.061661 \cdot 10^3$
0.0100	$2.147343 \cdot 10^3$	0.2000	$2.098378 \cdot 10^3$	0.4000	$2.066423 \cdot 10^3$
0.0125	$2.147233 \cdot 10^3$	0.2125	$2.093155 \cdot 10^3$	0.4125	$2.071954 \cdot 10^3$
0.0250	$2.146314 \cdot 10^3$	0.2250	$2.087317 \cdot 10^3$	0.4250	$2.079021 \cdot 10^3$
0.0375	$2.144796 \cdot 10^3$	0.2375	$2.081325 \cdot 10^3$	0.4375	$2.085473 \cdot 10^3$
0.0500	$2.142688 \cdot 10^3$	0.2500	$2.075334 \cdot 10^3$	0.4500	$2.089161 \cdot 10^3$
0.0625	$2.140018 \cdot 10^3$	0.2625	$2.069189 \cdot 10^3$	0.4625	$2.091004 \cdot 10^3$
0.0750	$2.136807 \cdot 10^3$	0.2750	$2.064580 \cdot 10^3$	0.4750	$2.092080 \cdot 10^3$
0.0875	$2.134021 \cdot 10^3$	0.2875	$2.060893 \cdot 10^3$	0.4875	$2.092230 \cdot 10^3$
0.1000	$2.130641 \cdot 10^3$	0.3000	$2.058588 \cdot 10^3$	0.5000	$2.092230 \cdot 10^3$
0.1125	$2.127261 \cdot 10^3$	0.3125	$2.056898 \cdot 10^3$	0.6500	$2.092230 \cdot 10^3$
0.1250	$2.123881 \cdot 10^3$	0.3250	$2.055823 \cdot 10^3$	0.7850	$2.092230 \cdot 10^3$
0.1375	$2.120194 \cdot 10^3$	0.3375	$2.055362 \cdot 10^3$		

(b) Do three computations using the low-Reynolds-number k-ω model, the Launder-Sharma k-ϵ model and the Spalart-Allmaras model. The radius of the cylinder is $R = 0.25$ ft, so that separation arclength, s_{sep}, is related to this angle by $\theta_{sep} = \pi - s_{sep}/R$.

4.29 Compute Driver and Seegmiller's $Re_H = 37500$ backstep flow using the Baldwin-Lomax algebraic model. Use Program **EDDY2C**, its menu-driven setup utility, Program **EDDY2C_DATA**, and the input data provided on the companion CD (see Appendix C).

(a) You must first run Program **EDDYBL** to establish flow properties at the upstream boundary. Modify the supplied input-data file *eddybl.dat*, using trial and error to adjust the "Maximum Arclength" (SSTOP) so that the Reynolds number based on momentum thickness is 5000.

(b) Modify the supplied input-data file *eddy2c.dat* for Program **EDDY2C** to run the computation 1000 timesteps (NEND).

(c) Make graphs of the "residual" and the value of reattachment length, x_r/H, as functions of timestep number.

(d) Discuss the value of x_r/H predicted by the Baldwin-Lomax model relative to the measured value and the values predicted by the k-ω and k-ϵ models.

NOTE: This computation will take about 30 minutes of CPU time on a 3-GHz Pentium-D microcomputer.

4.30 Compute Jovic's $Re_H = 5000$ backstep flow using the Baldwin-Lomax algebraic model. Use Program **EDDY2C**, its menu-driven setup utility, Program **EDDY2C_DATA**, and the input data provided on the companion CD (see Appendix C).

(a) You must first run Program **EDDYBL** to establish flow properties at the upstream boundary. Modify the supplied input-data file *eddybl.dat*, using trial and error to adjust the "Maximum Arclength" (SSTOP) so that the Reynolds number based on momentum thickness is 609.

(b) Modify the supplied input-data file *eddy2c.dat* for Program **EDDY2C** to run the computation 10000 timesteps (NEND).

(c) Make graphs of the "residual" and the value of reattachment length, x_r/H, as functions of timestep number.

(d) Discuss the value of x_r/H predicted by the Baldwin-Lomax model relative to the measured value and the value predicted by the k-ω model.

NOTE: This computation will take about 3 hours of CPU time on a 3-GHz Pentium-D microcomputer.

Chapter 5

Effects of Compressibility

For flows in which compressibility effects are important, we must introduce an equation for conservation of energy and an equation of state. Just as Reynolds averaging gives rise to the Reynolds-stress tensor, so we expect that similar averaging will lead to a turbulent heat-flux vector. We should also expect that new compressibility-related correlations will appear throughout the equations of motion. These are important issues that must be addressed in constructing a turbulence model suitable for application to compressible flows, which can be expected to apply to constant-property (low-speed) flows with heat transfer.

We begin with a discussion of observations pertaining to compressible turbulence. Then, we introduce the Favre mass-averaging procedure and derive the mass-averaged equations of motion. Next, we demonstrate an elegant turbulence-modeling development for the compressible mixing layer. We follow this analysis with an application of perturbation methods to the compressible log layer. We then apply several models to attached compressible boundary layers, including effects of pressure gradient, surface cooling and surface roughness. The chapter concludes with application of various models to shock-separated flows.

5.1 Physical Considerations

By definition, a compressible flow is one in which significant density changes occur, even when pressure changes are small. It includes low-speed flows with large heat-transfer rates. Models for high-speed flows seem to fit the limited data quite well (perhaps with the exception of combusting flows). Generally speaking, compressibility has a relatively small effect on turbulent eddies in wall-bounded flows. This appears to be true for Mach numbers up to about 5 (and perhaps as high as 8), provided the flow doesn't experience large pressure changes over a

short distance such as we might have across a shock wave. At subsonic speeds, compressibility effects on eddies are usually unimportant for boundary layers provided $T_w/T_e < 6$. Based on these observations, Morkovin (1962) hypothesized that the effect of density fluctuations on the turbulence is small provided they remain small relative to the mean density. So, Gatski and Sommer (1998) have confirmed the hypothesis for a Mach 2.55 flat-plate boundary layer, showing that DNS turbulence statistics match those of an incompressible boundary layer. This is a major simplification for the turbulence modeler because it means that, in practice, we need only account for the nonuniform mean density in computing compressible, shock-free, non-hypersonic turbulent flows.

There are limitations to the usefulness of **Morkovin's hypothesis** even at non-hypersonic Mach numbers. For example, it is not useful in flows with significant heat transfer or in flows with combustion because $\rho'/\bar{\rho}$ is typically not small. Also, density fluctuations generally are much larger in free shear flows, and models based on Morkovin's hypothesis fail to predict the measured reduction in spreading rate with increasing freestream Mach number for the compressible mixing layer [e.g., Papamoschou and Roshko (1988)]. As we will see in Section 5.5, the level of $\rho'/\bar{\rho}$ for a boundary layer at Mach 5 is comparable to the level found in a mixing layer at Mach 1. However, in addition, there seem to be qualitative changes in mixing-layer structure as Mach number increases.

On dimensional grounds, we expect the velocity in a turbulent boundary layer to depend, at a minimum, upon basic fluid properties such as Prandtl number, Pr_L, and specific-heat ratio, γ. We also expect it to depend upon the following three dimensionless groupings:

$$\underbrace{y^+ = \frac{u_\tau y}{\nu_w}}_{\substack{Sublayer\ scaled \\ distance}} \quad , \quad \underbrace{q_w^+ = \frac{q_w}{\rho_w c_p u_\tau T_w}}_{\substack{Dimensionless \\ heat\ transfer}}, \quad \underbrace{M_\tau = \frac{u_\tau}{a_w}}_{\substack{Turbulence \\ Mach\ number}} \tag{5.1}$$

where subscript w denotes surface value, q is heat flux, c_p is specific-heat coefficient at constant pressure, T is temperature and a is sound speed. Based on the mixing-length model and assuming that, in analogy to the incompressible case,

$$\frac{\partial U}{\partial y} \approx \frac{\sqrt{\tau_w/\rho}}{\kappa y} \tag{5.2}$$

where ρ now depends upon y. Van Driest (1951) argued[1] that by rescaling the velocity according to

$$\frac{u^*}{u_\tau} = \frac{1}{A}\left[\sin^{-1}\left(\frac{2A^2(U/u_\tau) - B}{\sqrt{B^2 + 4A^2}}\right) + \sin^{-1}\left(\frac{B}{\sqrt{B^2 + 4A^2}}\right)\right] \tag{5.3}$$

[1] The Van Driest argument also requires assuming the turbulent Prandtl number [defined in Equation (5.54)] is constant.

where A and B are functions of q_w^+ and M_τ [see Equation (5.101) below], the velocity is

$$\frac{u^*}{u_\tau} = \frac{1}{\kappa}\ell n y^+ + C \tag{5.4}$$

Equation (5.4) is the **compressible law of the wall**. Correlation of measurements shows that κ and C are nearly the same as for incompressible boundary layers [Bradshaw and Huang (1995)]. In principle, however, C is a function of M_τ and q_w^+ since it includes density and viscosity effects in the viscous wall region.

Section 5.6 provides additional detail that explains why we should expect the velocity to scale according to Equation (5.3) in a compressible boundary layer. In general, the compressible law of the wall correlates experimental data for adiabatic walls reasonably well (Section 5.7). It is less accurate for non-adiabatic walls, especially for very cold walls (probably because C varies with q_w^+, although data are scarce). An analogous variation of temperature with these parameters can be deduced that is satisfactory for low-speed flows. However, its use is limited because of sensitivity to pressure gradient, even in low-speed flows. Bradshaw and Huang (1995) provide additional detail.

As a final observation, note that the difficulty in predicting properties of the compressible mixing layer is reminiscent of our experience with free shear flows in Chapters 3 and 4. That is, we find again that the seemingly simple free shear flow case is more difficult to model than the wall-bounded case.

5.2 Favre Averaging

In addition to velocity and pressure fluctuations, we must also account for density and temperature fluctuations when the medium is a compressible fluid. If we use the standard time-averaging procedure introduced in Chapter 2, the mean conservation equations contain additional terms that have no analogs in the laminar equations. To illustrate this, consider conservation of mass. We write the instantaneous density, ρ, as the sum of mean, $\bar{\rho}$, and fluctuating, ρ', parts, i.e.,

$$\rho = \bar{\rho} + \rho' \tag{5.5}$$

Expressing the instantaneous velocity in the usual way [Equation (2.4)], substituting into the continuity equation yields

$$\frac{\partial}{\partial t}(\bar{\rho} + \rho') + \frac{\partial}{\partial x_i}(\bar{\rho}U_i + \rho' U_i + \bar{\rho}u_i' + \rho' u_i') = 0 \tag{5.6}$$

After time averaging Equation (5.6), we arrive at the Reynolds-averaged continuity equation for compressible flow, viz.,

$$\frac{\partial \bar{\rho}}{\partial t} + \frac{\partial}{\partial x_i}\left(\bar{\rho}U_i + \overline{\rho' u_i'}\right) = 0 \tag{5.7}$$

Some authors refer to this as the **primitive-variable form** of the continuity equation. Note that in order to achieve closure, an approximation for the correlation between ρ' and u_i' is needed. The problem is even more complicated for the momentum equation where the Reynolds-stress tensor originates from time averaging the product $\rho u_i u_j$ that appears in the convective acceleration. Clearly, a triple correlation involving ρ', u_i', and u_j' appears, thus increasing the complexity of establishing suitable closure approximations.

The problem of establishing the appropriate form of the time-averaged equations can be simplified dramatically by using the density-weighted averaging procedure suggested by Favre (1965). That is, we introduce the **mass-averaged** velocity, $\tilde{u}_i$, defined by

$$\tilde{u}_i = \frac{1}{\bar{\rho}} \lim_{T\to\infty} \frac{1}{T} \int_t^{t+T} \rho(\mathbf{x},\tau) u_i(\mathbf{x},\tau)\, d\tau \tag{5.8}$$

where $\bar{\rho}$ is the conventional Reynolds-averaged density. Thus, in terms of conventional Reynolds averaging, we can say that

$$\bar{\rho}\tilde{u}_i = \overline{\rho u_i} \tag{5.9}$$

where an overbar denotes conventional Reynolds average. The value of this averaging process, known as **Favre averaging**, becomes obvious when we expand the right-hand side of Equation (5.9). Performing the indicated Reynolds-averaging process, there follows

$$\bar{\rho}\tilde{u}_i = \bar{\rho}U_i + \overline{\rho' u_i'} \tag{5.10}$$

Inspection of Equation (5.7) shows that conservation of mass can be rewritten as

$$\frac{\partial \bar{\rho}}{\partial t} + \frac{\partial}{\partial x_i}(\bar{\rho}\tilde{u}_i) = 0 \tag{5.11}$$

This is a remarkable simplification as Equation (5.11) looks just like the laminar mass-conservation equation. What we have done is treat the momentum per unit volume, ρu_i, as the dependent variable rather than the velocity. This is a sensible thing to do from a physical point of view, especially when we focus upon the momentum equation in the next section. That is, the rate of change of momentum per unit volume, not velocity, is equal to the sum of the imposed forces per unit volume in a flow.

When we use Favre averaging, it is customary to decompose the instantaneous velocity into the mass-averaged part, $\tilde{u}_i$, and a fluctuating part, u_i'', wherefore

$$u_i = \tilde{u}_i + u_i'' \tag{5.12}$$

Now, to form the Favre average, we simply multiply through by ρ and do a time average in the manner established in Chapter 2. Hence, from Equation (5.12) we find

$$\overline{\rho u_i} = \bar{\rho}\tilde{u}_i + \overline{\rho u_i''} \tag{5.13}$$

But, from the definition of the Favre average given in Equation (5.9), we see immediately that, as expected, the Favre average of the fluctuating velocity, u_i'', vanishes, i.e.,

$$\overline{\rho u_i''} = 0 \tag{5.14}$$

By contrast, the conventional Reynolds average of u_i'' is not zero. To see this, note that

$$u_i'' = u_i - \tilde{u}_i \tag{5.15}$$

Hence, using Equation (5.10) to eliminate $\tilde{u}_i$,

$$u_i'' = u_i - U_i - \frac{\overline{\rho' u_i'}}{\bar{\rho}} \tag{5.16}$$

Therefore, performing the conventional Reynolds average, we find

$$\overline{u_i''} = -\frac{\overline{\rho' u_i'}}{\bar{\rho}} \neq 0 \tag{5.17}$$

As a final comment, do not lose sight of the fact that while Favre averaging eliminates density fluctuations from the averaged equations, it does not remove the effect the density fluctuations have on the turbulence. Consequently, **Favre averaging is a mathematical simplification, not a physical one.**

5.3 Favre-Averaged Equations

For motion in a compressible medium, we must solve the equations governing conservation of mass, momentum and energy. The instantaneous equations are as follows:

$$\frac{\partial \rho}{\partial t} + \frac{\partial}{\partial x_i}(\rho u_i) = 0 \tag{5.18}$$

$$\frac{\partial}{\partial t}(\rho u_i) + \frac{\partial}{\partial x_j}(\rho u_j u_i) = -\frac{\partial p}{\partial x_i} + \frac{\partial t_{ji}}{\partial x_j} \tag{5.19}$$

$$\frac{\partial}{\partial t}\left[\rho\left(e + \frac{1}{2}u_i u_i\right)\right] + \frac{\partial}{\partial x_j}\left[\rho u_j\left(h + \frac{1}{2}u_i u_i\right)\right] = \frac{\partial}{\partial x_j}(u_i t_{ij}) - \frac{\partial q_j}{\partial x_j} \tag{5.20}$$

where e is specific internal energy and $h = e + p/\rho$ is specific enthalpy. For compressible flow, the viscous stress tensor, t_{ij}, involves the second viscosity, ζ, as well as the conventional molecular viscosity, μ. Although it is not necessary for our immediate purposes, we eventually must specify an equation of state. For gases, we use the perfect-gas law so that pressure, density and temperature are related by

$$p = \rho R T \tag{5.21}$$

where R is the perfect-gas constant. The constitutive relation between stress and strain rate for a Newtonian fluid is

$$t_{ij} = 2\mu s_{ij} + \zeta \frac{\partial u_k}{\partial x_k} \delta_{ij} \tag{5.22}$$

where s_{ij} is the instantaneous strain-rate tensor [Equation (2.19)] and δ_{ij} is the Kronecker delta. The heat-flux vector, q_j, is usually obtained from Fourier's law so that

$$q_j = -\kappa \frac{\partial T}{\partial x_j} \tag{5.23}$$

where κ is thermal conductivity. We can simplify our analysis somewhat by introducing two commonly used assumptions. First, we relate second viscosity to μ by assuming

$$\zeta = -\frac{2}{3}\mu \tag{5.24}$$

This assumption is correct for a monatomic gas, and is generally used for all gases in standard CFD applications. Assuming Equation (5.24) holds in general guarantees $t_{ii} = 0$ so that viscous stresses do not contribute to the pressure, even when $s_{ii} = \partial u_i / \partial x_i \neq 0$. This is tidy, even if not necessarily true. Second, we assume the fluid is calorically perfect so that its specific-heat coefficients are constant, and thus the specific internal energy, e, and specific enthalpy, h, are

$$e = c_v T \qquad \text{and} \qquad h = c_p T \tag{5.25}$$

where c_v and c_p are the specific-heat coefficients for constant volume and pressure processes, respectively. Then, we can say that

$$q_j = -\kappa \frac{\partial T}{\partial x_j} = -\frac{\mu}{Pr_L} \frac{\partial h}{\partial x_j} \tag{5.26}$$

where Pr_L is the **laminar Prandtl number** defined by

$$Pr_L = \frac{c_p \mu}{\kappa} \tag{5.27}$$

In order to mass average the conservation equations, we now decompose the various flow properties as follows.

$$\left.\begin{aligned} u_i &= \tilde{u}_i + u_i'' \\ \rho &= \bar{\rho} + \rho' \\ p &= P + p' \\ h &= \tilde{h} + h'' \\ e &= \tilde{e} + e'' \\ T &= \tilde{T} + T'' \\ q_j &= q_{L_j} + q_j' \end{aligned}\right\} \tag{5.28}$$

Note that we decompose p, ρ and q_j in terms of conventional mean and fluctuating parts. Substituting Equations (5.28) into Equations (5.18) – (5.21) and performing the mass-averaging operations, we arrive at what are generally referred to as the **Favre (mass) averaged mean conservation equations.**

$$\frac{\partial \bar{\rho}}{\partial t} + \frac{\partial}{\partial x_i}(\bar{\rho}\tilde{u}_i) = 0 \tag{5.29}$$

$$\frac{\partial}{\partial t}(\bar{\rho}\tilde{u}_i) + \frac{\partial}{\partial x_j}(\bar{\rho}\tilde{u}_j\tilde{u}_i) = -\frac{\partial P}{\partial x_i} + \frac{\partial}{\partial x_j}\left[\bar{t}_{ji} - \overline{\rho u_j'' u_i''}\right] \tag{5.30}$$

$$\begin{aligned}\frac{\partial}{\partial t}\left[\bar{\rho}\left(\tilde{e} + \frac{\tilde{u}_i\tilde{u}_i}{2}\right) + \frac{\overline{\rho u_i'' u_i''}}{2}\right] + \frac{\partial}{\partial x_j}\left[\bar{\rho}\tilde{u}_j\left(\tilde{h} + \frac{\tilde{u}_i\tilde{u}_i}{2}\right) + \tilde{u}_j\frac{\overline{\rho u_i'' u_i''}}{2}\right] \\ = \frac{\partial}{\partial x_j}\left[-q_{L_j} - \overline{\rho u_j'' h''} + \overline{t_{ji}u_i''} - \overline{\rho u_j'' \tfrac{1}{2} u_i'' u_i''}\right] \\ + \frac{\partial}{\partial x_j}\left[\tilde{u}_i\left(\bar{t}_{ij} - \overline{\rho u_i'' u_j''}\right)\right]\end{aligned} \tag{5.31}$$

$$P = \bar{\rho}R\tilde{T} \tag{5.32}$$

Equations (5.29) and (5.32) are identical to their laminar counterparts and Equation (5.30) differs only by appearance of the Favre-averaged Reynolds-stress tensor, viz.,

$$\bar{\rho}\tau_{ij} = -\overline{\rho u_i'' u_j''} \tag{5.33}$$

As in the incompressible case, the Favre-averaged τ_{ij} is a symmetric tensor.

Equation (5.31), the Favre-averaged mean-energy equation for total energy, i.e., the sum of internal energy, mean-flow kinetic energy and turbulence kinetic energy has numerous additional terms, each of which represents an identifiable physical process or property. Consider first the double correlation between u_i'' and itself that appears in each of the two terms on the left-hand side. This is the kinetic energy per unit volume of the turbulent fluctuations, so that it makes sense to define

$$\bar{\rho}k = \frac{1}{2}\overline{\rho u_i'' u_i''} \tag{5.34}$$

Next, the correlation between u_j'' and h'' is the turbulent transport of heat. In analogy to the notation selected for the molecular transport of heat, we define

$$q_{T_j} = \overline{\rho u_j'' h''} \tag{5.35}$$

The two terms $\overline{t_{ji}u_i''}$ and $\overline{\rho u_j'' \frac{1}{2} u_i'' u_i''}$ on the right-hand side of Equation (5.31) correspond to molecular diffusion and turbulent transport of turbulence kinetic

energy, respectively. These terms arise because the mass-averaged total enthalpy appearing in the convective term of Equation (5.31) is the sum of mass-averaged enthalpy, mean kinetic energy and turbulence kinetic energy. They represent transfers between mean energy and turbulence kinetic energy that naturally arise when we derive the Favre-averaged turbulence kinetic energy equation. The simplest way to derive the equation for k is to multiply the primitive-variable form of the instantaneous momentum equation by u_i'' and time average.

$$\overline{\rho u_i'' \frac{\partial u_i}{\partial t}} + \overline{\rho u_i'' u_j \frac{\partial u_i}{\partial x_j}} = -\overline{u_i'' \frac{\partial p}{\partial x_i}} + \overline{u_i'' \frac{\partial t_{ji}}{\partial x_j}} \tag{5.36}$$

As in Chapter 2, the most illuminating way to carry out the indicated time-averaging operations is to proceed term by term, and to use tensor notation for all derivatives. Proceeding from left to right, we first consider the **unsteady term**.

$$\begin{aligned}
\overline{\rho u_i'' u_{i,t}} &= \overline{\rho u_i'' (\tilde{u}_i + u_i'')_{,t}} \\
&= \overline{\rho u_i''} \tilde{u}_{i,t} + \overline{\rho u_i'' u_{i,t}''} \\
&= \overline{\rho (\tfrac{1}{2} u_i'' u_i'')_{,t}} \\
&= \frac{\partial}{\partial t}(\bar{\rho} k) - \overline{\tfrac{1}{2} u_i'' u_i'' \frac{\partial \rho}{\partial t}}
\end{aligned} \tag{5.37}$$

Turning now to the **convective term**, we have the following.

$$\begin{aligned}
\overline{\rho u_i'' u_j u_{i,j}} &= \overline{\rho u_i'' [(\tilde{u}_j + u_j'') \tilde{u}_{i,j} + u_j u_{i,j}'']} \\
&= \overline{\rho u_i''} \tilde{u}_j \tilde{u}_{i,j} + \overline{\rho u_i'' u_j''}\ \tilde{u}_{i,j} + \overline{\rho u_j u_i'' u_{i,j}''} \\
&= -\bar{\rho} \tau_{ij} \tilde{u}_{i,j} + \overline{\rho u_j (\tfrac{1}{2} u_i'' u_i'')_{,j}} \\
&= -\bar{\rho} \tau_{ij} \tilde{u}_{i,j} + \overline{(\rho u_j \tfrac{1}{2} u_i'' u_i'')_{,j}} - \overline{\tfrac{1}{2} u_i'' u_i'' (\rho u_j)_{,j}} \\
&= -\bar{\rho} \tau_{ij} \tilde{u}_{i,j} + \left(\overline{\rho \tilde{u}_j \tfrac{1}{2} u_i'' u_i''} + \overline{\rho u_j'' \tfrac{1}{2} u_i'' u_i''} \right)_{,j} - \overline{\tfrac{1}{2} u_i'' u_i'' (\rho u_j)_{,j}} \\
&= -\bar{\rho} \tau_{ij} \frac{\partial \tilde{u}_i}{\partial x_j} + \frac{\partial}{\partial x_j} \left(\bar{\rho} \tilde{u}_j k + \overline{\rho u_j'' \tfrac{1}{2} u_i'' u_i''} \right) - \overline{\tfrac{1}{2} u_i'' u_i'' \frac{\partial}{\partial x_j} (\rho u_j)}
\end{aligned} \tag{5.38}$$

The **pressure-gradient term** simplifies immediately as follows.

$$\overline{u_i'' p_{,i}} = \overline{u_i''} P_{,i} + \overline{u_i'' p'_{,i}} = \overline{u_i''} \frac{\partial P}{\partial x_i} + \frac{\partial}{\partial x_i} \left(\overline{p' u_i''} \right) - \overline{p' \frac{\partial u_i''}{\partial x_i}} \tag{5.39}$$

Finally, the **viscous term** is simply rewritten as

$$\overline{u_i'' t_{ji,j}} = \frac{\partial}{\partial x_j}\left(\overline{t_{ji} u_i''}\right) - \overline{t_{ji}\frac{\partial u_i''}{\partial x_j}} \tag{5.40}$$

Thus, substituting Equations (5.37) through (5.40) into Equation (5.36), we arrive at the **Favre-averaged turbulence kinetic energy equation**. In arriving at the final result, we make use of the fact that the sum of the last terms on the right-hand sides of Equations (5.37) and (5.38) vanish since their sum is proportional to the two terms appearing in the instantaneous continuity equation. Additionally, to facilitate comparison with the incompressible turbulence kinetic energy equation [Equation (4.4)], we use the Favre-averaged continuity equation to rewrite the unsteady and convective terms in non-conservation form. The exact equation is as follows.

$$\begin{aligned}\bar{\rho}\frac{\partial k}{\partial t} + \bar{\rho}\tilde{u}_j\frac{\partial k}{\partial x_j} &= \bar{\rho}\tau_{ij}\frac{\partial \tilde{u}_i}{\partial x_j} - \overline{t_{ji}\frac{\partial u_i''}{\partial x_j}} + \frac{\partial}{\partial x_j}\left[\overline{t_{ji}u_i''} - \overline{\rho u_j'' \tfrac{1}{2} u_i'' u_i''} - \overline{p' u_j''}\right] \\ &- \underbrace{\overline{u_i''\frac{\partial P}{\partial x_i}}}_{\text{Pressure Work}} + \underbrace{\overline{p'\frac{\partial u_i''}{\partial x_i}}}_{\text{Pressure Dilatation}}\end{aligned} \tag{5.41}$$

Comparing the mean energy Equation (5.31) with the turbulence kinetic energy Equation (5.41), we see that indeed the two terms $\overline{t_{ji}u_i''}$ and $\overline{\rho u_j'' \frac{1}{2} u_i'' u_i''}$ on the right-hand side of the mean-energy equation are **Molecular Diffusion** and **Turbulent Transport** of turbulence kinetic energy. Inspection of the turbulence kinetic energy equation also indicates that the **Favre-averaged dissipation rate** is given by

$$\bar{\rho}\epsilon = \overline{t_{ji}\frac{\partial u_i''}{\partial x_j}} = \frac{1}{2}\overline{t_{ji}\left(\frac{\partial u_i''}{\partial x_j} + \frac{\partial u_j''}{\partial x_i}\right)} = \overline{t_{ji}s_{ij}''} \tag{5.42}$$

where s_{ij}'' is the fluctuating strain-rate tensor. This is entirely consistent with the definition of dissipation for incompressible flows given in Equation (4.6).

Comparison of Equation (5.41) with the incompressible equation for k [Equation (4.4)] shows that all except the last two terms, i.e., the **Pressure Work** and **Pressure-Dilatation** terms, have analogs in the incompressible equation. Both of these terms vanish in the limit of incompressible flow with zero density fluctuations. The **Pressure Work** vanishes because the time average of u_i'' is zero when density fluctuations are zero. The **Pressure-Dilatation** term vanishes because the fluctuating field has zero divergence for incompressible flow. Hence, Equation (5.41) simplifies to Equation (4.4) for incompressible flow with zero density fluctuations.

Note that the turbulence kinetic energy production, $\bar{\rho}\tau_{ij}\partial\tilde{u}_i/\partial x_j$, and pressure correlation terms represent a transfer from mean kinetic energy to turbulence kinetic energy. Also, dissipation is a transfer from turbulence kinetic energy to internal energy. Thus, since these transfers simply redistribute energy, they must cancel in the overall energy-conservation equation. Consequently, only the two terms involving spatial transport of turbulence kinetic energy appear in Equation (5.31).

Using a similar derivation (we omit the details here for the sake of brevity), the **Favre-averaged Reynolds-stress equation** assumes the following form:

$$\begin{aligned}\frac{\partial}{\partial t}\left(\bar{\rho}\tau_{ij}\right)+\frac{\partial}{\partial x_k}\left(\bar{\rho}\tilde{u}_k\tau_{ij}\right) &= -\bar{\rho}\tau_{ik}\frac{\partial\tilde{u}_j}{\partial x_k}-\bar{\rho}\tau_{jk}\frac{\partial\tilde{u}_i}{\partial x_k}+\bar{\rho}\epsilon_{ij}-\bar{\rho}\Pi_{ij}\\ &+ \frac{\partial}{\partial x_k}\left[-\overline{\left(t_{kj}u_i''+t_{ki}u_j''\right)}+\bar{\rho}C_{ijk}\right]\\ &+ \overline{u_i''}\frac{\partial P}{\partial x_j}+\overline{u_j''}\frac{\partial P}{\partial x_i} \qquad (5.43)\end{aligned}$$

where

$$\bar{\rho}\Pi_{ij}=\overline{p'\left(\frac{\partial u_i''}{\partial x_j}+\frac{\partial u_j''}{\partial x_i}\right)} \qquad (5.44)$$

$$\bar{\rho}\epsilon_{ij}=\overline{t_{kj}\frac{\partial u_i''}{\partial x_k}+t_{ki}\frac{\partial u_j''}{\partial x_k}} \qquad (5.45)$$

$$\bar{\rho}C_{ijk}=\overline{\rho u_i''u_j''u_k''}+\overline{p'u_i''}\delta_{jk}+\overline{p'u_j''}\delta_{ik} \qquad (5.46)$$

Taking advantage of the definitions given in Equations (5.33), (5.34), (5.35) and (5.42), we can summarize the Favre-averaged mean equations and turbulence kinetic energy equation in conservation form.

$$\frac{\partial\bar{\rho}}{\partial t}+\frac{\partial}{\partial x_i}\left(\bar{\rho}\tilde{u}_i\right)=0 \qquad (5.47)$$

$$\frac{\partial}{\partial t}\left(\bar{\rho}\tilde{u}_i\right)+\frac{\partial}{\partial x_j}\left(\bar{\rho}\tilde{u}_j\tilde{u}_i\right)=-\frac{\partial P}{\partial x_i}+\frac{\partial}{\partial x_j}\left[\bar{t}_{ji}+\bar{\rho}\tau_{ji}\right] \qquad (5.48)$$

$$\begin{aligned}\frac{\partial}{\partial t}(\bar{\rho}E)+\frac{\partial}{\partial x_j}(\bar{\rho}\tilde{u}_jH) &= \frac{\partial}{\partial x_j}\left[-q_{L_j}-q_{T_j}+\overline{t_{ji}u_i''}-\overline{\rho u_j''\tfrac{1}{2}u_i''u_i''}\right]\\ &+ \frac{\partial}{\partial x_j}\left[\tilde{u}_i(\bar{t}_{ij}+\bar{\rho}\tau_{ij})\right] \qquad (5.49)\end{aligned}$$

$$\begin{aligned}\frac{\partial}{\partial t}(\bar{\rho}k)+\frac{\partial}{\partial x_j}(\bar{\rho}\tilde{u}_jk) &= \bar{\rho}\tau_{ij}\frac{\partial\tilde{u}_i}{\partial x_j}-\bar{\rho}\epsilon+\frac{\partial}{\partial x_j}\left[\overline{t_{ji}u_i''}-\overline{\rho u_j''\tfrac{1}{2}u_i''u_i''}-\overline{p'u_j''}\right]\\ &- \overline{u_i''}\frac{\partial P}{\partial x_i}+\overline{p'\frac{\partial u_i''}{\partial x_i}} \qquad (5.50)\end{aligned}$$

$$P = \bar{\rho} R \tilde{T} \tag{5.51}$$

The quantities E and H are the **total energy** and **total enthalpy**, and include the kinetic energy of the fluctuating turbulent field, viz.,

$$E = \tilde{e} + \tfrac{1}{2}\tilde{u}_i\tilde{u}_i + k \qquad \text{and} \qquad H = \tilde{h} + \tfrac{1}{2}\tilde{u}_i\tilde{u}_i + k \tag{5.52}$$

5.4 Compressible-Flow Closure Approximations

As discussed in the preceding section, in addition to having variable mean density, $\bar{\rho}$, Equations (5.43) through (5.52) reflect effects of compressibility through various correlations that are affected by fluctuating density. For all but stress-transport models, diffusivity-type closure approximations are usually postulated for the mass-averaged Reynolds-stress tensor and heat-flux vector. Depending on the type of turbulence model used, additional closure approximations may be needed to close the system of equations defining the model.

This section briefly reviews some of the most commonly used closure approximations for compressible flows. Because of the paucity of measurements compared to the incompressible case, and the additional complexities attending compressible flows, far less is available to guide development of closure approximations suitable for a wide range of applications. As a result, modeling of compressibility effects is in a continuing state of development as we begin the twenty-first century. The closure approximations discussed in this, and following, sections are those that have either stood the test of time or show the greatest promise.

Before focusing upon specific closure approximations, it is worthwhile to cite important guidelines that should be followed in devising compressible-flow closure approximations. Adhering to the following items will lead to the simplest and most elegant models.

1. All closure approximations should approach the proper limiting value for Mach number and density fluctuations tending to zero.

2. All closure terms should be written in proper tensor form, e.g., not dependent upon a specific geometrical configuration.

3. All closure approximations should be dimensionally consistent and invariant under a Galilean transformation.

It should be obvious that Items 2 and 3 apply for incompressible flows as well. In practice, Galilean invariance seems to be ignored more often than any other item listed, especially for compressible flows. Such models should be

rejected as they violate a fundamental feature of the Navier-Stokes equation, and are thus physically unsound. We must be aware, for example, that total enthalpy, H, includes the kinetic energy and is not Galilean invariant, so its use as a dependent variable requires caution. For instance, it must not be used in diffusivity format in the manner that $\tilde{h}$ is used in Equation (5.54) below.

5.4.1 Reynolds-Stress Tensor

For zero-, one- and two-equation models, nearly all researchers use the Boussinesq approximation with suitable generalization for compressible flows. Specifically, denoting the eddy viscosity by μ_T, the following form is generally assumed.

$$\bar{\rho}\tau_{ij} \equiv \overline{-\rho u_i'' u_j''} = 2\mu_T \left(S_{ij} - \frac{1}{3}\frac{\partial \tilde{u}_k}{\partial x_k}\delta_{ij} \right) - \frac{2}{3}\bar{\rho}k\delta_{ij} \tag{5.53}$$

The most important consideration in postulating Equation (5.53) is guaranteeing that the trace of τ_{ij} is $-2k$. Note that this means the "second eddy viscosity" must be $-\frac{2}{3}\mu_T$ [recall Equation (5.24)].

5.4.2 Turbulent Heat-Flux Vector

The most commonly used closure approximation for the turbulent heat-flux vector, q_{T_j}, follows from appealing to the classical analogy [Reynolds (1874)] between momentum and heat transfer. It is thus assumed to be proportional to the mean temperature gradient, so that

$$q_{T_j} = \overline{\rho u_j'' h''} = -\frac{\mu_T c_p}{Pr_T}\frac{\partial \tilde{T}}{\partial x_j} = -\frac{\mu_T}{Pr_T}\frac{\partial \tilde{h}}{\partial x_j} \tag{5.54}$$

where Pr_T is the **turbulent Prandtl number**. A constant value for Pr_T is often used and this is usually satisfactory for shock-free flows up to low supersonic speeds, provided the heat transfer rate is not too high. The most common values assumed for Pr_T are 0.89 or 0.90, in the case of a boundary layer. Heat-transfer predictions can usually be improved somewhat by letting Pr_T vary through the boundary layer. Near the edge of a boundary layer and throughout a free shear layer, a value of the order of 0.5 is more appropriate for Pr_T.

5.4.3 Molecular Diffusion and Turbulent Transport

If a zero-equation model is used, the $\frac{2}{3}\bar{\rho}k\delta_{ij}$ contribution in Equation (5.53) is usually ignored as are the molecular diffusion, $\overline{t_{ji}u_i''}$, and turbulent transport, $\overline{\rho u_j'' \frac{1}{2} u_i'' u_i''}$, terms appearing in the mean-energy equation. Some researchers

ignore these terms for higher-order models as well. This is usually a good approximation for flows with Mach numbers up to the supersonic range, which follows from the fact that $\bar{\rho}k \ll P$ (and hence $k \ll \tilde{h}$) in most flows of engineering interest. However, at hypersonic speeds, it is entirely possible to achieve conditions under which $\bar{\rho}k$ is a significant fraction of P. To ensure exact conservation of total energy (which includes turbulence kinetic energy), additional closure approximations are needed. The most straightforward procedure for one-equation, two-equation and stress-transport models is to generalize the low-speed closure approximations for the molecular diffusion and turbulent transport terms. The most commonly used approximation is:

$$\overline{t_{ji}u_i''} - \overline{\rho u_j'' \tfrac{1}{2}u_i''u_i''} = \left(\mu + \frac{\mu_T}{\sigma_k}\right)\frac{\partial k}{\partial x_j} \tag{5.55}$$

5.4.4 Dilatation Dissipation

To understand what "dilatation dissipation" is, we must examine the turbulence-energy dissipation rate more closely. Recall from Equation (5.42) that

$$\bar{\rho}\epsilon = \overline{t_{ji}\frac{\partial u_i''}{\partial x_j}} \tag{5.56}$$

Hence, in terms of the instantaneous strain-rate tensor, s_{ij}, we have

$$\bar{\rho}\epsilon = \overline{\mu\left[2s_{ji}s_{ij}'' - \frac{2}{3}u_{k,k}u_{i,i}''\right]} \tag{5.57}$$

Assuming that the correlation between velocity-gradient fluctuations and kinematic viscosity fluctuations is negligible, we can rewrite this equation as

$$\bar{\rho}\epsilon = \bar{\nu}\left[2\overline{\rho s_{ji}''s_{ij}''} - \frac{2}{3}\overline{\rho u_{k,k}''u_{i,i}''}\right] \tag{5.58}$$

In terms of the fluctuating vorticity, ω_i'', there follows

$$\bar{\rho}\epsilon = \bar{\nu}\left[\overline{\rho\omega_i''\omega_i''} + 2\overline{\rho u_{i,j}''u_{j,i}''} - \frac{2}{3}\overline{\rho u_{i,i}''u_{i,i}''}\right] \tag{5.59}$$

Finally, we can say $u_{i,j}''u_{j,i}'' \approx (u_{i,i}'')^2$, which is exactly true for homogeneous turbulence, and is a very good approximation for high-Reynolds-number, inhomogeneous turbulence [see, for example, Tennekes and Lumley (1983)]. Hence, we conclude that the dissipation can be written as

$$\bar{\rho}\epsilon = \bar{\rho}\epsilon_s + \bar{\rho}\epsilon_d \tag{5.60}$$

where

$$\bar{\rho}\epsilon_s = \bar{\nu}\ \overline{\rho\omega_i''\omega_i''} \qquad \text{and} \qquad \bar{\rho}\epsilon_d = \frac{4}{3}\bar{\nu}\ \overline{\rho u_{i,i}'' u_{i,i}''} \tag{5.61}$$

Thus, we have shown that the compressible turbulence dissipation rate can logically be written in terms of the fluctuating vorticity and the divergence of the fluctuating velocity. Equivalently, we could have written the fluctuating velocity as the sum of a divergence-free and a curl-free component. At high Reynolds number, these components presumably are uncorrelated (again, an exact result for homogeneous turbulence), and Equation (5.59) would follow directly. The quantity ϵ_s is known as the **solenoidal dissipation**, while ϵ_d is known as the **dilatation dissipation**. Clearly, the latter contribution is present only for compressible flows.

Based on observations from some older Direct Numerical Simulations (DNS), Sarkar et al. (1989) and Zeman (1990) postulate that the dilatation dissipation should be a function of turbulence Mach number, M_t, defined by

$$M_t^2 = 2k/a^2 \tag{5.62}$$

where a is the speed of sound. They further argue that the k and ϵ equations should be replaced by

$$\bar{\rho}\frac{dk}{dt} = -\bar{\rho}\left(\epsilon_s + \epsilon_d\right) + \cdots \tag{5.63}$$

$$\bar{\rho}\frac{d\epsilon_s}{dt} = -C_{\epsilon 2}\bar{\rho}\epsilon_s^2/k + \cdots \tag{5.64}$$

where $C_{\epsilon 2}$ is a closure coefficient. Only the dissipation terms are shown explicitly in Equations (5.63) and (5.64) since no changes occur in any other terms. Particularly noteworthy, both Sarkar and Zeman postulate that the equation for ϵ_s is unaffected by compressibility. The dilatation dissipation is further assumed to be proportional to ϵ_s so that they say

$$\epsilon_d = \xi^* F(M_t)\ \epsilon_s \tag{5.65}$$

where ξ^* is a closure coefficient and $F(M_t)$ is a prescribed function of M_t. The Sarkar and Zeman formulations differ in the value of ξ^* and the functional form of $F(M_t)$, which we will discuss in Section 5.5.

Interestingly, while both Sarkar and Zeman arrive at similar formulations, their basic postulates are fundamentally different. Sarkar et al. postulate that ϵ_d "varies on a fast compressibility time scale relative to ϵ_s." As a consequence, they conclude that dilatation dissipation increases with M_t in a monotone manner. By contrast, Zeman postulates the existence of eddy shocklets, which are principally responsible for the dilatation dissipation. His analysis predicts that a threshold exists below which dilatation dissipation is negligible.

Although their arguments seem plausible when taken at face value, the premises are flawed. Most importantly, both draw from early DNS results for low-Reynolds-number, initially-isotropic turbulence subjected to strong compression or shear, where both dilatation dissipation and pressure-dilatation (see the next subsection) are significant. As pointed out by Ristorcelli et al. (1995), dilatation fluctuations occur mainly in the large eddies, where density fluctuations are large and viscous effects are small. That is, the mean-square dilatation fluctuation is virtually independent of Reynolds number, so ϵ_d varies as $1/Re$ and is therefore small at real-life Reynolds numbers.

DNS results for compressible thin shear layers [Coleman et al. (1995) and Huang et al. (1995) for channel flows, and Vreman et al. (1996) for mixing layers] show that dilatation dissipation is small or negligible, even in the presence of eddy shocklets and even at the fairly low Reynolds numbers of recent DNS studies. The channel results are consistent with the fact that compressibility corrections are not needed for boundary-layer flows. These DNS results also show insignificant pressure dilatation (see next subsection).

Nevertheless, the "dilatation-dissipation" corrections postulated by Zeman and Sarkar can, with adjustment of empirical coefficients, successfully correlate the decrease in mixing-layer growth rate with increasing Mach number. With care, they can also be arranged to have the desired lack of influence on non-hypersonic boundary layers, in which M_t is generally lower at given M_e because k/U_e^2 is smaller than in mixing layers. Evidently they should be regarded as completely empirical corrections rather than true models of dilatation dissipation. We return to the question of what these compressibility corrections really mean after discussing the other explicit compressibility terms in the turbulence kinetic energy equation, namely pressure diffusion and pressure dilatation.

5.4.5 Pressure Diffusion and Pressure Dilatation

Section 4.1 discusses the lack of information regarding diffusion by pressure fluctuations in incompressible flows. So little is known that it is simply ignored; by implication, it is lumped in with triple-product turbulent transport. Even less is known for compressible flows. However, given the fundamentally different role that pressure plays in a compressible medium relative to its essentially passive role at low speeds, we might reasonably suspect that ignoring pressure diffusion and pressure dilatation might lead to significant error. However, DNS research shows that, as with dilatation dissipation, these terms are very small for both mixing layers and boundary layers. As in the case of dilatation dissipation, the early homogeneous-strain simulations were misleading. As Zeman (1993) shows, pressure-dilatation is large in flows with a large ratio of turbulence-energy production to dissipation – typical of strongly-strained initially-isotropic flows. In thin shear layers, production and dissipation are roughly the same and

pressure-dilatation is small. (This is not a Reynolds-number effect: pressure-dilatation is determined by the large eddies, like mean-square dilatation, and does not involve viscosity.) Hence, models for these pressure terms, to the extent that they improve predictions, are ad hoc in nature and do not reflect the true physics of compressible turbulence.

New proposals, especially for the pressure-dilatation mean product, have been made by many authors [Sarkar et al. (1991,1992), Zeman (1991,1993) and Ristorcelli et al. (1993,1995)], but none has received general acceptance. For example, Sarkar (1992) proposes that the pressure dilatation can be approximated as

$$\overline{p' \frac{\partial u_i''}{\partial x_i}} = \alpha_2 \bar{\rho} \tau_{ij} \frac{\partial \tilde{u}_i}{\partial x_j} M_t + \alpha_3 \bar{\rho} \epsilon M_t^2 \tag{5.66}$$

where M_t is the **turbulence Mach number** defined in Equation (5.62). The closure coefficients α_2 and α_3 are given by

$$\alpha_2 = 0.15 \quad \text{and} \quad \alpha_3 = 0.2 \tag{5.67}$$

The model has been calibrated for a range of compressible-flow applications including the mixing layer and attached boundary layers (but apparently not with respect to DNS results for these flows).

5.4.6 Pressure Work

The pressure work term, $\overline{u_i''} P_{,i}$ (or $\overline{u_i''} P_{,j} + \overline{u_j''} P_{,i}$ for stress-transport models), arises because the time average of u_i'' does not vanish. It is proportional to the density/velocity correlation $\overline{\rho' u_i'}$, and illustrates how Favre averaging does not completely eliminate the need to know how these fluctuating properties are correlated.

Wilcox and Alber (1972) postulate an empirical model for this term that improves two-equation model predictions for hypersonic base flows. Oh (1974) proposes a closure approximation postulating existence of "eddy shocks" and accurately simulates compressible mixing layers with a one-equation turbulence model. Neither model is entirely satisfactory however as they both involve the mean velocity in a manner that violates Galilean invariance of the Navier-Stokes equation.

More recently, Zeman (1993) and Ristorcelli (1993) have argued that the time average of u_i'' for boundary layers behaves as

$$\overline{u_i''} \sim \frac{M_t k}{\bar{\rho} \epsilon} \tau_{ij} \frac{\partial \bar{\rho}}{\partial x_j} \tag{5.68}$$

Although corroborating measurements to verify this model are essentially nonexistent, we can at least say that it is dimensionally correct and does not violate Galilean invariance.

5.4.7 k-ω Model Equations for Compressible Flows

To summarize the ramifications of the closure approximations discussed above, it is instructive at this point to combine them into a closed set of equations for compressible flows. Since many of the compressible-flow applications to follow will be done with the k-ω model, we will focus on its equations. The Favre-averaged equations for conservation of mass, momentum, energy and the equations defining the k-ω model are as follows.

Mass Conservation:

$$\frac{\partial \bar{\rho}}{\partial t} + \frac{\partial}{\partial x_i}\left(\bar{\rho}\tilde{u}_i\right) = 0 \tag{5.69}$$

Momentum Conservation:

$$\frac{\partial}{\partial t}(\bar{\rho}\tilde{u}_i) + \frac{\partial}{\partial x_j}(\bar{\rho}\tilde{u}_j\tilde{u}_i) = -\frac{\partial P}{\partial x_i} + \frac{\partial}{\partial x_j}\left[\bar{t}_{ji} + \bar{\rho}\tau_{ji}\right] \tag{5.70}$$

Energy Conservation:

$$\begin{aligned}\frac{\partial}{\partial t}\left[\bar{\rho}\left(\tilde{e} + \frac{\tilde{u}_i\tilde{u}_i}{2} + k\right)\right] + \frac{\partial}{\partial x_j}\left[\bar{\rho}\tilde{u}_j\left(\tilde{h} + \frac{\tilde{u}_i\tilde{u}_i}{2} + k\right)\right] \\ = \frac{\partial}{\partial x_j}\left[\left(\frac{\mu}{Pr_L} + \frac{\mu_T}{Pr_T}\right)\frac{\partial \tilde{h}}{\partial x_j} + \left(\mu + \sigma^*\frac{\rho k}{\omega}\right)\frac{\partial k}{\partial x_j}\right] \\ + \frac{\partial}{\partial x_j}\left[\tilde{u}_i\left(\bar{t}_{ij} + \bar{\rho}\tau_{ij}\right)\right]\end{aligned} \tag{5.71}$$

Molecular and Reynolds-Stress Tensors:

$$\bar{t}_{ij} = 2\mu\bar{S}_{ij}, \qquad \bar{\rho}\tau_{ij} = 2\mu_T\bar{S}_{ij} - \frac{2}{3}\bar{\rho}k\delta_{ij}, \qquad \bar{S}_{ij} = S_{ij} - \frac{1}{3}\frac{\partial \tilde{u}_k}{\partial x_k}\delta_{ij} \tag{5.72}$$

Eddy Viscosity:

$$\mu_T = \frac{\bar{\rho}k}{\tilde{\omega}}, \qquad \tilde{\omega} = \max\left\{\omega,\ C_{lim}\sqrt{\frac{2\bar{S}_{ij}\bar{S}_{ij}}{\beta^*}}\right\}, \qquad C_{lim} = \frac{7}{8} \tag{5.73}$$

Turbulence Kinetic Energy:

$$\frac{\partial}{\partial t}(\bar{\rho}k) + \frac{\partial}{\partial x_j}(\bar{\rho}\tilde{u}_j k) = \bar{\rho}\tau_{ij}\frac{\partial \tilde{u}_i}{\partial x_j} - \beta^*\bar{\rho}k\omega + \frac{\partial}{\partial x_j}\left[\left(\mu + \sigma^*\frac{\bar{\rho}k}{\omega}\right)\frac{\partial k}{\partial x_j}\right] \tag{5.74}$$

Specific Dissipation Rate:

$$\begin{aligned}\frac{\partial}{\partial t}(\bar{\rho}\omega) + \frac{\partial}{\partial x_j}(\bar{\rho}\tilde{u}_j\omega) &= \alpha\frac{\omega}{k}\rho\tau_{ij}\frac{\partial \tilde{u}_i}{\partial x_j} - \beta\bar{\rho}\omega^2 + \sigma_d\frac{\bar{\rho}}{\omega}\frac{\partial k}{\partial x_j}\frac{\partial \omega}{\partial x_j} \\ &+ \frac{\partial}{\partial x_j}\left[\left(\mu + \sigma\frac{\bar{\rho}k}{\omega}\right)\frac{\partial \omega}{\partial x_j}\right]\end{aligned} \tag{5.75}$$

Closure Coefficients:

$$\alpha = \frac{13}{25}, \quad \beta = \beta_o f_\beta, \quad \beta^* = \frac{9}{100}, \quad \sigma = \frac{1}{2}, \quad \sigma^* = \frac{3}{5}, \quad \sigma_{do} = \frac{1}{8} \tag{5.76}$$

$$\beta_o = 0.0708, \quad Pr_T = \frac{8}{9}, \quad \sigma_d = \begin{cases} 0, & \dfrac{\partial k}{\partial x_j}\dfrac{\partial \omega}{\partial x_j} \le 0 \\ \sigma_{do}, & \dfrac{\partial k}{\partial x_j}\dfrac{\partial \omega}{\partial x_j} > 0 \end{cases} \tag{5.77}$$

$$f_\beta = \frac{1 + 85\chi_\omega}{1 + 100\chi_\omega}, \quad \chi_\omega \equiv \left| \frac{\Omega_{ij}\Omega_{jk}\hat{S}_{ki}}{(\beta^*\omega)^3} \right|, \quad \hat{S}_{ki} = S_{ki} - \frac{1}{2}\frac{\partial \tilde{u}_m}{\partial x_m}\delta_{ki} \tag{5.78}$$

There are a few subtle points worthy of mention regarding the precise form of these equations, which apply to both compressible and incompressible flows.

- The energy conservation Equation (5.71) ensures conservation of total energy, $E = \bar{\rho}(\tilde{e} + \frac{1}{2}\tilde{u}_i\tilde{u}_i + k)$, which includes the kinetic energy of the turbulence. Consequently, the equation's diffusion term includes explicit appearance of molecular and turbulent diffusion of k.
- The turbulence kinetic energy Equation (5.74) contains no special compressibility terms involving pressure work, diffusion or dilatation.
- Although a dilatation-dissipation modification to the k equation improves compressible mixing-layer predictions (see Section 5.5), the same modification has a detrimental effect on shock-separated flow predictions. Hence, it is omitted from the k equation for general applications.
- The stress-limiter modification [Equation (5.73)] uses the zero-trace version of the mean strain-rate tensor, viz., $\bar{S}_{ij} = S_{ij} - \frac{1}{3}\frac{\partial \tilde{u}_k}{\partial x_k}\delta_{ij}$. Some turbulence-model researchers prefer the magnitude of the vorticity vector in place of $(2\bar{S}_{ij}\bar{S}_{ij})^{1/2}$. Using the magnitude of the vorticity with 0.95 replacing 7/8 is satisfactory for shock-separated flow predictions up to Mach 3 (and possibly a bit higher). However, numerical experimentation with this k-ω model has shown that it has a detrimental effect on hypersonic shock-induced separation, some (but not all) attached boundary layers and some free shear flows (especially the mixing layer).
- The round-jet parameter, χ_ω, is computed with $\hat{S}_{ij} = S_{ij} - \frac{1}{2}\frac{\partial \tilde{u}_k}{\partial x_k}\delta_{ij}$, which, unlike the compressible strain-rate recommended by Papp and Dash (2001), is Galilean invariant. This is necessary because using S_{ki} or $\bar{S}_{ki}$ yields undesired effects in two-dimensional compressible flows.
- All of the closure coefficients in the compressible-flow version of the k-ω model are identical to those appearing in the incompressible-flow version [see Equations (4.39) - (4.41)].

5.5 Mixing-Layer Compressibility Corrections

The decrease in mixing-layer growth rate with increasing Mach number has been known for many years [e.g., Birch and Eggers (1972)]. This decrease is not likely to be the result of density changes across the layer. We know from the measurements of Brown and Roshko (1974) that low-speed mixing layers between flows of two different gases show only a moderate effect of density ratio. Most researchers believe no current turbulence model predicts the Mach-number dependence of spreading rate without an explicit compressibility correction.

We have seen above that the explicit compressibility terms in the k equation are small in practical cases. Also, empirical functions of turbulence Mach number, M_t, calibrated to reproduce compressibility effects in mixing layers, are liable to have unwanted effects on boundary layers. From this we can deduce two things. First, compressibility effects result from Mach-number dependence of the main terms in the equations, i.e., those which are present even in incompressible flow. Second, these effects appear mainly in the mixing layer, but are not entirely attributable to the typically higher M_t in mixing layers.

There is now fairly conclusive evidence, both from simulations [e.g., Vreman et al. (1996)] and experiment [e.g., Clemens and Mungal (1995)], that quasi-two-dimensional spanwise vortex rolls, which form the large-scale structure of low-speed mixing layers, become more three-dimensional as Mach number increases. This is in line with the Mach-number dependence of the most-unstable disturbances in laminar mixing layers, which are vortex rolls with gradually-increasing sweepback. This "inflection-point" instability is essentially inviscid, capable of growing in the presence of viscosity, and may therefore be at least qualitatively relevant to the behavior of large structure in the presence of small-scale turbulence.

It seems unlikely that laminar stability theory will lead directly to a quantitative correlation for turbulent flow, which must therefore rest on empiricism. An important question not yet settled by experiment is whether the spreading rate reaches an asymptotic value at high Mach number, or continues to decrease indefinitely. Acoustic radiation from the turbulence, which in the past was occasionally blamed entirely for the observed compressibility effects, will certainly become an important mechanism of energy loss at very high Mach number and may therefore prevent an asymptotic state from being reached.

The arguments above strongly suggest that compressibility effects manifest themselves in the pressure-strain "redistribution" term, Π_{ij}, defined in Equation (5.44) and a major term appearing in the Reynolds-stress transport equation for τ_{ij}, Equation (5.43). Unless some of the smaller unknown terms on the right-hand side of Equation (5.43) increase very greatly with Mach number, the empirical compressibility correction terms which are *added* to the turbulence equations are a substitute for compressibility *factors* on Π_{ij}. To date, most

compressibility corrections have been applied to the turbulence-energy equation, as used in two-equation models. In these models, the τ_{ij} equation is not treated explicitly, and corrections to Π_{ij} have not yet been explored.

5.5.1 The Sarkar/Zeman/Wilcox Compressibility Corrections

As noted in Subsection 5.4.4, focusing upon the k-ϵ model, Sarkar et al. (1989) and Zeman (1990) have devised particularly elegant models for the k equation that correct the deficiency for the compressible mixing layer. Although their physical arguments have since been shown to apply at best only to low-Reynolds-number, strained homogeneous flows (the subjects of early DNS studies), their models are nevertheless quite useful. Building upon the Sarkar/Zeman formulations, and upon dimensional analysis, Wilcox (1992b) has postulated a similar model that enjoys an important advantage for wall-bounded flows.

To implement the Sarkar or Zeman modification in the k-ω model, we begin by making the formal change of variables given by $\epsilon_s = \beta^* \omega k$. This tells us that

$$\bar{\rho} \frac{d\omega}{dt} = \frac{\bar{\rho}}{\beta^* k} \left[\frac{d\epsilon_s}{dt} - \frac{\epsilon_s}{k} \frac{dk}{dt} \right] \tag{5.79}$$

Consequently, a compressibility term must appear in the ω equation as well as in the k equation. Inspection of Equations (4.37) and (4.38) shows that the Sarkar/Zeman compressibility modifications correspond to letting closure coefficients β and β^* in the k-ω model vary with M_t. In terms of ξ^* and the compressibility function $F(M_t)$, β and β^* become:

$$\beta^* = \beta_i^* \left[1 + \xi^* F(M_t) \right], \qquad \beta = \beta_i - \beta_i^* \xi^* F(M_t) \tag{5.80}$$

where $\beta_i^* = 9/100$ and $\beta_i = \beta_o f_\beta$ are the corresponding incompressible values of β^* and β. The values of ξ^* and $F(M_t)$ for the three models are:

Sarkar's Model[2]

$$\xi^* = 1, \qquad F(M_t) = M_t^2 \tag{5.81}$$

Zeman's Model

$$\xi^* = 3/4, \qquad F(M_t) = \left[1 - e^{-\frac{1}{2}(\gamma+1)(M_t - M_{t_o})^2 / \Lambda^2} \right] \mathcal{H}(M_t - M_{t_o}) \tag{5.82}$$

Wilcox's Model

$$\xi^* = 2, \qquad M_{t_o} = 1/4, \qquad F(M_t) = \left[M_t^2 - M_{t_o}^2 \right] \mathcal{H}(M_t - M_{t_o}) \tag{5.83}$$

[2]When Sarkar's pressure-dilatation term, Equation (5.66), is used in combination with Equation (5.81), the coefficient ξ^* should be reduced to 1/2.

where γ is the specific-heat ratio and $\mathcal{H}(x)$ is the Heaviside step function. Zeman recommends using $\Lambda = 0.60$ and $M_{t_o} = 0.10\sqrt{2/(\gamma+1)}$ for free shear flows. For boundary layers, their values must increase to $\Lambda = 0.66$ and $M_{t_o} = 0.25\sqrt{2/(\gamma+1)}$. Zeman uses a different set of closure coefficients for boundary layers because he postulates that they depend upon the kurtosis, $\overline{u'^4}/(\overline{u'^2})^2$. The kurtosis is presumed to be different for free shear flows as compared to boundary layers. While this may be true, it is not much help for two-equation or stress-transport models since such models only compute double correlations and make closure approximations for triple correlations. Quadruple correlations such as $\overline{u'^4}$ are beyond the scope of these models.

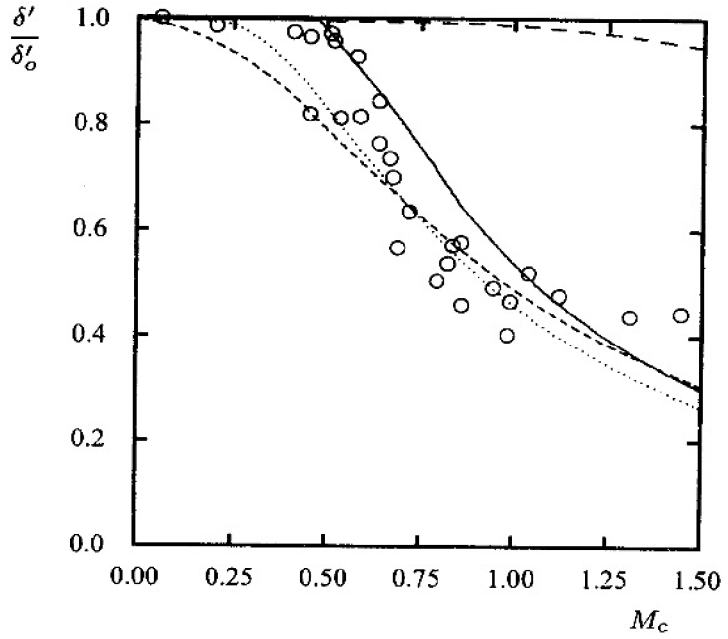

Figure 5.1: *Computed and measured spreading rate for a compressible mixing layer: – – Unmodified k-ω model; —— Wilcox, $\xi^* = 2$; - - - Sarkar, $\xi^* = 1$; · · · Zeman, $\xi^* = 3/4$; ○ Measured [Barone et al. (2006)].*

5.5.2 Applications

To illustrate how well these models perform, we consider mixing of a supersonic stream and a quiescent fluid with constant total temperature. For simplicity, we present results only for the k-ω model as k-ϵ results are similar. The equations of motion have been transformed to similarity form for the farfield and integrated using Program **MIXER** (see Appendix C). Figure 5.1 compares computed and measured [see Barone et al. (2006)] spreading rate, δ'. As in the incompressible case, spreading rate is defined as the difference between the values of y/x where

$(U - U_2)^2/(U_1 - U_2)^2$ is 9/10 and 1/10. The quantity δ'_o is incompressible spreading rate and $M_c \equiv (U_1 - U_2)/(a_1 + a_2)$ is convective Mach number [Papamoschou and Roshko (1988)]. The unmodified k-ω model fails to predict a significant decrease in spreading rate as Mach number increases. By contrast, the Sarkar, Zeman and Wilcox modifications, all applied to the k-ω model, yield close agreement between computed and measured spreading rates.

We turn now to the adiabatic-wall flat-plate boundary layer. The equations of motion for the k-ω model have been solved with Program **EDDYBL** (see Appendix C). Figure 5.2 compares the ratio of computed skin friction, c_f, to its incompressible-flow value, c_{f_o}, with a correlation of measured values for freestream Mach number between 0 and 5. In all computations, momentum-thickness Reynolds number is $Re_\theta = 10^4$. As shown, the unmodified model virtually duplicates measured skin friction. By contrast, the Sarkar compressibility modification yields a value for c_f at Mach 5 that is 18% lower than the value computed with $\xi^* = 0$. Using the Wilcox compressibility correction with $\xi^* = 2$ and $M_{t_o} = 0.25$ yields virtually no difference in skin friction.

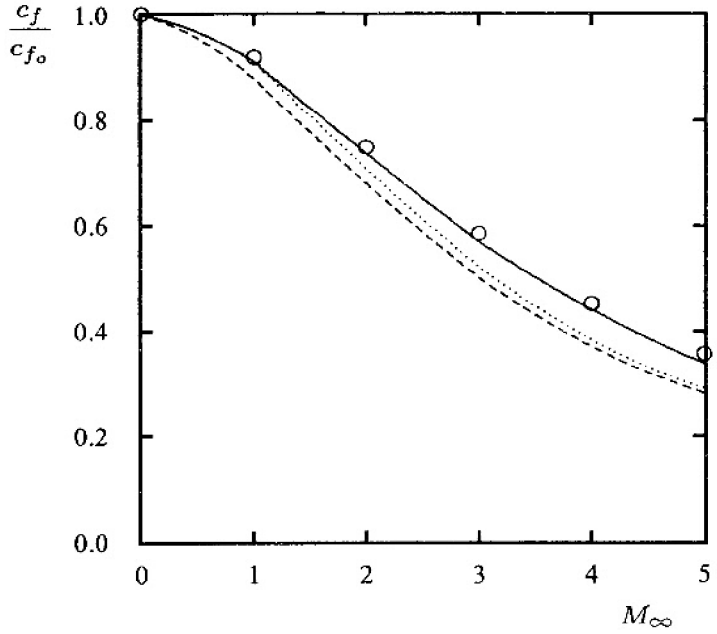

Figure 5.2: *Computed and measured k-ω model skin friction for a compressible flat-plate boundary layer:* —— *Wilcox with* $\xi^* = 0$ *and* $\xi^* = 2$; - - - *Sarkar,* $\xi^* = 1$; $\cdots$ *Zeman,* $\xi^* = 3/4$; $\circ$ *Van Driest correlation.*

Using $\Lambda = 0.60$ and $M_{t_o} = 0.10\sqrt{2/(\gamma + 1)}$ in Zeman's model, computed c_f at Mach 5 is 15% smaller than the value obtained with the unmodified model. Increasing the values of Λ and M_{t_o} to 0.66 and $0.25\sqrt{2/(\gamma + 1)}$, respectively, eliminates this discrepancy. However, using this large a value for M_{t_o} for the

mixing layer results in larger-than-measured spreading rates, with differences in excess of 100% between computed and measured spreading rate for $M_1 > 2.5$.

These results make it clear that neither the Sarkar nor the Zeman compressibility term is completely satisfactory for both the mixing layer and boundary layers. The Wilcox model was formulated to resolve this dilemma. Making β and β^* functions of M_t is a useful innovation, and is not the root cause of the problem. Rather, the postulated form of the function $F(M_t)$ is the weak link.

Inspection of turbulence Mach numbers in mixing layers and boundary layers shows that all we need is an alternative to the Sarkar and Zeman functional dependencies of ϵ_d upon M_t. Table 5.1 shows why the Sarkar term improves predictions for the mixing layer. The unmodified k-ω model predicts peak values of M_t in a mixing layer that are more than twice the values in a boundary layer for the same freestream Mach number. The Sarkar compressibility term reduces $(M_t)_{max}$ by about one third for the mixing layer when $M_\infty \geq 2$. Even with this much reduction, $(M_t)_{max}$ for the mixing layer at a Mach number of 2 remains higher than the largest value of $(M_t)_{max}$ in the boundary layer all the way up to Mach 5.

Table 5.1: *Maximum Turbulence Mach Number,* $(M_t)_{max}$.

	Boundary Layer		Mixing Layer	
M_∞	$\xi^* = 0$	$\xi^* = 1$	$\xi^* = 0$	$\xi^* = 1$
0	0	0	0	0
1	0.088	0.087	0.239	0.215
2	0.157	0.151	0.417	0.313
3	0.207	0.192	0.532	0.352
4	0.241	0.219	0.605	0.369
5	0.267	0.238	0.653	0.379

For Mach 1, the Sarkar term reduces mixing-layer spreading rate below measured values (Figure 5.1). Zeman's term predicts a somewhat larger spreading rate at Mach 1, mainly because of the Mach number threshold in Zeman's model. That is, Zeman postulates that the compressibility effect is absent for $M_t < M_{t_o}$. Zeman's Mach number threshold also yields smaller differences between computed and measured boundary-layer skin friction at lower Mach numbers (see Figure 5.2). Inspection of Table 5.1 makes it very clear why setting the threshold at $M_{t_o} = 0.25$ leaves boundary-layer properties unaffected by the dilatation-dissipation compressibility modification to the k-ω model. These observations show that an improved compressibility term can be devised by extending Zeman's threshold Mach number to a larger value of M_t. The Wilcox model simply combines the relative simplicity of Sarkar's functional form for $F(M_t)$ with Zeman's Mach number threshold to accomplish this end.

5.6 Compressible Law of the Wall

In this section, we use perturbation methods to examine k-ω and k-ϵ model predicted, compressible log-layer structure. The results are particularly illuminating and clearly demonstrate why the Sarkar and Zeman compressibility terms adversely affect boundary-layer predictions. We will also show that the presence of a cross-diffusion term in the ω equation distorts a model's implied compressible law of the wall.

5.6.1 Derivation

Recall from Section 4.6.1 that the log layer is the region sufficiently close to the solid boundary for neglect of convective terms and far enough distant for molecular diffusion terms to be dropped. As in the incompressible case, turbulence kinetic energy production and dissipation are nearly balanced, which means the stress limiter has no effect. Therefore, $\tilde{\omega} = \omega$ so that $\mu_T = \bar{\rho}k/\omega$. Thus, the log-layer form of the equations for the k-ω model simplify to the following.

$$\mu_T \frac{d\tilde{u}}{dy} = \bar{\rho}_w u_\tau^2 \tag{5.84}$$

$$\mu_T \frac{d}{dy}\left[\frac{c_p \tilde{T}}{Pr_T} + \frac{1}{2}\tilde{u}^2 + \sigma^* k\right] = -q_w \tag{5.85}$$

$$\sigma^* \frac{d}{dy}\left[\mu_T \frac{dk}{dy}\right] + \mu_T \left(\frac{d\tilde{u}}{dy}\right)^2 - \beta^* \bar{\rho}\omega k = 0 \tag{5.86}$$

$$\sigma \frac{d}{dy}\left[\mu_T \frac{d\omega}{dy}\right] + \sigma_d \frac{\bar{\rho}}{\omega}\frac{dk}{dy}\frac{d\omega}{dy} + \alpha\bar{\rho}\left(\frac{d\tilde{u}}{dy}\right)^2 - \beta\bar{\rho}\omega^2 = 0 \tag{5.87}$$

$$\bar{\rho}\tilde{T} = \bar{\rho}_w \tilde{T}_w \tag{5.88}$$

The quantity u_τ is friction velocity defined as $\sqrt{\tau_w/\bar{\rho}_w}$ where τ_w is surface shear stress and $\bar{\rho}_w$ is density at the surface. Also, $\tilde{T}_w$ is surface temperature, q_w is surface heat flux and c_p is specific heat at constant pressure. Finally, y is distance from the surface.

Since the flow is two dimensional, we have $f_\beta = 1$. We introduce Sarkar's compressibility modification [Equation (5.81)], so that Equation (5.80) for β^* and β simplifies to

$$\beta^* = \beta_i^* \left[1 + \xi^* M_t^2\right] \qquad \text{and} \qquad \beta = \beta_o - \beta_o^* \xi^* M_t^2 \tag{5.89}$$

Following Saffman and Wilcox (1974), we change independent variables from y to $\tilde{u}$. Consequently, derivatives transform according to

$$\mu_T \frac{d}{dy} = \mu_T \frac{d\tilde{u}}{dy}\frac{d}{d\tilde{u}} = \bar{\rho}_w u_\tau^2 \frac{d}{d\tilde{u}} \tag{5.90}$$

With this change of variables, we replace Equations (5.85) – (5.87) by

$$\frac{d}{d\tilde{u}}\left[\frac{c_p \tilde{T}}{Pr_T} + \frac{1}{2}\tilde{u}^2 + \sigma^* k\right] = -\frac{q_w}{\bar{\rho}_w u_\tau^2} \tag{5.91}$$

$$\sigma^* \frac{d^2 k}{d\tilde{u}^2} + 1 - \frac{\beta^* \bar{\rho}^2 k^2}{\bar{\rho}_w^2 u_\tau^4} = 0 \tag{5.92}$$

$$\sigma \frac{d^2\omega}{d\tilde{u}^2} + \frac{\sigma_d}{k}\frac{dk}{d\tilde{u}}\frac{d\omega}{d\tilde{u}} + \alpha\frac{\omega}{k} - \frac{\beta\bar{\rho}^2 k\omega}{\bar{\rho}_w^2 u_\tau^4} = 0 \tag{5.93}$$

Integrating Equation (5.91) yields the temperature, and hence the density, as a function of velocity and Mach number based on friction velocity, $M_\tau \equiv u_\tau / a_w$.

$$\frac{\tilde{T}}{\tilde{T}_w} = \frac{\bar{\rho}_w}{\bar{\rho}} = 1 - (\gamma - 1) Pr_T M_\tau^2 \left[\frac{1}{2}\left(\frac{\tilde{u}}{u_\tau}\right)^2 + \frac{q_w}{\bar{\rho}_w u_\tau^3}\left(\frac{\tilde{u}}{u_\tau}\right) + \sigma^*\left(\frac{k}{u_\tau^2}\right)\right] \tag{5.94}$$

Next, we assume a solution of the form:

$$\bar{\rho} k = \Gamma \bar{\rho}_w u_\tau^2 \tag{5.95}$$

where Γ is a constant to be determined. Substituting Equations (5.94) and (5.95) into Equation (5.92), and noting that $M_t^2 = 2\Gamma M_\tau^2$, leads to the following quartic equation for Γ.

$$\beta_i^* \left[1 + 2\xi^* M_\tau^2 \Gamma\right]\left[1 + (\gamma - 1) Pr_T \sigma^* M_\tau^2 \Gamma\right]\Gamma^2 = 1 \tag{5.96}$$

As can easily be verified, when $M_\tau^2 \ll 1$ the asymptotic solution for Γ is

$$\Gamma = \frac{1}{\sqrt{\beta_i^*}} - \left[\frac{\xi^* + \frac{(\gamma-1)}{2} Pr_T \sigma^*}{\beta_i^*}\right] M_\tau^2 + \cdots \tag{5.97}$$

Finally, in terms of Γ, Equation (5.93) simplifies to

$$\sigma \frac{d^2\omega}{d\tilde{u}^2} + \frac{\sigma_d}{k}\frac{dk}{d\tilde{u}}\frac{d\omega}{d\tilde{u}} + \left[\alpha - \left(\beta_o - 2\beta_i^* \xi^* M_\tau^2 \Gamma\right)\Gamma^2\right]\frac{\bar{\rho}\,\omega}{\bar{\rho}_w u_\tau^2 \Gamma} = 0 \tag{5.98}$$

Combining Equations (5.94) and (5.95) yields the density as a function of velocity and Γ.

$$\frac{\bar{\rho}_w}{\bar{\rho}} = \frac{1 - \frac{(\gamma-1)}{2} Pr_T M_\tau^2 \left[\left(\frac{\tilde{u}}{u_\tau}\right)^2 + \frac{2q_w}{\rho_w u_\tau^3}\left(\frac{\tilde{u}}{u_\tau}\right)\right]}{1 + (\gamma - 1) Pr_T \sigma^* \Gamma M_\tau^2} \tag{5.99}$$

Equation (5.99) assumes a more compact form if we introduce the freestream velocity, U_∞. A bit more algebra yields

$$\frac{\bar{\rho}_w}{\bar{\rho}} = \frac{1 + Bv - A^2 v^2}{1 + (\gamma - 1) Pr_T \sigma^* \Gamma M_\tau^2} \tag{5.100}$$

where

$$\left.\begin{aligned} v &= \tilde{u}/U_\infty \\ A^2 &= \tfrac{(\gamma-1)}{2} Pr_T M_\infty^2 (\tilde{T}_\infty / \tilde{T}_w) \\ B &= -Pr_T q_w U_\infty / (c_p \tilde{T}_w \tau_w) \end{aligned}\right\} \tag{5.101}$$

Using Equations (5.97), (5.100) and (5.101), and retaining terms up to $O(M_\tau^2)$, Equation (5.98) assumes the following form,

$$\frac{d^2\omega}{dv^2} + \frac{\sigma_d}{\sigma}\left[\frac{B - 2A^2 v}{1 + Bv - A^2 v^2}\right]\frac{d\omega}{dv} - \left[\frac{\kappa_\omega^2 (U_\infty/u_\tau)^2}{1 + Bv - A^2 v^2}\right]\omega = 0 \tag{5.102}$$

where the constant κ_ω is defined by

$$\kappa_\omega^2 = \kappa^2 - \left[\frac{(2 + \alpha + \beta_o/\beta_i^*)\xi^*}{\sigma} + \frac{(\gamma - 1) Pr_T (3\alpha - \beta_o/\beta_i^*)\sigma^*}{2\sigma}\right] M_\tau^2 + \cdots \tag{5.103}$$

and κ is Kármán's constant. Because $U_\infty/u_\tau \gg 1$, we can use the WKB method [see Kevorkian and Cole (1981) or Wilcox (1995a)] to solve Equation (5.102). Noting that ω decreases as $\tilde{u}/U_\infty$ increases, the asymptotic solution for ω is

$$\omega \sim C_0 \left[1 + Bv - A^2 v^2\right]^{(1 - 2\sigma_d/\sigma)/4} \exp\left[-\kappa_\omega u^*/u_\tau\right] \tag{5.104}$$

where C_0 is a constant of integration and u^* is defined by

$$\frac{u^*}{U_\infty} = \frac{1}{A}\left[\sin^{-1}\left(\frac{2A^2 v - B}{\sqrt{B^2 + 4A^2}}\right) + \sin^{-1}\left(\frac{B}{\sqrt{B^2 + 4A^2}}\right)\right] \tag{5.105}$$

The second $\sin^{-1}$ term is needed to ensure $u^* = 0$ when $v = 0$. Combining Equations (5.84), (5.95) and (5.104), we can relate velocity and distance, y.

$$\int \left[1 + Bv - A^2 v^2\right]^{-(1 - 2\sigma_d/\sigma)/4} \exp\left[\kappa_\omega u^*/u_\tau\right] dv \sim \frac{C_0 y}{\Gamma U_\infty} \tag{5.106}$$

We integrate by parts to generate the asymptotic expansion of the integral in Equation (5.106) as $U_\infty/u_\tau \to \infty$. Hence,

$$\left[1 + Bv - A^2 v^2\right]^{(1 + 2\sigma_d/\sigma)/4} \exp\left[\kappa_\omega u^*/u_\tau\right] \sim \frac{\kappa_\omega C_0 y}{\Gamma u_\tau} \tag{5.107}$$

Finally, we set the constant of integration $C_0 = \Gamma u_\tau^2/(\kappa_\omega \nu_w)$. Taking the natural log of Equation (5.107), we conclude that

$$\frac{u^*}{u_\tau} \sim \frac{1}{\kappa_\omega} \ell n \left(\frac{u_\tau y}{\nu_w} \right) + C_\omega \tag{5.108}$$

The quantity C_ω is the effective "constant" in the law of the wall defined by

$$C_\omega = C + \frac{1}{\kappa_\omega} \ell n \left(\frac{\bar{\rho}}{\bar{\rho}_w} \right)^{(1+2\sigma_d/\sigma)/4} = C + \frac{1}{\kappa_\omega} \ell n \left(\frac{\bar{\rho}}{\bar{\rho}_w} \right)^{3/8} \tag{5.109}$$

where C is a true constant and we use the fact that $\sigma_d = 1/8$ and $\sigma = 1/2$.

Most of the analysis above holds for the k-ϵ model. The only significant difference is in the ϵ equation which is as follows.

$$\sigma_\epsilon^{-1} \frac{d}{dy} \left[\mu_T \frac{d\epsilon}{dy} \right] + C_\mu C_{\epsilon 1} \bar{\rho} k \left(\frac{d\tilde{u}}{dy} \right)^2 - C_{\epsilon 2} \frac{\bar{\rho} \epsilon^2}{k} = 0 \tag{5.110}$$

Equations (5.95), (5.97) and (5.100) are still valid for the turbulence kinetic energy and density, provided σ^* is replaced by σ_k^{-1}. The transformed equation for ϵ is

$$\frac{d^2\epsilon}{dv^2} - \left[\frac{\kappa_\epsilon^2 (U_\infty/u_\tau)^2}{1 + Bv - A^2 v^2} \right] \epsilon = 0 \tag{5.111}$$

where the constant κ_ϵ is defined by

$$\kappa_\epsilon^2 = \kappa^2 - \left[(C_{\epsilon 1} + C_{\epsilon 2}) \sigma_\epsilon \xi^* + \frac{(\gamma - 1) Pr_T \left(3C_{\epsilon 1} - C_{\epsilon 2} \right) \sigma_\epsilon}{2\sigma_k} \right] M_\tau^2 + \cdots \tag{5.112}$$

In arriving at Equation (5.112), recall from Equation (4.133) that the k-ϵ model's closure coefficients are related by

$$\kappa^2 = \sqrt{C_\mu} \left(C_{\epsilon 2} - C_{\epsilon 1} \right) \sigma_\epsilon \tag{5.113}$$

The asymptotic solution for ϵ is

$$\epsilon \sim C_1 \left[1 + Bv - A^2 v^2 \right]^{1/4} \exp \left[-\kappa_\epsilon u^*/u_\tau \right] \tag{5.114}$$

where C_1 is a constant of integration. Velocity and distance from the surface are related by

$$\int \left[1 + Bv - A^2 v^2 \right]^{3/4} \exp \left[\kappa_\epsilon u^*/u_\tau \right] dv \sim C_1 y \tag{5.115}$$

Consequently, Equation (5.107) is replaced by

$$\left[1 + Bv - A^2 v^2 \right]^{5/4} \exp \left[\kappa_\epsilon u^*/u_\tau \right] \sim C_2 y \tag{5.116}$$

where C_2 is another constant of integration. Finally, the law of the wall for the k-ϵ model is

$$\frac{u^*}{u_\tau} \sim \frac{1}{\kappa_\epsilon} \ell n \left(\frac{u_\tau y}{\nu_w} \right) + C_\epsilon \tag{5.117}$$

where C_ϵ is given by

$$C_\epsilon = C + \frac{1}{\kappa_\epsilon} \ell n \left(\frac{\bar{\rho}}{\bar{\rho}_w} \right)^{5/4} \tag{5.118}$$

Equations (5.108) and (5.117) are very similar to the compressible law of the wall deduced by Van Driest (1951) [cf. Equation (5.4)]. There are two ways in which these equations differ from the Van Driest law.

The first difference is the effective Kármán constants, κ_ω and κ_ϵ, which vary with M_τ according to Equation (5.103) for the k-ω model and according to Equation (5.112) for the k-ϵ model. In terms of each model's closure coefficients, κ_ω and κ_ϵ are given by (for $\gamma = 1.4$ and $M_\tau \ll 1$):

$$\kappa_\omega^2 \sim \kappa^2 \left[1 - (41.33\xi^* + 1.03) M_\tau^2 + \cdots \right] \tag{5.119}$$

and

$$\kappa_\epsilon^2 \sim \kappa^2 \left[1 - (23.92\xi^* + 3.07) M_\tau^2 + \cdots \right] \tag{5.120}$$

Table 5.2 summarizes results obtained in the boundary-layer computations of Section 5.5 for the unmodified k-ω model ($\xi^* = 0$) and for the k-ω model with the Sarkar compressibility term ($\xi^* = 1$). The value of κ_ω for the unmodified model deviates from its implied Kármán constant, $\kappa = 0.40$, by less than 0.5% for freestream Mach numbers between 0 and 5. By contrast, when $\xi^* = 1$, the deviation is as much as 4%. This large a deviation in the effective Kármán constant is consistent with the observed differences between computed and measured skin friction. Similarly, with $M_\tau = 0.05$, κ_ϵ differs from its implied κ by 0.4% and 3.4% for $\xi^* = 0$ and 1, respectively. Thus the Sarkar compressibility term has a somewhat smaller effect on κ for the k-ϵ model relative to the effect on κ for the k-ω model.

Table 5.2: *Effective Kármán Constant for the k-ω Model.*

M_∞	$M_\tau\|_{\xi^*=0}$	κ_ω	$M_\tau\|_{\xi^*=1}$	κ_ω
0	0	0.400	0	0.400
1	0.032	0.399	0.031	0.392
2	0.048	0.399	0.046	0.382
3	0.052	0.398	0.049	0.379
4	0.050	0.398	0.046	0.382
5	0.048	0.399	0.043	0.384

To see why a small perturbation in κ corresponds to a larger perturbation in c_f, differentiate the law of the wall with respect to κ. Noting that $c_f = \frac{1}{2}u_\tau^2/U_\infty^2$, a little algebra shows that

$$\frac{dc_f}{d\kappa} \approx \frac{2}{\kappa}c_f \tag{5.121}$$

Thus, we should expect $\Delta c_f/c_f$ to be double the value of $\Delta\kappa/\kappa$. The numerical results indicate somewhat larger differences in c_f, but the trend is clear.

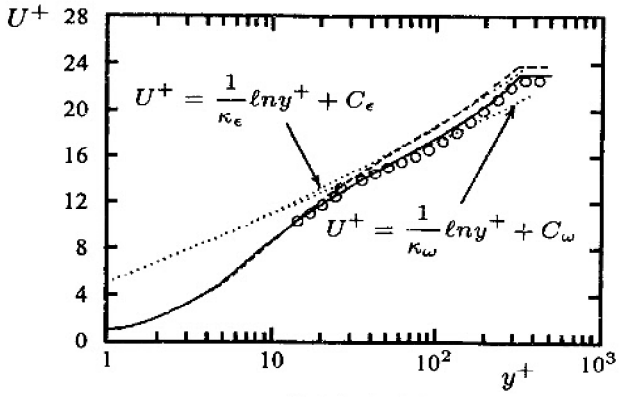

(a) Mach 4.5

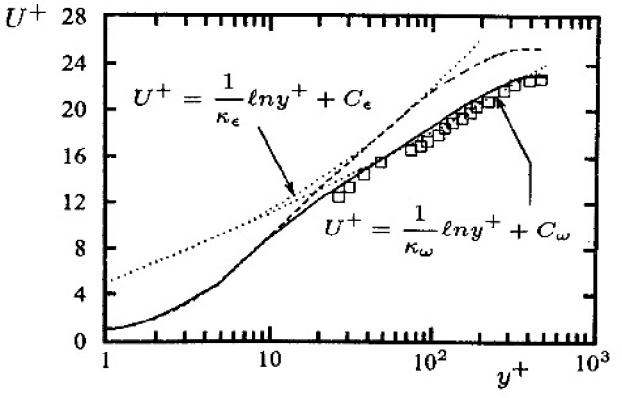

(b) Mach 10.3

Figure 5.3: *Computed and measured velocity profiles for compressible flat-plate boundary layers:* —— *Wilcox (2006) k-ω;* - - - *Chien k-ϵ;* ○ *Coles;* □ *Watson.*

The second difference between Equations (5.108) and (5.117) and the Van Driest compressible law of the wall is in the effective variation of the "constants" C_ω and C_ϵ with $(\bar{\rho}/\bar{\rho}_w)$. Because the exponent is only 3/8 for the k-ω model, the effect is minor. By contrast, the exponent is 5/4 for the k-ϵ model. This large an exponent has a much stronger effect on predicted boundary-layer properties. Figure 5.3 compares computed and measured [Fernholz and Finley (1981)] velocity profiles for adiabatic-wall boundary layers at Mach numbers 4.5 and 10.3.

Computed results are for the Wilcox (2006) k-ω model and for Chien's (1982) low-Reynolds-number k-ϵ model. Equations (5.108) and (5.117) are also shown to underscore the importance of each model's variable "constant" in the compressible law of the wall.

These results are consistent with the analysis of Huang, Bradshaw and Coakley (1992), which shows how poorly the k-ϵ model performs for compressible boundary layers. Since $\bar{\rho}/\bar{\rho}_w > 1$ for all but strongly cooled walls, compressibility increases the model's "constant" in the law of the wall with a corresponding decrease in c_f. The Sarkar and Zeman terms will thus amplify this inherent deficiency of the k-ϵ model.

5.6.2 The Effect of Cross Diffusion

Recall that the ϵ equation is equivalent to the ω equation with a cross-diffusion coefficient $\sigma_d = 2\sigma$ [see Equations (4.101) and (4.102)]. Thus, both the k-ω and k-ϵ models predict that the constant in the compressible law of the wall is

$$C_\omega = C + \frac{1}{\kappa_\omega} \ell n \left(\frac{\bar{\rho}}{\bar{\rho}_w} \right)^{(1+2\sigma_d/\sigma)/4} \tag{5.122}$$

which yields the exponent of 5/4 in Equation (5.118). Clearly, the presence of a cross-diffusion term in the ω equation increases the value of C_ω.

To illustrate the impact of cross diffusion on compressible boundary-layer predictions, Table 5.3 lists the exponent $(1 + 2\sigma_d/\sigma)/4$ for several k-ω models and the k-ϵ model. With no cross-diffusion term, the Wilcox (1988a) model has the smallest exponent of the models listed, and thus the smallest deviation from the compressible law of the wall. The newer Wilcox (2006) version increases the exponent from 1/4 to 3/8, which proves to be of no great consequence. The exponent is 3/4 for the model developed by Kok, which will cause nontrivial distortion. Hellsten's (2005) k-ω model and the k-ϵ model feature values of 1.193 and 5/4, respectively, which are totally unacceptable for Mach numbers in excess of about 3.

Table 5.3: *Exponent in the Compressible Law of the Wall "Constant".*

Model	σ_d	σ	$(1 + 2\sigma_d/\sigma)/4$
Wilcox (1988a)	0	0.500	0.250
Wilcox (2006)	0.125	0.500	0.375
Kok (2000)	0.500	0.500	0.750
Hellsten (2005)	1.000	0.530	1.193
k-ϵ	1.538	0.769	1.250

To put these results in proper perspective, don't lose sight of the fact that the k-ϵ model requires the use of either wall functions or viscous damping functions in order to calculate wall-bounded flows. If these functions have an effect that persists well into the log layer — as they do for Chien's model — it may be possible to suppress the k-ϵ model's inherent flaws at low Reynolds numbers. However, the perturbation analysis above shows that such a model will not be asymptotically consistent with the compressible law of the wall at high Reynolds numbers. In effect, such a model would have compensating errors that fortuitously yield reasonably close agreement with the law of the wall at low Reynolds numbers.

Zhang et al. (1993) provide an example of such compensating errors with their low-Reynolds-number k-ϵ model that yields close agreement with constant-pressure boundary layer data for Mach numbers up to 10. The model is based on the work of Coleman and Mansour (1991), which shows that the exact Favre-averaged equation for solenoidal dissipation, ϵ_s, includes a term proportional to the rate of change of the kinematic viscosity, $\bar{\nu}$, viz.,

$$\bar{\rho}\frac{d\epsilon_s}{dt} = \frac{\bar{\rho}\epsilon_s}{\bar{\nu}}\frac{d\bar{\nu}}{dt} + \cdots \quad \Longrightarrow \quad \bar{\rho}\bar{\nu}\frac{d}{dt}\left(\frac{\epsilon_s}{\bar{\nu}}\right) = \cdots \tag{5.123}$$

This corresponds to an effective change of dependent variable in the ϵ_s equation. Assuming a power-law for viscosity, i.e., $\bar{\mu} \propto \tilde{T}^n$, the effective rescaled dependent variable would be $\bar{\rho}^{(1+n)}\epsilon_s$. Correspondingly, the exponent 5/4 in Equation (5.118) would become $(n + 1/4)$. For a typical value $n = 7/10$, the new coefficient would be 0.95. Hence this term should yield only a slight improvement in the model's distorted law of the wall. Through a series of closure approximations, Zhang et al. combine this and other terms to arrive at a rescaling that effectively leads to using $\bar{\rho}^{-0.61}\epsilon_s$. This corresponds to replacing the exponent 5/4 by -1.36, which would yield even more distortion.

As a final comment, had we used $\rho\epsilon$ as the dependent variable in Equation (5.110) instead of ϵ, the exponent 5/4 in Equation (5.118) would be reduced to 1/4. This change would improve k-ϵ model predictions for compressible boundary layers. The effect of this rescaling on the mixing layer is unclear.

5.7 Compressible Boundary Layers

Most turbulence models are capable of providing reasonably accurate predictions for constant-pressure, adiabatic-wall boundary layers provided the Mach number does not exceed about 5. Similar to the incompressible situation, adverse pressure gradients continue to be anathema to the k-ϵ model, while presenting no major problem for the k-ω model. When surface heat transfer is present, model predictions often show nontrivial discrepancies from measured values.

Algebraic models such as the Cebeci-Smith and Baldwin-Lomax models (see Subsections 3.4.1 and 3.4.2) require no special compressibility corrections. For the sake of clarity, recall that the Cebeci-Smith model uses the velocity thickness, δ_v^*, defined in Equation (3.115) for both compressible and incompressible flow. The velocity thickness differs from the displacement thickness, δ^*, which is defined for compressible flows by

$$\delta^* = \int_0^\infty \left(1 - \frac{\bar{\rho}}{\bar{\rho}_e}\frac{\tilde{u}}{\tilde{u}_e}\right) dy \tag{5.124}$$

The primary reason algebraic models should fare well for compressible boundary layers without special compressibility modifications is illustrated by Maise and McDonald (1967). Using the best experimental data of the time for compressible boundary layers, they inferred the mixing-length variation. Their analysis shows that for Mach numbers up to 5:

- Velocity profiles for adiabatic walls correlate with the incompressible profile when the Van Driest (1951) scaling is used, i.e.,

$$\frac{u^*}{U_\infty} = \frac{1}{A}\sin^{-1}\left(A\frac{\tilde{u}}{U_\infty}\right), \qquad A^2 = \frac{(\gamma-1)}{2}M_\infty^2(\tilde{T}_\infty/\tilde{T}_w) \tag{5.125}$$

- The Van Driest scaling fails to correlate compressible velocity profiles when surface heat transfer is present, especially for very cold surfaces.

- The classical mixing length is independent of Mach number.

Using singular-perturbation methods, Barnwell (1992) shows that algebraic models are consistent with the Maise-McDonald observations. Many researchers have applied the Cebeci-Smith model to compressible boundary layers, showing excellent agreement with measurements for adiabatic walls and somewhat larger differences when surface heat transfer is present. The Baldwin-Lomax model yields similar predictions.

Because the length scale employed in most older k-equation oriented one-equation models is patterned after the mixing length, they should also be expected to apply to compressible flows without ad hoc compressibility modifications. This is indeed the case, especially for these and for newer models, which have been designed for compressible-flow applications.

As we have seen in the last subsection, the issue is more complicated for two-equation turbulence models. The log-layer solution indicates that the length scale for the k-ω and k-ϵ models varies linearly with distance from the surface, independent of Mach number. The models even predict the Van Driest velocity scaling. Thus, two-equation models are consistent with two of the most important observations made by Maise and McDonald, at least in the log layer.

However, we have also seen that the ϵ equation includes a nonphysical density effect that distorts the model's log-layer structure [see Equations (5.117) and (5.118)], and precludes a satisfactory solution. By contrast, the ω equation is entirely consistent with the Maise-McDonald observations. As shown in Figures 5.2 and 5.3, the k-ω model provides good quantitative agreement with measurements for Mach numbers up to at least 10.

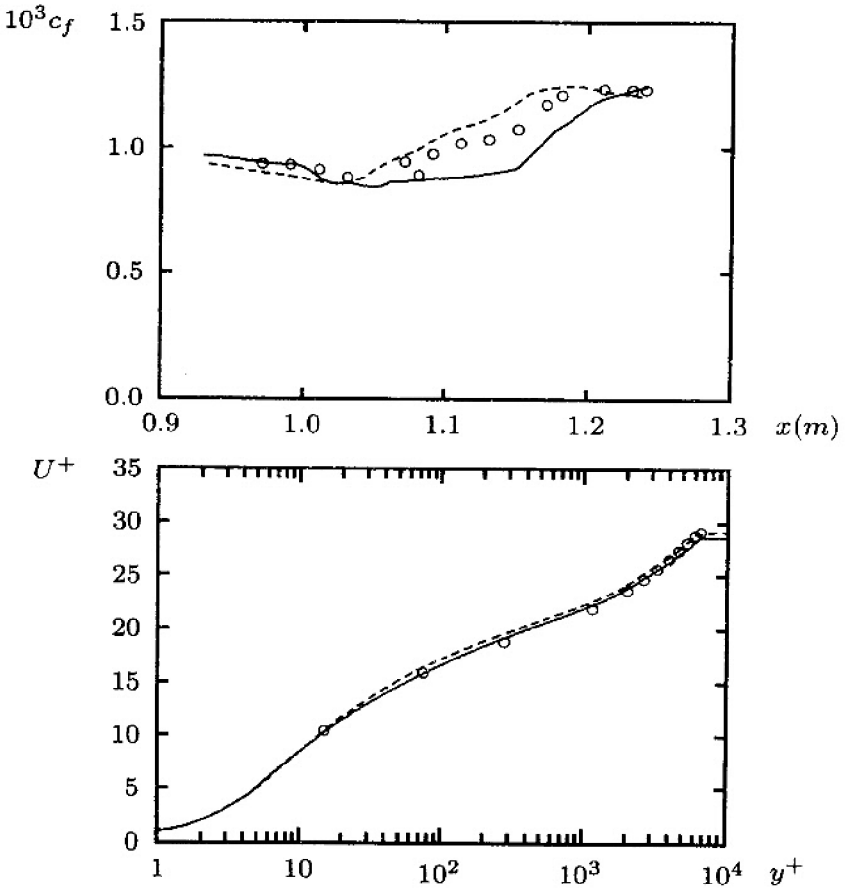

Figure 5.4: *Comparison of computed and measured skin friction and velocity profile for a Mach 4, adiabatic-wall boundary layer with an adverse pressure gradient:* —— *Wilcox (2006) k-ω model;* - - - *Chien k-ϵ model;* ○ *Zwarts.*

Turning to effects of pressure gradient, Figure 5.4 compares computed and measured skin friction and velocity profiles a compressible boundary layer with adverse pressure gradient, corresponding to a Mach 4, adiabatic-wall experiment conducted by Zwarts [see Kline et al. (1981) — Flow 8411]. The figure includes computed results for the Wilcox (2006) k-ω model without viscous corrections and for the Chien (1982) k-ϵ model. Neither computation has been done with a compressibility correction. As shown, k-ω model skin friction is within 10% of measured c_f. Consistent with results shown in Figure 5.3(a), the k-ϵ model's skin

friction is 8% lower than measured at the beginning of the computation where the Mach number is 4. Because the flow is decelerating, the Mach number decreases with distance, falling to 3 by the end of the run. As a result, $\bar{\rho}_e/\bar{\rho}_w$ is only half its upstream value, and the corresponding distortion of the k-ϵ model's log-layer velocity profile is greatly reduced. Consequently, the k-ϵ model's velocity profile is fortuitously in close agreement with the measured profile.

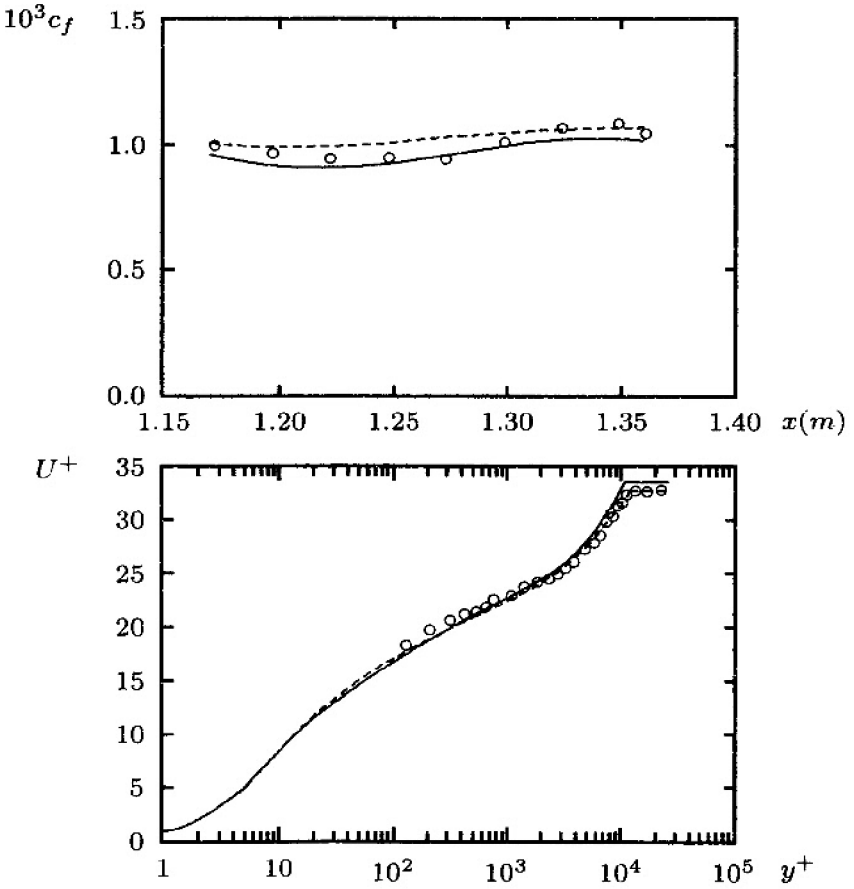

Figure 5.5: *Comparison of computed and measured flow properties for a Mach 2.65, heated-wall boundary layer with an adverse pressure gradient:* — *Wilcox (2006) k-ω model;* - - - *Chien k-ϵ model;* ○ *Fernando and Smits.*

Figure 5.5 presents a similar comparison for a Mach 2.65 boundary layer [Fernholz and Finley (1981)] with adverse pressure gradient and mild surface heating. The ratio of wall temperature to the adiabatic-wall temperature, T_w/T_{aw}, varies between 1.07 and 1.13 for the flow. Again, because the Mach number is in the low supersonic range, the density term in the k-ϵ model's law of the wall is small. The value of $\kappa_\epsilon^{-1} ln(\bar{\rho}/\bar{\rho}_w)^{5/4}$ ranges between 0.50 at $y^+ = 100$ to 1.45 at $y^+ = 5000$. By comparison, the distortion in the k-ω model's law of the wall is less than a third of these values.